





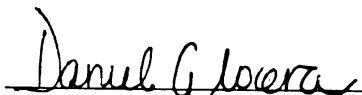
This is to certify that the  
dissertation entitled  
The Role of Solvation Dynamics in  
Inverted Region Electron Transfer

presented by

Jeffrey M. Zaleski

has been accepted towards fulfillment  
of the requirements for

Ph.D. degree in Chemistry

  
Major professor

Date 22 September 1993

**LIBRARY  
Michigan State  
University**

**PLACE IN RETURN BOX** to remove this checkout from your record.  
**TO AVOID FINES** return on or before date due.

| DATE DUE | DATE DUE | DATE DUE |
|----------|----------|----------|
| _____    | _____    | _____    |
| _____    | _____    | _____    |
| _____    | _____    | _____    |
| _____    | _____    | _____    |
| _____    | _____    | _____    |
| _____    | _____    | _____    |
| _____    | _____    | _____    |

**MSU is An Affirmative Action/Equal Opportunity Institution**

c:\circ\datedue.pm3-p.1

**THE ROLE OF SOLVATION DYNAMICS IN INVERTED REGION  
ELECTRON TRANSFER REACTIONS**

**By**

**Jeffrey M. Zaleski**

**A DISSERTATION**

**Submitted to  
Michigan State University  
in partial fulfillment of the requirements  
for the degree of**

**DOCTOR OF PHILOSOPHY**

**Department of Chemistry**

**1993**



TH

T

porphyr  
(acetate  
selected  
spectros  
H<sub>2</sub>), a zi  
and a zi  
produce  
excitatio  
ion-pair  
the ion-  
which is  
profiles.  
energeti  
H<sub>2</sub>(=O)  
recombi  
rate cons  
(ΔG<sub>CR</sub> =  
Cu(=C(

## ABSTRACT

### THE ROLE OF SOLVATION DYNAMICS IN INVERTED REGION ELECTRON TRANSFER

By

Jeffrey M. Zaleski

The charge recombination (CR) kinetics of cofacially linked porphyrin-porphyrin and porphyrin-chlorin ion-pairs in a variety of solvents (acetates, nitriles, dichloromethane, acetone, dimethylformamide, and selected alcohols) have been investigated by picosecond transient absorption spectroscopy. The ion-pairs of a magnesium/free base diporphyrin ( $\text{Mg}-\text{H}_2$ ), a zinc porphyrin/free base dicyanomethide chlorin ( $\text{Zn}-\text{H}_2(=\text{C}(\text{CN})_2)$ ), and a zinc porphyrin/ $\text{Cu}(\text{II})$  dicyanomethide chlorin ( $\text{Zn}-\text{Cu}(=\text{C}(\text{CN})_2)$ ) are produced from a  $\pi\pi^*$  excited state of the heterodimers within 6 ps of excitation. For a zinc-porphyrin/free base ketochlorin ( $\text{Zn}-\text{H}_2(=\text{O})$ ), an ion-pair intermediate was observed only in dichloromethane. In each case, the ion-pair is clearly distinguished in the transient absorption spectrum, which is a composite of the respective radical cation and anion absorption profiles. Consistent with electrochemical and steady-state spectral data, the energetically favored charge-separated species were  $\text{Mg}^+-\text{H}_2^-$ ,  $\text{Zn}^+-\text{H}_2(=\text{O})^-$ ,  $\text{Zn}^+-\text{H}_2(=\text{C}(\text{CN})_2)^-$ , and  $\text{Zn}^+-\text{Cu}(=\text{C}(\text{CN})_2)^-$ . Charge-recombination occurs in the Marcus inverted region and, as expected, the rate constants of the more highly inverted  $\text{Mg}^+-\text{H}_2^-$  charge recombination ( $\Delta G_{\text{CR}} = -1.9$  V) are slower than those of  $\text{Zn}^+-\text{H}_2(=\text{C}(\text{CN})_2)^-$  or  $\text{Zn}^+-\text{Cu}(=\text{C}(\text{CN})_2)^-$  charge recombinations ( $\Delta G_{\text{CR}} = -1.6$  V). We find that the

observ

system

$(k_{\text{obs}}(N$

$4.6 \times 10$

$k_{\text{obs}}(\text{CF}$

$1.5 \times 10$

correlat

same

porphy

$\text{Cu}(\text{=C}$

solvents

the sam

finds its

dominat

recomb

consiste

controlle

observed CR rate constants ( $k_{\text{obs}}(\text{CR})$ ) are strongly solvent dependent for all systems. Although they are slow with respect to solvent motion ( $k_{\text{obs}}(\text{Mg}^+ - \text{H}_2^-) = 0.6 - 4.0 \times 10^9 \text{ s}^{-1}$ ;  $k_{\text{obs}}(\text{Zn}^+ - \text{Cu}(=\text{C}(\text{CN})_2)^-) = 1.0 - 4.6 \times 10^{10} \text{ s}^{-1}$ ;  $k_{\text{obs}}(\text{Zn}^+ - \text{H}_2(=\text{C}(\text{CN})_2)^-) = 1.6 - 8.3 \times 10^{10} \text{ s}^{-1}$ ), the values of  $k_{\text{obs}}(\text{CR})$  correlate with the inverse of the solvent relaxation time ( $1/\tau_s = 1.5 \times 10^{10} - 1.6 \times 10^{12} \text{ s}^{-1}$ ). For the  $\text{Mg}^+ - \text{H}_2^-$  cofacial pair, a linear correlation between  $k_{\text{obs}}(\text{CR})$  and  $1/\tau_s$  is observed only when solvents of the same series are considered. This is not the case for the Zn-porphyrin/dicyanomethide chlorin heterodimers. The  $k_{\text{obs}}(\text{CR})$  of  $\text{Zn}^+ - \text{Cu}(=\text{C}(\text{CN})_2)^-$  linearly depends on  $1/\tau_s$  for all non-nitrogen donating solvents, whereas the linear correlation observed for  $\text{Zn}^+ - \text{H}_2(=\text{C}(\text{CN})_2)^-$  is the same irrespective of the solvent series. The solvent dependence of CR finds its origins in dynamics effects, with the overall rates for CR being dominated by a diffusional activation barrier. The kinetics of the charge-recombination of the heterodimers in the various solvent systems are self-consistent within the framework of theoretical predictions for solvent-controlled adiabatic electron transfer reactions.

in  
con  
Wi  
care

the e  
every  
glue  
funct.  
worki

mainta  
to be d  
were us  
you fix  
grateful

Th  
overlook  
bail me o  
Colleen  
the moon  
commend  
was alw

## ACKNOWLEDGMENTS

During my five year stay at Michigan State, I have had to privilege to interact with many intelligent, helpful and caring people. They have all contributed in some way to my personal and scientific development. Without the friendships developed from these interactions, my graduate career would not have been nearly as enjoyable.

I was extremely fortunate to have the ever so resourceful services of the electronic designer Marty Raab. He provided me with “Marty Boxes” of every shape, size and function imaginable. Many times his devices were the glue that held the scotch tape on, that was keeping a piece of an instrument functioning. His patience was an important part of finally getting things working correctly.

The machine, glass and electronic shops were all instrumental in maintaining supporting equipment to do that one last experiment that needed to be done a week ago for the paper due a month prior. Their contributions were usually in response to the same type of problem, “This is broken, can you fix it.....today?” They were always incredibly understanding and I am grateful for their swiftness in turning around jobs.

The support of many friends from within the department cannot be overlooked. Hak-Hyun Nam was always there to provide a good laugh and bail me out of quantum mechanics problem sets at 3 am during my first year. Colleen Partigianoni initiated me into the Nocera group by showing me what the moon really looks like over Rt. 96. In addition to deserving special commendation for his perseverance as my four-year roommate, Liam Moran was always helpful for providing solid scientific feedback, federal

expressing forgotten poster figures or for introducing me to new homebrew recipes in order to better analyze those troubling experimental results, or lack thereof. Tun-Li Shen and Jerry Godbout are thanked for their contributions to the scientifically rigorous LASER Lab presentation entitled Beer Spectroscopy. The friendship, bagels and coffee provided by Tom Halasinski during those last “plenty friendly” months cannot go without mention. I am also grateful for his help in preparing final copies of figures etc. such that everything was completed on time (relatively).

The knowledge and friendship gained through interactions with other group members was priceless. I would like to especially thank JP Kirby, Zoe Pikramenou and Janice Kadis for many enjoyable discussions, both scientific and personal. Dan Engebretsen, Ann Macintosh and Adrian Ponce also deserve recognition for allowing me to collaborate and learn about their science. I still wonder why none of those experiments ever seemed to work quite right.

I am exceptionally grateful to Professor Chang for his gracious supply of compounds and his willingness to provide much needed background in porphyrin chemistry at any time. I am equally thankful for Professor Cukier’s tireless efforts to help me understand the underpinnings of ET theory. His comments were greatly appreciated, as they were always clear and insightful.

My advisors, George Leroi and Dan Nocera, have shown me how to truly think about science. George’s sense of diplomacy and constant encouragement as well as Dan’s enthusiasm and relentless rigor provided the perfect combination of perspective and focus needed to maintain a healthy attitude. When that balance was lost, both extended the necessary gestures required to restore normalcy. Whereas gratitude for George’s comments

was  
requir  
serve  
indebt

times  
unders  
Their s  
result, I

C  
stay at  
thought  
confider  
from m  
instrume  
always t  
graduate  
for each  
solving  
fostered  
scientific



was usually immediate, appreciation for Dan's remarks occasionally required time to develop. Regardless, their wisdom and experience always served as a faithful guide through dark scientific passages. I am deeply indebted to both of them for all they have done.

The strength and love of my parents has always made the difficult times seem bearable. I am especially thankful for their patience and understanding during those abbreviated visits at times of scientific crisis. Their support has helped me to maintain a strong commitment and as a result, I owe a large part of everything I have and will accomplish to them.

Claudia has probably had the greatest impact on my life during my stay at Michigan State. She taught me how to push myself harder than I thought possible and to strive to be independent. She also helped me to gain confidence in my abilities, yet be more self-criticizing, so that I could learn from my mistakes. I learned many of these things early on, when our instrument was a mess and neither of us had any idea why. Although not always the most enjoyable, those days were by far the most important to my graduate career, both personally and scientifically. The trust we developed for each others opinions, as well as our own, has always been helpful in solving new and challenging problems. The long-lasting friendship that fostered from that trust has since far surpassed the rewards of any of those scientific accomplishments.

LIST O

LIST O

CHAPT

## TABLE OF CONTENTS

|                      |    |
|----------------------|----|
| LIST OF TABLES.....  | x  |
| LIST OF FIGURES..... | xi |

### CHAPTER I INTRODUCTION

|  |    |
|--|----|
| A. BACKGROUND .....  | 1  |
| B. CHARGE SEPARATION IN PHOTOSYNTHESIS .....                                 | 2  |
| C. CHARGE SEPARATION IN NATURAL SYSTEMS .....                                | 9  |
| D. PREVALENCE OF MEDIUM EFFECTS IN<br>CHARGE SEPARATION.....                 | 12 |
| E. MOLECULAR DYNAMICS SIMULATIONS.....                                       | 14 |
| F. EXPERIMENTAL TECHNIQUES FOR ENVIRONMENTAL<br>EFFECTS ON CHARGE SEPARATION |    |
| 1. X-RAY DIFFRACTION.....  | 16 |
| 2. NMR TECHNIQUES.....   | 17 |
| 3. MÖSSBAUER SPECTROSCOPY.....   | 17 |
| 4. ULTRAFAST LASER KINETICS.....   | 18 |
| G. SOLVENT DYNAMICS .....  | 19 |
| 1. THEORETICAL MODELS OF ET.....   | 20 |
| 2. EXPERIMENTAL INVESTIGATIONS OF<br>SOLVATOCHROISM.....                     | 27 |
| H. SOLVENT DYNAMICS IN ACTIVATED ET.....                                     | 32 |
| 1. STRATEGY OF ACTIVATED CHARGE<br>SEPARATED STATES.....                     | 33 |



|  |     |
|--|-----|
| 2. GUST AND MOORE SYSTEMS.....   | 34  |
| 3. OTHER D—A RIGID ASSEMBLIES.....   | 35  |
| <br><b>CHAPTER II EXPERIMENTAL METHODS</b>   |     |
| A. SAMPLE PREPARATION .....  | 47  |
| 1. COFACIAL DIMER SYNTHESIS.....   | 47  |
| 2. DRIVING FORCE DETERMINATION<br>VIA CYCLIC VOLTAMMETRY.....                                      | 49  |
| 3. SAMPLE PREPARATION FOR<br>PHOTOPHYSICAL MEASUREMENTS.....                                       | 50  |
| B. PICOSECOND TRANSIENT ABSORPTION .....   | 52  |
| 1. APPARATUS.....  | 52  |
| 2. GENERAL ALIGNMENT PROCEDURE.....  | 63  |
| 3. TRANSIENT ABSORPTION<br>DATA ANALYSIS.....  | 68  |
| C. NANOSECOND TRANSIENT ABSORPTION.....  | 69  |
| D. TIME-CORRELATED PHOTON COUNTING.....  | 70  |
| <br><b>CHAPTER III THE ROLE OF SOLVATION DYNAMICS IN ACTIVATED<br/>ELECTRON TRANSFER REACTIONS</b> |     |
| A. BACKGROUND.....   | 72  |
| B. RESULTS   |     |
| 1. ELECTROCHEMISTRY.....   | 79  |
| 2. ELECTRONIC SPECTROSCOPY .....   | 82  |
| 3. TRANSIENT ABSORPTION SPECTROSCOPY...  | 92  |
| 4. SOLVENT DYNAMICS.....   | 106 |
| C. DISCUSSION.....   | 108 |

CHAPTER

CHAPTER

LIST OF

|                                |  |            |
|--------------------------------|--|------------|
| <b>CHAPTER IV</b>              | <b>THE ROLE OF SOLVATION DYNAMICS IN NEAR-<br/>ACTIVATIONLESS ELECTRON TRANSFER REACTIONS.</b> |            |
| <b>A.</b>                      | <b>BACKGROUND.....</b>   | <b>114</b> |
| <b>B.</b>                      | <b>RESULTS</b>   |            |
| 1.                             | ELECTROCHEMISTRY.....  | 121        |
| 2.                             | ELECTRONIC SPECTROSCOPY .....  | 121        |
| 3.                             | TRANSIENT ABSORPTION SPECTROSCOPY..  | 131        |
| 4.                             | SOLVENT DYNAMICS.....  | 149        |
| <b>C.</b>                      | <b>DISCUSSION.....</b>   | <b>149</b> |
| <b>CHAPTER V</b>               | <b>CONCLUDING REMARKS .....</b>  | <b>154</b> |
| <b>LIST OF REFERENCES.....</b> |  | <b>161</b> |

Tab

I

II

III

IV

V

VI

VI



## LIST OF TABLES

| Table  | Page |
|--|------|
| I Properties of Internal Motions of Proteins .....   | 13   |
| II Electrochemical Data for Mg and Free Base Model Porphyrins<br>in Different Solvent .....  | 80   |
| III Selected Photophysical Properties of the Heterodimers in<br>Dichloromethane .....  | 91   |
| IV Luminescence Lifetimes of Mg—H <sub>2</sub> and Zn—H <sub>2</sub> (=O) in<br>Selected Solvents .....  | 95   |
| V Optical Properties of Zn—H <sub>2</sub> (=C(CN) <sub>2</sub> ) and Zn—<br>Cu(=C(CN) <sub>2</sub> ) Porphyrin-Chlorin Heterodimers in<br>CH <sub>2</sub> Cl <sub>2</sub> .....              | 128  |
| VI Luminescence Lifetimes of Zn—H <sub>2</sub> (=C(CN) <sub>2</sub> ) and Zn—<br>Cu(=C(CN) <sub>2</sub> ) in Selected Solvents .....   | 129  |
| VII Comparison of Solvent Dependence of the Charge<br>Recombination Rate Constants of Mg—H <sub>2</sub> ., Zn—<br>Cu(=C(CN) <sub>2</sub> ) and Zn—H <sub>2</sub> (=C(CN) <sub>2</sub> )..... | 156  |

Figur

1

2

3

4

5  
I  
s  
P  
to  
C

## LIST OF FIGURES

| <b>Figure</b> |   | <b>Page</b> |
|---------------|---|-------------|
| 1             | The electron transport chain in the photosynthetic RC of purple bacteria (top), together with the approximate standard reduction potentials of the RC components (bottom).....  | 4           |
| 2             | Schematic of the thylakoid membrane of chloroplast showing components of the ET chain (top) and the energetics or Z-scheme for photosynthetic ET in green plants (bottom).....  | 6           |
| 3             | Illustration of the dependence of the electron transfer rate constant on the driving force for the reaction as described by Marcus' classical expression. This defines three regions of electron transfer, normal, activationless and inverted.....   | 23          |
| 4             | Diabatic representation of harmonic potential surfaces of a common frequency, displaced vertically by $\Delta G^\circ$ and horizontally such that the reorganization energy is $\lambda$ , crossing at $x^*$ in (a) the normal region and (b) the inverted ET regimes. The length $x_{ET}$ characterizes the region over which the surfaces are coupled; as $x_{ET}$ shrinks to zero the transition becomes localized to the crossing $x^*$ . The curved arrow indicates the motion along the reaction coordinate with rate characterized by $k_D$ and the straight arrow indicates the crossing motion with rate constant $k_{ET}$ . Figure taken from ref. 70. .... | 25          |
| 5             | Illustration depicting transient solvation of a polar excited state (top), where $X_G^{eq}$ and $X_E^{eq}$ represent the solvent polarization in the ground and excited state, respectively, together with the resulting fluorescence Stokes shift of the Coumarin 153 emission band (bottom).....  | 30          |

1

11

12

13  
S  
s  
n

14 D  
nr  
de  
ins

|    |  |    |
|----|--|----|
| 6  | Original configuration of the picosecond laser system, excimer pulsed-dye amplifier and transient absorption spectrometer.....   | 54 |
| 7  | Current configuration of the picosecond laser system, regenerative amplifier and transient absorption spectrometer..   | 57 |
| 8  | Cofacial porphyrin-porphyrin and porphyrin-chlorin probe molecules used in solvation dynamics studies of activated ET reactions. The diporphyrins are denoted Mg—H <sub>2</sub> and Mg—Cu while the chlorin is designated as Zn—H <sub>2</sub> (=O).....         | 75 |
| 9  | Electronic absorption spectrum of Mg—H <sub>2</sub> in the Soret and Q regions, obtained at sample concentrations of 10 <sup>-5</sup> M in CH <sub>2</sub> Cl <sub>2</sub> . The Q band region is magnified by a factor of 8.....                                | 83 |
| 10 | Electronic absorption spectrum of Mg—Cu in the Soret and Q regions, obtained at sample concentrations of 10 <sup>-5</sup> M in CH <sub>2</sub> Cl <sub>2</sub> . The upper trace shows an 8-fold magnification of the Q band region..                            | 84 |
| 11 | Electronic absorption spectrum of the porphyrin-chlorin complex Zn—H <sub>2</sub> (=O) (10 <sup>-5</sup> M) in (a) <i>n</i> -propyl acetate and (b) CH <sub>2</sub> Cl <sub>2</sub> , at 22 °C. The Q band wavelength region is multiplied by a factor of 8..... | 86 |
| 12 | Emission spectrum of Mg—H <sub>2</sub> and Zn—H <sub>2</sub> (=O) in degassed CH <sub>2</sub> Cl <sub>2</sub> . Samples were prepared in 1 cm quartz cuvettes with an absorbance of 0.1 at λ <sub>exc</sub> = 585 nm. ....                                       | 89 |
| 13 | Luminescence decay of the Mg—Cu diporphyrin following 585 nm sample excitation. The inset shows the decay of the short-lived component, which is essentially instrument response limited. ....   | 90 |
| 14 | Decay of the Mg—H <sub>2</sub> dimer luminescence in CH <sub>2</sub> Cl <sub>2</sub> at 640 nm following 588 nm sample excitation. The lifetimes derived from the biexponential decay kinetics are given in the inset. ....                                      | 93 |

18

19

20

r  
o  
lu  
co  
as  
sta  
ion  
spe

|    |  |     |
|----|--|-----|
| 15 | Luminescence decay of the porphyrin-chlorin complex Zn—H <sub>2</sub> (=O) in CH <sub>2</sub> Cl <sub>2</sub> at 640 nm. Samples were excited at 575 nm with a 6 ps pulse. The emission decays biexponentially with lifetimes shown in the inset... ..   | 94  |
| 16 | Transient absorption spectra of Mg <sup>+</sup> —H <sub>2</sub> <sup>-</sup> in CH <sub>2</sub> Cl <sub>2</sub> at 0, 60, 120, 300, 500, and 1000 ps after sample excitation at 588 nm. Included in the inset is the biexponential fit to the decay of the absorption profile at 665 nm.....   | 97  |
| 17 | Time evolution of the disappearance of the picosecond transient absorption spectrum of the photogenerated Mg <sup>+</sup> —H <sub>2</sub> <sup>-</sup> charge-separated state in <i>n</i> -propyl acetate. The spectra were obtained at 50, 600, 1100, and 2000 ps after sample excitation at 588 nm. The biexponential fit to the decay of the absorption profile at 665 nm is shown as an inset .....  | 98  |
| 18 | Picosecond transient absorption spectra of Zn—H <sub>2</sub> (=O) in (a) CH <sub>2</sub> Cl <sub>2</sub> at 0, 100, 200, 300 and 3000 ps after a 575 nm, 6 ps excitation pulse, and (b) <i>n</i> -propyl acetate recorded at 40, 2000, and 6000 ps after excitation with the same pulse.....   | 100 |
| 19 | Transient absorption spectra of the <sup>1</sup> (ππ*) excited state of Zn—H <sub>2</sub> (=O) in DMF at 0, 500 and 3 ns following 575 nm excitation. The Zn-porphyrin excited state absorbs strongly at 450 nm while the free base ketochlorin is responsible for the excited state features at 500 nm and the intense ground state bleaching at 645 nm. The absorption at 520 nm is characteristic of both the Zn-porphyrin and ketochlorin excited states.....  | 102 |
| 20 | Decay of the <sup>1</sup> (ππ*) state absorption of Zn—H <sub>2</sub> (=O) at 460 nm in DMF. The state decays biexponentially with lifetimes of 300 ps and 4 ns. The latter value is consistent with the luminescence lifetime of Zn—H <sub>2</sub> (=O) as measured by time-correlated single photon counting, while the former is associated with the decay of the 1.5 ns Zn-porphyrin excited state, possibly convolved with a weak contribution from an ion pair intermediate not observed in the transient absorption spectra in the 600-800 nm region..... | 103 |

|    |  |     |
|----|--|-----|
| 21 | Transient absorption spectra of the $^1(\pi\pi^*)$ state of the Mg—Cu diporphyrin complex in <i>n</i> -propyl acetate at 0, 0.2, 1.5 and 4.0 ns after the 588 nm excitation pulse. The decay of the transient absorption at 473 nm is included (inset). . . . .  | 105 |
| 22 | Plot of the observed CR rate constants of $\text{Mg}^+ \text{—} \text{H}_2^-$ in acetone (Ac), dichloromethane (DCM), N,N-dimethylformamide (DMF), propionitrile (PN), <i>n</i> -butyronitrile (BN), <i>n</i> -valeronitrile (VN), and methyl, ethyl, <i>n</i> -propyl, and <i>n</i> -butyl acetates (MeOAc, EtOAc, PrOAc, BuOAc, respectively) vs. the reciprocal of the microscopic relaxation times (taken from reference 76).....  | 107 |
| 23 | Reaction surface diagram for $\text{Mg}^+ \text{—} \text{H}_2^-$ , which is formed from the photoinduced electron transfer of the $^1(\pi\pi^*)$ excited state of Mg—H <sub>2</sub> . Diffusional motion governed by solvent dynamics in the $\text{Mg}^+ \text{—} \text{H}_2^-$ well is represented by the rate constant $k_D$ . The nonadiabatic electron transfer rate for bringing the charge-separated complex to its neutral ground state is denoted by $k_{ET}$ . . . . . | 112 |
| 24 | Probe molecules used to investigate solvation dynamics effects in near-activationless ET reactions. The cofacial porphyrin-chlorin probes are designated as Zn—H <sub>2</sub> (=C(CN) <sub>2</sub> ) and Zn—Cu(=C(CN) <sub>2</sub> ).....  | 119 |
| 25 | Electronic absorption spectra of (a) Zn—H <sub>2</sub> (=C(CN) <sub>2</sub> ) and (b) Zn—Cu(=C(CN) <sub>2</sub> ) in CH <sub>2</sub> Cl <sub>2</sub> .....   | 122 |
| 26 | Electronic absorption spectra of (a) Cu(=C(CN) <sub>2</sub> ) and (b) H <sub>2</sub> (=C(CN) <sub>2</sub> ) in CH <sub>2</sub> Cl <sub>2</sub> . . . . .   | 124 |
| 27 | Luminescence spectra of Zn—H <sub>2</sub> (=C(CN) <sub>2</sub> ) and Zn—Cu(=C(CN) <sub>2</sub> ) in degassed CH <sub>2</sub> Cl <sub>2</sub> . Samples were prepared in 1 cm quartz cuvettes with absorbances of 0.1 at $\lambda_{exc} = 585$ nm. The emission spectrum of Zn—H <sub>2</sub> (=C(CN) <sub>2</sub> ) has been offset for clarity. . . . .   | 126 |



- 28 Luminescence decay of the of  $\text{Zn—H}_2(=\text{C}(\text{CN})_2)$  in *n*-butyl acetate following 575 nm sample excitation with a 6 ps pulse. The inset shows the lifetime components and relative percentages of the decay..... 130
- 29 Transient absorption spectra of  $\text{Zn}^+—\text{H}_2(=\text{C}(\text{CN})_2)^-$  in BuOAc immediately after sample excitation at 575 nm with a 6 ps pulse. Absorption features at 450 and 670 nm are related to the Zn-porphyrin cation, while those at 505 and 745 nm are characteristic of the  $\text{H}_2(=\text{C}(\text{CN})_2)$  anion. Samples were prepared in 2 mm quartz cuvettes at concentrations of  $5 \times 10^{-4}$  M ..... 132
- 30 Transient absorption spectra of the (a) Zn-porphyrin and (b) free base dicyanomethide chlorin at 15 ps (solid) and 5 ns (dashed) in *n*-propyl acetate with 6 ps sample excitation. Samples were prepared at concentrations of  $1 \times 10^{-3}$  M in 2 mm quartz cuvettes..... 133
- 31 Picosecond transient absorption spectra of  $\text{Zn}^+—\text{H}_2(=\text{C}(\text{CN})_2)^-$  in *n*-propyl acetate obtained at pump/probe delay times of 5, 10, 15, 20, 25, 30, 40, 50, 75, and 200 ps. The inset shows the monoexponential decay of the transient absorption of the free base chlorin anion at 750 nm..... 135
- 32 Picosecond transient absorption spectra of  $\text{Zn}^+—\text{H}_2(=\text{C}(\text{CN})_2)^-$  charge separated state in *n*-butyl acetate at 0, 20, 30, 40, 60, 100 and 1000 ps after the 6 ps 575 nm excitation pulse. The transient absorption at 502 nm decays according to unimolecular kinetics with a rate constant  $1.6 \times 10^{10} \text{ s}^{-1}$  as shown by the inset..... 136
- 33 Picosecond transient absorption spectra of  $\text{Zn}^+—\text{H}_2(=\text{C}(\text{CN})_2)^-$  in acetone at 0, 5, 10, 15, 20, 25, 30, 35, 50, 75 and 100 ps after the 6 ps 575 nm excitation pulse. The inset shows the monoexponential decay of the transient absorption of the free base chlorin anion at 750 nm ..... 138

- 34 Transient absorption spectrum Zn—Cu(=C(CN)<sub>2</sub>) in *n*-propyl acetate following 6 ps excitation at 580 nm. The sample was prepared at a concentration of  $5 \times 10^{-4}$  M in a 2 mm quartz cuvette. Spectra are displayed at 15 ps (solid) and 5 ns (dashed) ..... 139
  
- 35 Time evolution of the transient absorption of Zn—Cu(=C(CN)<sub>2</sub>) in degassed *n*-propyl acetate at 0, 5, 10, 15, 20, 30, 40, 50, 60, 70, 80, 100, 150, 400, 1000 and 5000 ps following 580 nm excitation. Samples were prepared in 2 mm quartz cuvettes at a concentration of  $5 \times 10^{-4}$  M. The inset shows the biexponential fit to the decay of the charge separated state and characteristic lifetime ..... 140
  
- 36 Time dependent transient absorption spectra of Zn<sup>+</sup>—Cu(=C(CN)<sub>2</sub>)<sup>-</sup> in degassed *n*-propyl acetate at pump/probe delay times of 0, 10, 20, 70, 150 and 1000 ps. The inset shows the biexponential decay of the transient absorption of the Cu-chlorin anion at 770 nm..... 142
  
- 37 Transient absorption spectra of the (a) Zn-porphyrin and (b) Cu dicyanomethide chlorin at 15 ps (solid) and 5 ns (dashed) in *n*-propyl acetate with 6 ps excitation at 575 nm. (Spectra of the Zn-porphyrin are repeated for convenience). Samples were prepared at concentrations of 1 mM in 2 mm quartz cells..... 143
  
- 38 Decay of the long-lived Zn—Cu(=C(CN)<sub>2</sub>) transient absorption spectrum in *n*-propyl acetate at (a) 530 nm and (b) 730 nm. Samples ( $5 \times 10^{-4}$  M) were excited with a 580-nm, 10 ns pulse. The residual absorption in (a) is assigned to population of the <sup>3</sup>( $\pi\pi^*$ ) state of the Zn-porphyrin as it is efficiently quenched by addition of O<sub>2</sub> to the sample. .... 144

- 39 Decay of the long-lived  $\text{Cu}(=\text{C}(\text{CN})_2)$  transient absorption spectrum in *n*-propyl acetate at (a) 530 nm and (b) 730 nm following sample excitation at 580 nm with a 10 ns pulse. Transient absorption spectra were obtained at sample concentrations of  $5 \times 10^{-4}$  M in a 2 mm cell. The lifetimes derived from these monoexponential fits are labeled appropriately. The negative signal at 0 ms in (b) is the result of stimulated emission from trace amounts of the free base complex..... 145
- 40 Picosecond transient absorption spectra of the  $\text{Zn}^+ - \text{Cu}(=\text{C}(\text{CN})_2)^-$  charge-separated state in acetone at 0, 5, 10, 15, 20, 25, 30, 35, 40, 50, 60, 70, 80 and 100 ps after the 6 ps, 580-nm excitation pulse. The transient absorption at the peak maximum between 510-530 nm decays biexponentially as shown by the inset. The lifetime of the charge separated state is 38 ps. .... 147
- 41 Time-dependence of the picosecond transient absorption spectrum of the  $\text{Zn}^+ - \text{Cu}(=\text{C}(\text{CN})_2)^-$  charge-separated state in acetone. Spectra are shown at pump/probe delay times of 0, 10, 15, 20, 25, 30, 35, 40, 50, 60, 70, 80 and 100 ps. The biexponential decay of the transient absorption of the Cu-chlorin anion at 770 nm is shown in the inset. .... 148
- 42 Dependence of the CR rate constants for the  $\text{Zn}^+ - \text{Cu}(=\text{C}(\text{CN})_2)^-$  charge-separated state on the inverse of the solvent relaxation time ( $\tau_s$ ). Solvents compared include dichloromethane (DCM), acetone (Ac) N,N-dimethylformamide (DMF), propionitrile (PN), *n*-butyronitrile (BN), *n*-valeronitrile (VN), and methyl, ethyl, *n*-propyl, and *n*-butyl acetates (MeOAc, EtOAc, PrOAc, BuOAc, respectively).  $\tau_s$  values taken from reference 76..... 150

- 43 Plot of the observed CR rate constants for the  $\text{Zn}^+ - \text{H}_2(\text{C}(\text{CN})_2)^-$  in acetone (Ac), N,N-dimethylformamide (DMF), propionitrile (PN), *n*-butyronitrile (BN), *n*-valeronitrile (VN), and methyl, ethyl, *n*-propyl, and *n*-butyl acetates (MeOAc, EtOAc, PrOAc, BuOAc, respectively) as well as 1-propanol (PrOH) and 1-butanol (BuOH) vs. the reciprocal of the microscopic relaxation times (taken from reference 76)..... 151
- 44 Cumulative plot of the observed CR rate constants of (a)  $\text{Mg}^+ - \text{H}_2^-$ , (b)  $\text{Zn}^+ - \text{Cu}(\text{C}(\text{CN})_2)^-$ , and (c)  $\text{Zn}^+ - \text{H}_2(\text{C}(\text{CN})_2)^-$  vs. the reciprocal of the microscopic relaxation times of dichloromethane (DCM), acetone (Ac), N,N-dimethylformamide (DMF), propionitrile (PN), *n*-butyronitrile (BN), *n*-valeronitrile (VN) and methyl, ethyl, *n*-propyl, and *n*-butyl acetates (MeOAc, EtOAc, PrOAc, BuOAc, respectively) as well as 1-propanol (PrOH) and 1-butanol (BuOH)..... 155

## **CHAPTER I**

### **INTRODUCTION**

#### **A. Background**

Photoinduced electron transfer (ET) reactions hold a central position in the overall chemistry of life. Through the photosynthetic reactions of living organisms, the earth's atmosphere was abundantly populated with oxygen, providing nourishment for higher forms of life. Photoinduced ET reactions remained a virtual mystery until as recently as the 18th century. Even with the great contributions to chemical and physical sciences of the 1600s, photosynthesis continued to be regarded as having divine origins among philosophers and scholars alike. The French chemist A. L. Lavoisier (1743—1794), who developed the law of conservation of mass and is partially responsible for identifying the chemical composition of air, eloquently captured in verse the common understanding of light and the chemical reactions it initiates,<sup>1</sup> "By means of light, the benevolence of the Deity has filled the earth with organization, sensation, and intelligence. The fable of Prometheus might perhaps be considered as giving a hint of this philosophical truth even to the ancients." With great interest Lavoisier pursued the fundamental principles behind light induced chemical reactions. Among his scientific contributions, he was the first to discover

and correctly describe the concept of oxidation by examining the red solid produced from the reaction of mercury with oxygen. Although first described as a photoinitiated process, it was later determined to be a thermal reaction that had been originally cited in 1599.<sup>2</sup> Nevertheless, Lavoisier's work fostered interest in examining chemical reactions stimulated by light.

An English contemporary of Lavoisier, Joseph Priestley (1733—1804), realized the importance of the chemistry that derived from light and was the first to discover that green plants could “restore air that had been injured by the burning of candles.” In his classic experiment, Priestley placed a sprig of mint in a vessel of water under an inverted jar. He found that after several days the environment in the jar would neither extinguish a candle nor was it uncomfortable to a mouse.<sup>3</sup> Although not fully understanding the importance of his observations, Priestly concluded that  $O_2$  must be a product of the light induced chemical reactions that plants undergo, the process known today as photosynthesis.

## **B. Charge Separation in Photosynthesis**

Tremendous progress has been made since the initial observations of Lavoisier and Priestly in defining the overall photosynthetic reaction sequence, as well as the structure and function of its specific substrates and cofactors. It is now known that a complex protein assembly is employed to aid in the energy conversion and storage process performed by the photosynthetic reaction centers (RCs) of purple bacteria and green plants.<sup>4</sup> The energy storage scheme is manifested in net chemical reactions resulting

from a series of exothermic electron transfer (ET) steps that produce oxidizing and reducing equivalents at specific RC sites via long range electron/hole pairs. The protein plays a key role in this event by stabilizing particular conformations of the redox active subunits in order to expedite the electron transfer sequence. Isolation of pure RC proteins from a number of purple bacteria and the recent solution of the crystal structures of *Rhodopseudomonas viridis*<sup>5</sup> and *Rhodobacter sphaeroides*,<sup>6</sup> have revealed the orientation of the membrane bound chromophores involved in photosynthetic charge separation reactions.

The kinetics and thermodynamics of the primary ET steps have been elucidated through ultrafast transient optical spectroscopy<sup>7</sup> and magnetic resonance techniques.<sup>8</sup> Although both RCs are very similar, a vast majority of the physical data regarding structure and function has been obtained on the protein from *Rb. sphaeroides*, making placement of the chromophores inside the membrane of particular interest. The chromophores are bound in a  $C_2$  symmetric arrangement, with the primary axis of rotation lying perpendicular to the length of the membrane (Figure 1). A pair of  $Mg^{+2}$  bacteriochlorophyll *a* (BChl *a*) molecules are oriented close to the edge of the membrane in a nearly coplanar fashion, creating a strongly coupled dimer known as P865. Two BChl *a* molecules are located on either side of P865 at a  $\sim 70^\circ$  angle in an edge-to-edge configuration. Adjacent to these molecules lie two bacteriopheophytin *a* (BPh *a*) moieties, which are in close proximity to two quinones known as  $Q_A$  and  $Q_B$ . Although only subtle differences exist between the chromophores on both sides of the RC, only the L side is photochemically active.

The primary donor in the electron transport chain within the RC is P865. The lowest energy transition in the optical absorption spectrum of

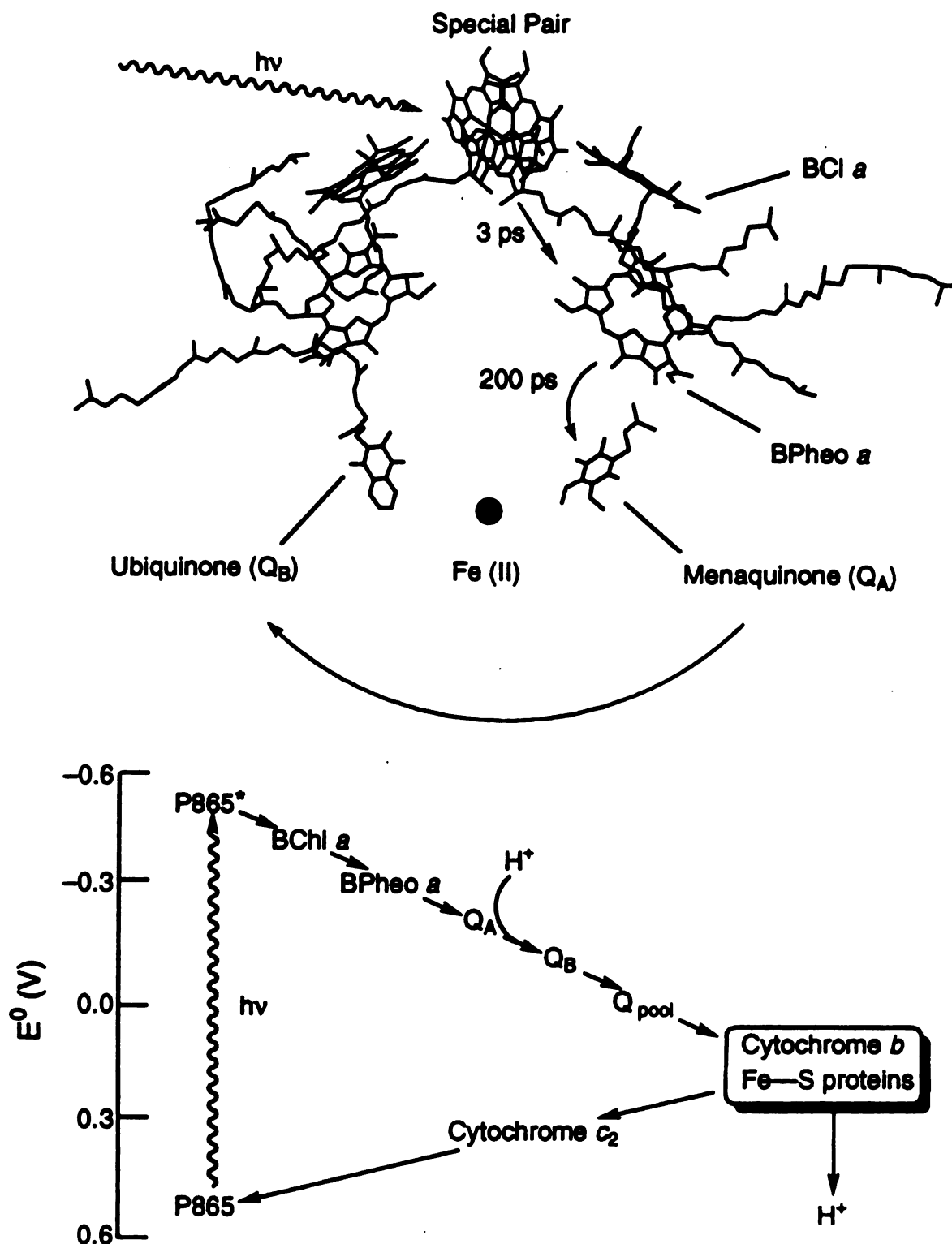


**Figure 1.** The ET transport chain in photosynthetic RC of purple bacteria (top) together with the approximate standard reduction potentials of the RC components (bottom).



P865 is redshifted by  $1300\text{ cm}^{-1}$  with respect to the individual monomeric units, due to the strong  $\pi\pi^*$  interactions of the macrocycles. This creates a low energy excited state that is accessible via energy transfer (EnT) following optical excitation of any of the protein bound chromophores in the vicinity. The EnT step is typically completed within 150 fs of excitation<sup>9</sup> and subsequently results in a unity quantum yield of ET from P865 to the BPh<sub>L</sub> *a* in 2.8 ps.<sup>10</sup> The rapidity of this reaction is thought to preclude participation of the intervening BCh<sub>L</sub> *a* in the electron transfer sequence, but recent reports have suggested that BCh<sub>L</sub> *a*<sup>-</sup> is present as a short-lived intermediate at low concentrations.<sup>11</sup> Further charge separation occurs as the BPh<sub>L</sub> *a* reduces Q<sub>A</sub> in ~200 ps, followed by subsequent electron transfer to Q<sub>B</sub> in 100  $\mu$ s. Interestingly, in the absence of Q<sub>A</sub>, the (BCh<sub>L</sub>)<sub>2</sub><sup>+</sup>—BPh<sub>L</sub><sup>-</sup> radical pair possesses a 12 ns lifetime,<sup>12</sup> which is sufficiently long-lived with respect to the forward electron transfer rate to insure a high quantum yield of charge separation. Remarkably, in the absence of Q<sub>B</sub>, the (BCh<sub>L</sub>)<sub>2</sub><sup>+</sup>—Q<sub>A</sub><sup>-</sup> species lives for approximately 100 ms.<sup>12</sup> The ability of the RC to stabilize oxidizing and reducing equivalents at separation distances of 35 Å is vital to subsequent biochemical reactions.

The charge separation scheme in green plant photosynthesis is similar to that of the bacterial RCs, but it is somewhat more complex. Two different reaction centers, designated as photosystems I and II (PS I and PS II respectively), are involved in the energy conversion process and are located within the thylakoid membrane of chloroplast (Figure 2). The membrane forms into stacks of small flattened vesicles containing proteins that bind light harvesting antenna pigments such as chlorophyll *a* (Chl *a*), in order to funnel energy into the primary electron donors of PS I and PS II. Although both RC subunits function cooperatively, each performs a

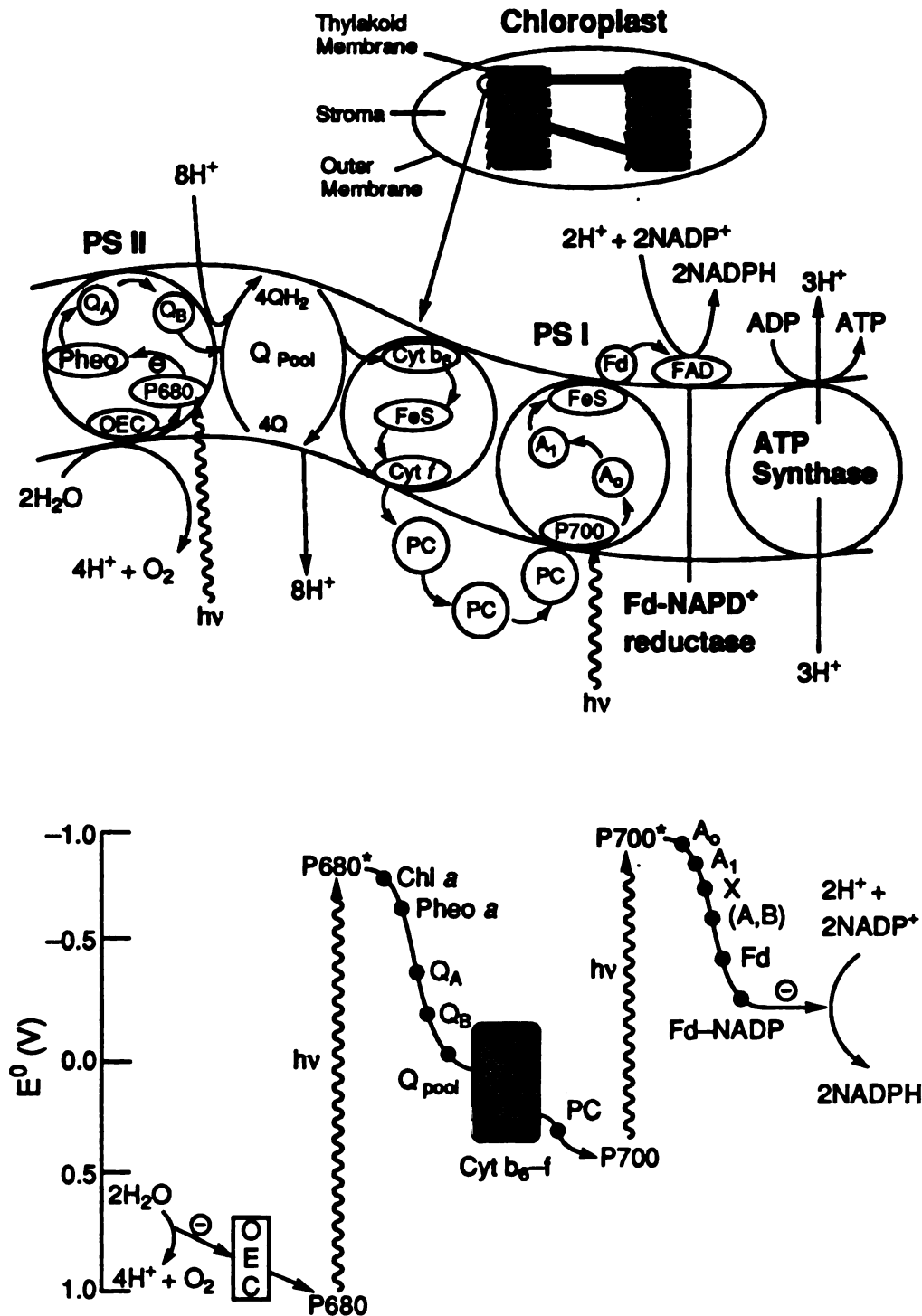


**Figure 2.** Schematic of the thylakoid membrane of chloroplast showing components of the ET chain (top) and the energetics or Z-scheme for photosynthetic ET in green plants (bottom).

specific function. PS I serves to ultimately reduce  $\text{CO}_2$  to six-carbon sugars ( $\text{CO}_2$  fixation) while PS II provides the oxidizing equivalents required to split water into protons and dioxygen.

The primary electron donor in PS I is thought to be a Chl *a* dimer known as P700.<sup>13</sup> Upon absorption of light, the dimer reduces an electron accepting chlorophyll ( $\text{A}_0$ ) in 10 ps<sup>14</sup> creating  $-1.1$  V of reducing potential in the most powerful biomolecular reductant known. Subsequent ET from  $\text{A}_0$  to a secondary acceptor thought to be a menaquinone<sup>15</sup> ( $\text{A}_1$ ) occurs in 40 ps.<sup>16</sup> The  $\text{P700}^+ - \text{A}_1^-$  species lives for 100 ms in the presence of reduced Fe—S clusters, which serve as subsequent electron acceptors in the neutral form. The reduced Fe—S clusters ultimately transport electrons to ferredoxin (Fd), a water soluble protein containing a  $2\text{Fe} - 2\text{S}$  center. Two molecules of ferredoxin each uptake a proton to then reduce  $\text{NADP}^+$  (nicotinamide adenine dinucleotide phosphate) to NADPH by hydrogenation of the nicotinamide ring. This reaction is catalyzed by Fd-NADP<sup>+</sup> reductase, a flavoprotein with a quinoid containing FAD (flavin adenine dinucleotide) prosthetic group. Interestingly, the semiquinone form of FAD serves as an intermediate in the production of one molecule of NADPH by two molecules of ferredoxin. The product is released into the stroma where soluble enzymes utilize NADPH and ATP synthesized by the thylakoids to convert  $\text{CO}_2$  into sugar through a series of successive dark reactions.

Concomitant with these ET steps is the photoinduced electron transport chain of PS II. The redox partners of PS II are analogous to those found in purple photosynthetic bacteria, with the primary electron donor (P680) likely consisting of a pair of weakly coupled Chl *a* molecules in a nearly coplanar arrangement. Absorption of a photon by carotenoid

and chlorophyll antenna pigments funnels energy into P680, inducing a rapid charge separation step to yield the  $\text{P680}^+ \text{---Pheo } \alpha^-$  species in 3 ps.<sup>17</sup> Stabilization of this state against charge recombination is achieved by the oxidation of  $\text{Pheo } \alpha^-$  by a plastoquinone in 500 ps.<sup>18</sup> In the absence of a subsequent quinone acceptor, the  $\text{P680}^+ \text{---Pheo } \alpha^-$  radical pair possesses a 35 ns lifetime, which decays by charge recombination (CR) to give a substantial yield of the  $^3\pi\pi^*$  state of P680.<sup>19</sup> A second plastoquinone molecule,  $\text{Q}_\text{B}$ , oxidizes  $\text{Q}_\text{A}^-$  in 100–200  $\mu\text{s}$ <sup>20</sup> and continues the electron transport chain to the quinone pool, cytochrome  $\text{b}_6\text{-f}$  and the blue copper protein plastocyanin. This latter species subsequently reduces the photogenerated  $\text{P700}^+$  center of PS I. The photoinitiated  $\text{P680}^+$  is reduced in 40–250 ns by a redox active tyrosine residue that subsequently oxidizes the Mn ion-containing oxygen evolving complex (OEC).<sup>21</sup> The oxidizing equivalents stored at this site are thermodynamically capable of splitting water into protons and oxygen, thereby completing the oxidation side of the cycle.

The kinetics of these photosynthetic ET steps are influenced in a static sense by the well defined thermodynamics of the individual reactions. Since the chromophores are bound within a flexible protein,<sup>22</sup> the rate constants for ET can also be affected by the dynamics of the protein environment. Therefore, vibrational contributions from both covalent and hydrogen-bonded linkages are important to the kinetics of the ET process. Okura and Feher have shown these effects to be prominent through determination of kinetic isotope ratios ( $k_\text{H}/k_\text{D}=0.8$ ) for the charge separation reaction between the special pair and  $\text{Q}_\text{A}$ .<sup>23</sup> Their observations are consistent with theoretical descriptions of the primary ET processes in photosynthetic systems, which stress the importance of intramolecular and

intermolecular vibrational motion in the ET reaction.<sup>24</sup> Since the interplay between statics and dynamics is important to the rates of ET in photosynthetic systems, contributions from both need to be considered when describing these ET reactions.

### C. Charge Separation in Other Natural Systems

Various metalloproteins undergo ET reactions in order to sustain biological function.<sup>25</sup> Hoffman and coworkers have measured ET rate constants within hemoglobin by substituting Mg, Zn or H<sub>2</sub> for Fe in one of the heme subunits.<sup>26</sup> From the temperature dependence of the ET rate, the reorganization energy for the system was determined to be 2.1 eV. In comparison to the energetics of ET, this contribution from the protein is large, demonstrating that protein matrices can contribute substantially to the thermodynamics of biological ET.

Other examples of role of the peptide in ET have come from studies of Ru-modified metalloproteins.<sup>27</sup> Early transient absorption studies by Gray and coworkers have shown that bimolecular ET quenching of photoexcited <sup>3</sup>Ru(bpy)<sub>3</sub><sup>2+</sup> by the fully oxidized pentaammineruthenium modified cytochrome c (Ru<sup>III</sup>Fe<sup>III</sup>) yields the thermodynamically favored product, Ru<sup>III</sup>Fe<sup>II</sup>, upon scavenging of the donor cation with EDTA.<sup>28</sup> From temperature dependence measurements of the Ru<sup>III</sup>(His33)<sup>3+/2+</sup> and the Fe<sup>3+/2+</sup> redox couples, estimates of  $\Delta H^\circ$ ,  $\Delta S^\circ$  and  $\Delta G^\circ$  were made for this reaction. These parameters were used in conjunction with the temperature dependence of the ET rate constants to determine values for the electronic coupling ( $H_{AB}$ ) and reorganization energy ( $\lambda$ ). The results

revealed a large reorganization energy and significant decay of the electronic coupling with D—A separation, the latter of which was attributed to inhomogeneity of the protein medium. Since a clear understanding of the electronic coupling effects requires confident values of  $H_{AB}$  and  $\lambda$ , substitution of  $Fe^{II}$  by Zn was used to increase the ET reaction exothermicity, thereby enhancing the accuracy of these parameters. Interestingly,  $\lambda$  was determined to have inner sphere contributions from Ru-ammine and metalloporphyrin complex rearrangements within the protein, as well as outer sphere contributions from the peptide matrix and exterior water molecules. The inner sphere components were calculated to be small (0.2 eV)<sup>29</sup> while the outer sphere contributions are more significant. Calculations based on the dielectric continuum model indicate that the solvent is responsible for a 0.6 eV contribution to the outer sphere reorganizational energy,<sup>26</sup> while only 0.2 eV is expected to come from the peptide matrix.<sup>30</sup> This result suggests that compared to polar solvent, the protein undergoes a small dielectric relaxation upon oxidation of the heme. Moreover, on the basis of these temperature dependence data, the attenuation in the electronic coupling ( $\beta$ ) was calculated to be large (2.0 Å<sup>-1</sup>) and was again attributed to poor D—A overlap through the protein framework. Although manifested within different ET parameters, this result further emphasizes the role that the environment plays in ET.

ET rates have also been measured for Ru-modified derivatives of the blue copper proteins azurin, plastocyanin and stellacyanin, as well as a series of histidine derivatives of Fe-cyt c and myoglobin.<sup>27</sup> Based on a summary of the data collected for these systems and Ru-modified cyt c described above, the reorganization energy for Ru-modified proteins is

approximately 1.2 eV and not very sensitive to D—A separation. However, the electronic coupling varies dramatically and is not accounted for by an exponential decay with distance, as expected from semi-classical ET theory. Beratan and Onuchic have addressed this issue by suggesting an ET pathway dependent model in which the electronic coupling between redox centers can be described by a combination of through-bond, through-hydrogen bond and through-space channels.<sup>31</sup> The model has proven successful in systems where single coupling pathways dominate the D—A interaction, as they do in *cyt c*.<sup>32</sup> For systems such as myoglobin, where many competing pathways exist, correlation with the attenuation in the electronic coupling has been poor.

Electron transfer within protein-protein complexes of cytochrome *c* (*cyt c*), cytochrome *b<sub>5</sub>* (*cyt b<sub>5</sub>*), cytochrome *c* peroxidase (CcP) and plastocyanin (pc) have also been investigated to determine in part, the influence of specific protein residues in docking interactions.<sup>33</sup> In general, the ET reactions within hybrid complexes of these proteins are described reasonably well by classical Marcus theory, with the notable exception of the absence of inverted region kinetics due to the diffusional dependence of interprotein ET. Of more specific interest to the role of the protein in the ET event, are the studies of the *cyt c*/CcP complex. By employing site-directed mutagenesis on the surface of CcP, McLendon has investigated the contributions from individual amino acids in the protein interactions.<sup>34</sup> His results provide solid evidence for binding of the oxidized and reduced *cyt c* at different sites on the CcP surface, in addition to identifying surface diffusion as a key process in forming complexes with more facile ET rates than others. For systems that cannot undergo surface diffusion, ET rate constants were determined to be small.<sup>35</sup> The large *cyt c*/CcP complex

reorganization energy (1.5 eV), extracted from temperature dependent studies of the ET rate constant, further supports the influence of interfacial protein-protein dynamics in these ET reactions.

#### **D. Prevalence of Medium Effects in Charge Separation**

The prevalent theme to emerge from studies of ET in photosynthetic RCs and metalloproteins is that the peptide plays a central role in governing the ET event. Important progress has been made in molecular dynamics simulations and various experimental techniques to gain a better understanding of these protein motions. This is especially important in biological systems as peptide response to rapid changes in oxidation state of the active sites is not well understood.

Polypeptide chains consist of successive residues linked by methylene ( $-\text{CH}_2-$ ) and amide ( $-\text{CONH}-$ ) groups possessing covalent bonds capable of free rotation.<sup>36</sup> Typical thermal motion within a protein matrix is governed by torsional oscillations of these groups about the single bond linking them together. The large thermodynamic investment in deforming these bonds results in only small displacements of the independent atoms, but collectively, these rigid group displacements produce a dynamic modulation of the protein framework, ranging from rapid local motions of specific groups to slower variations of larger portions of the protein framework (Table I). On timescales less than 100 ps, the small amplitude motions of the residues resemble the dynamics of molecular liquids. These motions can be complete within a few picoseconds, thus allowing the



**Table I. Properties of Internal Motions of Proteins<sup>36</sup>**

| <b>Motion</b>                                   | <b>Spatial Extent<br/>(nm)</b> | <b>Amplitude<br/>(nm)</b> | <b>-Log<sub>10</sub><br/>Relaxation<br/>Time (s<sup>-1</sup>)</b> |
|---|--------------------------------|---------------------------|---|
| Relative vibration of bonded atoms              | 0.2–0.5                        | 0.001–0.01                | 13–14   |
| Longitudinal motions of bases in double helices | 0.5                            | 0.01                      | 13–14   |
| Lateral motions of bases in double helices      | 0.5                            | 0.1                       | 12–13   |
| Global stretching                               | 1–30                           | 0.03–0.3                  | 11–13   |
| Global twisting                                 | 1–30                           | 0.1–1.0                   | 11–13   |
| Elastic vibration of global region              | 1–2                            | 0.005–0.05                | 11–12   |
| Sugar repuckering                               | 0.5                            | 0.2                       | 9–12  |
| Rotation of sidechains at protein surface       | 0.5–1.0                        | 0.5–1.0                   | 10–11   |
| Torsional libration of buried groups            | 0.5–1.0                        | 0.5                       | 9–11  |
| Relative motion different global regions        | 1.0–2.0                        | 0.1–0.5                   | 7–11  |
| Global bending                                  | 10–100                         | 5–20                      | 7–10  |
| Rotation of sidechains in interior proteins     | 0.5                            | 0.5                       | 0–4   |
| Allosteric transitions                          | 0.5–4.0                        | 0.1–0.5                   | 0–5   |
| Local denaturation                              | 0.5–1.0                        | 0.5–1.0                   | 0–5   |

protein to sample many different conformations on the timescale commensurate with ET.

## **E. Molecular Dynamics Simulations**

Recent advances in computer technology have extended the limits of molecular dynamics simulations to include the motion of larger molecular weight peptides. Simulations have been carried out involving a variety of proteins including cytochrome *c*,<sup>37</sup> myoglobin<sup>38,39</sup> and the photosynthetic RC of PS II.<sup>40</sup> The motion of typical atoms in proteins of this type can be larger in certain directions than in others. This anharmonic displacement is especially pronounced for atoms near the protein periphery or those at the ends of side chains. Effects of this type are also manifested within the heart of the protein, as a combination of atomic motions may produce a configuration energetically similar to the original protein structure. These motions can be collective in nature, leading to longer timescale protein responses resulting from higher frequency anharmonic normal modes of local atomic groups. Such motions are prevalent in cytochrome *c*, as fluctuations in the peptide framework are approximately 50% anharmonic, thus producing both fast and slow protein modulations.

Molecular dynamics simulations have also been used to examine specific chemical aspects of biological function such as ligand binding and release. An interesting example of this approach is a simulation of CO diffusion within the protein environment of myoglobin.<sup>39</sup> A 100 ps simulation was carried out employing 60 carbon monoxide (CO) molecules embedded within the protein, all with different initial velocities. The

ligands were determined to spend a considerable amount of time within intraprotein cavities before being energetically permitted to jump to either a subsequent site or the protein exterior. The simulation determined that five principal routes existed for either entrance or exit of the ligand from the matrix.

Yet other simulations have set out to examine the role of protein dynamics in the primary photosynthetic ET steps.<sup>40</sup> The complexity of the RC makes a full molecular dynamics simulation difficult. However, by assuming only local structural variations about the chromophores participating in the initial charge-transfer step, the simulation becomes manageable. Analysis of the special pair and pheophytin energies following an instantaneous change in oxidation state of the two moieties revealed a small structural relaxation of the protein that stabilized the ensuing charge-separated state. Solvation of the molecular ion pairs destroys the resonance condition with the neutral state and therefore effectively inhibits the charge recombination step in favor of further ET to the quinone. The solvation process was determined to result from small motions of many local groups, rather than large positional variations of selected sidechains. These effects are also observed in a simulation performed at 10 K, which is consistent with temperature dependent experimental data.<sup>41</sup> An interesting result of this study is that protein relaxation is complete within femtoseconds of initiation, while the experimentally determined ET time (3 ps) is sluggish in comparison. This suggests that in addition to initial solvation, energetic contributions not necessarily related to the protein also strongly affect the ET kinetics in PS II.

## **F. Experimental Techniques for Environmental Effects on Charge Separation**

### ***1. X-Ray Diffraction***

Significant progress has also been made in application of experimental techniques to the understanding of protein dynamics. X-ray diffraction studies have been used extensively to determine the average positions of particular atoms in proteins. Although time dependence information is not available from these data, the atomic coordinates are generally useful in initiating molecular dynamics simulations. A time-dependent connection can be made to the electron density profile of the protein by comparing crystal structure data to the average displacement obtained from the simulation, and subsequently using this criterion to assess atomic displacements of particular groups.<sup>42</sup> Although complications arise from atomic disorder due to cooling during preparation of the protein crystal, the comparison of the mean square displacements of atoms in both myoglobin and cytochrome *c* have shown reasonable correlation with the results of molecular dynamics simulations.<sup>37,39</sup> However, a more detailed comparison of the simulation with X-ray data becomes difficult because anharmonic displacements of particular groups (like those known to be prevalent in cytochrome *c*) are cumbersome to consider in the experimental data analysis.

## 2. *NMR Techniques*

NMR has emerged as a more valuable technique in this field because structural as well as dynamics information can be obtained about specific sites within the peptide. Rapid motions of the protein are generally reflected in nuclear spin relaxation times and cross relaxation of pairs of nuclei (NOE). Application of  $^{13}\text{C}$  NMR to these dynamics has proven especially useful, as magnetic field fluctuations are governed by the motion of bonded protons to these well defined  $\text{sp}^3$  sites. Since C—H relaxations can occur on timescales from a few ps to a few ns, longer timescale reorientations or diffusive motions can also be probed.<sup>43</sup> Methyl group displacements within bovine pancreatic trypsin inhibitor (BPTI) have been obtained from both NMR data<sup>44</sup> and molecular dynamics simulations. Comparison of these results demonstrates that although the simulation agrees qualitatively with the experimentally determined displacements, the predicted values are an order of magnitude smaller.<sup>45</sup> Similar studies have employed proton NMR to examine protein dynamics via hydrogen exchange.<sup>46</sup> The protons in the matrix can be easily substituted with deuterium or tritium by suspension of the protein in solution. To date, the difficulty in identifying which protons exchange in a given time period has limited the applicability of this technique, but advances in NMR spin decoupling and assignment strategies have begun to address these problems.

## 3. *Mössbauer Spectroscopy*

Several attempts have also been made to use Mössbauer spectroscopy as a probe of peptide motion.<sup>47</sup> These investigations have examined gamma

ray absorption by  $^{57}\text{Fe}$  atoms in heme proteins to obtain mean square displacements occurring on the timescale of the nuclear excited state lifetime ( $10^{-7}$ – $10^{-9}$  s). By measuring  $\gamma$  ray absorption as a function of Doppler shift of a translating source, frequency domain measurements possessing characteristic chemical shifts and linewidths are observed in a similar manner to NMR. Since there are generally only a few probe atoms of this type in the peptide, obtaining an accurate description of molecular motion is difficult, even upon isolation of temperature dependent vibrational effects. However, conclusions from these studies have provided additional support for the importance of collective motions of local groups in contributing to Fe atom displacement within the matrix. One advantage of the Mössbauer technique is its relative insensitivity to low frequency thermal modes of the peptide, which has proven useful in separating static and dynamic contributions to atomic displacements observed in X-ray diffraction studies.<sup>48</sup>

#### *4. Ultrafast Laser Kinetics*

Recent advances in ultrafast laser technology have made fluorescence anisotropy a valuable tool for assessing protein dynamics. Upon excitation of the peptide with polarized light, emission from aromatic residues is monitored as a function of time and polarization angle. The resulting depolarization of the fluorescence is caused by reorientation of the protein, which occurs with a characteristic time constant. This rotational correlation time can be calculated directly from the lifetime of the state and the emission radiant power detected for parallel and perpendicular polarization orientations. Values of these rotational constants for specific

chromophores in various regions of the peptide can be compared to local group relaxations from molecular dynamics simulations. Such a comparison has been made between fluorescence anisotropy and simulation for the tyrosine ring reorientations in BPTI.<sup>49</sup> The results of theory and experiment show strong correlation of the timescales and amplitudes of the mean square displacements for atoms in the tyrosine ring, further establishing the usefulness of this experimental technique. Although fluorescence anisotropy does not provide insight into structural features of the protein, it does offer the ability to apply picosecond time resolution to the role of protein dynamics in ET reactions.

## **G. Solvation Dynamics**

From the experimental and theoretical investigations of protein dynamics is that rapid fluctuations occurring on the picosecond timescale produce instantaneous structures that vary significantly from time averaged geometries. The implications of these conclusions to both biology and chemistry are significant. Although the biological chemistry of metalloproteins and RCs typically occurs on diffusion controlled timescales, the primary ET rate constants are competitive with these fast protein motions and therefore may be strongly influenced by them. This condition is a direct consequence of the protein matrix acting as a non-uniform dielectric solvent. The complexity of the protein makes data pertaining to these solvation motions challenging to obtain and interpret. Therefore, much of our current view of solvation dynamics effects in ET has stemmed from studies conducted in neat solvents. The results of studies

to date are far from definitive, further stressing the need for detailed investigations of solvation dynamics effects in ET.

The recognition that solvent dynamics can affect the rates of ET and chemical reactions has led to the development of the concept of solvent friction.<sup>50</sup> This describes the process by which solvent motion is required for the system to surmount the activation barrier between reactants and products in both chemical reactions and ET processes. In many cases, the solvent serves to dissipate the energy of the reaction, thereby diminishing the rate of diffusive passage over the barrier below that predicted by transition state theory (overdamped limit).<sup>51</sup> For reactions where the activation energy is considered to have large contributions from the solvent, barrier passage is exclusively dependent on the nuclear motion of the medium. Since each solvent molecule possess a molecular moment of inertia, the individual rotation times of particular solvent dipoles are influenced by those of its neighbors. Therefore, overdamped solvent motion is more appropriately viewed as a collective process depending intricately upon the surrounding bath modes of the medium. This property has particularly important implications to electron transfer reactions as the rates of passage from the D—A surface to that of the  $D^+—A^-$  state can be influenced by solvent motion, in addition to the more well known static solvent effects such as polarity.

### *1. Theoretical Models of Electron Transfer*

The theoretical underpinnings of static contributions to ET have been in place since Marcus' classical description of ET in the mid 1950s.<sup>52</sup> In



these landmark accounts, Marcus established the relationship between the reaction free energy and the rate of the ET according to,

$$k = A \exp \left[ \frac{-\Delta G^*}{k_B T} \right] \quad (1.1)$$

$$\Delta G^* = \left[ \frac{(\lambda + \Delta G^\circ)^2}{4\lambda} \right] \quad (1.2)$$

where  $\Delta G^\circ$  is the driving force for the ET,  $\lambda$  is the sum of the energies required to reorganize the inner ( $\lambda_i$ ) and outer ( $\lambda_o$ ) sphere coordinates, and  $A$  is the frequency prefactor for the ET reaction. Marcus assumed that the ET process was adiabatic; that is for a unimolecular reaction,  $A = \kappa kT/h$  and the transmission coefficient  $\kappa$ , is near unity. The parabolic dependence of eq 1.1 and 1.2 predicts that as the driving force for the ET increases, the ET rate will initially increase until  $\Delta G^\circ$  becomes larger than the nuclear reorganizational energy of the system; thereafter the ET rate will decrease. This defines three regimes of ET, the normal ( $|\Delta G^\circ| < \lambda$ ), activationless ( $|\Delta G^\circ| = \lambda$ ) and inverted regions ( $|\Delta G^\circ| > \lambda$ ), as illustrated in Figure 3.

The strong influence of quantum mechanics, coupled with experimental data not well described by the classical expression, prompted refinement of eq 1.1. Marcus<sup>53</sup> and Levich<sup>54</sup> used Fermi's Golden Rule for the quantum mechanical probability of a transition between two states, derived from the original treatment of Landau and Zener,<sup>55</sup> to show that the activated ET rate takes the form,

$$k = (2\pi / \hbar) V_R^2 (FC) \quad (1.3)$$

where  $V_R^2 = V_o^2 \exp(-\beta R)$  describes the electronic coupling between the donor and the acceptor as a function of distance,  $\beta$  is a constant describing the decay of the electronic coupling with distance, and FC is the vibrational overlap of the reactant and product states (Franck-Condon factor). Marcus has shown that in the high temperature limit, this nonadiabatic ET expression can be written with  $FC = (4\pi\lambda k_B T)^{-1/2} \exp[-(\Delta G^o + \lambda)^2 / 4\lambda k_B T]$ ,<sup>53</sup> or in the context of eq 1.1, the prefactor has the form given in eq 1.4.

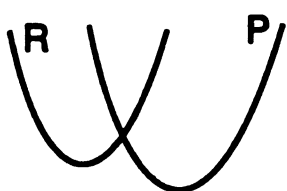
$$A = (2\pi / \hbar) V_R^2 (4\pi\lambda k_B T)^{-1/2} \quad (1.4a)$$

In the nonadiabatic limit, the probability of electron transfer is small because of poor D—A electronic coupling. This forces the electronic motion to be rate limiting, and no dependence on the nuclear motion of the solvent is anticipated. In simple terms, the significance of eq 1.1-1.4a lies in the dependence of the ET rate constant on “static” solvent properties, namely the outer sphere reorganizational ( $\lambda_o$ ) and the driving force for the ET reaction. In this limit, the observed ET rate is completely independent of the relaxation time of the solvent.

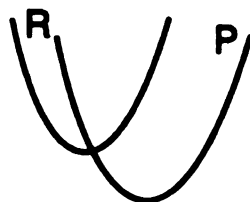
But the dynamics of solvent motion can also affect the ET rate. If fluctuations in the medium become slow compared to the ET rate, then they, and not the electronic motion can become rate limiting and the nonadiabatic expression is forced into the solvent-controlled adiabatic limit.<sup>56</sup> In the context of eq 1.1, the prefactor A is now given by eq 1.4b.

$$A = \frac{1}{\tau_s} \left[ \frac{\Delta G^*}{\pi k_B T} \right]^{1/2} \quad (1.4b)$$

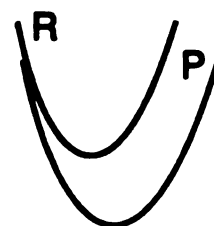
Normal Region      Activationless      Inverted Region



$$|\Delta G^0| < \lambda$$



$$|\Delta G^0| = \lambda$$



$$|\Delta G^0| > \lambda$$

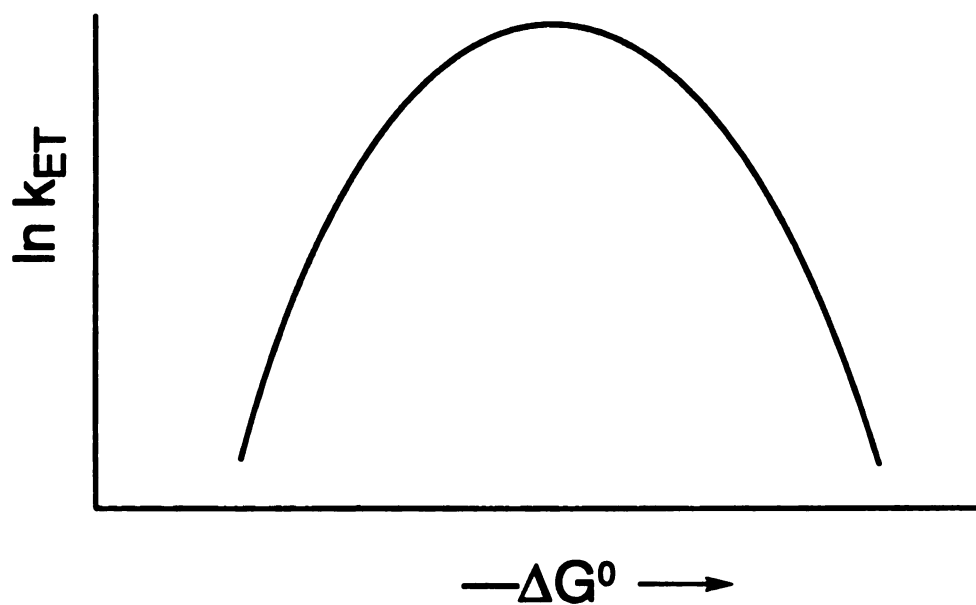


**Figure 3.** Illustration of the dependence of the electron transfer rate constant on the driving force for the reaction as described by Marcus' classical expression. This defines three regions of electron transfer, normal, activationless and inverted.

Here,  $\tau_s$  is the average microscopic relaxation time of the solvent. The key result of eq 1.4b is that the ET rate constant in terms of eq 1.1 is now dependent on the dynamics of solvent motion and not simply on the polarity of the environment.

The dependence of the ET rate on solvent dynamics is better highlighted within a consecutive reaction formalism where the important dimension in the reaction between the neutral and charge-separated donor-acceptor potential surfaces is a solvent polarization coordinate. If the nuclear motions of the system are viewed classically, the actual donor-acceptor potential surface intersection will be localized to a crossing point,<sup>67</sup> and the ET rate constant takes the form,<sup>66</sup>

$$k_{\text{obs}} = \frac{k_D k_{\text{ET}}}{k_D + k_{\text{ET}}} \quad (1.5)$$

where diffusion along the solvent reaction coordinate is described by the rate constant  $k_D$ , followed by surface crossing electron transfer with rate constant  $k_{\text{ET}}$ <sup>68,69</sup> (Figure 4) given by eq 1.6 and 1.7.

$$k_D = \frac{1}{\tau_s} \left( \frac{\Delta G^*}{\pi k_B T} \right)^{1/2} \exp(-\Delta G^* / k_B T) \quad (1.6)$$

$$k_{\text{ET}} = |V|^2 \left( \frac{2\pi}{\hbar} \right) (4\pi\lambda k_B T)^{-1/2} \exp(-\Delta G^* / k_B T) \quad (1.7)$$

Within the consecutive reaction formalism of eq 1.5, solvent dynamics information is included in  $k_D$ . Solvent dynamics will influence the observed rate when  $k_{\text{ET}}$  is large with respect to  $k_D$ . In this case,  $k_{\text{ET}} \gg k_D$

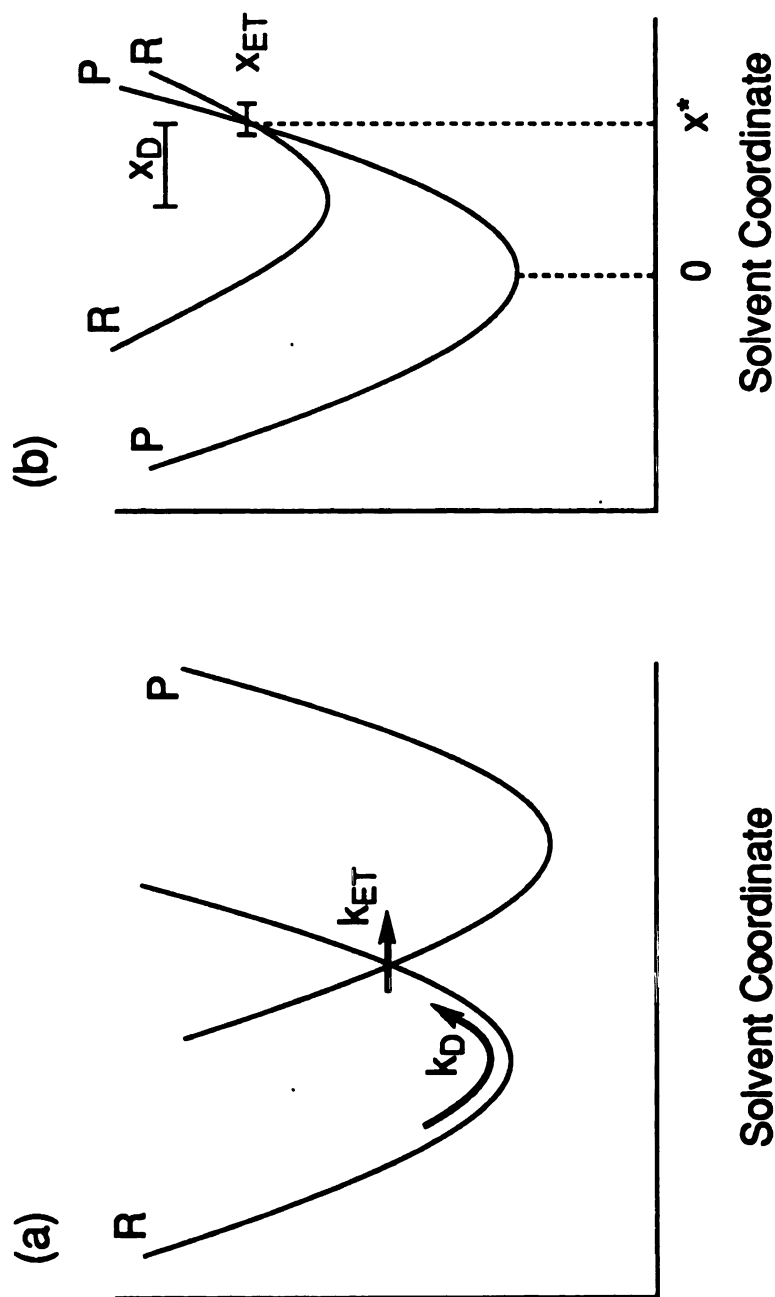


**Figure 4.** Diabatic representation of harmonic potential surfaces of a common frequency, displaced vertically by  $\Delta G^0$  and horizontally such that the reorganization energy is  $\lambda$ , crossing at  $x^*$  in (a) the normal and (b) the inverted ET regimes. The length  $x_{ET}$  characterizes the region over which the surfaces are coupled; as  $x_{ET}$  shrinks to zero the transition becomes localized to the crossing  $x^*$ . The curved arrow indicates the motion along the reaction coordinate with rate characterized by  $k_D$  and the straight arrow indicates the crossing motion with rate constant  $k_{ET}$ . Figure adopted from ref. 70.

and in eq 1.5,  $k_{\text{obs}} = k_D$ . Consequently, the observed electron transfer rate will depend intimately on the microscopic relaxation time of the solvent ( $\tau_s$ ); when static solvent contributions are isolated,  $k_{\text{obs}}$  should vary linearly with  $1/\tau_s$ . In the solvent-controlled adiabatic regime of electron transfer,  $k_{\text{obs}}$  is independent of the electronic coupling. If well dynamics are rapid relative to crossing (*i.e.*,  $k_D \gg k_{\text{ET}}$ ) the system will equilibrate and the conventional static rate expression is obtained (*i.e.*,  $k_{\text{obs}} = k_{\text{ET}}$ ). If the actual electron transfer event is very nonadiabatic, due to poor electronic coupling, then  $k_{\text{ET}}$  will be rate limiting and solvent dynamics information will not be experimentally accessible.

This consecutive reaction scheme is valid for adiabatic or nonadiabatic electron transfer so long as the electron transfer transition is sufficiently localized in the reaction coordinate, relative to the diffusion length along the reaction coordinate. (In the inverted regime, the overall process will always involve a transition between two surfaces, so the reaction is never adiabatic in the sense of a process taking place on one Born-Oppenheimer potential energy surface. Here, the term adiabatic refers to strong electronic coupling in the Marcus rate constant  $k_{\text{ET}}$  in the expression for  $k_{\text{obs}}$  in eq 1.5.) This result stands in contrast to normal region electron transfer kinetics, where a consecutive reaction scheme is not viable for the case of strong electronic coupling.<sup>70</sup> Rather, the overall process corresponds to passage over one potential surface and can be treated by a Kramers' analysis.<sup>63</sup>

The above formalism is well suited for activated ET processes, but as the barrier approaches zero, eq 1.5 no longer properly describes dynamics effects in ET. Rips and Jortner have developed explicit expressions for the

near activationless case where the barrier height is generally considered to small,<sup>65</sup>

$$k_{\text{obs}} \cong 1/\tau_s \quad (1.8)$$

The ramifications of eq 1.5-1.7 and eq 1.8 are far reaching as solvent dynamics are not only expected to influence near-activationless ET reactions typically occurring on the timescale of solvent motion, but they may govern less facile activated ET events as well.

For the case of truly activationless ET (barrier height within  $k_B T$ ), the dependence on solvent dynamics is lost as the ET process is now described in terms of high frequency vibrational coupling between the donor and acceptor, in addition to electron-nuclear coupling through the solvent. Considering that intramolecular vibrational relaxation typically occurs on the femtosecond timescale, while solvent reorganization is a picosecond timescale process, the former dominates the ET rate constant and no dependence on the nuclear motion of the solvent is expected.<sup>71</sup> This formalism has been used to treat ET rate constants obtained in highly viscous solvents that are a factor 10-1000 times larger than the solvent relaxation time.

## 2. *Experimental Investigations of Solvatochromism*

Most experimental investigations of solvent dynamics have relied on dynamic solvatochromism. In the simplest case, the solvent can be viewed as a dielectric continuum<sup>72,73</sup> with a characteristic response  $\hat{\epsilon}(\omega)$ , as described in the Debye form.

$$\hat{\epsilon}(\omega) = \epsilon_{\infty} + \frac{\epsilon_s - \epsilon_{\infty}}{1 + i\omega\tau_D} \quad (1.9)$$

Here,  $\epsilon_{\infty}$  and  $\epsilon_s$  are the optical and static dielectric constants of the solvent, and,  $\tau_D$  is the Debye dielectric relaxation time, which is related to the reorientation time of a single solvent dipole. According to this model, the microscopic correlation function,  $C(t)$ , should decay exponentially according to the expression,

$$C(t) = \exp(-t / \tau_L) \quad (1.10)$$

with

$$\tau_L \approx \frac{\epsilon_{\infty}}{\epsilon_s} \tau_D \quad (1.11)$$

where  $\tau_L$  is the so-called longitudinal relaxation time of the solvent.<sup>74,75</sup> A manifestation of eq 1.11 is that the solvation time  $\tau_L$  is significantly shorter than  $\tau_D$ . Physically, this can be viewed as the difference between the decay of an applied current across the solvent due to medium relaxation, and the decay of voltage from an instantaneous charge jump, also determined as a function of solvent reorientation. This latter description is more closely related to the solvation of charged molecular excited states, and therefore  $\tau_L$  provides a better description of ion pair solvation in D—A ET reactions than does  $\tau_D$ .

Experimentalists have examined the basic concepts of dielectric relaxation by employing time-resolved fluorescence spectroscopy of highly luminescent probe molecules.<sup>76,77</sup> These probes typically have charge



transfer excited states (resulting from charge redistribution upon excitation and not conventional ET) possessing modest lifetimes ( $<5$  ns). A few of the many examples include the well-known laser dyes Coumarin 102 and 153, in addition to 1-aminonaphthalene and 4-aminonaphthalimide. Optical excitation of the probe molecule produces a nonequilibrated solvent population about the dipolar excited state. Subsequent relaxation over the lifetime of the state induces a time-dependent Stokes shift of the emission spectrum (Figure 5), which can be analyzed within the framework of the microscopic solvent dynamics correlation function,  $C(t)$ ,

$$C(t) = \frac{\nu(t) - \nu(\infty)}{\nu(0) - \nu(\infty)} \quad (1.12)$$

where  $\nu(0)$ ,  $\nu(t)$  and  $\nu(\infty)$  are the frequencies of the emission intensity maximum immediately following excitation, at some later time, and at a time corresponding to post equilibrium conditions. From dielectric continuum theory, the decay of this function should follow monoexponential kinetics according to eq. 1.10. This correlation is generally poor, as  $C(t)$  is often better fit by a sum of exponentials of the form,

$$C(t) = A_1 \exp(-t / \tau_1) + A_2 \exp(-t / \tau_2) + A_3 \exp(-t / \tau_3) \quad (1.13)$$

where  $A_1$ ,  $A_2$  and  $A_3$  represent the amplitude weighting factors for the respective decay times ( $\tau_1$ ,  $\tau_2$  and  $\tau_3$ ), which can be influenced by the nature of the probe molecule. Consequently, the average solvation time  $\langle \tau_s \rangle$ , corresponding to the amplitude weighted average of this range of solvation times, is typically reported in addition to the independent

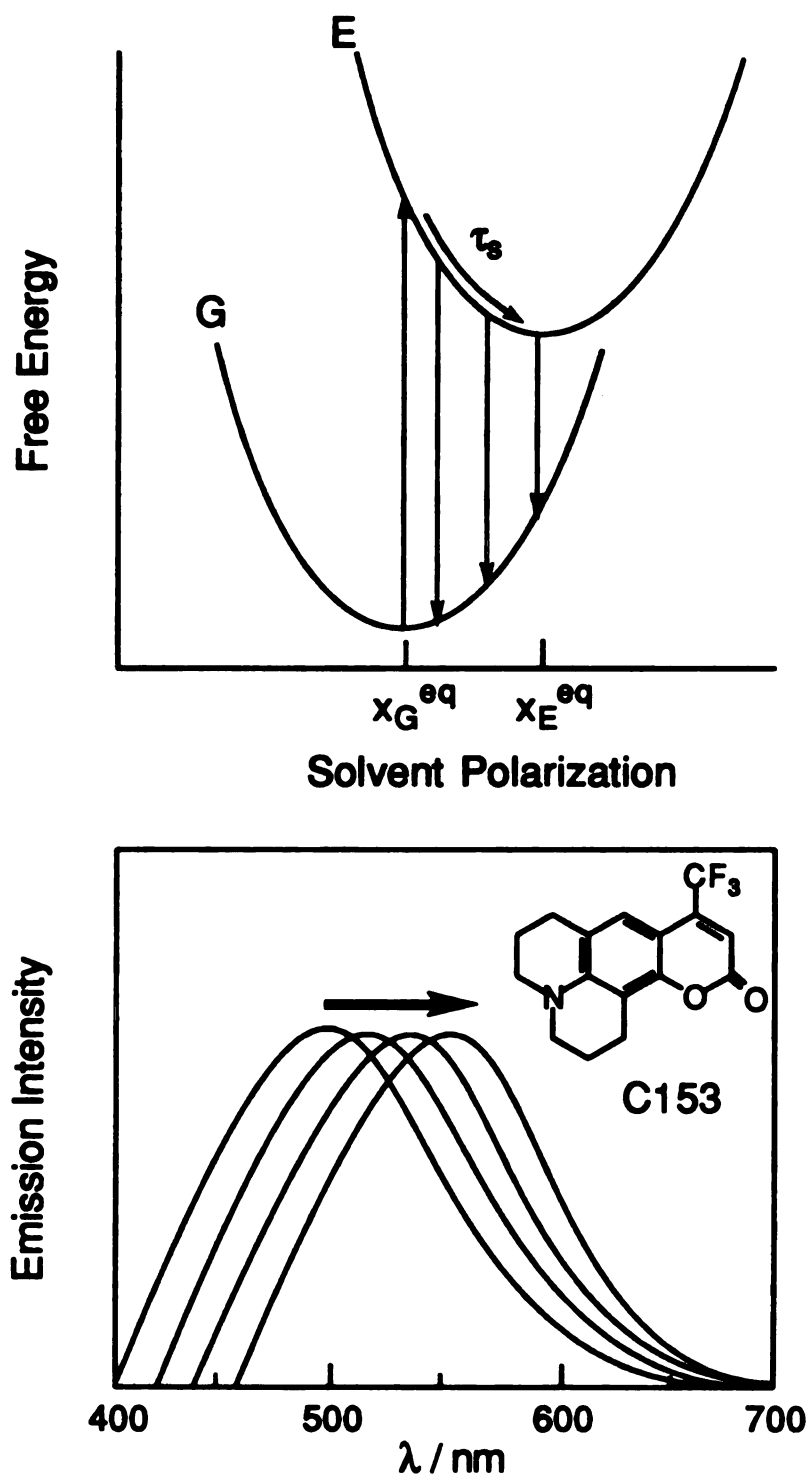


**Figure 5.** Illustration depicting transient solvation of a polar excited state (top), where  $x_G^{eq}$  and  $x_E^{eq}$  represent the solvent polarization in the ground and excited state, respectively, together with the resulting fluorescence Stokes shift of the Coumarin 153 emission band (bottom).

components of the relaxation time. In many cases  $\tau_1$  is rapid ( $\sim 150$  fs), corresponding to a short timescale inertial component, while  $\tau_2$  and  $\tau_3$  represent a somewhat slower ( $\sim 0.5$ – $10.0$  ps) diffusive motion. The value of  $\langle \tau_s \rangle$  is often a better estimate of solvent dynamics behavior than the  $\tau_L$  from dielectric continuum theory, primarily due to the inclusion of shorter timescale components that can be competitive with rapid ET.

More contemporary theoretical treatments have extended these descriptions of solvation dynamics by viewing the solvent as a non-uniform dielectric medium<sup>79</sup> and accounting for the use of non-spherical probe molecules.<sup>80</sup> Additional studies have viewed the dynamics of a structured solvent described by a mean spherical approximation.<sup>81,82</sup> Yet others have discussed the validity of the Inverted Snowball approach of Onsager, where solvent far from the probe is suggested to relax more quickly than solvent at the interface.<sup>83,84</sup> Generally, no single theoretical approach or experimental protocol seems to effectively describe all aspects of dynamic solvent relaxation for a wide range of solvents. However, simulation and data analysis of multicomponent  $C(t)$  functions has broadened our understanding of dielectric response to charged species in solution.

In an effort to apply this knowledge to the role of solvation dynamics in ET, solvatochromism studies have advanced to include probes that rely on charge transfer following excitation of a locally excited (LE) state, rather than transient solvation of an excited state with polar character. Two popular probe molecules fitting this criterion are 9,9'-bianthryl (BA) and 4-(9-anthryl)-N,N-dimethylaniline (ADMA), which form a twisted intramolecular charge transfer state (TICT) following excitation of a local  $\pi\pi^*$  state (LE).<sup>76</sup> The interconversion rate between these states was determined by analyzing the decay of the time-dependent emission

spectrum within the context of eq 1.12 and 1.13. Interestingly, the charge transfer rate constants were found to comparable to those obtained from transient solvation times of standard Coumarin probes. The rate constants are also consistent with the low LE/TICT interconversion barrier height for these reactions, which were determined to be on the order of  $kT$ . These observations of solvent-controlled, activationless ET processes have been confirmed by other researchers using probe molecules with similar electronic structures.<sup>85</sup>

## H. Solvation Dynamics in Activated Electron Transfer

Although the previous studies have demonstrated that solvent dynamics can control ET rate constants occurring on the timescale of solvent motion, most chemical or biological systems possess intrinsic barriers to the ET reaction which significantly retard the rate. From the activated rate expression of eq 1.5-1.7, it is evident that the barrier height is dependent upon the static properties of the solvent, and needs to be accounted for in order to discuss the effects of dynamics in ET. Weaver has performed the most thorough analysis of these effects by extracting the outer-sphere component of the activation barrier ( $\Delta G_{os}^*$ ) from the optical and static dielectric constants, and the internuclear distance between the relative donor and acceptor as describe by <sup>86</sup>

$$\Delta G_{os}^* = \frac{e^2}{4} \left[ \frac{1}{a} - \frac{1}{R_H} \right] \left[ \frac{1}{\epsilon_{op}} - \frac{1}{\epsilon_s} \right] \quad (1.14)$$

where  $a$  is the reactant radius,  $R_H$  is the internuclear distance, and  $\epsilon_{op}$  and  $\epsilon_s$  are the optical and static dielectric constants of the solvent, respectively (Pekar factor). Contributions from the solvent to  $\Delta G_{os}^*$  are then used in conjunction with the self exchange ET rate constant derived from NMR line broadening or electrochemical techniques to determine the correlation between the ET rate and solvent dynamics according to eq 1.15.

$$\log \kappa_{el} \nu_n = \log k_{ex} - \log K_p + \left[ \frac{\Delta G_{os}^*}{k_B T} \right] \quad (1.15)$$

Here,  $k_{ex}$  is the experimentally determined self exchange rate constant,  $K_p$  is the pre-equilibrium constant for complex formation, and  $\kappa_{el}$  is the electronic transmission coefficient. Solvent dynamics effects are manifested within the nuclear barrier crossing frequency  $\nu_n$ , as this term governs progress along the potential energy surface. For moderate activation barriers,  $\nu_n \approx 1/\tau_L$  where  $\tau_L$  is the longitudinal relaxation time of the solvent as discussed previously. Weaver has shown that by correcting for variations in the barrier height, the activated ET rate constants for self exchange reactions can be effectively correlated with solvent dynamics via eq 1.15. This is a remarkable result considering the diffusion controlled nature of this experimental approach.

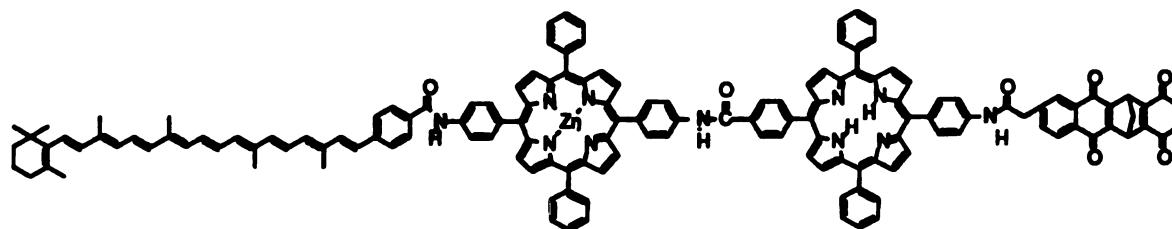
### *1. Strategy of Activated Charge Separated States*

Since numerous studies of fixed distance D—A assemblies possessing a variety of geometric and electronic properties are known in the literature,<sup>87</sup> the use of photoinduced charge separation to study solvent

dynamics in activated ET is an obvious avenue of attack. However, choice of probe molecule is not straightforward as the energetics of the ET step must be finely tuned in order for the reaction to be dynamically controlled. Also, experimental detection of well defined ion-pair intermediates is a pivotal requirement for investigating the effects of solvent motion on ET rates. Although many of the systems reported appear to satisfy these criteria, they are actually more effective for studying conceptual issues of ET theory than they are for revealing dynamics effects in ET.

## 2. *Gust and Moore Systems*

Gust and Moore have investigated the ET and energy transfer (EnT) kinetics of carotenoid-diporphyrin-diquinone complexes and various pentad precursors.<sup>88</sup>



1

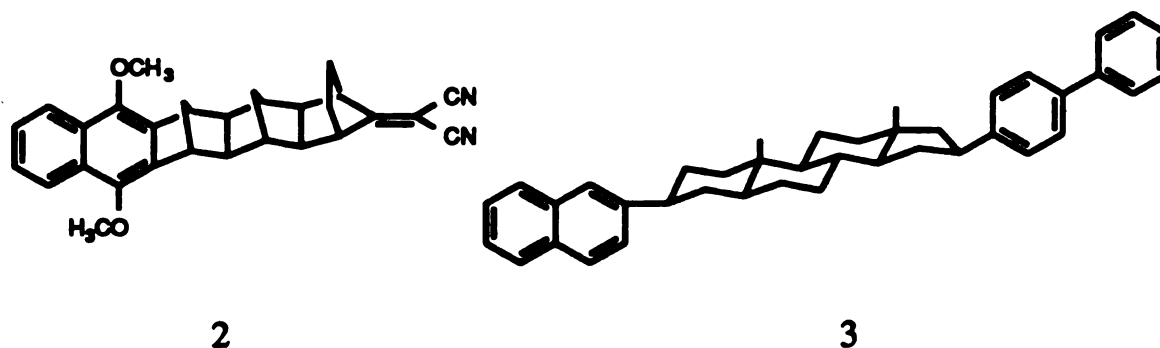
Amazingly, molecules in this class (1) have produced quantum yields for ion-pair formation of 0.83 while maintaining charge separation for 55  $\mu$ s. They have also been shown to have EnT quantum yields as high as 0.53. Although these systems have potential applications in biomimicry, their geometric and electronic structural complexity makes them poor probes of solvation dynamics in ET. Also, the tendency of (1) to undergo efficient

EnT coincident with ET induces spectroscopic complications in obtaining solvent dependent rate data. Furthermore, the rate constants for ET are significantly retarded with respect to the timescale expected for dynamical solvent control of ET.

Osuka and Maruyama have also observed rapid EnT and ET in dicarotenoid-porphyrin and carotenoid-porphyrin-pyromellitimide complexes. However, it is not clear from their results whether singlet energy transfer from the carotenoid occurs prior to, or following oxidation of the porphyrin by the covalently linked pyromellitimide.<sup>89</sup> Regardless, the rapidity of the forward ET step (40 ps) and the relative retardation of the CR step (15 ns) promotes these systems as better probes of dynamics effects in ET than those of Gust and Moore. However, the real drawback to employing large assemblies as probes of solvation dynamics is their lack of structural rigidity and complex excited state manifolds. By limiting the number of active chromophores in the donor-acceptor complex, contributions from intramolecular reorganizations and extraneous excited state population are reduced, which simplifies the interpretation of dynamics effects on the ET rate. Therefore, the systems described above are not well designed to pursue studies of solvent dynamics in ET.

### *3. Other D—A Rigid Spacer Assemblies*

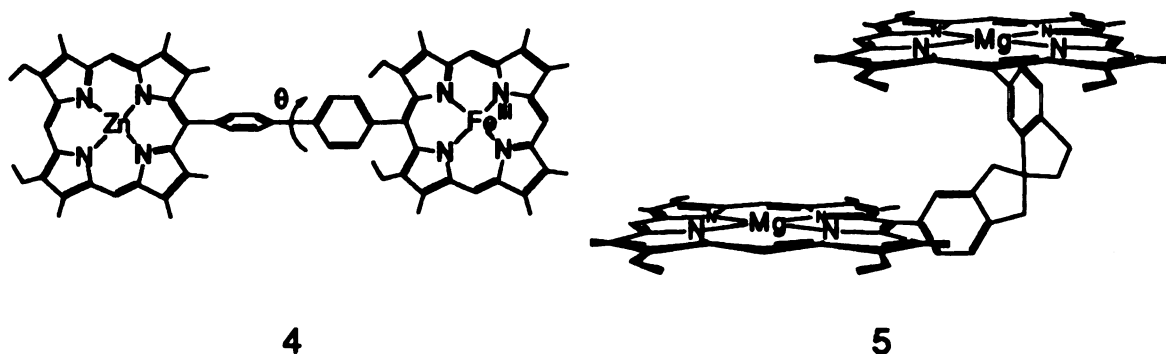
Important insights into phototoinduced ET across rigid, bicyclic hydrocarbon spacers (2) and steroid linkages of varying length (3) have derived from the work of Paddon-Row<sup>90</sup> and Closs and Miller,<sup>91</sup> respectively.



The rate constants for ET through the bicyclic hydrocarbon bridge (1) have been shown to be dependent upon the cis/trans isomerism of the carbon framework. Similarly in the steroid D—A complexes (2), rate constants for ET from the biphenylene donor to fused aromatic acceptors are uniquely distance dependent and can only be treated by considering equatorial and axial isomers of the bridge. This latter class of compounds is also famous for providing the first experimental glimpses into the Marcus inverted region.<sup>92</sup> The well defined structure of (2) and (3) favor application of these systems to the study of solvent dynamics in ET more-so than (1) but their use is thwarted by two additional problems. First, the electronic coupling for the relatively long range ET process is assuredly poor, and thus the contribution to the ET rate from electronic term is more likely to be rate limiting than solvent dynamical motion, as describe by the consecutive reaction formalism of eq 1.5-1.7. Secondly, a more subtle problem arises from the solvent dependence of the electronic coupling as ET studies described above have shown that the nature of the bridge plays a key role in the ET event. What is not well formulated however, is how these effects vary across different solvents. Both factors, coupled with the absence of a good spectroscopic chromophore, makes (2) and (3) poor choices for the study of solvent dynamics in ET.



Other possible topologies for discrete, activated, charge transfer studies of solvent dynamics include many porphyrin-porphyrin D—A complexes prepared with preferential spatial orientations. McLendon has painstakingly synthesized a series of side-by-side phenylene-bridged bis-porphyrin adducts where the dihedral angle governing overlap of the porphyrin  $\pi$  orbitals has been systematically varied.<sup>93</sup> The angular dependence of the ET rate constants from the Zn porphyrin donor to the  $\text{Fe}^{\text{III}}$  porphyrin acceptor in (4) is surprising, as the results follow a  $\cos 2\theta$  and not the  $\cos \theta$  dependence expected on the basis of simple  $\pi$ — $\pi$  orbital overlap. Rather, a minimum in the ET rate constant is observed near  $\theta=45^\circ$  with maxima at both  $0^\circ$  and  $90^\circ$ . Although this behavior is not immediately intuitive, it was theoretically anticipated by Cave, Marcus and Siders.<sup>94</sup> Their model suggests that the nodal structure of the porphyrin monomer is influenced by symmetric and antisymmetric wavefunction combinations, which produce a convolved  $\sin \theta$  and  $\cos \theta$  dependence of the orbital overlap between the two porphyrins.

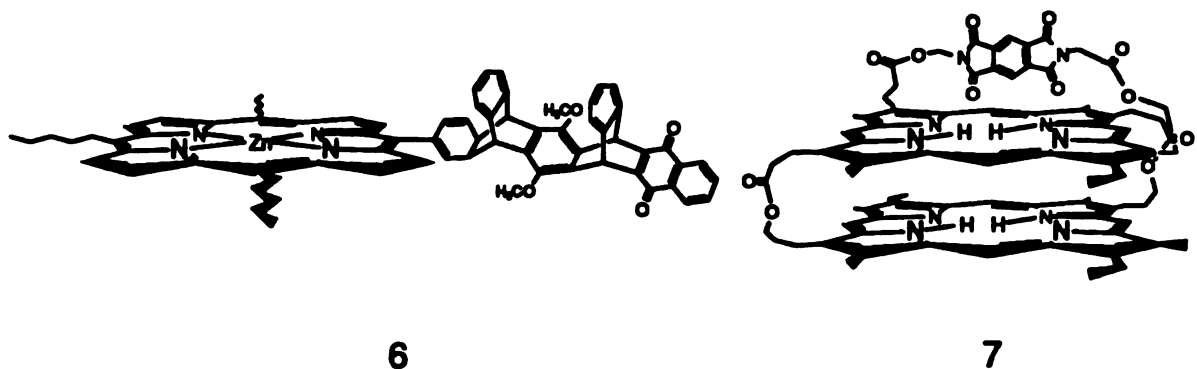


Although (4) is one of the most spectroscopically well defined systems available for the study of ET, the dependence of the electronic coupling on the nature and orientation of the spacer presents new problems. Presumably, for a fixed angular orientation between the donor and

acceptor, the electronic coupling should remain solvent independent. The magnitude of this energy may not be large enough, even at the maximum value of  $H_{AB}$  near  $\theta = 45^\circ$ , to permit observation of these effects is important to solvent dynamics control of ET. Without further studies pertaining to these concerns, investigation of other molecular architectures may prove more straightforward.

Orientational effects on orbital overlap have also been examined by Osuka and Maruyama through cofacially staggered diporphyrin conformers (5).<sup>95</sup> However, in these homologous dimers (5), no charge transfer transients were observed upon optical excitation, but the observation of split Soret bands in the ground state absorption spectrum is indicative of strong electronic coupling between these subunits. It is important to note that the absence of an observable charge transfer state is easily rectified by judicious substitution of one of the metal centers in the dimer. Also, the observation of strong electronic coupling between the respective subunits, provides promise for this structure in the study of solvent dynamics in ET.

Covalently attaching substituted quinone-like acceptors to general porphyrin motifs has been used to enhance the driving for the ET so that structural effects can be further examined. Wasielewski has comprehensively investigated the picosecond photophysics of a plethora of linear porphyrin-quinone complexes in this class (6),<sup>96</sup> while Harrison and coworkers<sup>97</sup> have studied the ET kinetics in cofacial arrangements of both diad and triad complexes (7).



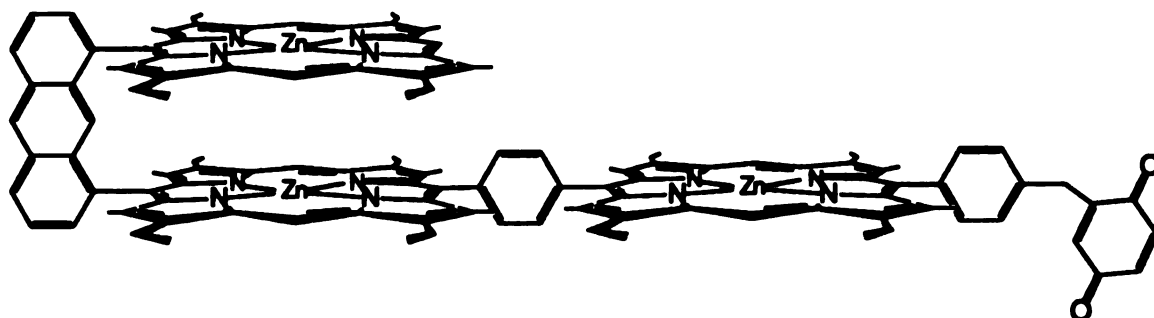
Similar to the results of Paddon-Row<sup>94</sup> and Closs and Miller,<sup>95</sup> a strong syn/anti conformational effect of the bridge is observed in the ET rate constants of (6). Wasielewski has attributed these effects to better overlap of the spacer wavefunctions in the anti versus the syn configuration. Furthermore, an enhanced rate of CR was observed when the dimethoxybenzene substituted spacer was used rather than its normal benzene counterpart. This result was attributed to an electronic configuration of the bridge that contains contributions from the dimethoxybenzene cation intermediate. Due to the intervening effects of the spacer in the ET sequence, these systems are not well designed for investigating solvent dynamics in ET. Dependence of the ET rate constant on spacer energetics introduces a new static concern which would need to be systematically explored through a solvent dependence of spacer energetics. Although unraveling these effects is not incomprehensible, elimination of potential interference from the spacer is a wiser approach.

The ET kinetics obtained for (7) were found to be 3 orders of magnitude faster ( $10^{10} \text{ s}^{-1}$ ) than those observed in edge-to-edge complexes comprised of the same components. The authors cite geometric variations between the cofacial and linear structures as the source of the rate constant disparity even though direct orbital overlap between the porphyrin and the

pyromellitimide acceptor would appear to substantiate the experimental results. Since D—A coupling through the seven atom ester linkage is not likely to support such facile ET rates, it is not considered to participate electronically in the ET event. This a key result pertaining to the potential use of (7) as a potential probe of solvation dynamics in ET. Unlike some of the systems discussed previously, no dependence on the bridge between the donor and acceptor is expected and therefore solvent contributions to the electronic coupling are reduced. The ET rate constant is sufficiently large that dynamics effects have the potential to be rate limiting. These advantages are offset by the structural complexity of the system, due in large part to the presence of the additional porphyrin.

The porphyrin-quinone diad studies of Osuka, Maruyama and Mataga have shown some promise for observing dynamically controlled ET rates in this general D—A structure. They have determined the energy gap and temperature dependence of the CS and CR reactions between the porphyrin donor and the quinone acceptor. Interestingly, they find the temperature dependent ET rate constant trends difficult to interpret on the basis on classical ET theory and have therefore invoked quantum mechanical tunneling via high frequency vibrational coupling to the solvent as a potential explanation of the data.<sup>98</sup> It is not clear whether this mechanism or a model which includes the influence of solvation dynamics, better describes the temperature dependence of the ET rate constants.

Osuka and Maruyama and their coworkers have also prepared porphyrin triads and tetrads with covalently linked quinones.<sup>99</sup>

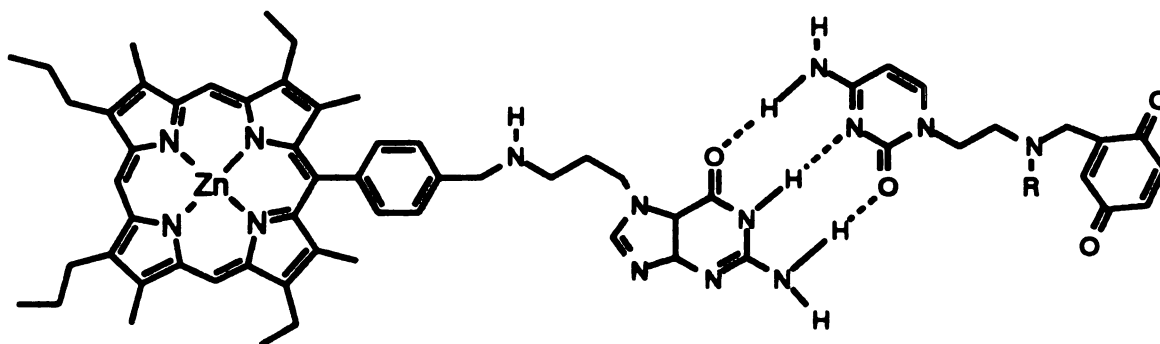


8

The authors find that electron transfer occurs between the covalently linked porphyrin-quinone moieties, with a subsequent dark electron transfer from the cofacial pair to the central porphyrin. These conclusions were drawn from transient optical spectroscopy and are consistent with greater than 90% fluorescence quenching of the Zn-porphyrin monomer excited state. From an ET point of view, this system is intriguing, but it is far too complex, both structurally and electronically, to be an effective probe of solvation dynamics. It has many potential problems such as lack of well defined structure, poor spectroscopic separation of the multistep ion-pair states and the inability to exclusively prepare an excited state of one specific chromophore. Also, the anthracene bridge can present problems within the cofacial pair as it is thought to participate in an intradimer ET scheme when an appreciable driving force exists between the two porphyrins.<sup>100</sup> Additionally, the affinity for protonation of reduced quinones in all of these donor-acceptor systems will impede straightforward interpretation of solvent dynamics trends in the ET rates. The presence of a proton transfer pathway convolved with the ET reaction(s) will introduce a solvent pH dependence into the ET rates.

Accounting for these effects is cumbersome and therefore best eluded through choice of D—A probe molecule.

Problems stemming from a pH dependence of the ET rate constants for quinoid-like structures are further amplified in some of the more novel D—A assemblies, which employ a hydrogen bonds to link donors and acceptors in a lock and key arrangement. In addition to problems induced by solvation effects at the interface, proton motion within hydrogen bonds can be rapid, thereby influencing the ET rate in parallel to the dynamics of solvation. Turró and coworkers stressed the importance of proton motion with their observation of a significant kinetic isotope effect in ET rate constants measured between a Zn-porphyrin donor and dinitrobenzene acceptor, assembled by a 2 point carboxylic acid hydrogen-bonded network.<sup>101</sup> From transient absorption studies, they determined the deuterium to proton ET rate constant ratio ( $k_H/k_D$ ) to be 1.6, indicating a strong dependence on the nature of the interface. Similar studies by Harriman, Kubo and Sessler have determined the ET kinetics between a Zn-porphyrin and benzoquinone via a 3 point cysteine-guanine hydrogen-bonded linkage (9).<sup>102</sup>



Both of these architectures are particularly interesting to the ET community because they permit the study of D—A coupling as a function of the number and directionality of hydrogen bonds while maintaining a relatively constant driving force and reorganizational energy. Additionally, the concept of self-assembly minimizes the need for complex synthetic methodologies and purification procedures. Photophysical studies of (9) show weak fluorescence quenching of the Zn-porphyrin by the hydrogen-bonded benzoquinone acceptor. Unfortunately, the absence of radical cation/anion transient absorption spectra leaves some question as to the identity of the quenching mechanism. Also, the lack of structural rigidity in this particular system inhibits accurate determination of distance dependence of the electronic coupling ( $\beta$ ), which is a key parameter in comparing through-space and through-bond D—A interactions.

In a subsequent work, the authors report a more rigidly structured system, which assumes a bent geometry upon removal of the four-atom linkages between guanine and the Zn-porphyrin donor, and the cytosine and benzoquinone acceptor. Association of the quinone causes moderate quenching ( $\tau=710$  ps) of the 1.8 ns Zn-porphyrin excited state lifetime. From the quenching rate constant, the unimolecular ET rate constant was calculated to be  $8.6 \times 10^9 \text{ s}^{-1}$ . This value is not unreasonable in consideration of other fixed distance ET rate constants measured through hydrogen-bonded pathways in metalloproteins. Although studies of self-assembled hydrogen bonded systems cannot be used directly to examine the effects of solvent motion on the ET rate constants, they represent the next level of sophistication in the future of dynamics effects in ET.

Determining the role of solvent dynamics in activated ET is most effectively accomplished by studying well defined charge transfer reactions





occurring in the Marcus inverted region as dynamics effects are not eclipsed by static contributions from the solvent. With the comprehensive background developed in fixed distance D—A ET, we have chosen to employ rigid cofacial diporphyrin and porphyrin-chlorin complexes to investigate dynamics effects in ET. Preliminary work employing these systems confirmed the presence of a solvent-dependent charge-separated state, thus identifying these particular diporphyrins as possible molecular probes of dynamics effects in ET. These complexes also have several experimental advantages; they are structurally rigid, thus diminishing diffusive and torsional contributions to the ET rate, the excited state energies and characteristic ion-pair absorption features are spectroscopically accessible to our laser apparatus, and the redox properties of the compounds are tunable via metal substitution of the macrocycle or functionalization at the porphyrin periphery. This latter property is vital to the investigation of solvent dynamics effects on ET rate constants as a function of driving force.

The goal of the research presented in this dissertation is to assess the role of solvent dynamics in activated ET processes. From the results of transient solvation experiments presented herein, it is known that solvent dynamics can control activationless ET reactions which are competitive with solvent motion. However, since most ET reactions possess appreciable barriers, examination of dynamics effects in activated ET serves as a more chemically valuable model. In this case, care must be taken to account for energetic variations in the barrier height, as this will dramatically affect the observed rate constants. By studying fixed distance intramolecular ET reactions, the energetics associated with D—A complex formation are eliminated. Additionally, since most ET reactions involve

discrete charge-separated intermediates and not polar excited states, there exists a need for better molecular probes of solvent dynamics in ET than those used in typical transient solvation studies.

The experimental details of ET rate constant determination are discussed in chapter II. Proper procedures for obtaining nanosecond and picosecond transient optical data, as well as time correlated single photon counting lifetimes are described. A general discussion pertaining to compound synthesis, sample preparation and redox potential measurements is also given.

In chapter III, the results of ET rate constant measurements for Mg—H<sub>2</sub> and Mg—Cu diporphyrin systems, as well as the Zn—H<sub>2</sub>(=O) porphyrin-chlorin dimer, in acetone, N,N-dimethylformamide, dichloromethane and the nitrile and acetate solvent series are described. On the basis of their redox properties, these systems have activated charge recombination (reverse ET) rate constants lying deep in the Marcus inverted region. From recent theoretical treatments, these conditions are most likely to reveal solvent dynamics effects on ET rate constants. In order to correlate these rate constants with dynamics, we have employed solvents where the average solvent relaxation times ( $\tau_s$ ) have been measured by ultrafast fluorescence Stokes shift techniques. Also, we have attempted to correlate ET rates measured within a homologous solvent series, as this will diminish variations in the activation barrier due to differences in the dielectric constant.

Chapter IV continues in this theme by discussing the ET kinetics of the porphyrin-chlorin complexes denoted as Zn—H<sub>2</sub>(=C(CN)<sub>2</sub>) and Zn—Cu(=C(CN)<sub>2</sub>). The charge recombination step for these systems has been shifted toward the near-activationless limit by substituting the porphyrin

periphery with the strongly electron withdrawing dicyanomethide group. As expected from inverted region ET arguments, this substitution increases the ET rates by an order of magnitude.

Finally, in Chapter V a summary of the trends derived from these studies as well as some perspectives on future work within this class of compounds, are given.

## CHAPTER II

### EXPERIMENTAL METHODS

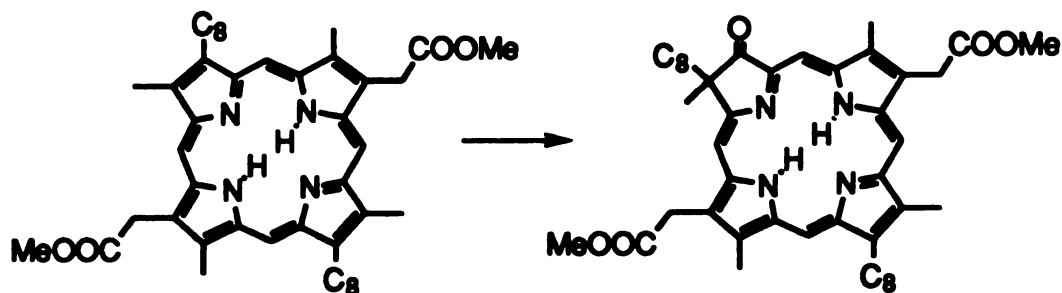
#### A. Sample Preparation

##### *1. Cofacial Dimer Synthesis*

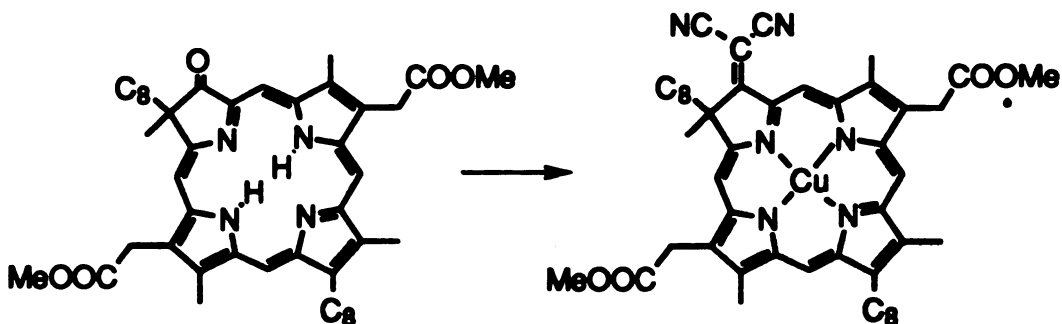
All of the cofacial diporphyrin complexes used for the solvation dynamics studies were prepared in the laboratory of Professor C. K. Chang in the Chemistry Department at Michigan State University. The Mg—H<sub>2</sub> dimer had been prepared in the late 1970s and was synthesized according to this literature procedure.<sup>103</sup> The syntheses of the Mg—Cu diporphyrin and the porphyrin-chlorin complexes followed the same preparative scheme with Zn—H<sub>2</sub>(=O) and Zn—Cu(=C(CN)<sub>2</sub>) as precursors to Zn—H<sub>2</sub>(=C(CN)<sub>2</sub>).

The parent compound, dimethyl 3,13-dioctyl-2,7,12,17-tetramethylporphine-8,18-diacetate, was prepared by the standard dipyrromethene condensation as described previously.<sup>104</sup> This parent porphyrin was first converted to the ketochlorin in about 30% yield by an acid-catalyzed pinacolic rearrangement of the vicinal diol resulting from an OsO<sub>4</sub> oxidation of the porphyrin.<sup>105</sup>

1



The keto group of the chlorin was subsequently converted into the strongly electron-withdrawing dicyanomethide by a general procedure that was developed for synthesizing red-light absorbing porphyrin dyes used in photodynamic therapy.<sup>106</sup>



The Cu(II) complex (0.2 g) was dissolved in dry CHCl<sub>3</sub>, TiCl<sub>4</sub> (2 ml) was added, and the mixture was allowed to reflux for 10 mins. A solution consisting of malononitrile (2 g) and pyridine (1 ml) in 15 ml of CHCl<sub>3</sub> was added to the refluxing mixture and heating was maintained for 6 h to achieve nearly quantitative transformation. After cooling, the solution was filtered, and the precipitates were washed with CH<sub>2</sub>Cl<sub>2</sub> before being discarded. The combined organic solution containing the product was subsequently washed with water and evaporated to dryness. To remove the copper ion, the crude product was dissolved and stirred in concentrated sulfuric acid (15 ml) for 2 h. The mixture was cooled in an ice bath and methanol (300 ml) was slowly added. After 6 h, the solution was diluted

with  $\text{CH}_2\text{Cl}_2$  and washed with aqueous NaOAc and water. The product in the organic layer was purified by chromatography on silica gel plates using  $\text{CH}_2\text{Cl}_2$  as the eluent to give the green colored Cu(II) complex (yield 76%). The structures of the chlorins were confirmed by  $^1\text{H}$ -NMR, UV-vis, IR, and mass spectra.

The chlorin dimethyl esters were hydrolyzed in formic acid and HCl; for the case of the dicyanomethide, no reaction involving the cyano groups was observed. The corresponding acid chlorides were formed by heating the hydrolyzed acid with oxalyl chloride in  $\text{CH}_2\text{Cl}_2$ . The porphyrin/chlorin dimers were obtained by the condensation of Zn(II) porphyrin diamine with the chlorin diacid chlorides.<sup>104,105</sup>

The resultant cofacial systems easily separated into the “syn” and “anti” isomers when isolated on silica gel TLC plates. Based on previous experience with other cofacial diporphyrins, the faster moving component was tentatively assigned as the “anti” form. Electron transfer studies were carried on the “anti” isomers owing to their greater abundance.

## *2. Driving Force Determination via Cyclic Voltammetry*

Owing to the difficulty in synthesizing the cofacial dimers, sufficient quantities of  $\text{Mg—H}_2$  were not available to comprehensively investigate the solvent dependence of the redox potentials. Therefore, the solvent dependence of the reduction potentials of MgOEP and  $\text{H}_2\text{OEP}$  (OEP represents 1,2,3,4,5,6,7,8-octaethylporphyrin) were obtained by cyclic voltammetry employing a PAR 173 potentiostat, 175 programmer, and a 179 digital coulometer. The electrochemical cell configuration employed a Pt button working electrode referenced to a stable Ag wire potential. A Pt

mesh counter electrode was placed in a separate cell compartment conductively bridged by a porous glass frit. The current measured at the working electrode was transcribed using a Houston X-Y recorder and the Ag wire potential referenced to the SCE scale by using the ferrocene/ferrocenium redox couple as an internal standard ( $E_{1/2}(\text{Fc}^{+/0}) = 0.31 \text{ V vs SCE}$ ).<sup>107</sup>

The  $E_{1/2}$  values for the Zn(II) porphyrin diamine, free base keto-chlorin ( $\text{H}_2(=\text{O})$ ), free base dicyanomethinide chlorin ( $\text{H}_2(=\text{C}(\text{CN})_2)$ ), Cu(II) dicyanomethinide chlorin ( $\text{Cu}(=\text{C}(\text{CN})_2)$ ) and Mg—Cu diporphyrin systems were measured using a Bioanalytical Systems CV-1A potentiostat interfaced to a Linseis X-Y recorder. In a low volume electrochemical cell, a platinum wire working electrode referenced to Ag/AgCl and a Pt wire counter electrode were immersed in  $\text{CH}_2\text{Cl}_2$  containing 0.1 M tetrabutylammonium perchlorate. The reduction potentials for the porphyrin and chlorin species were obtained using typical sample concentrations of  $\sim 1 \times 10^{-3} \text{ M}$ .

### *3. Sample Preparation for Photophysical Measurements*

The solvents employed for the solvation dynamics studies were obtained commercially in the highest purity available from Burdick and Jackson Laboratories and Aldrich Chemical Company. Prior to use, solvents were dried over 4 Å sieves that had been previously dehydrated by baking at 100 °C and  $2 \times 10^{-5}$  torr for 36 h. The nitrile solvents were additionally dried over 3 Å sieves for at least 36 h prior to use.

Samples for transient absorption measurements were prepared by introducing a given quantity of the cofacial dimer into a specially designed



spectroscopic cell produced in the Scientific Glassblowing Laboratory, at Michigan State University. The cell was equipped with a 2 mm quartz cuvette, two Kontes high-vacuum teflon stopcocks, a glass bulb used as a solvent reservoir, and a 24/40 ground glass joint for attachment to a high vacuum line. Solvents were introduced into the bulb either directly or by vacuum distillation, and subjected to seven freeze-pump-thaw cycles to remove dissolved oxygen. Upon dissolution, the concentration of the cofacial dimer was adjusted by addition or removal of solvent until the optical absorption at the pump wavelength was roughly 1.0 absorbance units. Depending on compound solubility, this typically produced samples for transient absorption experiments with donor/acceptor concentrations of 0.1–2.0 mM, as determined from estimated extinction coefficients for the Q bands between 500–700 nm. Sample integrity was monitored by recording UV-vis absorption spectra with a Cary 2300 spectrophotometer before and after transient absorption measurements.

Quantum yields were recorded on a high resolution emission instrument constructed at Michigan State.<sup>108</sup> Absolute fluorescence quantum yields were determined from the corrected emission spectrum of dichloromethane solutions of the respective heterodimers obtained at  $22 \pm 2$  °C. Samples were prepared with absorbances of  $\sim 0.1$  at the excitation wavelength of 585 nm; the luminescence standard was  $\text{Mo}_2\text{Cl}_4(\text{PMe}_3)_4$  ( $\phi_e = 0.26$  in 2-methylpentane<sup>109</sup>) and appropriate corrections were made for differences in molar absorptivities.<sup>110</sup>

## **B. PICOSECOND TRANSIENT ABSORPTION MEASUREMENTS**

### *1. Apparatus*

Direct observation of ultrafast photoinduced electron transfer (ET) processes in covalently linked donor/acceptor complexes has become routine owing to advances in laser technology and pulse compression techniques.<sup>111</sup> Because these processes can occur on the sub-nanosecond timescale, optical methods afford the only option for obtaining the time resolution required to accurately determine ultrafast intramolecular ET rate constants. Within this framework, one of the most effective techniques employed to determine the rates of ET is transient absorption. The success of this technique is based on the high extinction coefficients of the ion pair intermediates produced upon optical excitation. Short-lived charge-separated states of the cofacial systems gives rise to large transient absorbances that can be readily detected from a white light background for excited state concentrations  $\geq 1 \mu\text{M}$ . Furthermore, the kinetics of these absorption changes provide valuable information regarding the electronic structure and excited state decay pathways intrinsic to the transient species under investigation.

The most efficient and widely employed method for obtaining time-resolved transient spectra utilizes a pump/probe arrangement where both the excitation source and the white light probe beam are pulsed with an adjustable intervening time delay. These criteria are satisfied by using one laser beam to excite the sample directly while another beam, acting as a probe, traverses a variable optical delay line. The discrete frequency probe beam can then be transformed into a white light continuum by a

nonlinear optical process known as self-phase modulation.<sup>111</sup> This produces pump and probe pulses with identical temporal profiles at a continuously variable time relationship, which can be used to investigate the time evolution of the transient absorption spectrum.

The picosecond transient absorption apparatus employed for the ET rate constant measurements described in this dissertation is housed in the LASER Laboratory at Michigan State and shown in Figure 6. Sample excitation pulses are initially produced by a Coherent Antares (76-s) modelocked Nd:YAG laser operating at 76 MHz. Optical alignment of the cavity is achieved by monitoring the pulse train propagating inside the laser cavity with an Antel Optronics silicon avalanche photodiode interfaced to a Tektronix 7904A fast sampling oscilloscope equipped with both Tektronix sampling (model 7S11) and sampling sweep (model 7T11A) units. The 1064-nm output of this laser (400 nJ/pulse and FWHM = 70 ps) is frequency doubled by a temperature controlled KTP (KTiOPO<sub>4</sub>) crystal, resulting in 532-nm pulses (~ 40 nJ/pulse) of 70 ps duration. The resulting 532 nm output pulse train is frequency summed with the laser fundamental in a  $\beta$ -barium borate crystal housed in a Coherent 7950 THG assembly to produce 354.7-nm output pulses (13 nJ/pulse). The second and third harmonic outputs of the Nd:YAG laser are then used to synchronously pump two Coherent 702 dye lasers retrofitted with model 7950 cavity dumpers. The dye lasers are optically configured for dyes in the red and blue regions of the spectrum and are almost exclusively run with Rhodamine 590 ( $\lambda_{\text{out}} = 570\text{--}620$  nm, 80 nJ/pulse at 3.8 MHz) and Stilbene 420 ( $\lambda_{\text{out}} = 420\text{--}470$  nm, 40 nJ/pulse at 3.8 MHz) as their lasing media. Dye laser cavity length adjustments and output pulse width determinations are performed by displaying the output of two Inrad Model 5-14

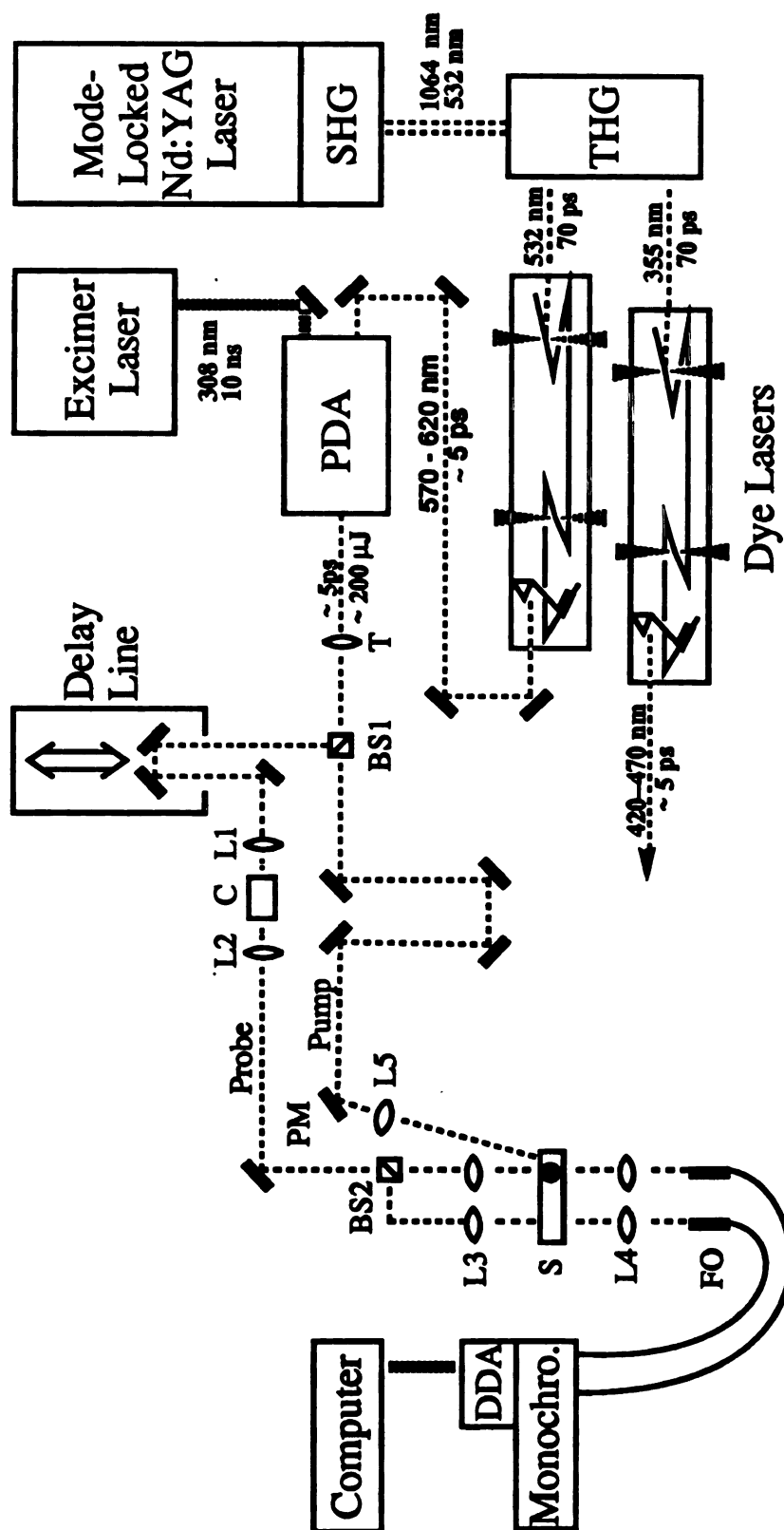


**Figure 6.** Original configuration of the picosecond laser system, pulsed dye amplifier, and transient absorption spectrometer.

autocorrelators on two Tektronix 2225 oscilloscopes. The dye lasers are typically run without the use of a saturable absorber jet in order to obtain maximum output power. Unfortunately, this configuration does not allow pulse widths below 5 ps to be readily obtained.

Since the magnitude of the transient absorption signal is directly proportional to the concentration of transient species produced upon excitation, higher energy pulses at lower repetition rates are most desirable. Accordingly, the output of the synchronously-pumped dye lasers are amplified by six orders of magnitude and repetition rates are reduced to less than 100 Hz, as described below.

Early transient absorption measurements were made by amplifying the output of the red dye laser with Rhodamine 590 in a four-stage pulsed dye-amplifier (Lambda-Physik FL2003) pumped by the 308 nm output of a XeCl excimer laser (Lambda-Physik EMG 102 MSC) operating at 50 Hz. Pulse amplification was obtained by spatially and temporally overlapping both the 702 dye laser pulse and the excimer laser pulse (FWHM = 10 ns) to produce output pulse energies of 200–400  $\mu\text{J}$  at 588 nm. Synchronization of the 1 MHz dye laser pulse train with the 50 Hz excimer laser was performed by using the attenuated signal from the SYNC OUT of the cavity dumper driver to trigger the excimer laser via an external rep-rate control module (Lambda-Physik FL2013), which outputs coincident trigger pulses at rates of 1–100 Hz. Temporal drifts in the firing of the excimer's thyatron were compensated by monitoring the optical pulse arrival time at a photodiode placed in the excimer laser beam path. The time average of several output pulses from the photodiode was used as a temporal reference in a feedback circuit (Lambda-Physik EMG 97), which modified the timing of the external trigger pulse to the excimer laser.

Proper adjustment of these timing devices was critical to laser performance, as the most efficient amplification is obtained when the excimer laser (pump) and dye laser (seed) pulses are temporally overlapped. This condition results because the population of excited state dye molecules formed by the excimer flash is greatest upon excitation, thus allowing the highest possible number of stimulated emission photons to be produced by the seed pulse from the dye laser. Although the 200–400  $\mu\text{J}$  output energy from the amplifier system was sufficient to conduct transient absorption measurements using the remaining optics shown in Figure 6, the poor pulse-to-pulse stability and long term power degradation frequently resulted in signal-to-noise ratios of only 10 and occasionally perturbed the lifetime determination of the transient species.

In an effort to correct these problems and produce higher pulse energies, a Nd:YAG regenerative amplifier system (Continuum model RGA60) and two pulsed dye amplifiers (Continuum model PTA60) were purchased and implemented into our existing mode-locked laser system as shown in Figure 7. There are three main advantages of the regenerative amplifier system over the excimer pumped pulsed dye-amplifier (PDA) apparatus. First, the pulse-to-pulse stability of the regenerative amplifier is greatly enhanced over the excimer/PDA system due to a decrease in the timing jitter between the pump laser for the dye-amplifier and the dye laser seed pulse. Second, the quantum efficiency of common dyes is increased when excited with the 532 nm and 355 nm pump wavelengths of the RGA60, producing higher output powers than those obtained from the 308 nm excitation of the XeCl excimer laser. Last, the superior long term stability of Nd:YAG based lasers over their chemical laser counterparts can greatly enhance the reliability of transient absorption kinetic data because

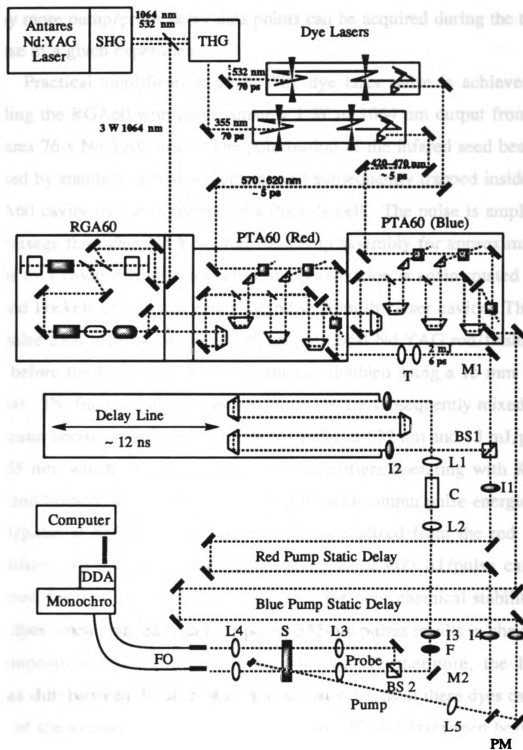


**Figure 7.** Current configuration of the picosecond laser system, regenerative amplifier and transient absorption spectrometer.

many more pump/probe delay data points can be acquired during the time-course of a given experiment.

Practical amplification of the 702 dye laser pulse is achieved by seeding the RGA60 with approximately 1 W of 1064 nm output from the Antares 76-s Nd:YAG laser. The polarization of the infrared seed beam is rotated by standard optical waveplates and subsequently trapped inside the RGA60 cavity by the triggering of a Pockels cell. The pulse is amplified by passage through a Nd:YAG rod/flashlamp assembly for approximately 40 ns ( $\sim 7$  cavity round trips) before the polarization is again rotated by a second Pockels cell, which ejects the pulse from the laser cavity. The 50 Hz pulse train is further amplified by an additional Nd:YAG rod/flashlamp unit before the 1064-nm output is frequency doubled using a 15 mm KTP crystal. The fundamental and second harmonic are subsequently mixed in a  $\beta$ -barium borate crystal producing 24 mJ/pulse at 532 nm and 13 mJ/pulse at 355 nm, which are used to pump dye-amplifiers operating with Kiton Red and Stilbene 420, respectively. Highly stable output pulse energies of 2 mJ/pulse at 585 nm and 50 Hz are easily realized from the red dye-amplifier. At 420 nm, output pulse energies of 400  $\mu$ J/pulse can be obtained for the first hour of operation, but the poor chemical stability of blue dyes when pumped with high power 355-nm pulses results in chemical decomposition and rapid power degradation. Furthermore, the large Stokes shift between the absorption and emission bands of these dyes causes 75% of the average power from the Coherent 702 dye laser seed beam to be detected after traversing the amplifier. The large disparity between the 50 Hz repetition rate of the RGA60 and the 76 MHz of the Coherent 702 dye laser (CW mode) causes the output of the dye-amplifier to be characterized by 2 nJ pulses from the dye laser propagating 13 ns apart



with a 400  $\mu$ J pulse also at 420 nm occurring every 20 ms. Since many of the porphyrin systems being investigated by transient absorption have  $^3\pi\pi^*$  states with lifetimes of several milliseconds, the initial ground state repopulation does not recover before re-excitation by another 702 dye laser pulse occurs. Consequently, photo-accumulation occurs in the  $^3\pi\pi^*$  state, which reduces population of other excited states of interest and can interfere with accurate interpretation of transient optical data. Currently, implementation of a Pockels cell to selectively introduce pulses into the dye-amplifier at 50 Hz, as well as larger volume, water cooled dye circulators, are among modifications being investigated to improve the performance of the blue dye-amplifier.

Output pulses from either dye-amplifier system are collimated with a telescope (T) and split 50/50 by a cube beamsplitter (BS1) for sample excitation and continuum generation as shown in Figure 7. The probe beam traverses an optical delay line equipped with two retro-reflectors (Melles Griot) mounted on a carriage under stepping motor control (Klinger CC1.1). The stepping motor is capable of producing optical delays of  $\sim 70$  fs/step for a single pass and 12 ns total delay when a third retro-reflector is used at the head of the delay line in the double pass configuration. The probe pulses are then focused by an f/7 plano-convex lens (L1) into a 5 cm pathlength quartz cell (C) containing a saturated  $\text{ZnCl}_2$  solution. The strong electric field of the ultrafast optical pulse generates an intensity dependent increase in the index of refraction of the solution, thus frequency chirping the optical pulse to give a white light continuum about the central laser frequency.<sup>111</sup> The continuum is collimated with a 2 in lens (L2) and passed through either a short or long wavelength transmittance dielectric filter (F) to remove the central laser

line from the remaining white light. This provides a 6 ps probe pulse for transient absorption measurements from  $\sim 390\text{--}570\text{ nm}$  or from  $\sim 600\text{--}900\text{ nm}$ . The white light is then split 50/50 by a second cube beamsplitter (BS2) and vertically displaced such that both beams can be passed through different regions of the sample. The beams are focused into the sample (S) by two 1 in f/7 glass achromatic doublet lenses (L3). These particular lenses were chosen because they minimize chromatic aberration across all wavelengths present in the continuum. The two beams are then collected and refocused by two 1 in f/4 glass lenses (L4) onto two fiber optics (FO) interfaced to an ISA HR-320 single monochromator with a 300 gr/mm grating blazed at 500 nm. The images from the two fiber optics are projected onto individual 512 pixel arrays of a dual diode array detector (Princeton Instruments DDA-512) interfaced to a detector controller and Compaq 320 sc personal computer.

Upon production of the pump components at BS1, the pump pulse train is passed through a stationary delay line in order to temporally overlap the pump and probe components at the sample for a given variable delay setting. The pump beam is then focused onto the sample with a 1 in. f/10 lens (L5) at an angle of incidence of  $13^\circ$  and spatially overlapped the with probe component entering the lower of the two vertically displaced optical fibers. Quality transient absorption kinetics data are then obtained by temporally superimposing the pump and probe pulses (zero-time) and accurately referencing the subsequent optical delays between them. These spectra are characteristic of the excited state lifetime and the wavelength dependent differential extinction coefficients of the excited molecules.

An alternative optical arrangement has been devised to use the 355 nm beam directly out of the RGA60 regenerative amplifier head to pump

samples that do not absorb in the 570–620 nm region. In this configuration, a quartz prism is inserted inside the red PTA60 to intercept the third harmonic as it passes through this dye-amplifier en route to the blue PTA60. The subsequent 90° turn ejects the pulse from the dye amplifier to the table where the transient absorption spectrometer is located. Another quartz prism directs the 355 nm beam along the edge of the table to a third prism placed in the beam path designated for the pump component of the blue dye-amplifier. In this mode of operation, half of the pulse train from the red PTA60 is terminated following BS1 (Figure 7), while the remaining pulses are allowed to propagate through the optical delay line and subsequently used for continuum generation. Termination of the amplified pulse train at BS1 is chosen rather than reconfiguration of the optics about the delay line because the alignment of the latter is cumbersome at best and crucial to the success of transient absorption kinetics measurements. Additionally, sufficient continuum intensity is generated with <1 mJ pulses of 585 nm radiation and thus employment of the greater pulse energies has been unnecessary to date.

The quantitative transient absorption signal or optical density (OD) at a given wavelength is determined by comparing the intensity of the transmitted light through the sample in the presence and absence of optical excitation according to

$$\Delta OD = -\log\left(\frac{I_0}{I}\right) \quad (1)$$

where  $I_0$  represents the intensity of the probe component traversing the region of the sample not excited by the pump beam (top) and  $I$  denotes the intensity of the second half of the probe component which passes through

the excited region of the sample (bottom). This relationship derives from the attenuation of the radiant intensity of the probe beam impinging upon the sample and is obtained through an extension of Beer's Law.<sup>112</sup> Due to differences in sensitivity of the independent diode array detectors and minor variations in the chromatic transmittance/reflectance of BS2, the observed intensities of these beams as a function of wavelength are not identical and therefore need to be normalized. This is accomplished by collecting scans of the top and bottom probe components in the absence of sample excitation at each time delay interval and multiplying the point-by-point ratio of the averaged light intensity ( $I_b/I_t$ ) by  $I_o/I$  from eq 1. Additionally, since the detectors possess an inherent dark current that can accumulate significantly during data acquisition, averaged exposures for both top and bottom arrays are obtained at the beginning of the experiment in the absence of light ( $B_t$  and  $B_b$ ) and subtracted from all subsequent white light intensity data files. Typically, 400 scans are acquired at an exposure time of 0.33 sec/scan across a 130 nm spectral window for a each optical delay in both pump and no pump configurations. The determination of  $\Delta OD$  is then performed through computer calculation using the expression,<sup>113</sup>

$$\Delta OD = -\log \left\{ \frac{(I_o - B_t)(I_b - B_b)}{(I - B_b)(I_t - B_t)} \right\} \quad (2)$$

where  $I_o$  and  $I$  are as defined in eq 1. Evaluation of eq 2 for a series of variable delay stage positions in a given spectral window produces spectroscopic as well as kinetic information about the excited state decay pathway. Complete transient spectral characteristics can be obtained at a fixed optical delay by collecting spectra at any of 20 monochromator

settings calibrated by employing atomic emission lines from either Hg or Cu/Zn/Fe/Mn hollow cathode lamps. The spectral characteristics of the lamps were determined using a scanning emission spectrometer with a 1200 gr/mm grating.<sup>6</sup> The calibration files are known to be accurate to within 1 nm, based on both HeNe laser and gaseous Hg emission lines.

## ***2. General Alignment Procedure***

Upon optimization of the output power of the RGA60 and PTA60 regenerative pulsed dye amplifiers, the pulse train is passed through a collimating telescope (T, Figure 7) and turned 90° to the table where the transient absorption spectrometer is based. The position of the beam should be examined on the two alignment irises placed along the pump beam path, in addition to those located at the entrance of the delay line and in front of the last turning mirror prior to the sample (M2). At these four points the beam should be centered and  $\leq 5$  mm in diameter. Any angular displacement of the beam should be corrected using a dual optic manipulation of the turning mirror immediately following the telescope (M1) and the final mirror inside the PTA60. Diligence in this initial step is critical as the variable delay line will be precisely aligned for only one specific input beam position as defined by the collection of alignment irises. As long as the position of the cube beamsplitter (BS1) directing the beam into the delay line is strictly maintained, these alignment tools will provide an accurate method for retaining instrument alignment. At this point, the four irises should be opened and a pinhole or tightly closed iris placed at the focal point of the lower of the two lenses. The user should place a white card shortly after this iris and while moving the delay line to the

longest optical delay, monitor the projection of the beam exiting the pinhole on the white card. No change in the spatial distribution of the beam should be observed for the entire travel distance of the delay line. If this condition cannot be achieved, then the initial alignment sequence should be repeated. If the angular displacement persists, complete re-alignment of the cube beamsplitter (BS1), the delay line optics and the four irises must be conducted.

Once the beam is properly aligned through the optics, a focused continuum should be observed at the sample and at both fiber optic detectors. Generally, if the initial phase of the alignment procedure is executed with little difficulty, then no adjustments of the focusing lenses need to be made. The user should place the appropriate dielectric filter into the continuum beam, depending on which region of the spectrum the experiment will be conducted in. Once the sample is introduced into the beam path, the fiber optics leading to the detector are adjusted through the use of micrometer positioners. The carriage should be moved to center the lower continuum beam on the center of the fiber optic face while simultaneously monitoring the detector output on the computer. This is performed by free-running the detector in the Princeton Instruments software by initiating the batch file, "abs.bat" and loading the stored experiment filename, "I." If the blue trace (lower detector) is saturating the diode array, the monochromator slits should be closed to  $\sim 5-10\ \mu\text{m}$  and the iris following the continuum cell tightened. The upper portion of the continuum should be aligned into the second fiber optic by adjusting the mirror mounted vertically above the cube beamsplitter (BS2). When properly aligned, both continuum beams should have a minimum amount of horizontal displacement at both the sample and last focusing lenses (L4).

Also the intensity of signal arising from each of these beams should appear within 15% of one another across the spectral window, as judged by monitoring the detector output on the computer screen in the free-running mode. The excitation pulse should now be visually overlapped with the lower of the two continuum beams inside the 2 mm quartz cuvette by adjusting the pump mirror (PM, Figure 7) such that the beams intersect at the center of the cell. Provided zero-time is known to within  $\pm 100$  ps, the spatial overlap of these beams can be optimized by moving the delay line to positive time (pump/probe delay  $> 10$  ps) and adjusting the pump mirror to induce the largest change in the intensity of the free-running detector signal from the continuum light impinging upon the bottom diode in the presence and absence of the pump beam. This change may be positive or negative depending on the sign of the differential extinction coefficient. This method usually produces the best pump/probe overlap. In the event that the temporal relationship between the pump and probe pulses is completely ambiguous, initial estimates of zero-time can be made within 500 ps by introducing the overlapped pulses into a Si avalanche photodiode and monitoring the resulting signal with a Tektronix DSA 602A digital signal analyzer which is capable of resolving 1 ns (FWHM) photodiode response functions. By moving the delay line, the temporal relationship of the pulses will be directly observed. Temporal overlap within 10 ps can be obtained by monitoring the intensity of the stimulated emission signal in the 600 nm region from a  $10^{-2}$  M solution of 3,3'-diethyloxadicarbocyanine iodide (DODCI) in methanol. As the pump and probe pulses are brought closer to temporal resonance, the emission of this dye molecule will be strongly enhanced by the presence of the probe beam and can be easily observed in the detector, free-running mode. The intensity of the

stimulated emission will easily saturate the detector so the slits should be closed down below 5  $\mu\text{m}$  such that only small amounts of continuum reach the diode arrays in the absence of the pump beam. This technique can be used to obtain zero-time to within  $\pm 10$  ps for 6 ps pump/probe pulses generated with  $\sim 580$  nm PTA60 output, but cannot be used effectively with greater pulse widths or in other wavelength regions. For these cases, zero-time can be determined by obtaining a cross-correlation trace of the pump and probe pulses by monitoring the rise and decay of a strongly absorbing transient species which has an excited state lifetime shorter than the optical pulse width, such as iron octaethylporphyrin chloride (FeOEPCl,  $\tau < 100$  fs). Alternatively, the maximum of the cross-correlation can be inferred to within 6 ps from the rise of a strong transient absorption in the 400-500 nm region from samples such as DODCI or Zn-substituted porphyrins. In these cases, the short wavelength band-pass filter must be employed to allow continuum in this region to be transmitted and the monochromator grating must be moved to the 120 setting. This method is especially useful because zero-time for many experiments can be determined using the actual sample under investigation, provided it does not possess a time-dependent rise to the strongly absorbing excited state (or ground state bleach) being monitored. Once zero-time is known to within 10 ps, the delay line should be adjusted in 2 ps increments (15 steps in the double pass configuration) to determine the exact maximum in the pump/probe cross-correlation, which corresponds to the best peak-to-peak overlap of the pulses. Occasionally, a partial transient absorption spectrum is observed which is indicative of the blue edge of the continuum pulse arriving prior to the red edge. This signature is especially useful for determining zero-time when the sample under investigation possesses a



rapidly decaying transient ( $\sim 30$  ps), but tends to be unnecessary when relatively slow excited state kinetics processes are examined. In the former situation, the 6 ps time-spread of the pulse can be easily mapped out by moving the delay line in 1 ps increments and monitoring the absorption signal “progress” from the blue edge of the spectral window to the red. The precise origin of this temporal behavior is not fully understood, but interestingly, it produces a wavelength distribution counter to that expected on the basis of group velocity dispersion or spectral chirp from self-phase modulation. Therefore, the most likely cause is temporal spread through the ISA HR-320 single monochromator. Weak pulse broadening does not interfere with the kinetics determination of transients that have appreciable lifetimes. However, in order to access the femtosecond time regime, a subtractive double monochromator may be required.

Once zero-time has been determined, spectra should be taken at fractional time intervals characteristic of lifetime of the excited state being monitored. Generally, the same data acquisition parameters are used for all spectra and are contained in the stored experiment filenames “e” (collection of top ( $I_o$ ) and bottom (I) signals with sample excitation), “n” (collection of top ( $I_t$ ) and bottom ( $I_b$ ) files for array normalization with no sample excitation), and “b” (stores the background dark current of top ( $B_t$ ) and bottom ( $B_b$ ) arrays). All six filenames are collected using 400 array scans at 0.33 sec/exposure. These files are used in a FORTRAN program (TA.for) to calculate  $\Delta OD$  according to eq 2. The transient absorption profile can then be viewed using a standard spreadsheet package.

### 3. *Transient Absorption Data Analysis*

Several transient absorption spectra corresponding to various optical delay times are taken for a given spectral window. The spectra are closely monitored during the course of the experiment to minimize erratic data points due to occasional laser power fluctuations. Once a complete set of delay times has been obtained, the time evolution of the transient absorption can be plotted using a simple spreadsheet package, as the data from TA.exe program are exported in ASCII format. For a single transient species decaying to the ground state, the absorption profile should decay according to monoexponential kinetics across the entire spectral window. Like many highly conjugated organic systems, porphyrinic compounds possess  $^1\pi\pi^*$  and  $^3\pi\pi^*$  excited states that have variable differential extinction coefficients, and thus the kinetics of these states can be convolved due to overlapping transient absorption spectra. Therefore, the determination of excited state decay (or ground state recovery) should be carried out in a region of the spectrum where the species of interest strongly dominates the observed  $\Delta OD$ . In this scenario, the decay of the absorption can be fit to either a sum of exponential functions or the natural logarithm can be taken of the  $\Delta OD$  values and each decay component fit separately to a linear expression. In this manner, all of the transient absorption rate constants reported in this work were determined by monitoring the decay of the absorption maximum of either the  $^1\pi\pi^*$  excited state or the charge-separated state where applicable in the 400–550 nm and/or the 600–850 nm regions [ $\lambda_{\text{max}}$  ( $\text{Mg}^+ - \text{H}_2^-$ )  $\sim$  665 nm,  $\lambda_{\text{max}}$  ( $\text{Zn}^+ - \text{H}_2(=\text{C}(\text{CN})_2)^-$ )  $\sim$  750 nm,  $\lambda_{\text{max}}$  ( $\text{Zn}^+ - \text{H}_2(=\text{O})^-$ )  $\sim$  675 nm ]. Since the differential extinction coefficients for the charge-separated species are

large between 600–850 nm and those of the simultaneously produced  $^1\pi\pi^*$  excited states of these dimers are significantly smaller than in the 400–500 nm region, most transient absorption experiments were conducted between 600–850 nm. This method generally produced  $\Delta OD$  values  $> 0.20$ , which were easily monitored as function of probe delay time. Typically, 10–15  $\Delta OD$  values obtained for a given spectral feature at various delay times were used to determine the lifetime of a particular state. The repopulation rate of the ground state was also determined by monitoring the recovery of the bleaching features for either the porphyrin Soret bands of Mg—H<sub>2</sub> (~410 nm) or the free base chlorin Q<sub>y</sub> band [~650 nm for Zn—H<sub>2</sub>(=O) and 693 nm for Zn—H<sub>2</sub>(=C(CN)<sub>2</sub>).

### C. NANOSECOND TRANSIENT ABSORPTION MEASUREMENTS

Nanosecond transient absorption measurements were conducted only for the Zn—Cu(=C(CN)<sub>2</sub>) dimer and the respective monomeric components of this complex, by utilizing the basic configuration of the nanosecond transient absorption spectrometer described previously.<sup>114</sup> Briefly, sample excitation at 580 nm was achieved using a Quanta Ray pulsed dye laser (Rhodamine 610) pumped with the second harmonic of a Quanta Ray DCR2-A Nd:YAG laser externally triggered at 5 Hz. The white light probe beam was generated from a 150-W pulsed OSRAM Xe arc lamp (XBO150/S) mounted in a Photon Technology International (PTI) A1000 lamp housing and driven with a PTI LPS1000 power supply. The probe beam was collimated and focused onto the sample (0.2 cm path length) by two 2 in, f/7.0 fused silica lenses. The excitation and probe

beams were nearly collinear, with an incidence angle of  $11^\circ$ . The lamp was pulsed (5 Hz repetition rate) to  $\sim 12$  A for a duration of 5 ms, and the white light was passed through a Uniblitz 23X mechanical shutter. The triggering of the Nd:YAG laser, pulsing of the lamp, and opening and closing of the shutter were orchestrated by synchronization electronics designed and built by Martin Rabb, Electronics Design Engineer, Chemistry Department, Michigan State University. The light transmitted by the sample was collimated by an f/7.0 lens and focused by a second lens (f/4.0) onto the entrance slit of a SPEX 1680A monochromator through either Schott long wavelength transmittance filters or Andover Corp. short wavelength pass filters in order to reject scattered excitation light. The signal obtained from a Hamamatsu R928 photomultiplier tube was amplified using a LeCroy 6103 dual amplifier/trigger. The amplifier output was passed into a LeCroy TR8828D transient recorder, and the digitized signal was stored in two MM8104 memory modules arranged in a series configuration. The amplifier, digitizer, memory modules, and a LeCroy 6010 GPIB interface were housed in a LeCroy 8013A minicrate. Data, acquired and processed by a Compaq 386 computer, were typically averaged over 1000 pulses.

#### **D. TIME-CORRELATED PHOTON COUNTING MEASUREMENTS**

In an effort to clarify the complicated transient absorption kinetics, luminescence lifetime decays for all cofacial dimers were obtained using a time-correlated single photon counting instrument housed in the LASER laboratory at Michigan State.<sup>115</sup> Luminescence decays were typically

acquired at 640 nm, which is representative of the red luminescence emanating from the all samples during the transient absorption experiment. Sample excitation wavelengths (575–600 nm) for all samples were conserved between the absorption and lifetime experiments. Typical excitation powers for the latter experiments were <10 mW at repetition rates of ~3.8 MHz. Long wavelength transmittance Schott glass filters (RG-610 and RG-630) were used to prevent scattered excitation light from entering the monochromator. Monochromator slit widths of 0.5 mm were used for micro-channel plate voltages of 3100 V, which resulted in time-to-amplitude conversion (TAC) rates of 1 kHz for TAC settings of  $0.10 \mu\text{s} \times 1.5$ . The lifetime decays were taken in the H1 window of the multi-channel analyzer (MCA) software, at a gain of 8192 channels. These software parameters are appropriate when an optical delay of 80 ns is used for the TAC stop pulse and 25 ns of coaxial cable delay is employed before the TAC start input. These experimental conditions are typical but not exclusive to all luminescence measurements made on the cofacial diporphyrin complexes.

## CHAPTER III

### THE ROLE OF SOLVATION DYNAMICS IN ACTIVATED ELECTRON TRANSFER REACTIONS

#### A. Background

Ultrafast laser kinetics investigations of solvent dynamics have highlighted activationless charge separation (CS) and charge recombination (CR) reactions occurring in donor-acceptor assemblies.<sup>76-80</sup> Because energetic or “static” effects can mask dynamical contributions, it was reasoned that in the activationless limit, solvent relaxation dynamics become rate limiting. From Figure 4 (eq 1.5-1.7), if the diffusion length along the potential surface,  $x_D$ , is small due to a low activation barrier for the ET reaction, then the observed rate constant will become independent of solvent motion. Indeed, this is the basic description of solvent dynamics in ET, as discussed early on by Calef and Wolynes.<sup>60</sup> However, the activationless regime does not best emphasize solvent dynamics. Weaver’s studies were the first to stress activated ET for the study of solvent dynamics.<sup>86,116</sup> A pitfall in this area is that in addition to its influence on the dynamics, the solvent can perturb the ET rate constants in a static sense, through solvent-dependent variations in the driving force and reorganizational energy. Weaver has circumvented part of this problem by

studying self-exchange reactions. Here, solvent-dependent free energy contributions to the activation barrier for ET are eliminated; and therefore judicious design of the system permits solvent reorganization contributions to the barrier to be reliably isolated from dynamics effects. However, a drawback to Weaver's approach is that the solvent can govern the reactants' precursor formation<sup>117</sup> and the geometry and energetics of this precursor complex.<sup>118</sup> A complementary methodology to these studies is the investigation of solvation dynamics in intramolecular electron transfer reactions, where energetic contributions from donor-acceptor diffusion are eliminated. Since static and dynamic contributions will have parallel effects on the ET rate constant in normal region ET kinetics, true dynamics effects are more likely to become evident in strongly adiabatic, activated ET, occurring in the inverted region.

We have chosen to study the CR kinetics of cofacial porphyrin-porphyrin and porphyrin-chlorin complexes. Through metal substitution or functionalization of the individual macrocycles, the redox properties of these dimers can be tuned to drive the ET event (or in the case of these systems, charge recombination) into the inverted region.

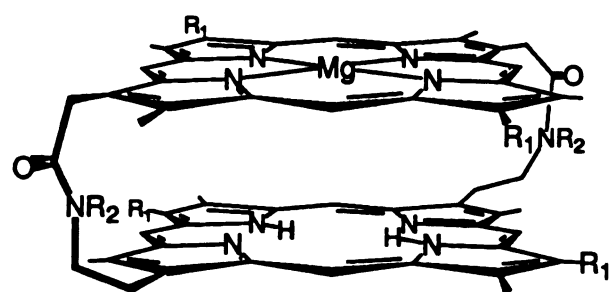
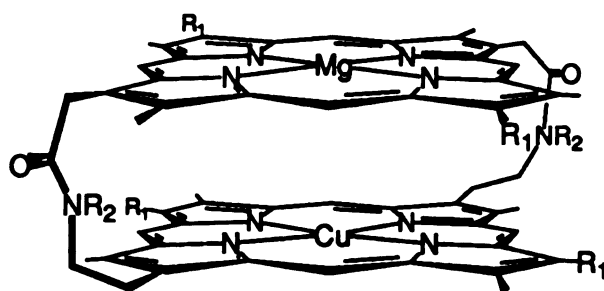
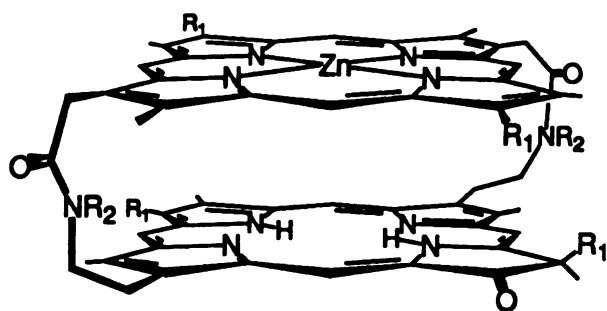
The use of porphyrin-chlorin systems to study solvent effects in ET is not without precedent. Wasielewski has used the driving force advantages of the chlorin subunit to study the solvent dependent photophysics of Zn-porphyrin-chlorophyll diads and Zn-porphyrin-chlorophyll-quinoid triads. He demonstrates that highly exothermic CR kinetics can be strongly influenced by the solvent for moderately coupled systems. For the Zn-porphyrin-chlorophyll diad, the rate constants for excited state nonradiative decay were found to correlate strongly with solvent polarity, even though formation of distinct ion-pair intermediates

was only verified in polar solvents. Wasielewski suggests that production of charge-separated states is not required to induce these effects, but rather, it is sufficient to merely mix charge transfer character with the excited states of the diad. Although the solvent-dependent CR kinetics support these conclusions, the apparent sensitivity of the charge-separated state energetics to solvent polarity demonstrates the need to be wary of static solvent effects when pursuing dynamics information using porphyrin-chlorin systems.

The solvent-dependent CR kinetics within the chlorophyll-Zn-porphyrin-quinoid triads (ZC-ZP-Q) are not simply described by solvent polarity considerations, but are interpreted within the framework of a superexchange mechanism. Here, solvent viscosity is shown to strongly affect the energy of the initially prepared  $ZC-ZP^+-Q^-$  state prior to formation of the thermodynamically favored  $ZC^+-ZP-Q^-$  species. What is most intriguing about this work is that in addition to this mechanism, dielectric relaxation is proposed to stabilize ion-pair intermediates. An apparent conflict arises in that solvent dynamics describe a frequency domain process and therefore, are unable to influence equilibrated charge-separated state energies. Correlation of the  $ZC-ZP^+-Q^-$  state energy with solvent viscosity reveals that statics are at the root of the solvent dependent CR rate constants and that true dielectric relaxation effects are obscured. However, the large CR rate constants in both the diad and triad systems are redeeming and suggest that similar motifs may be effective at providing glimpses of solvent dynamics control of ET rates.

This chapter reports the solvent dependence of the CR reactions of the three cofacial systems shown in Figure 8 (where  $R_1 = n$ -octyl,  $R_2 = n$ -butyl). Netzel *et al.* have examined the transient spectroscopy and ET



**Mg—H<sub>2</sub>****Mg—Cu****Zn—H<sub>2</sub>(=O)**

**Figure 8.** Cofacial porphyrin-porphyrin and porphyrin-chlorin probe molecules used in solvation dynamics studies of activated ET reactions. The diporphyrins are denoted Mg—H<sub>2</sub> and Mg—Cu while the chlorin is designated as Zn—H<sub>2</sub>(=O).

kinetics of  $\text{Mg—H}_2$  and  $\text{Zn—Fe}^{\text{III}}\text{Cl}$  diporphyrin complexes, linked by varying length amide sidechains.<sup>119</sup> They have shown that upon excitation of either the Mg or Zn porphyrin based  $^1\pi\pi^*$  state, rapid ET produces the  $\text{Mg}^+—\text{H}_2^-$  or  $\text{Zn}^+—\text{Fe}^{\text{II}}\text{Cl}$  state within 6 ps, followed by a less facile charge recombination reaction. The CR rate constants are strongly solvent dependent, varying by an order of magnitude for  $\text{Mg}^+—\text{H}_2^-$  or  $\text{Zn}^+—\text{Fe}^{\text{II}}\text{Cl}$  in solvents ranging from dichloromethane (DCM) and pyridine to N,N-dimethylformamide (DMF) and tetrahydrofuran (THF), respectively. Moreover, the solvent dependence of the CR rate constants of  $\text{Mg—H}_2$  are intriguing as they are largest in DCM, a modestly polar solvent, and smallest in DMF, which has a significantly larger dielectric constant ( $\epsilon_{\text{DCM}}=8.93$ ,  $\epsilon_{\text{DMF}}=36.7$ ). This behavior is contrary to that expected on the basis of simple static solvent effects, as predicted by dielectric continuum theory.<sup>53,54</sup> Although these data represent a very limited ensemble of solvents and dielectric properties, they do provide further experimental evidence that medium effects in inverted region (or more generally, activated) ET reactions may not be exclusively manifested in the polarity of the solvent, as suggested by recent theoretical treatments of solvent controlled ET.<sup>56-67</sup> It was with this motivation that the covalently linked, cofacial porphyrin-porphyrin and porphyrin-chlorin compounds were chosen as molecular probes of solvation dynamics in activated ET reactions.

The  $\text{Mg—Cu}$  diporphyrin and  $\text{Zn—H}_2(=\text{O})$  porphyrin-chlorin system are newly prepared compounds and have not be previously studied, whereas the ET kinetics of  $\text{Mg—H}_2$  have been well documented by Netzel and coworkers.<sup>123</sup> In their early studies, rapid formation of the  $\text{Mg}^+—\text{H}_2^-$  state ( $k_{\text{obs}}(\text{CS}) > 10^{11} \text{ s}^{-1}$ ), accompanied by less facile CR rate constants

ranging from  $5 \times 10^9 \text{ s}^{-1}$  in DCM to  $7.7 \times 10^8 \text{ s}^{-1}$  in DMF, was in contrast to the observation of only  $\pi\pi^*$  excited states in THF. The charge-separated state was shown to be effectively stabilized with the addition of  $\text{Cl}^-$ , due to anion coordination at the Mg center. Although significant quenching of the porphyrin luminescence was observed, formation of the ion-pair intermediate was not exclusive, as residual transient absorption remained following charge recombination. Netzel *et al.* postulated that the long-lived excited state could be associated with formation of a triplet biradical. Their observation of a 13 ns lifetime for the Mg—H<sub>2</sub> transient absorption between 600–800 nm better supports this assignment than that of a  $^3(\pi\pi^*)$  excited state of the dimer, as the latter is expected to have a lifetime of several milliseconds based on characteristics of the Mg and free base porphyrin monomer triplet states.

These assignments were challenged by studying the transient absorption kinetics of Mg—H<sub>2</sub> in the presence of iodobenzene and *p*-benzoquinone (BQ). While the former is known to enhance the  $\text{S}_1 \rightarrow \text{T}_1$  intersystem crossing rate between  $\pi\pi^*$  excited states, the latter quenches excited state population by ET. Their assessment of solvent-dependent formation of the charge-separated state was consistent with the dramatic increase in the intersystem crossing rate in THF/iodobenzene, and the relative insensitivity of the transient absorption kinetics of Mg—H<sub>2</sub> in a 1:1 DCM/iodobenzene solvent mixture. Similarly, excited state quenching of Mg—H<sub>2</sub> by BQ in THF results in decay rate constants comparable to those observed for the quenching of  $^1(\pi\pi^*)$  and  $^3(\pi\pi^*)$  states of free base TPP. This is in contrast to the rate constants obtained in DCM/BQ, which show the presence of a >15 ns transient suspected to arise from the  $\text{Mg}^+ \text{—} \text{H}_2(\text{BQ}^-)$  state.

Confirmation of the difference in the nonradiative decay pathways for Mg—H<sub>2</sub> in these two solvents support the initial assignment of the long-lived transient absorption observed in DCM following CR, to that of triplet biradical formed in competition with  $^1\text{CT} \rightarrow ^1\text{S}_0$  decay. Further evidence for this mechanism derives from the results of *ab initio* configuration interaction calculations for Mg—H<sub>2</sub>, which show that the energetics of the CT and porphyrin  $\pi\pi^*$  states are consonant with the proposed nonradiative decay pathways suggested by Netzel and coworkers.<sup>120</sup> It was also suggested that the  $^3\text{CT}$  may decay via the  $^3(\pi\pi^*)$  manifold of the dimer as this process is expected to be a more facile route to ground state than a direct  $^3\text{CT} \rightarrow ^1\text{S}_0$  transition. Levanon *et al.* have verified the presence of a  $^3\text{CT}$  state following 580 nm laser excitation by low temperature, flash EPR measurements.<sup>121</sup> They propose a mechanism that includes formation of the locally excited  $\pi\pi^*$  state of the Mg-porphyrin subunit of the dimer ( $^1\text{Mg}^*-\text{H}_2$ ), followed by rate ET and subsequent radical pair intersystem crossing to yield the  $^3(\text{Mg}^+-\text{H}_2^-)$  state. This species decays by two pathways. The ion-pair intermediate further reacts with duroquinone (DQ) to produce a  $^1(\text{Mg}^+-\text{H}_2)(\text{DQ}^-)$  intermediate, similar to that postulated by Netzel *et al.* in the picosecond BQ quenching studies. Concurrently, CR produces the lowest energy triplet state of the dimer, which is localized on the free base subunit (Mg— $^3\text{H}_2$ ). As expected on the basis of the forward ET reaction exothermicity, excitation of Mg—H<sub>2</sub> at 620 nm populates the (Mg— $^1\text{H}_2$ ) state which is not sufficiently energetic to produce direct charge-separated products.

Application of these results to the nonradiative pathway governing charge-separated state decay is difficult as the rate constants for intersystem crossing and ET are strongly temperature dependent, thereby influencing

the mechanism for excited state deactivation. Moreover, since the presence of integer spin multiplicities are generally EPR silent, triplet products formed in low yields are easily observed, and therefore, care must be taken in proposing predominant mechanisms for ground state repopulation based solely on these data. Nevertheless, the observation of  $^3\text{CT}$  products lends experimental evidence to the formation of this state in picosecond transient absorption measurements.

## B. Results

### 1. *Electrochemistry*

The oxidation and reduction potentials of the  $\text{Mg—H}_2$  cofacial porphyrin have been measured previously in selected aprotic solvents; these data are collected in Table II along with the solvent dependence of the reduction potentials of  $\text{Mg}$  and free base octaethyl porphyrins. The first oxidation process of  $\text{Mg—H}_2$  results in the one-electron oxidation of the  $\text{Mg}$  porphyrin whereas the first reduction is localized on the free base porphyrin ring. Within the limited solvent series listed in Table II, the  $\Delta E$  for oxidation and reduction of the diporphyrin exhibits only a minor solvent dependence. Because we were interested in verifying this marginal solvent dependence, the appropriate oxidation-reduction potentials of monomer subunits were determined for the wide range of solvents employed in our picosecond kinetics studies. As has been discussed previously for linked diporphyrin assemblies,<sup>122</sup> the reduction potentials for cofacial porphyrin dimers are approximated by that of the monomer subunits, which is particularly convenient for our studies owing to the

**Table II.** Electrochemical Data for Mg and Free Base Model Porphyrins in Different Solvents

| Solvent <sup>a</sup> | $E_{1/2}(\text{MgOEP}^{+/0})^b$ | $E_{1/2}(\text{H}_2\text{OEP}^{0/-})^b$ | $\Delta E$ | $\Delta E(\text{Mg}—\text{H}_2)$ |
|----------------------|---------------------------------|---|------------|----------------------------------|
| DCM                  | 0.31                            | -1.70                                   | -2.01      | -1.80 <sup>c</sup>               |
| Ac                   | 0.45                            | -1.54                                   | -1.99      |                                  |
| DMF                  | 0.46                            | -1.53                                   | -1.99      | -1.86 <sup>c</sup>               |
| MeOAc                | 0.50                            | -1.55                                   | -2.05      |                                  |
| EtOAc                | 0.47                            | -1.54                                   | -2.01      |                                  |
| PrOAc                | 0.44                            | -1.57                                   | -2.01      |                                  |
| PN                   | 0.43                            | -1.49                                   | -1.92      |                                  |
| BN                   | 0.41                            | -1.56                                   | -1.97      |                                  |
| VN                   | 0.41                            | -1.54                                   | -1.95      |                                  |

<sup>a</sup>Solvents are abbreviated as follows: dichloromethane (DCM), acetone (Ac), N,N-dimethylformamide (DMF), methyl, ethyl, and *n*-propyl acetates, (MeOAc, EtOAc, PrOAc, respectively), propionitrile (PN), butyronitrile (BN) and valeronitrile (VN). <sup>b</sup>Obtained by cyclic voltammetry with tetrabutylammonium tetrafluoroborate as the supporting electrolyte. Potentials measured vs  $\text{Fc}^+/\text{Fc}$  potential but reported here vs SCE ( $E_{1/2}(\text{Fc}^{+/0}) = 0.31 \text{ V vs SCE}$ ). <sup>c</sup>Ref 119a.

large amount of cofacial porphyrin that would be required for investigating the complete solvent series. Comparison of the reduction potentials for  $\text{MgOEP}^{+/0}$  and  $\text{H}_2\text{OEP}^{0/-}$  monomers listed in Table II to those of the dimer reveal that  $\Delta E$ s of the former are slightly greater. This trend has been observed previously for other cofacial/monomer porphyrin systems; and indeed the  $\sim 200$  mV difference observed in Table II between monomers and dimer is in the same range observed by Collman and coworkers for a variety of cofacially-linked/monomer porphyrin systems possessing nonelectroactive metal centers.<sup>122</sup> A reduction in  $\Delta E$  for cofacially juxtaposed porphyrins is predicted from simple molecular orbital considerations of the splitting of the occupied  $\pi$  and empty  $\pi^*$  orbitals resulting from dimerization, which is manifested in a destabilized HOMO and stabilized LUMO level.<sup>122</sup> However, the important issue here is the relative dependence of  $\Delta E$  across the solvent series. Inspection of the data confirms the earlier results of the native cofacial system that  $\Delta E$  exhibits only a minor dependence on solvent. Despite a large variation of the dielectric constants through the solvent series, the range in  $\Delta E$  is only 0.13 V.

For the Mg—Cu system, the redox properties of the dimer were measured directly in  $\text{CH}_2\text{Cl}_2$ . On the basis of the similarity between literature values of the first reduction potentials of free base and Cu porphyrin macrocycles ( $E_{1/2}[\text{H}_2\text{P}^{0/-}] = E_{1/2}[\text{CuP}^{0/-}] = -1.46$  V),<sup>123</sup> the  $\Delta E$  for this systems was expected to be identical to that of Mg—H<sub>2</sub>, and therefore a viable probe for solvation dynamics. Unfortunately, this was not the case as  $\Delta E$  was found to lie  $\sim 0.5$  V<sup>124</sup> greater in energy than Mg—H<sub>2</sub>. From a direct comparison of the first oxidation potential of the Mg porphyrin monomer and the first reduction potential of the Cu and free

base porphyrin monomers, it is apparent that the increase in  $\Delta E$  is mostly due to a shift of the Mg porphyrin oxidation potential (see Table II) to more positive values ( $E_{1/2}[\text{Mg—Cu}^{+/0}] = +0.72 \text{ V}$ ). The first reduction potential is shifted to more negative potential, but to a lesser degree ( $E_{1/2}[\text{Mg—Cu}^{0/-}] = -1.57 \text{ V}$ ). The increased endothermicity of these electrochemical potentials places the  $\text{Mg}^+ \text{—} \text{Cu}^-$  charge transfer state above the first  $^1(\pi\pi^*)$  state, causing the forward ET process to be endothermic.

Introduction of the keto group to the  $\pi$  rings to form the chlorin results in a shift in the oxidation-reduction chemistry. The reduction potentials of the ketochlorin subunit of the cofacial dimer in  $\text{CH}_2\text{Cl}_2$  is  $E_{1/2}[\text{H}_2(=\text{O})^{0/-}] = -1.36$ , vs SCE. As expected, the reduction of the macrocycle is enhanced by the electron-withdrawing keto group inducing a shift of  $+0.10 \text{ V}$  to more positive potential.

## 2. *Electronic Spectroscopy*

The ground state optical absorption spectra of  $\text{Mg—H}_2$  and  $\text{Mg—Cu}$  are shown in Figures 9 and 10, respectively. As discussed previously for this class of compounds,<sup>125</sup> the absorption spectrum is suggestive of a weak excitonic interaction between the porphyrin subunits. Relative to the respective monomers transitions, the dimer Soret band is characteristically blue-shifted (392 nm) and the Q-bands for the Mg and free base subunits of the cofacial pair are shifted 5-10 nm to the red spectral region. Although the macrocycles are coplanar at a separation distance of approximately  $4\text{ \AA}$ , no exciton splitting of the Soret bands is observed. For both  $\text{Mg—H}_2$  and  $\text{Mg—Cu}$  diporphyrin complexes, the Soret transition maxima are not



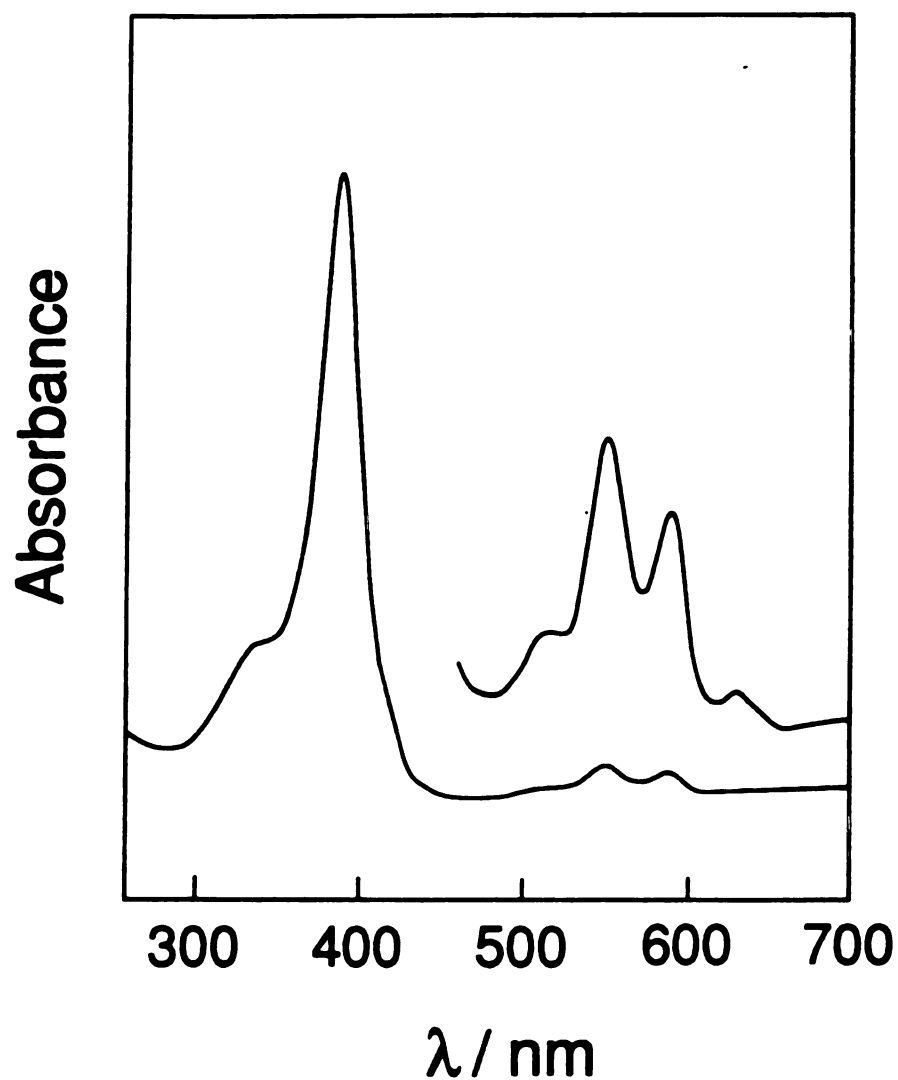


**Figure 9.** Electronic absorption spectrum of Mg—H<sub>2</sub> in the Soret and Q regions, obtained at sample concentrations of 10<sup>-5</sup> M in CH<sub>2</sub>Cl<sub>2</sub>. The Q band region is magnified by a factor of 8.

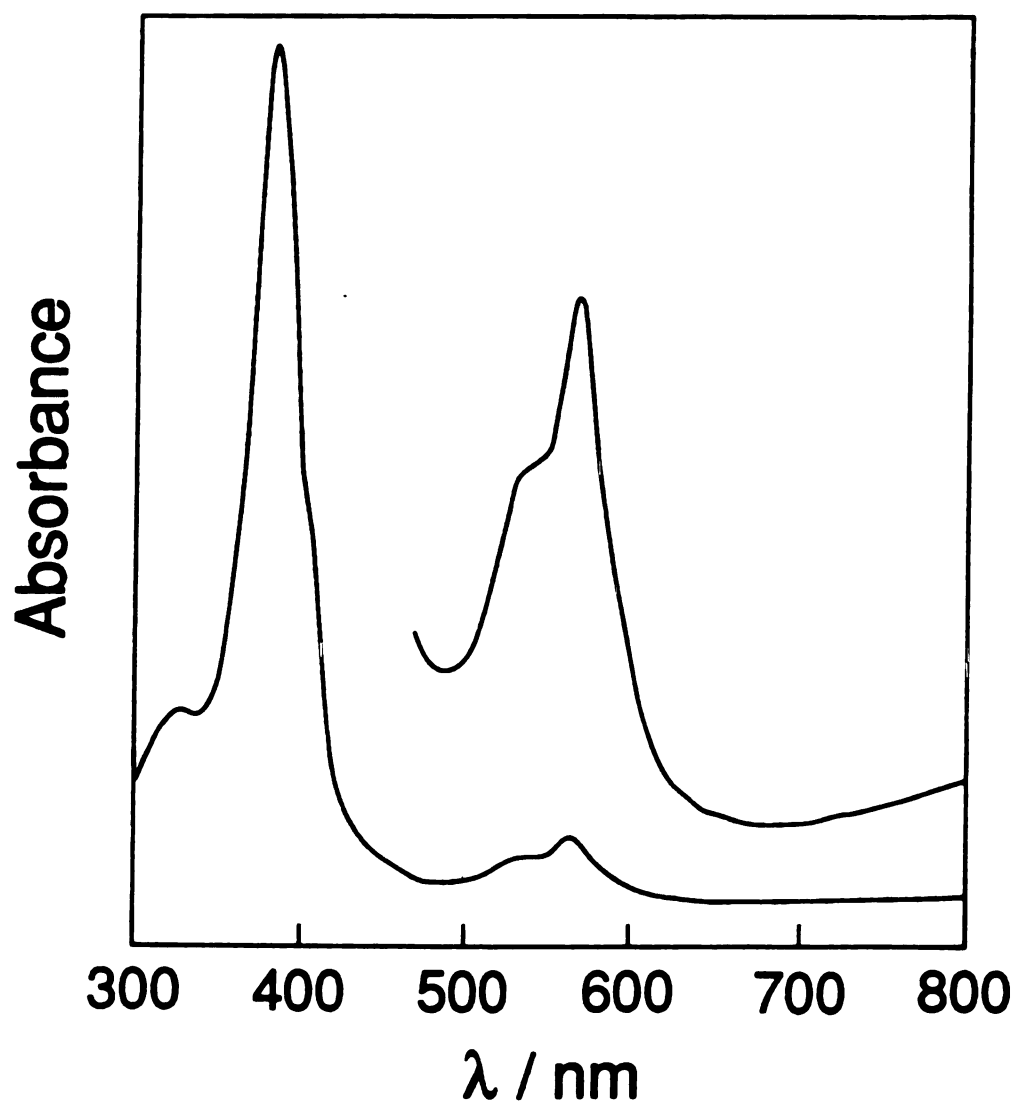


**Figure 10.** Electronic absorption spectrum of Mg—Cu in the Soret and Q regions, obtained at sample concentrations of  $10^{-5}$  M in  $\text{CH}_2\text{Cl}_2$ . The upper trace shows an 8-fold magnification of the Q band region.

appreciably perturbed from the monomeric porphyrins in dichloromethane solution. This is not the case for the respective Q bands, as shifts of 5–10 nm are observed in both the Mg-porphyrin Q(1,0) and Q(0,0) bands observed for Mg—H<sub>2</sub> at 544 nm and 584 nm respectively, and in the free-base porphyrin transitions Q<sub>y</sub>(1,0) and Q<sub>x</sub>(0,0) at 510 nm and 624 nm. The Q<sub>y</sub>(0,0) and Q<sub>x</sub>(1,0) at 530 nm and 570 nm of the free-base porphyrin monomer are obscured by the higher oscillator strength of the Mg-porphyrin transitions. Similar trends are apparent in the optical spectrum of Mg—Cu, where no exciton splitting of the Soret transition at 386 nm is observed, even though the respective Mg-porphyrin and Cu-porphyrin Soret transitions are nearly resonant. The Q band region of the Mg—Cu absorption spectrum is characterized by a broad absorption with a maximum at 588 nm and a strong shoulder at 564 nm. These transitions are also shifted from the Mg-porphyrin and Cu-porphyrin monomer Q(0,0) maxima which occur at 578 nm and 566 nm, respectively. The Q(1,0) bands of the individual porphyrin monomers do not appear as pronounced features in the Mg—Cu optical spectrum owing to the broad overlapping absorption profile induced by the more intense Q(0,0) transitions.

The absorption spectrum of Zn—H<sub>2</sub>(=O) approximates the overlapped spectra of the Zn-porphyrin and free-base ketochlorin monomer subunits. However, the absorption bands exhibit a noticeable variation in breadth and intensity with solvent. Figure 11 displays the absorption spectrum for Zn—H<sub>2</sub>(=O) in *n*-propyl acetate and dichloromethane. The UV–Vis absorption spectrum of Zn—H<sub>2</sub>(=O) in *n*-propyl acetate is characterized by overlapping Zn-porphyrin (412 nm) and ketochlorin (403 nm) Soret transitions, which result in a maximum at 405

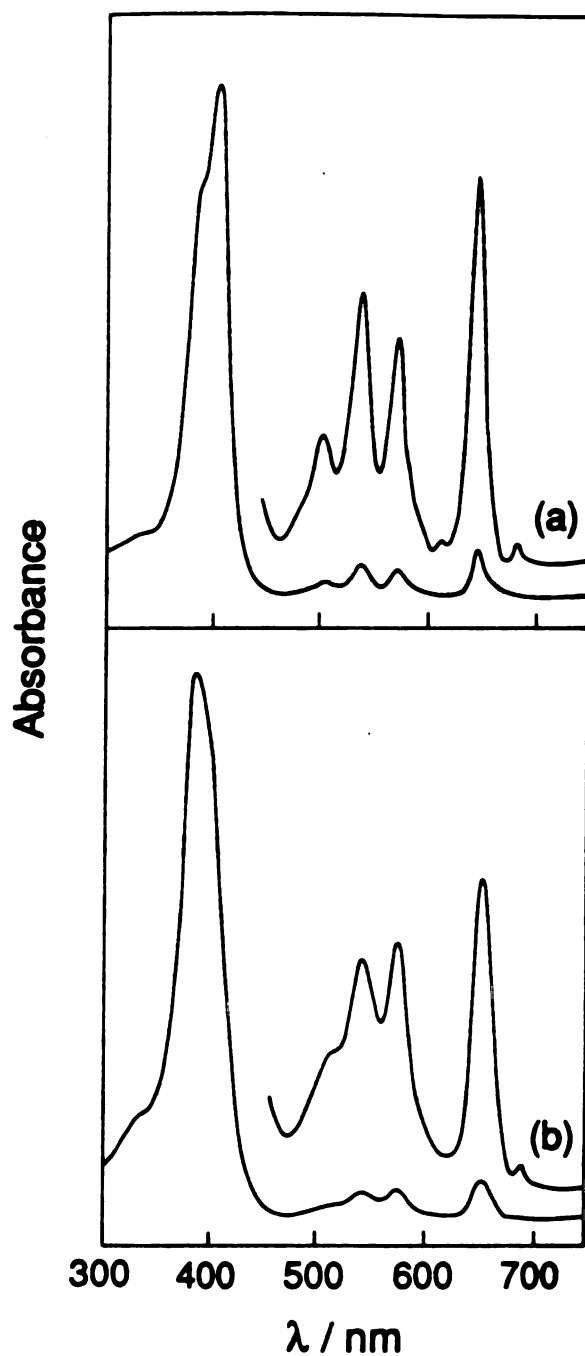


**Figure 11.** Electronic absorption spectrum of the porphyrin-chlorin complex  $\text{Zn—H}_2(=\text{O})$  ( $10^{-5}$  M) in (a) *n*-propyl acetate and (b)  $\text{CH}_2\text{Cl}_2$ , at 22 °C. The Q band wavelength region is multiplied by a factor of 8.

nm with a strong shoulder at 385 nm. To lower energy, the intense Q bands of the Zn-porphyrin subunit are coincident with the less strongly absorbing Q transitions of the ketochlorin moiety, resulting in four prominent absorption features at 504, 536, 572, and 644 nm. The bands at 504 and 644 nm are predominantly chlorin-based Q bands ( $Q_x(1,0)$  and  $Q_y(0,0)$ ), while the features at 536 nm and 572 nm primarily result from Zn-porphyrin localized  $Q(1,0)$  and  $Q(0,0)$  transitions. The optical spectra obtained in other polar solvents such as DMF, *n*-propionitrile and acetone closely resemble the absorption profile obtained in *n*-propyl acetate. However, the relative oscillator strength, energy and FWHM of these transitions vary markedly in dichloromethane (Figure 11b). The Soret band is broadened and the absorption maximum is shifted to 388 nm with a shoulder near 400 nm. The energies of these transitions closely resemble those observed in *n*-propyl acetate but the respective oscillator strengths are strongly solvent dependent. Similarly, the Q bands of both the Zn-porphyrin and free base ketochlorin also exhibit pronounced broadening with  $\leq 6$  nm wavelength shifts with respect to those observed in *n*-propyl acetate. This pronounced solvent dependence of the absorption spectrum is not observed for any of the other compounds reported herein, and its origin appears to be associated with a strong interaction between the ketone functionality of the chlorin moiety and solvent.

In general, the observed shifts in the optical spectra of the diporphyrin and porphyrin-chlorin complexes suggest that the  $\pi$  systems of the individual macrocycles are only weakly coupled, despite the structural proximity of the cofacial pair. This may be due in large part to the fact that the energy levels of the subunits of the heterodimers are nonresonant, thereby leading to a reduced excitonic coupling in these systems.

Similarly, the cofacial disposition of the subunits does not strongly influence the oscillator strengths of the porphyrin or chlorin monomer electronic transitions, as intensity relationships are generally maintained in the optical spectrum of the diporphyrin and porphyrin-chlorin heterodimers. The differences in the spectra of the subunits permit us to excite the more pronounced Mg-porphyrin and Zn-porphyrin Q transitions (575-590 nm) to obtain enhanced population of the metalloporphyrin based  $^1(\pi\pi)^*$  excited state.

All three heterodimers exhibit luminescence that is characteristic of the respective monomeric units. The emission spectra of Mg—H<sub>2</sub> and Zn—H<sub>2</sub>(=O) in CH<sub>2</sub>Cl<sub>2</sub> are shown in Figure 12. For both compounds, the metalloporphyrins luminesce strongly near 645 nm, while distinct emission bands are observed at 625 nm and 690 nm for the free base porphyrin and 630, 658 and 682 nm for the ketochlorin monomer. The emission spectra of the dimers are essentially intensity weighted composites of the metalloporphyrin and free base subunits emission spectra.

The luminescence lifetimes of the three systems also possess characteristics related to the monomeric subunits. The Mg—Cu system is the most complicated as a three component luminescence lifetime decay is observed (Table III, Figure 13). Since Cu porphyrins are known to have very short lived ( $\pi\pi^*$ ) excited states, little or no luminescence is expected from the Cu porphyrin moiety. This is consistent with an instrument response-limited component (0.04 ns) of the luminescence. Since the Mg porphyrin monomer is known to possess a ~9 ns lifetime in solution,<sup>126</sup> the remaining long lived luminescence is attributed to this subunit.

For Mg—H<sub>2</sub> and Zn—H<sub>2</sub>(=O), the luminescence intensity is related to the free energy for charge separation. Table III lists the luminescence

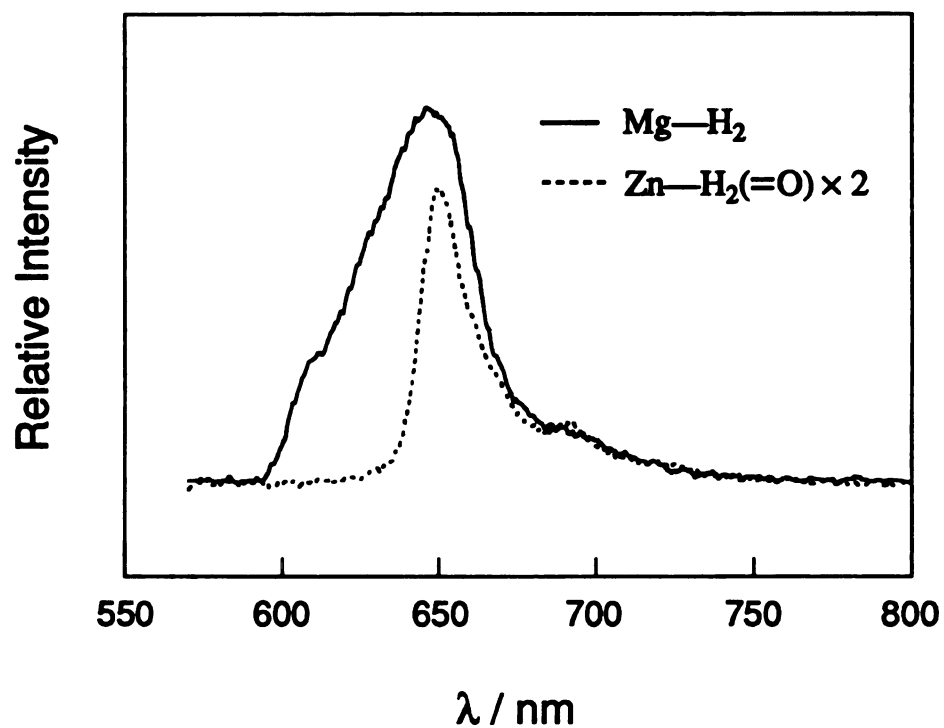


**Figure 12.** Emission spectrum of  $\text{Mg-H}_2$  and  $\text{Zn-H}_2(=\text{O})$  in degassed  $\text{CH}_2\text{Cl}_2$ . Samples were prepared in 1 cm quartz cuvettes with an absorbance of 0.1 at  $\lambda_{\text{exc}} = 585 \text{ nm}$ .





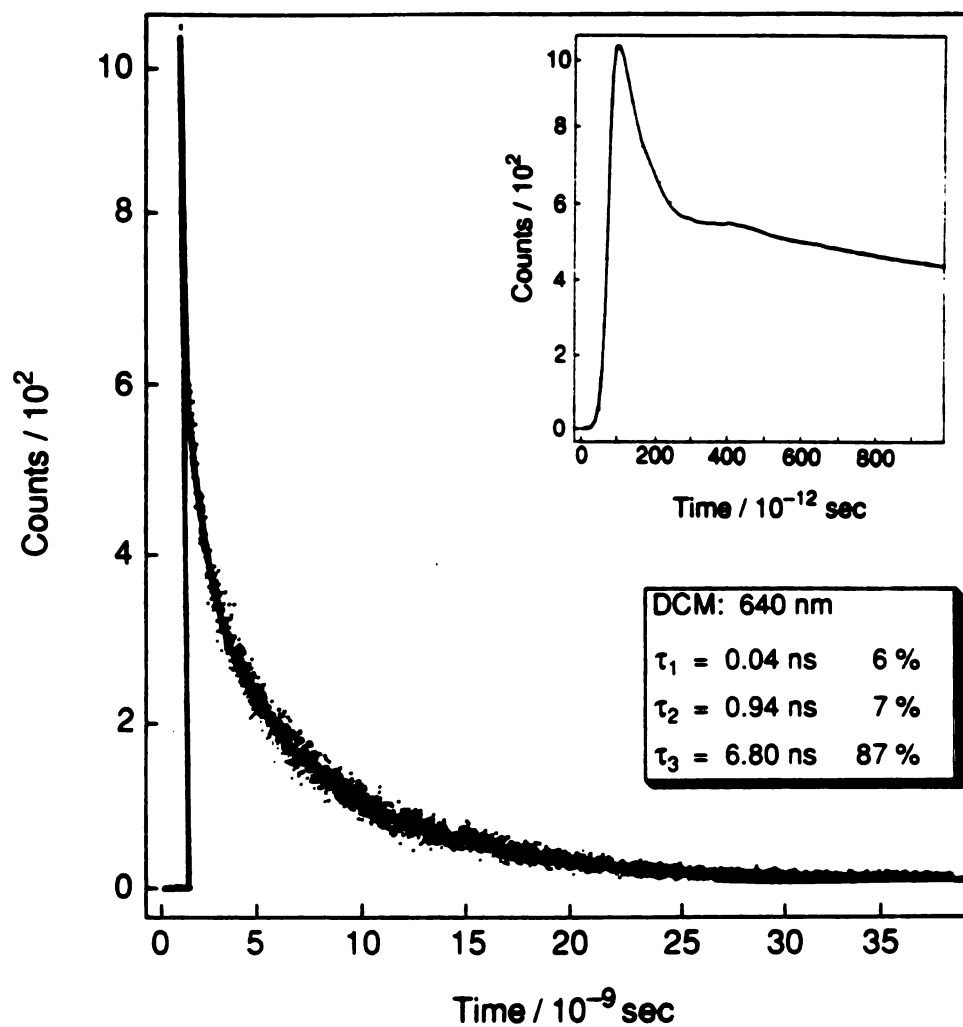


**Figure 13.** Luminescence decay of the Mg—Cu diporphyrin following 585 nm sample excitation. The inset shows the decay of the short-lived component, which is essentially instrument response limited.

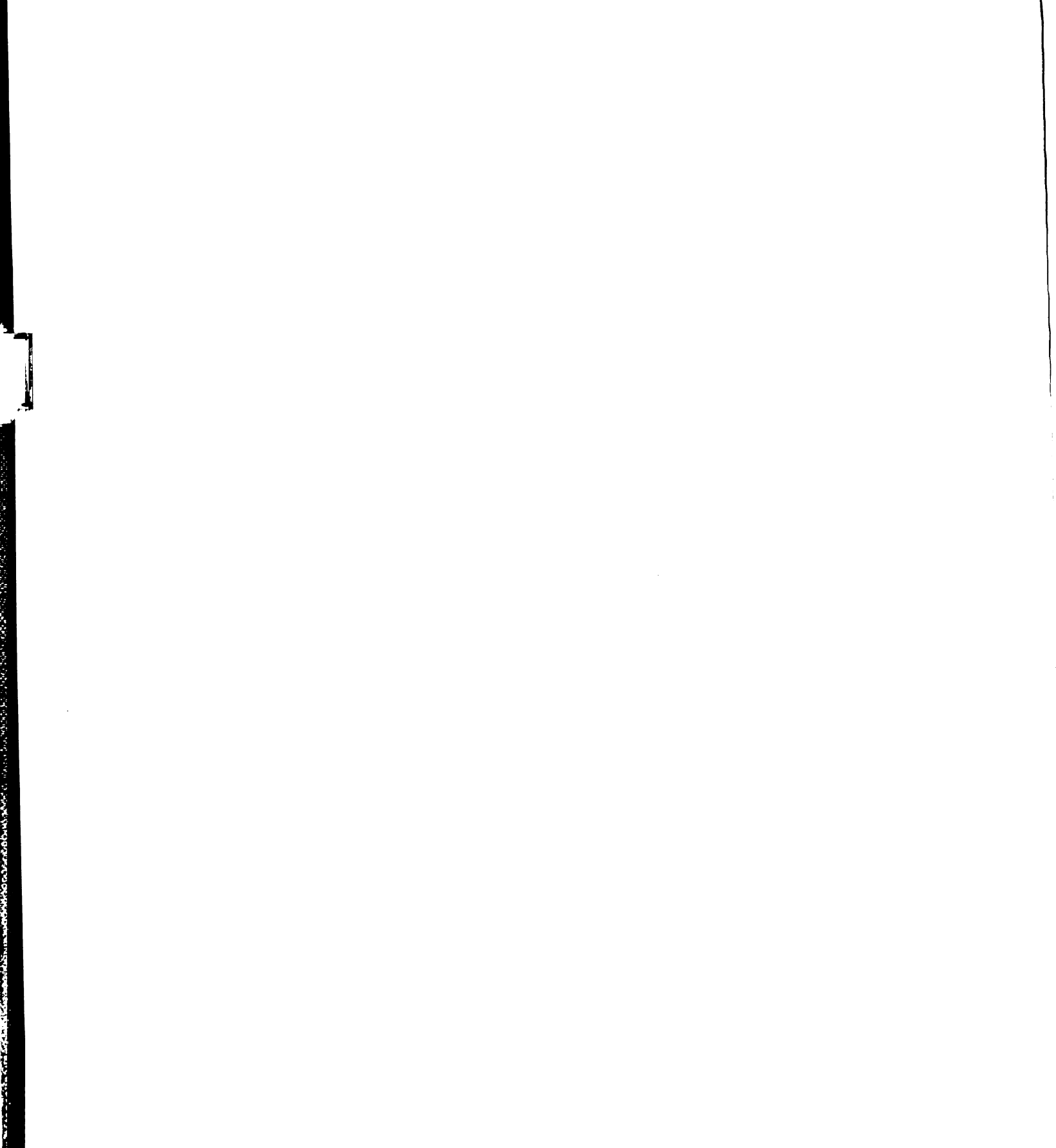


**Table III.** Selected Photophysical Properties of the Heterodimers in Dichloromethane

| Heterodimer            | $\lambda_{\text{em,max}} / \text{nm}$ | $\phi_e / 10^{-3}^{\text{a}}$ | $\tau/\text{ns}^{\text{b}}$ |
|------------------------|---------------------------------------|-------------------------------|-----------------------------|
| Mg—Cu                  | —                                     | —                             | [0.04, 0.94] (13), 6.8 (87) |
| Mg—H <sub>2</sub>      | 648                                   | 5.4                           | 2.8 (10), 8.3 (90)          |
| Zn—H <sub>2</sub> (=O) | 650                                   | 3.8                           | 1.5 (10), 4.9 (90)          |

<sup>a</sup>Luminescence quantum yield referenced to Mo<sub>2</sub>Cl<sub>4</sub>(PMe<sub>3</sub>)<sub>4</sub> in 2-methylpentane ( $\lambda_{\text{exc}} = 585 \text{ nm}$ ). <sup>b</sup>Decay profiles fit to biexponential kinetics indicated by two lifetimes. Numbers in parenthesis represent the percentage contribution of lifetime to the decay curve.

quantum yields and other selected photophysical data for the Mg—H<sub>2</sub> and Zn—H<sub>2</sub>(=O) in dichloromethane at 22 °C. Both of these heterodimers exhibit similar driving forces of 0.1 V for charge separation from a luminescence excited state that is localized on the Zn or Mg porphyrin. Conversely, the driving force for charge separation is indeed predicted to be slightly endergonic for those excited states whose parentage is localized on the free base porphyrin or chlorin. Lifetime measurements from the time-correlated single photon counting technique reveal a biexponential decay for the Mg—H<sub>2</sub> and Zn—H<sub>2</sub>(=O) systems with lifetimes similar to those observed for the porphyrin and keto-chlorin monomers (Figures 14 and 15).<sup>127</sup> These lifetimes are relatively solvent independent, typically varying less than 30% across all solvents as shown in Table IV. The diminished quantum yields in these systems as compared to those expected on the basis of the monomeric quantum yields suggests that the nonradiative charge separation competes more effectively with radiative decay. This nonradiative pathway involving ET may be directly investigated by transient absorption spectroscopy.

### *3. Transient Absorption Spectroscopy*

Excitation of the <sup>1</sup>ππ\* state of Mg—H<sub>2</sub> at 588 nm in all the solvents investigated prompts charge separation within the 6 ps excitation pulse of our apparatus.<sup>128</sup> Figures 16 and 17 show the transient absorption spectra of Mg—H<sub>2</sub> in dichloromethane and propyl acetate at various pump/probe delay times; the same spectral profile is obtained in all solvents. Prominent absorption features appearing at 625 nm and 665 nm correspond to the free base porphyrin anion and Mg porphyrin cation radicals, respectively.<sup>119</sup>

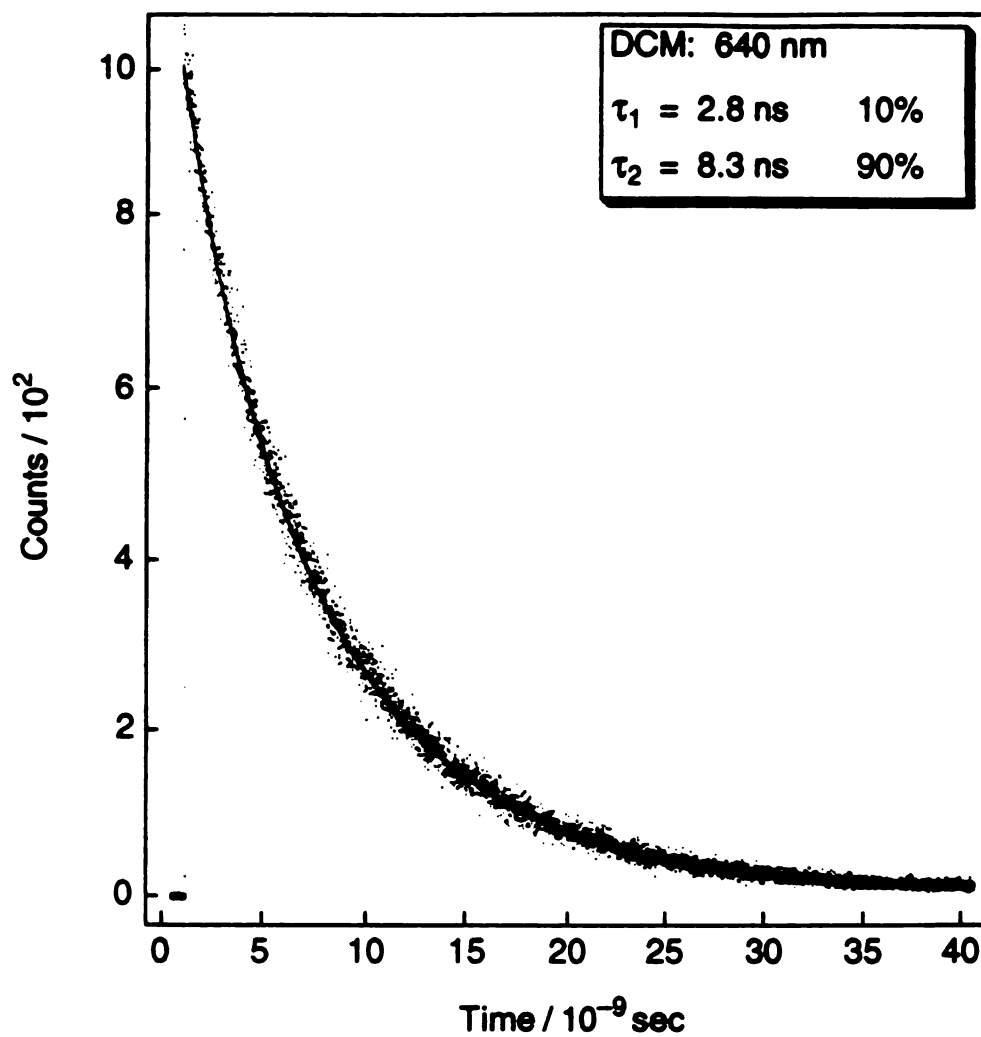


**Figure 14.** Decay of the Mg—H<sub>2</sub> dimer luminescence in CH<sub>2</sub>Cl<sub>2</sub> at 640 nm following 588 nm sample excitation. The lifetimes derived from the biexponential decay kinetics are given in the inset.

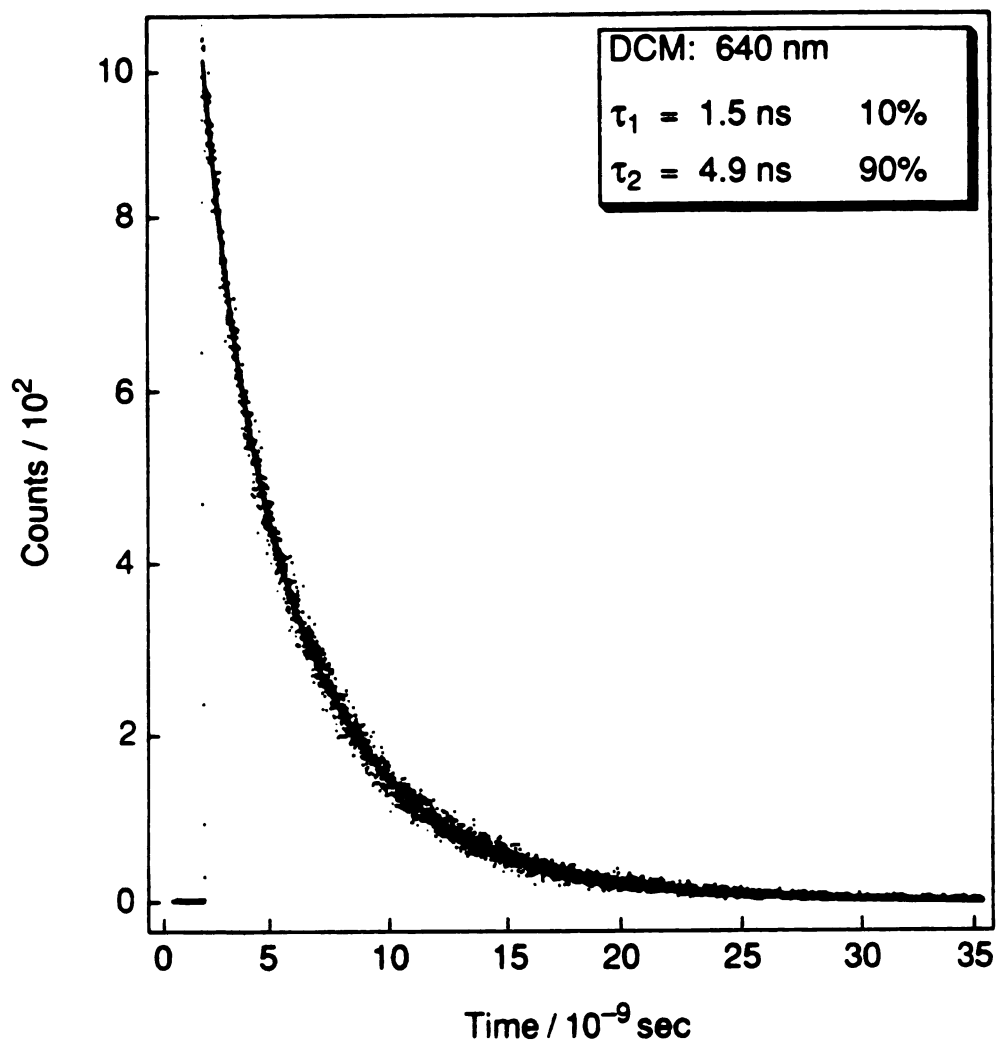
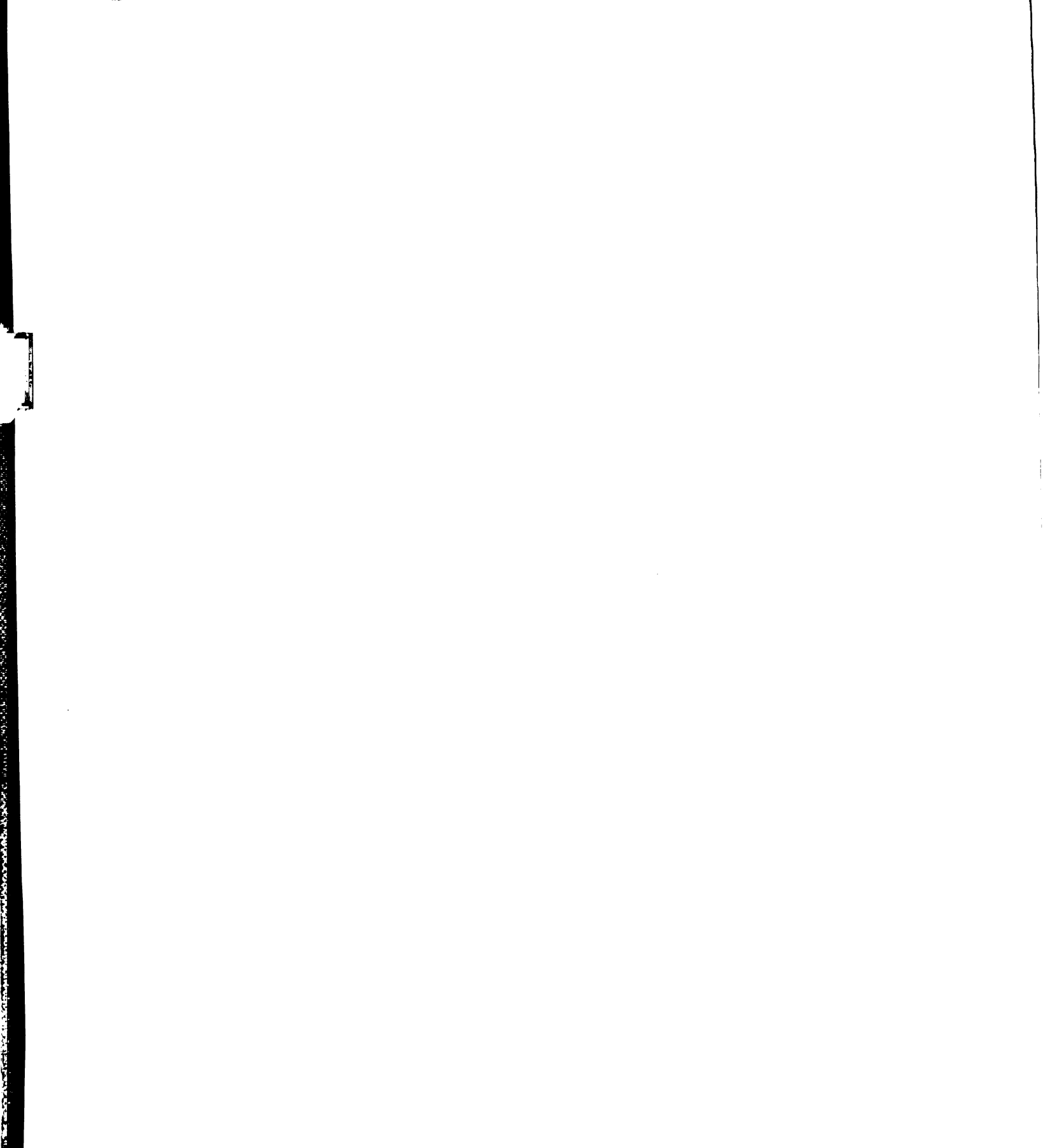


**Figure 15.** Luminescence decay of the porphyrin-chlorin complex Zn—H<sub>2</sub>(=O) in CH<sub>2</sub>Cl<sub>2</sub> at 640 nm. Samples were excited at 575 nm with a 6 ps pulse. The emission decays biexponentially with lifetimes shown in the inset.

**Table IV. Luminescence Lifetimes of Mg—H<sub>2</sub> and Zn—H<sub>2</sub>(=O) in Selected Solvents**

| Solvent <sup>a</sup> | Mg—H <sub>2</sub><br>$\tau/\text{ns}^{\text{b,c}}$ | Zn—H <sub>2</sub> (=O)<br>$\tau/\text{ns}^{\text{c,d}}$ |
|----------------------|--|---|
| DCM                  | 2.8 (9), 8.0 (91)                                  | 1.5 (10), 4.9 (90)                                      |
| Ac                   |  | 2.3 (8), 5.2 (92)                                       |
| DMF                  |  | 1.8 (15), 4.7 (85)                                      |
| PN                   | 1.9 (6), 8.8 (94)                                  | 1.9 (21), 4.7 (79)                                      |
| BN                   | 3.3 (10), 7.9 (90)                                 |   |
| PrOAc                | 2.2 (11), 9.6 (89)                                 |   |
| MeOH                 | 1.9 (31), 7.5 (69)                                 |   |
| EtOH                 | 2.3 (30), 8.9 (70)                                 | 2.3 (8), 5.2 (92)                                       |
| PrOH                 | 2.8 (24), 9.6 (76)                                 |   |
| BuOH                 | 2.4 (20), 9.4 (80)                                 |   |

<sup>a</sup>Solvents are abbreviated as follows: dichloromethane (DCM), acetone (Ac), N,N-dimethylformamide (DMF), propionitrile (PN), butyronitrile (BN), *n*-propyl acetate (PrOAc), methanol (MeOH), ethanol (EtOH), 1-propanol (PrOH) and 1-butanol (BuOH). <sup>b</sup>Luminescence lifetimes measured at  $\lambda_{\text{exc}} = 588 \text{ nm}$ . <sup>c</sup>Luminescence lifetimes measured at  $\lambda_{\text{exc}} = 575 \text{ nm}$ . <sup>d</sup>Decay profiles fit to biexponential kinetics indicated by two lifetimes. Numbers in parenthesis represent percentage contribution of the lifetime to the decay curve.





This  $\text{Mg}^+ - \text{H}_2^-$  spectral profile is consistent with electrochemical studies, which show that the Mg porphyrin subunit undergoes more facile oxidation than free base porphyrin whereas the opposite is true for reduction.<sup>129</sup> The transient absorbances of photogenerated  $\text{Mg}^+ - \text{H}_2^-$  species decay monotonically in all solvents to a residual absorbance shown by the 1 ns and 2 ns spectra in Figures 16 and 17, respectively. Concurrent with this absorption decay is the recovery of the bleach of the Soret band at 405 nm. The repopulation of the ground state, as monitored in the Soret spectral region, occurs concomitantly with the decay of the  $\text{Mg}^+ - \text{H}_2^-$  transient absorption profile. Owing to the residual absorbance of a transient a long times, the spectral changes shown in Figures 16 and 17 evolve according to biexponential kinetics (inset). However, the disappearance of the  $\text{Mg}^+ - \text{H}_2^-$  transient effectively follows unimolecular kinetics because of the disparity in lifetimes of the ion-pair and the long-lived transient. Charge recombination occurs with rate constants ranging from  $3.85 \times 10^9 \text{ s}^{-1}$  in dichloromethane to  $5.38 \times 10^8 \text{ s}^{-1}$  in *n*-propyl acetate. The slowness of the CR as compared to the CS electron transfer is consistent with the early proposal that CS and CR for this compound are in the Marcus normal and inverted regions, respectively ( $\Delta G^\circ(\text{CR}) = -1.9 \text{ eV}$ ,  $\Delta G^\circ(\text{CS}) = -0.1 \text{ eV}$ ). As shown in Table II, this driving force exhibits only a small dependence on solvent owing to the insensitivity of  $\Delta E$ .

The residual absorbance in the 600-730 nm region of the transient spectrum has been observed previously for  $\text{Mg} - \text{H}_2$ .<sup>119</sup> The absorption decay is slow ( $\sim 6 \text{ ns}$ ) with respect to charge recombination, and occurs on the same timescale as observed for the luminescence decay of  $\text{Mg} - \text{H}_2$  (see Table III). The transient spectral data for the longer-lived transient show

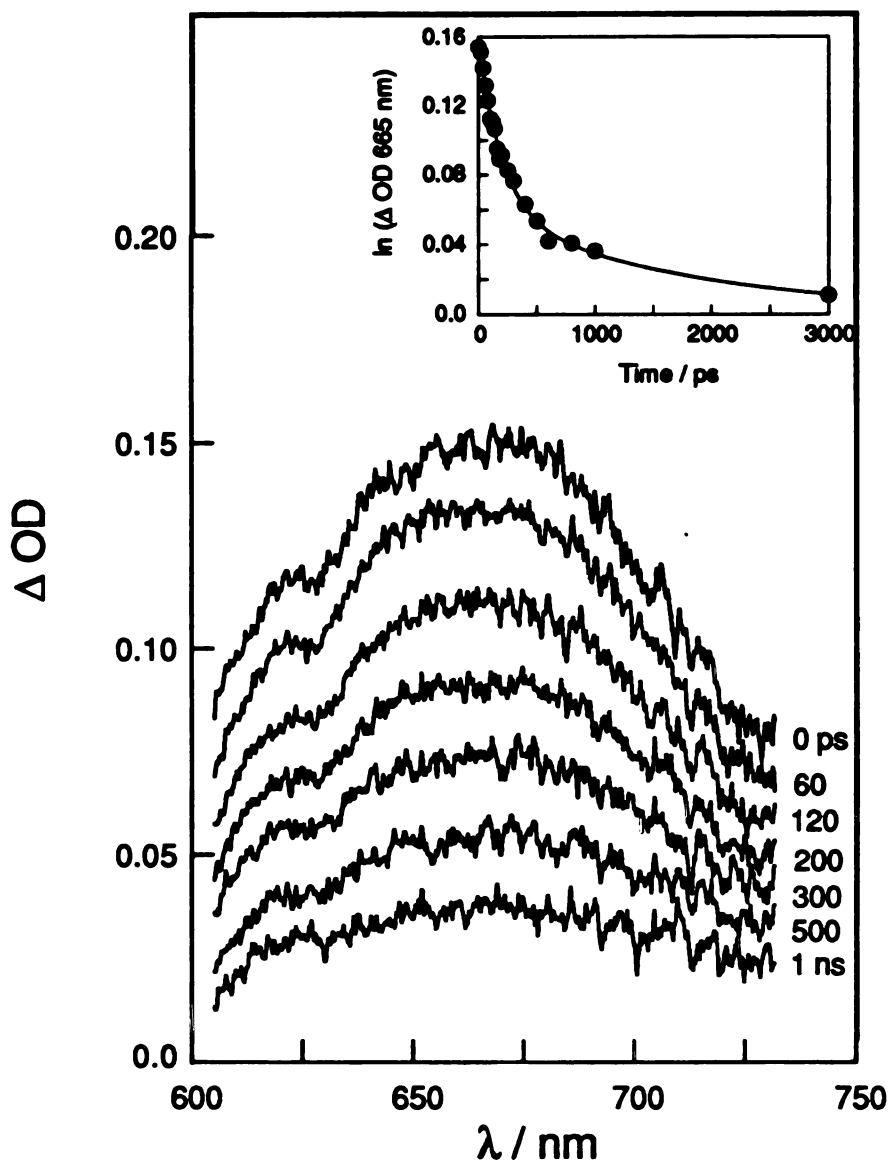


**Figure 16.** Transient absorption spectra of  $\text{Mg}^+ - \text{H}_2^-$  in  $\text{CH}_2\text{Cl}_2$  at 0, 60, 120, 300, 500 ps, and 1 ns after sample excitation at 588 nm. Included (inset) is the biexponential fit to the decay of the absorption profile at 665 nm.

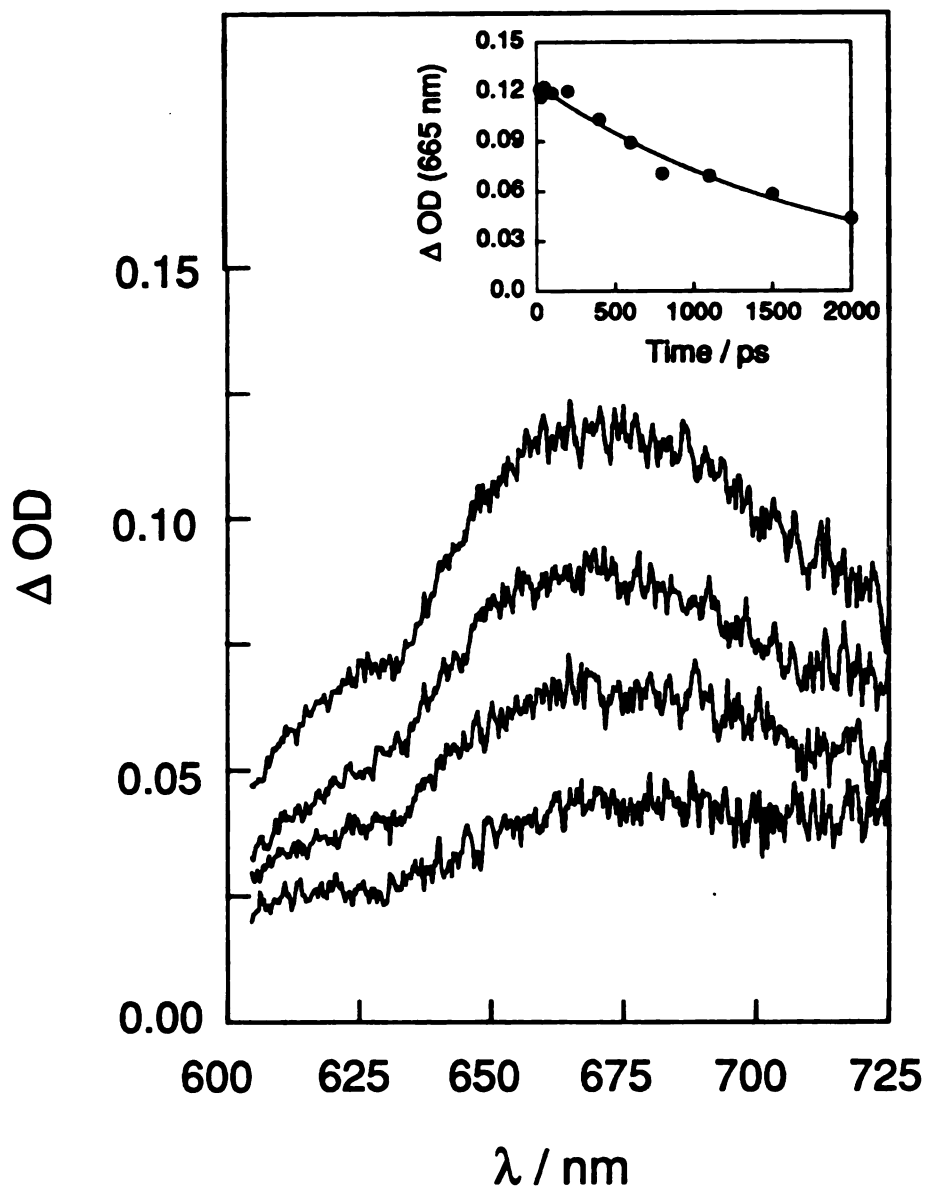


**Figure 17.** Time evolution of the disappearance of the picosecond transient absorption of the photogenerated  $\text{Mg}^+ \text{---} \text{H}_2^-$  charge-separated state in n-propyl acetate. The spectra were obtained at 50, 600, 1100 and 2000 ps after sample excitation at 588 nm with a 6 ps pulse. Included (inset) is the biexponential fit to the decay of the absorption profile at 665 nm.

no correlation to the CR process, implying the simultaneous existence of an emissive, porphyrin-based excited state and a distinct ion-pair intermediate.

The sensitivity of the absorption spectrum of  $\text{Zn}-\text{H}_2(=\text{O})$  to solvent in the ground state is also observed in the excited state. Figure 18a shows the differences in transient absorption features between 625-750 nm for  $\text{Zn}-\text{H}_2(=\text{O})$  in dichloromethane and *n*-propyl acetate following excitation of the Zn-porphyrin based Q(0,0) band at 575 nm. The time-dependent spectral profile in dichloromethane shows an excited-state absorption feature between 625 and 750 nm and a strong chlorin  $\text{Q}_y$  bleach at 655 nm. This broad absorption has been observed in the transient spectra of other Zn-porphyrin-keto chlorin-like diads and triads.<sup>130</sup> In these complexes, the Zn-porphyrin radical cation absorbs in the same region as the  $\text{Q}_y$  band (625-700 nm) and the radical anion of the keto chlorin absorbs to the red (680-800 nm). Similar to  $\text{Mg}-\text{H}_2$ , charge separation to the  $\text{Zn}^+-\text{H}_2(=\text{O})^-$  state is weakly exergonic ( $\Delta G^\circ(\text{CS}) = -0.1$  eV), and the subsequent charge recombination occurs at high driving force ( $\Delta G^\circ(\text{CR}) = -1.9$  eV). Moreover the decay characteristics of  $\text{Zn}^+-\text{H}_2(=\text{O})^-$  in dichloromethane resemble  $\text{Mg}-\text{H}_2$  inasmuch as the bleach of the Soret and absorptions of the radical cation and anion decay to a long-lived transient. A biexponential fit of the transient absorption at 705 nm yields rate constants of  $7.1 \times 10^9 \text{ s}^{-1}$  and  $\sim 1.5 \times 10^8 \text{ s}^{-1}$  for the short and long components, respectively. As with  $\text{Mg}-\text{H}_2$ , the ion-pair decays effectively by monoexponential kinetics owing to the long lifetime of the other component, which is commensurate with the luminescence decay rate constants listed in Table II.

The formation of  $\text{Zn}^+-\text{H}_2(=\text{O})^-$  is unusual. The transient absorption spectrum of  $\text{Zn}-\text{H}_2(=\text{O})$  in most solvents does not yield a

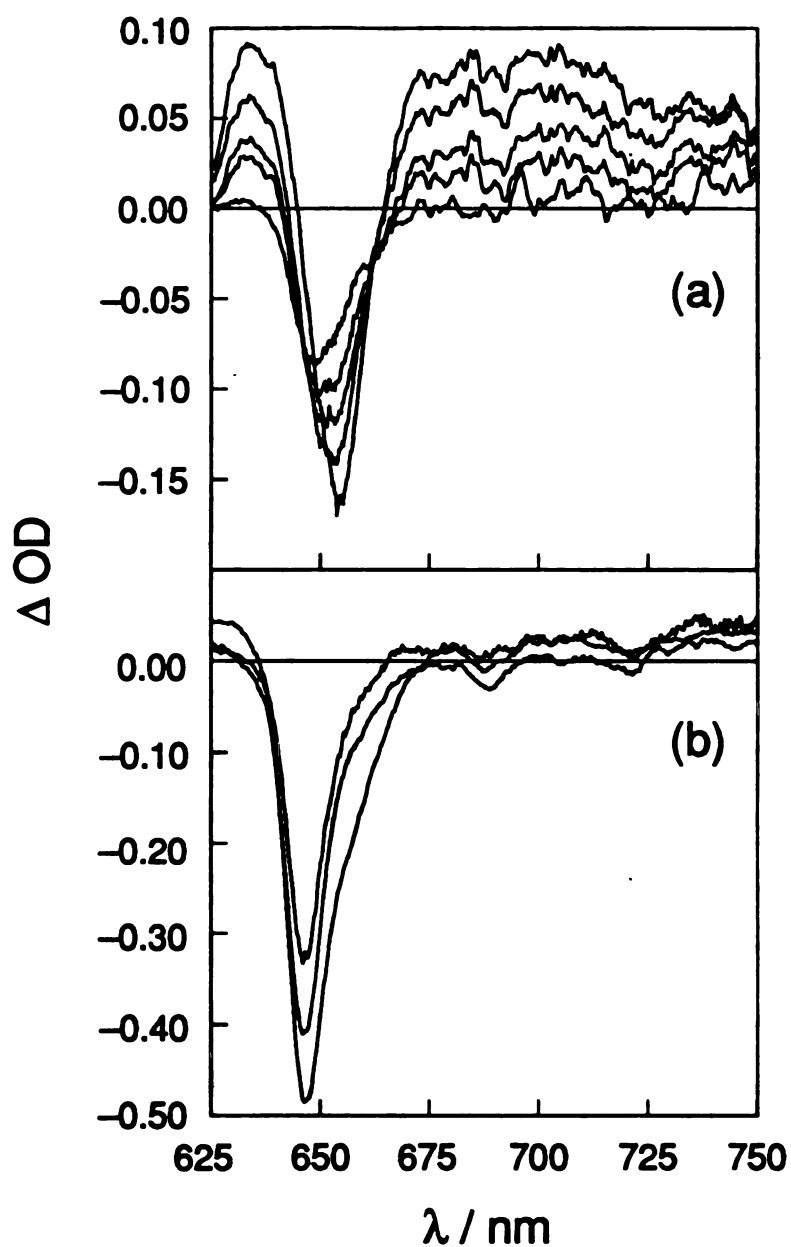
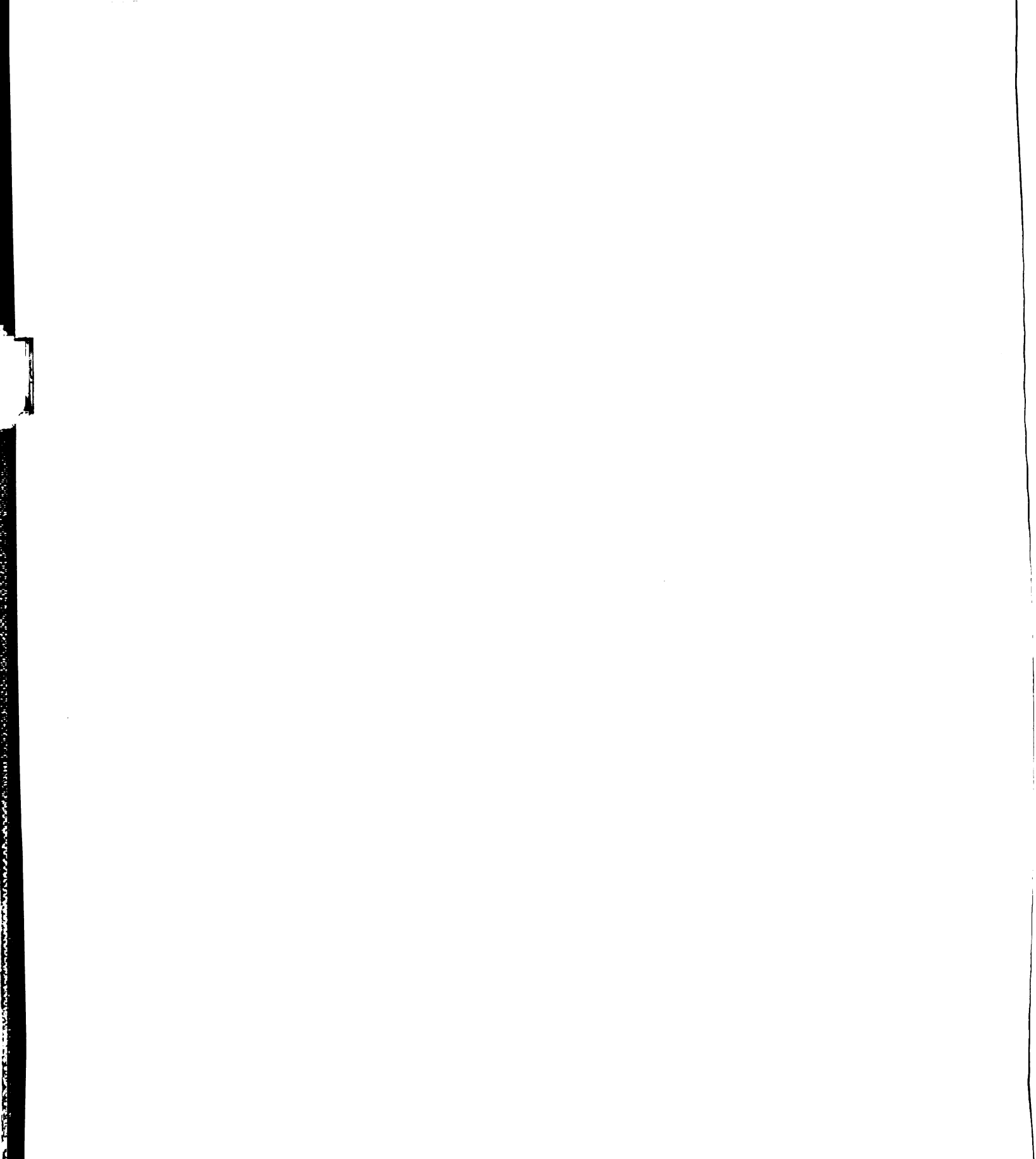


**Figure 18.** Picosecond transient absorption spectra of  $\text{Zn—H}_2(=\text{O})$  in (a)  $\text{CH}_2\text{Cl}_2$  at 0, 100, 200, 300, 3000 ps after a 575 nm, 6 ps excitation pulse, and (b) *n*-propyl acetate recorded at 40, 2000 and 6000 ps after excitation with the same pulse.



charge separated state. Figure 18b shows a representative spectrum of Zn—H<sub>2</sub>(=O) with propyl acetate as the solvent. The spectrum is characteristic of overlapping porphyrin and chlorin based singlet excited states. A pronounced bleach of the Q<sub>y</sub> band is present at zero pump/probe delay and it is maintained at delay times greater than 6 ns. The transient absorption decay constant of  $6.7 \times 10^7 \text{ s}^{-1}$  is nearly equivalent to that observed for emission decay. Moreover, there is little or no absorption discernible in the 675-800 nm spectral region, which is characteristic for the chlorin radical anion; this indicates that only a small amount, if any, of the charge separated state is produced upon excitation.

Interestingly, evidence for ion pair formation in the transient absorption spectrum of Zn—H<sub>2</sub>(=O) is also observed in DMF (Figure 19). The absorption profile in the 425-550 nm region displays three distinct maxima at 460, 490 and 520 nm. The origin of these overlapping transitions is not clear, as both the Zn porphyrin cation and free base ketochlorin anion have spectrally similar transient absorptions in this region. These spectral features decay biexponentially with rate constants of  $3.5 \times 10^9 \text{ s}^{-1}$  and  $2.6 \times 10^8 \text{ s}^{-1}$  (Figure 20). The former rate constant is approximately 5 times larger than the that derived from the 1.5-ns decay of the Zn porphyrin excited state, which would indicate the existence of a nonradiative quenching process such as energy or electron transfer. However, discrete ion pair formation by ET does not seem to be the dominant excited state decay pathway as the transient absorption in the 600-800 nm region shows no evidence of Zn-porphyrin cation or ketochlorin anion absorption features similar to those observed for Zn—H<sub>2</sub>(=O) in DCM (Figure 18a). These observations in DMF are consistent with the long lived luminescence and transient species observed in *n*-propyl acetate

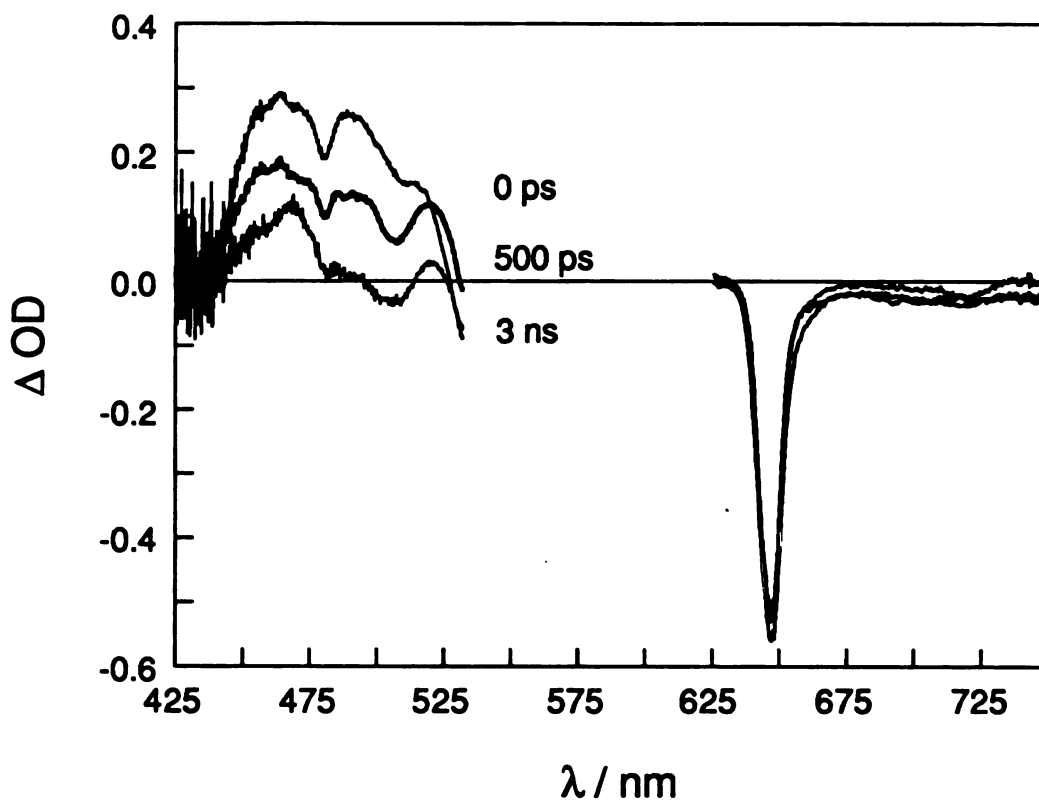


**Figure 19.** Transient absorption spectra of the  $^1(\pi\pi^*)$  excited state of Zn—H<sub>2</sub>(=O) in DMF at 0, 500 ps and 3 ns following 575 nm excitation. The Zn porphyrin excited state absorbs strongly at 450 nm while the free base ketochlorin is responsible for the excited state features at 500 nm and the intense ground state bleaching at 645 nm. The absorption at 520 nm is characteristic of both the Zn-porphyrin and ketochlorin excited states.



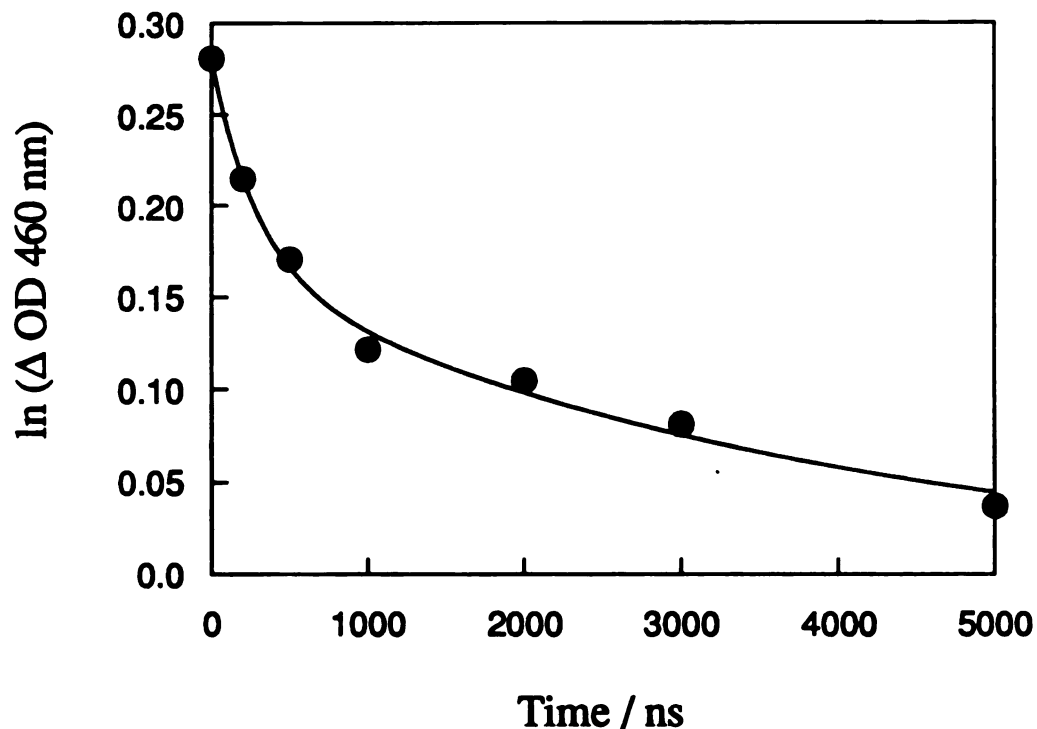
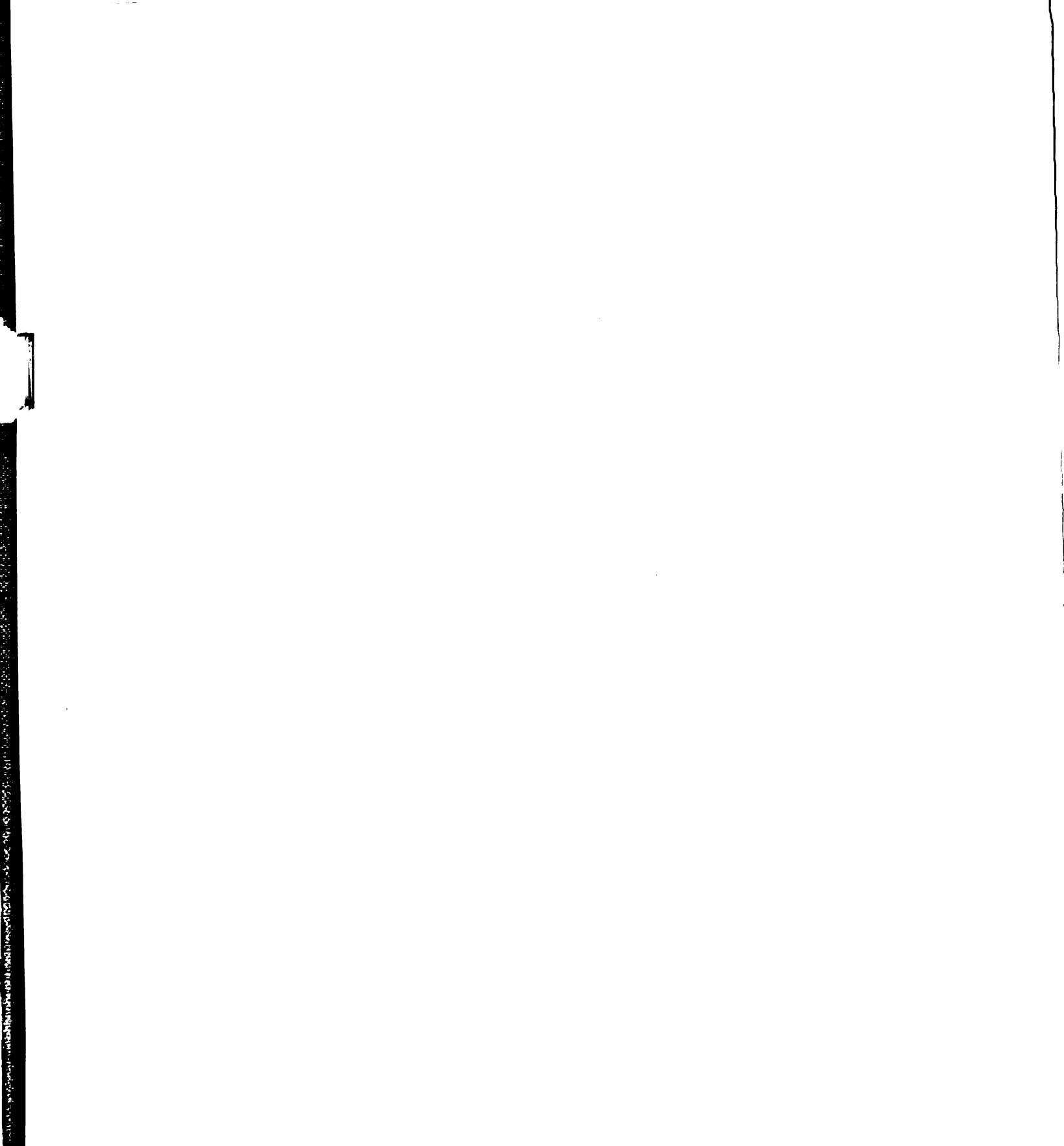


**Figure 20.** Decay of the  $^1(\pi\pi^*)$  state absorption of Zn—H<sub>2</sub>(=O) absorption at 460 nm. The state decays biexponentially with lifetimes of 300 ps and 4 ns. The latter value is consistent with the luminescence lifetime of Zn—H<sub>2</sub>(=O) as measured by time correlated single photon counting, while the former is associated with the decay of the 1.5 ns Zn porphyrin excited state, possibly convolved with a weak contribution of an ion pair intermediate not observed in the transient absorption spectra in the 600–800 nm region.



(vide infra) in the same spectral region. The most conceivable explanation for the quenching of the absorption between 425-550 nm is modest formation of a  $\text{Zn}^+ - \text{H}_2(=\text{O})^-$  charge-separated state, which has contributing absorption superimposed upon features originating from a significant population of the  $^1(\pi\pi^*)$  excited state of the dimer. Further spectroscopic studies are required to definitely identify the decay pathway of the transient absorption profiles observed for  $\text{Zn}-\text{H}_2(=\text{O})$  in DMF.

Although the decay of the ion-pair is easily monitored, the transient absorption spectra of  $\text{Mg}-\text{H}_2$  or  $\text{Zn}-\text{H}_2(=\text{O})$  heterodimers are complicated by the presence of long-lived species. The weak excitonic coupling in these systems permits localized excited states of the porphyrin subunits to be prepared. However, although we attempt to be selective in our excitation, the subunit that most effectively leads to charge separation cannot exclusively be prepared. Even if this were possible, energy transfer to the lower energy state of the cofacial pair<sup>131</sup> may compete with charge separation. For the case of  $\text{Mg}-\text{H}_2$  and  $\text{Zn}-\text{H}_2(=\text{O})$ , ET from the Mg and Zn porphyrin subunits of  $\text{Mg}-\text{H}_2$  and  $\text{Zn}-\text{H}_2(=\text{O})$ , respectively, is slightly exergonic whereas ET from their free base counterparts in the heterodimer is isoenergetic or slightly endergonic.<sup>132</sup> Because excitation of the subunits is not exclusive, relaxation of the localized excited states via radiative decay can compete with the nonradiative pathway of charge separation. And for both these systems, we observe that the lifetime of the transient is similar to the luminescence lifetimes of the heterodimers. These correlations suggest that the emissive and long-lived transient species for these heterodimers are of the same parentage.

The transient spectroscopy of the  $\text{Mg}-\text{Cu}$  system is less complex. Figure 21 shows the time evolution of the transient absorption



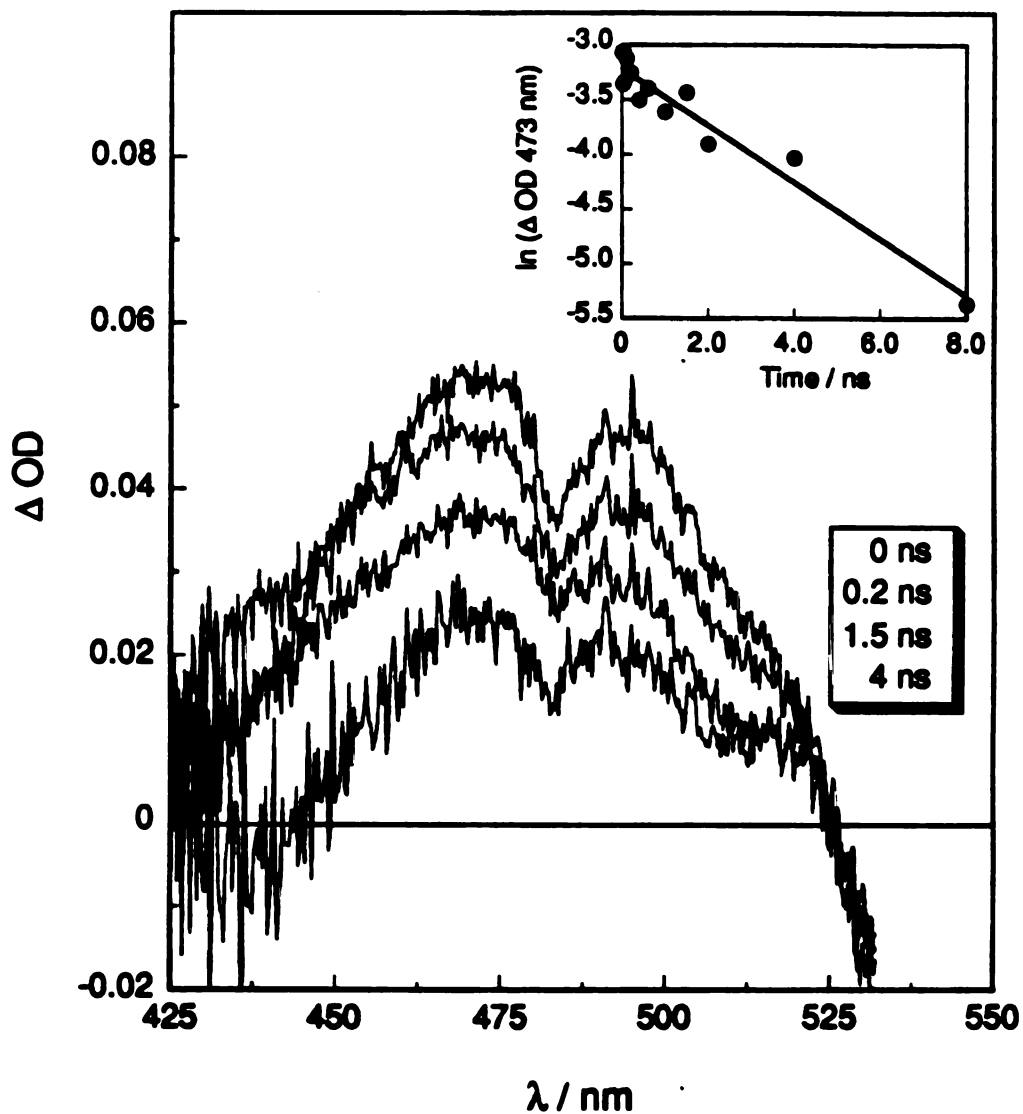


**Figure 21.** Transient absorption spectra of the  $^1(\pi\pi^*)$  state of the Mg—Cu diporphyrin complex in *n*-propyl acetate at 0, 0.2, 1.5 and 4.0 ns after the 588 nm excitation pulse. The decay of the transient absorption at 473 nm is included (inset).

spectrum of Mg—Cu in *n*-propyl acetate. Two maxima are observed, at 470 nm and 490 nm, which result from overlapping Mg-porphyrin  $^1(\pi\pi^*)$  and Cu-porphyrin “tripdoublet”  $^2T(\pi\pi^*)$  excited state absorption features. Because the maxima of these excited state absorptions are shifted by 20 nm relative to each other (MgOEP~455 nm, CuOEP~433 nm),<sup>126</sup> the transient spectrum of the dimer does not reflect the individual bands of the monomeric subunits. The spectral profile between 425-530 nm decays monotonically with a rate constant of  $2.5 \times 10^8 \text{ s}^{-1}$ , which is commensurate with the decay of the long component of the luminescence as given in Table III. The transient absorption profile between 600-750 nm also decays with a similar rate constant, suggesting that the excited state population is primarily localized in the excited  $\pi\pi^*$  manifold of the dimer. This is consistent with the endothermic forward charge separation step, as determined by the oxidation-reduction chemistry of the Mg—Cu diporphyrin.

#### 4. Solvent Dynamics

Transient absorption measurements show that Mg—H<sub>2</sub> is the only probe in Figure 8 suitable for the study of solvent dynamics in ET, owing to production of the Mg<sup>+</sup>—H<sub>2</sub><sup>−</sup> state in several solvents including DCM, DMF and Ac, as well as the nitrile and acetate families. The Mg—Cu and Zn—H<sub>2</sub>(=O) systems are not considered because formation of the charge-separated state was not detectable in most solvents. The CR rate constants for Mg<sup>+</sup>—H<sub>2</sub><sup>−</sup> exhibit a marked solvent dependence. Figure 22 plots the observed rate constant for Mg<sup>+</sup>—H<sub>2</sub><sup>−</sup> charge recombination versus the inverse of the solvent relaxation time  $\tau_s$ . The CR rate constant generally

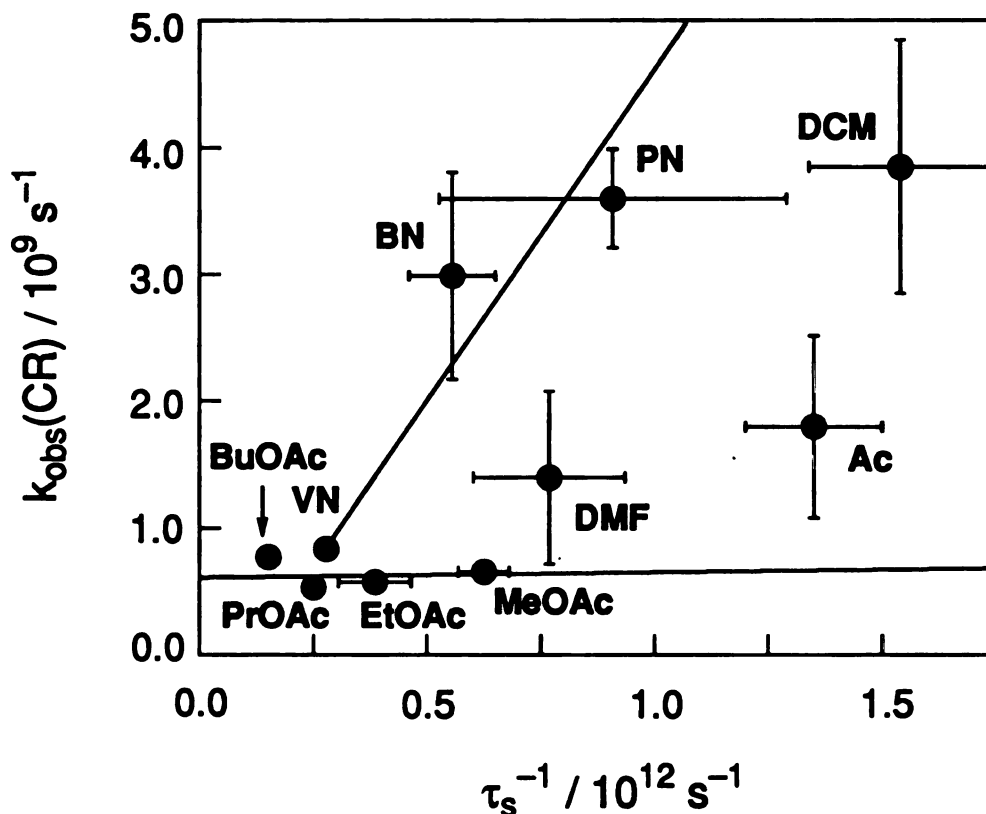


**Figure 22.** Plot of the observed CR rate constants of  $\text{Mg}^+ - \text{H}_2^-$  in acetone (Ac) dichloromethane (DCM), *N,N*-dimethyl formamide (DMF), propionitrile (PN), *n*-butyronitrile (BN), *n*-valeronitrile (VN) and methyl, ethyl, *n*-propyl, and *n*-butyl acetates (MeOAc, EtOAc, PrOAc, BuOAc, respectively) vs. the reciprocal of the microscopic relaxation times (taken from ref. 76).

increases as the microscopic relaxation time of the solvent decreases, but it varies linearly with  $1/\tau_s$ , as predicted by eq 1.5-1.7, only within a homologous solvent series. The population of emissive or nonemissive long-lived transients appears to be competitive with charge separation, but due to the disparate timescales for decay of these species, the kinetics of CR are easily isolated from those of the long-lived transients.

### C. DISCUSSION

Interpretation of the picosecond transient absorption kinetics of the Mg—Cu diporphyrin is the most straightforward of the heterodimers shown in Figure 8. Excitation of the dimer produces only long-lived transient species originating from  $\pi\pi^*$  states of the porphyrin subunits. No ion-pair formation is observed for Mg—Cu in either DCM or PrOAc. On the basis of luminescence lifetime measurements, the identity of the long-lived species certainly contains contributions from the  $^1(\pi\pi^*)$  of the Mg-porphyrin subunit, as the dominant luminescence component decays with a comparable rate constant to that of the Mg-porphyrin monomer. Similarly, the short decay component ( $\tau_{\text{fl}} < 50$  ps) is thought to arise from the Cu-porphyrin  $\pi\pi^*$  emission which is rapidly quenched by the low-lying d-d states of the  $\text{Cu}^{+2}$  center. The slow decay of the transient absorption of Mg—Cu is also consistent with the rate constants observed for traditional  $\pi\pi^*$  photophysics of the Mg-porphyrin and  $^2\text{T}$  and  $^4\text{T}$  manifolds of the Cu-porphyrin.<sup>126</sup> The absence of ion-pair intermediates upon excitation of this complex are supported by the  $\sim 0.3$  V endothermicity of the charge separation reaction as determined by electrochemical measurements performed on the Mg—Cu dimer.



The spectroscopy of  $\text{Zn—H}_2(=\text{O})$  strongly influenced by specific solvation effects, which perturb the ground state electronic absorption spectrum as the energetics of the  $\text{Zn}^+—\text{H}_2(=\text{O})^-$  charge-separated state. Observation of distinct ion-pair intermediates in the transient absorption spectrum of this compound in DCM is coincident with pronounced broadening of the ground state absorption profile. The CR rate constant is very similar to that previously reported for  $\text{Mg—H}_2$  in DCM, as expected on the basis of the comparable charge recombination reaction exothermicities.<sup>119</sup> The formation of a long-lived transient suggests that the excited state decay pathway may also be similar to that proposed for  $\text{Mg—H}_2$  in this solvent.<sup>119-121</sup>

In contrast, photoexcitation of  $\text{Zn—H}_2(=\text{O})$  in PrOAc produces only  $\pi\pi^*$  excited state population, with no detectable formation of charge-separated products. This result correlates with the well defined electronic absorption spectrum of  $\text{Zn—H}_2(=\text{O})$  in this solvent, further supporting the premise that static solvation effects in the ground state are influencing the energetics of the ion-pair intermediate. The similarity of the luminescence decay rate constants of  $\text{Zn—H}_2(=\text{O})$  in these two solvent demonstrates that the emitting state is uncoupled from the kinetics of the charge-separated state.

Formation of the  $\text{Zn}^+—\text{H}_2(=\text{O})^-$  species does not predominate in other solvents such as acetone, DMF or ethanol. Consistent with these observations, the optical absorption spectrum of  $\text{Zn—H}_2(=\text{O})$  in these solvents closely resemble features observed in the spectrum obtained in PrOAc. However, some evidence for charge-separated product formation exists in DMF, but the quantum yield is assuredly low. It is apparent that static solvation effects are responsible for these inconsistent results, but the

solvent dependent trends are not intuitive as DCM would not be expected to stabilize a charge-separated state more strongly than DMF. Static effects of this sort have been shown to dominate the excited state decay kinetics of other Zn-porphyrin-chlorin systems possessing ketone functionalities.<sup>130</sup> The prominent dependence of the ET rate constants on statics short-circuits the ability to correlate ET rates with solvation dynamics for this system.

The Mg—H<sub>2</sub> cofacial diporphyrin in Figure 8 undergoes efficient charge separation (<6 ps) upon excitation of a localized <sup>1</sup>( $\pi\pi^*$ ) excited state. The disappearance of the radical and cation absorptions of the ion-pair are accompanied by the recovery of the strong bleach in the Soret and Q band regions on the 10<sup>2</sup>-10<sup>3</sup> ps time scale. The slower rates for charge recombination, whether from a singlet or triplet ion pair,<sup>121</sup> are consistent with ET occurring in the inverted region. The presence of transient absorption at times >6 ns in all solvents are consistent with the earlier observations of Netzel and coworkers. The correlation between the decay of Mg—H<sub>2</sub> luminescence and the disappearance of the residual absorption suggest the long-lived transient results at least in part from <sup>1</sup>( $\pi\pi^*$ ) and <sup>3</sup>( $\pi\pi^*$ ) parentage. However, on the basis of optical data, it is impossible to rule out the existence of a <sup>3</sup>(Mg<sup>+</sup>—H<sub>2</sub><sup>-</sup>) state produced by radical pair intersystem crossing. This state has been shown to form from the locally excited singlet state of the Mg-porphyrin following 580 nm excitation. Since production of the ion-pair state is instantaneous, and the likelihood that the radical pair intersystem crossing rate is greater than 10<sup>11</sup> s<sup>-1</sup> for this system, it is within reason to assume that the photoinitiated charge-separated state is of singlet origin. This is consistent with the mechanisms proposed for the nonradiative decay pathway in Mg—H<sub>2</sub>.<sup>119-121</sup>

The data displayed in Figure 22 show the CR rate constants for  $\text{Mg}^+ - \text{H}_2^-$  are markedly solvent dependent. Unlike other porphyrin dimers,<sup>133</sup> however, the CR trends in Figure 22 are difficult to rationalize solely on the basis of static solvent effects. Firstly, in contrast to linear porphyrin diads, the separation distance of the ion-pair is much shorter in a cofacial arrangement, and the effect of solvent on the energetics of the ion pair, as determined from electrochemistry, is minimized. Secondly, for the small solvent dependence that is observed, the CR rate constants lack any consistent correlation with expected free energy predictions. Charge recombination will be less exothermic as the solvation of the charge separated state of the cofacial porphyrin systems increases. Inverted regime arguments would predict the rate to be fastest in these more strongly solvating media, but it is not. Some of the fastest recombination rates are observed in Figure 22 for solvents that provide the least stabilization of the charge separated state. Therefore static solvent effects do not account for the origins of the solvent dependence for the CR reaction of the heterodimer systems.

Correlation of the CR rate constants for  $\text{Mg}^+ - \text{H}_2^-$  with  $1/\tau_s$  is observed only within a homologous solvent series. The rate constant  $k_D$  represents an activated process, and thus even though the well dynamics may be fast, the activation barrier for diffusion to the surface crossing point must be surmounted for charge recombination to occur (Figure 23). It is this activation energy, characteristic of the inverted nature of this process, that accounts for the differences between the  $k_{\text{obs}}(\text{CR})$  vs  $1/\tau_s$  plots for the acetate and nitrile solvent series and the incongruous behavior of the rate constants in DMF, acetone, and dichloromethane (see Figure 22). The activation energy contains the contributions of solvent reorganization



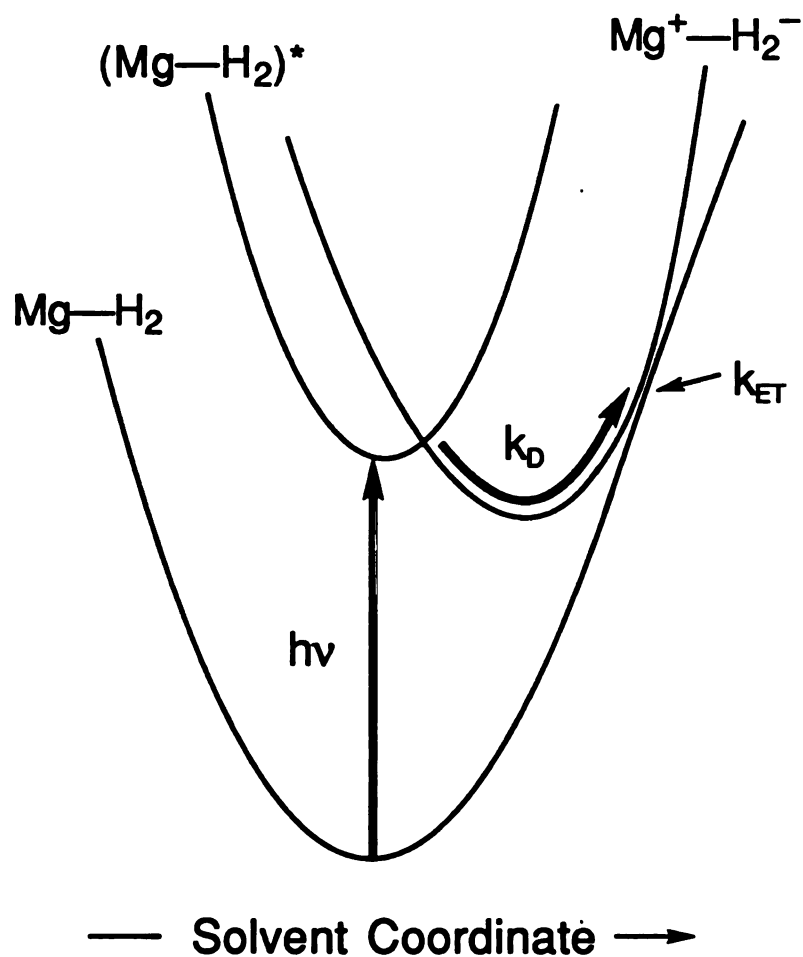


**Figure 23.** Reaction surface diagram for  $\text{Mg}^+—\text{H}_2^-$ , which is formed from the photoinduced electron transfer of the  $^1(\pi\pi^*)$  excited state of  $\text{Mg—H}_2$ . Diffusional motion governed by solvent dynamics in the  $\text{Mg}^+—\text{H}_2^-$  well is represented by the rate constant  $k_D$ . The nonadiabatic electron transfer rate for bringing the charge-separated complex to its neutral ground state is denoted by  $k_{ET}$ .

and free energy; therefore, changes in these parameters will affect  $\Delta G^*$  in eqs 1.5-1.7 and lead to nonlinearity in a plot of rate constant vs  $1/\tau_s$ . By measuring the CR kinetics within a homologous solvent series, variations in the solvent reorganization and free energy are minimized and the contribution of  $\Delta G^*$  to the overall rate should be relatively constant. This is observed in Figure 22 for the nitrile or acetate series. But across the two solvent series, differences in  $\Delta G^*$  are not normalized. The more polar nitrile solvents possess a greater reorganization energy for CR and they can better stabilize the charge separated state (by at least 0.13 V). Both of these effects serve to decrease the activation barrier for ET in the inverted region. Hence the observed slope for the  $k_{\text{obs}}(\text{CR})$  vs  $1/\tau_s$  plot for the nitriles is greater than that observed for the less polar acetates.

## CHAPTER IV

# THE ROLE OF SOLVATION DYNAMICS IN NEAR- ACTIVATIONLESS ELECTRON TRANSFER REACTIONS

### A. Background

Recent investigations of solvent dynamics in low barrier ET reactions have transcended the problems associated with electronic relaxation of polar dye molecules by incorporating distinct donor and acceptor elements into new molecular probes. Barbara has implemented this strategy by investigating the nonradiative ET process in 2,6-diphenyl-4-(2,4,6-triphenyl-1-pyridinio) phenylate (betaine-30) which occurs in the inverted region.<sup>134</sup> Betaine-30 is unique in that the ground state is charge-separated ( $D^+ - A^-$ ), while the excited state is neutral and possesses a low barrier to the charge recombination reaction. This complex is energetically well suited for studying dynamics as the donor and the acceptor are strongly coupled ( $H_{AB} \sim 2900 \text{ cm}^{-1}$ ), forcing the CR reaction into the solvent-controlled, adiabatic limit.

The rate constants for ET in betaine-30 in typical polar, aprotic solvents, have been determined to be on the order of  $10^{12} \text{ s}^{-1}$  and mildly correlated with  $1/\tau_s$ . However, the rates are slightly larger than predicted

by the classical theory of Sumi and Marcus.<sup>59</sup> Barabara has shown that the enhanced rate constants can only be accounted for by invoking a quantum treatment of vibrational mode coupling between the donor and acceptor potential surfaces that considers contributions from dynamic solvent effects, as discussed by Jortner and Bixon.<sup>135</sup> When quantum vibrations are included in the description of the rate constant, the ET no longer occurs at a localized crossing as described by classical theory, but rather, it can occur at several points along the surface, corresponding to the *vibronic* crossing of the  $D^+—A^-$  and  $D—A$  wells.<sup>136</sup> The key premise is that both solvent dynamics and high frequency vibrational modes are required to accomplish the ET and the traditional representation of a solvent coordinate is more accurately depicted as a solvent/vibronic coordinate.<sup>138</sup>

The Jortner/Bixon model also dictates that at  $\Delta G^*=0$ , the ET rate should be nearly equal to the solvation rate ( $k_{ET} \cong 1/\tau_s$ ), and indeed, the ET rates observed for betaine-30 are better described within this framework for solvents such as the nitrile series. However, this is not the case in highly viscous, slowly relaxing media, where the ET rates were determined to be significantly greater than  $1/\tau_s$ . Here, even inclusion of high frequency vibronic coupling between  $D—A$  and  $D^+—A^-$  states of betaine-30 could not account for the invariance of solvent dynamics on the ET rate.

Jortner and Bixon have very recently extended the description of ET in the *activationless* regime beyond the typical electron/nuclear coupling to medium modes to include contributions from high frequency vibrations modes of the donor and acceptor.<sup>71</sup> They suggest that in the activationless case, the ET cannot be described by a diffusional process to a crossing point on the potential surface. Instead, vibronic coupling between the  $D—A$  and  $D^+—A^-$  surfaces serves to deplete the excited state without



dependence on dielectric relaxation. In this limit, the ET rate constant reduces to the traditional nonadiabatic ET expression, which is strongly dependent on the electronic coupling and not limited by medium relaxation dynamics. This result is somewhat in contrast to early discussions of solvent effects in activationless ET, where the rate constant was shown to be dependent on  $1/\tau_s$ .<sup>65,135</sup> Nevertheless, inclusion of high frequency accepting modes in the activationless limit, reveal that the ET rate can exceed the value of  $1/\tau_s$  in accordance with the studies of betaine-30 in viscous solvents.

The determination of ET rate constants greater than  $1/\tau_s$  for betaine-30 is not anomalous as similar results have been obtained in Zn-porphyrin-(quinone)<sub>n</sub> cyclophane (n=1,2) (Zn—Q) and Nile blue/dimethylaniline (NB/DMA) complexes.<sup>137,138</sup> The ET rate constants for the Zn—Q system were found to be  $5 \times 10^{11} \text{ s}^{-1}$  and independent of solvent relaxation effects while those obtained for the NB/DMA complex were determined to be  $\gg 1/\tau_s$ . Both of these observations are closely associated with those of betaine-30 and are adequately described within the framework of Bixon and Jortner's recent discussions of the effects of high frequency vibrational modes of the donor and acceptor on the ET rate in the activationless limit.

The experimental and theoretical studies described above lend critical insight into solvent dynamics effects in low barrier ET processes. These reactions have been shown to be effective for diminishing static contributions to the ET event and isolating the dependence of the rate constant on  $1/\tau_s$ . However, if the barrier height is reduced to within  $k_B T$ , the ET rate becomes independent of the medium relaxation and no correlation with  $1/\tau_s$  is expected.

Although solvent dynamics will predominate for activated ET in the inverted region, the static solvent contributions to the CR rate constants of Mg—H<sub>2</sub> significantly disrupts the correlation between  $k_{\text{obs}}(\text{CR})$  and  $1/\tau_s$  as shown in Figure 22. By lowering the activation barrier to the CR step, variations in  $\Delta G^*$  (eq 1.1-1.7) can be minimized and the CR rate constants should *approach* the activationless solvent-controlled adiabatic limit.<sup>65,135</sup>

Yet spectroscopically complex excited state manifolds of the donor-acceptor probe can also cause dynamics effects to be masked by convolution with radiative and nonradiative excited state decay. Fortuitously, dynamics effects upon the CR rate constants for the Mg—H<sub>2</sub> diporphyrin system discussed in Chapter III occurred on a disparate timescale with  $^1(\pi\pi^*)$  excited state decay and therefore were effectively separable. Nevertheless, elimination of other excited state alternatives to charge separation and charge recombination is desirable for definitively assessing dynamics effects upon ET rate constants.

Reduction of the number of accessible kinetic pathways upon photoexcitation can be achieved within the cofacial diporphyrin motif by substitution of a non-closed shell metal atom into the center of the porphyrin or chlorin macrocycle. This effectively quenches the traditional  $^1(\pi\pi^*)$  and  $^3(\pi\pi^*)$  excited states of the free base and metalloporphyrin or chlorin systems by introducing lower energy deactivation pathways through the d-d states of the metal. Since these states typically have poor oscillator strength, they are not likely to spectroscopically interfere with the decay of the cofacial dimer charge-separated state.

As a result of these issues, we have chosen the Zn—H<sub>2</sub>(=C(CN)<sub>2</sub>) and Zn—Cu(=C(CN)<sub>2</sub>) cofacial porphyrin-chlorin heterodimers shown in Figure 24 for our investigation of solvent dynamics in near-activationless

ET. By introducing the electron withdrawing dicyanomethide group to the  $\pi$  ring system, the driving force for the CR step is diminished, thus lowering the activation energy for the reaction in the inverted region. As a consequence, the CR reaction now occurs on comparable timescales to solvent motion but remains slightly activated in order to maintain a dependence on  $1/\tau_s$ . Spectroscopically, the Zn-porphyrin cation and chlorin anion absorption features are well defined, providing a strong basis for the determination of ET rates for these new compounds by transient optical spectroscopy. Introduction of the Cu center is designed to simplify the analysis of ET rate constants derived from the analogous free base chlorin system by eliminating competitive excited states while maintaining a the same driving force as the free base complex.

Although the ET energetics for the Cu-chlorin are the same as the free base complex, spectroscopic characteristics of Cu complexes are somewhat different than more traditional, closed-shell porphyrins. The  $d^9$  electron configuration of the Cu atom couples the  $S = 1/2$  metal-based spin system with the existing  $^1(\pi\pi^*)$  and  $^3(\pi\pi^*)$  excited state manifolds of the porphyrin or chlorin. Through this interaction, the electronic states of the Cu-substituted macrocycle attain somewhat different parentage. The ground state is designated as  $^2S_0$  while the traditional porphyrin or chlorin excited states are now higher multiplicity hybrids of the excited states of the macrocycle and the  $Cu^{+2}$  center, and are denoted as the singdoublet ( $^2Q$ ), tripdoublet ( $^2T$ ) and tripquartet ( $^4T$ ). The kinetics of these excited states are strongly influenced by the half-filled  $d_{x^2-y^2}$  orbital as d-d states can become stabilized upon addition of an axial ligand to the Cu center.<sup>139,140</sup> These effects combine to produce large radiationless decay rate constants and very low emission quantum yields for Cu systems.

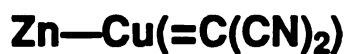
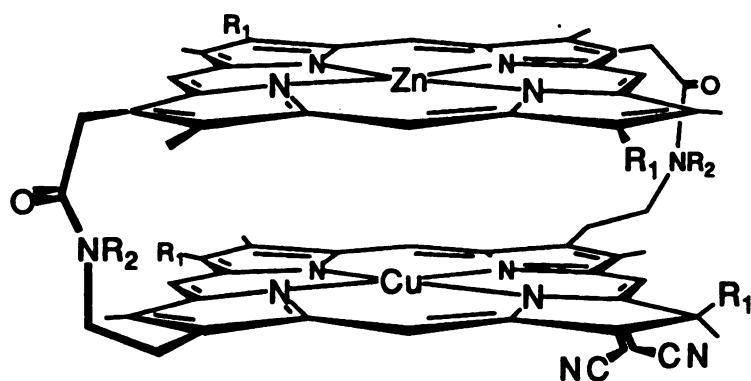
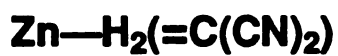
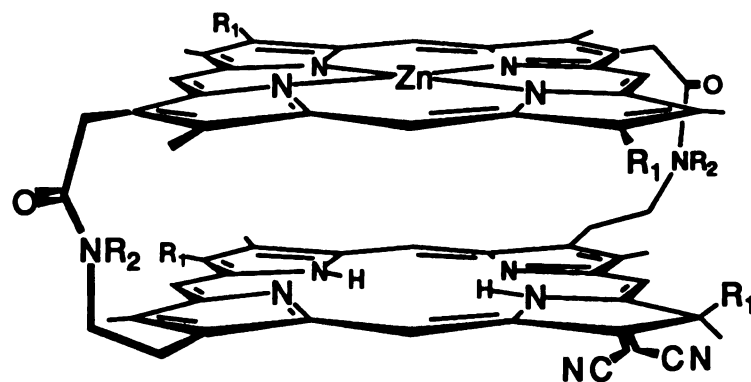


**Figure 24.** Probe molecules used to investigate solvation dynamics effects in near-activationless ET reactions. The cofacial porphyrin-chlorin probes are designated as  $\text{Zn}-\text{H}_2(=\text{C}(\text{CN})_2)$  and  $\text{Zn}-\text{Cu}(=\text{C}(\text{CN})_2)$ .

Our observation of  $^1(\pi\pi^*)$  excited states of  $\text{Mg}-\text{H}_2$  that decay on significantly longer timescales than the photogenerated  $\text{Mg}^+-\text{H}_2^-$  intermediate has fostered interest in using Cu systems to quench population of these additional excited states. One of the possible mechanisms describing the origin of these states is energy transfer from the first excited  $^1(\pi\pi^*)$  state of the donor metalloporphyrin to the lowest energy excited state of acceptor porphyrin or chlorin. Energy transfer pathways of this type have been observed between covalently linked Zn and Cu-porphyrins and Zn and free base porphyrin systems arranged in both cofacial<sup>131a</sup> and linear orientations.<sup>141,142</sup> Although some controversy exists as to whether the Zn or Cu porphyrin states are lowest in energy, this issue is unequivocal in our cofacial systems. The free base and Cu-chlorin monomer absorption spectra are strongly redshifted from that of the Zn-porphyrin subunit and therefore the former possess the lower energy excited state. Since the presence of an energy transfer pathway in the cofacial heterodimers shown in Figure 24 is only circumvented by rapid quenching of the lowest energy chlorin excited state, we can use the principles outlined above to simplify our experimental determination of ET rate constants.

## B. Results

### 1. *Electrochemistry*

Functionalization of the porphyrin periphery with the electron withdrawing dicyanomethide group to form the corresponding chlorin results in a significant perturbation of the  $\pi\pi^*$  HOMO-LUMO energy gap ( $\Delta E$ ). This is manifested in a shift of the reduction potentials of the free base and Cu dicyanomethide chlorins by  $\sim 0.46$  V to positive potential with respect to their octaethyl porphyrin counterparts.<sup>123</sup> The well-known electroinactivity of  $\text{Cu}^{2+}$  complexed in porphyrin or chlorin rings<sup>143</sup> is in evidence from the similarity of its reduction potential with the free base chlorin ( $E_{1/2}[(\text{H}_2(=\text{C}(\text{CN})_2)^{0/-}] = -1.00$ , and  $E_{1/2}[(\text{Cu}(=\text{C}(\text{CN})_2)^{0/-}] = -0.98$  V in  $\text{CH}_2\text{Cl}_2$  vs SCE). This fortuitous occurrence allows us to examine the CR rate constants for both of these systems at essentially the same reaction exothermicity and to compare similarities and differences between the free base and Cu systems.

### 2. *Electronic Spectroscopy*

The ground state optical spectra of  $\text{Zn}-\text{H}_2(=\text{C}(\text{CN})_2)$  and  $\text{Zn}-\text{Cu}(=\text{C}(\text{CN})_2)$  chlorins are a composite of their respective porphyrin and chlorin monomer spectra. This is not to imply, however, that the absorption spectra of these cofacial pairs are straightforward. As Figure 25 shows, the cofacial chlorin-porphyrin systems display many more features in the Soret and Q regions than do the diporphyrin complexes discussed in Chapter III, owing to a strong red-shift of the chlorin based

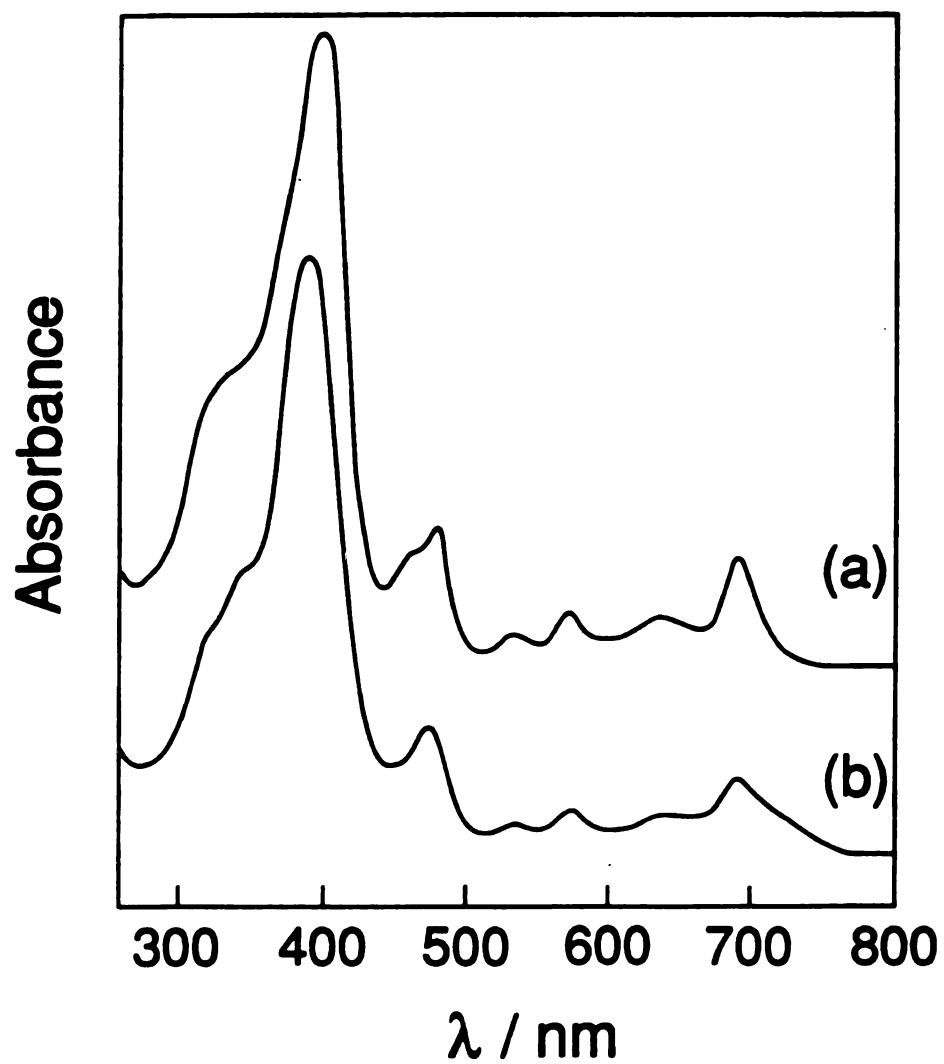


**Figure 25.** Electronic absorption spectra of (a)  $\text{Zn—H}_2(\text{C}=(\text{CN})_2)$  and (b)  $\text{Zn—Cu}(\text{C}=(\text{CN})_2)$  in  $\text{CH}_2\text{Cl}_2$ .

transitions, thus removing the accidental degeneracy of the porphyrin-chlorin monomer absorptions. The 320-500 nm spectral region of the Cu(II) and free base dicyanomethide chlorin monomers is rich with structure (Figure 26). Interestingly, the optical spectra of these monomers are not those typically observed for the chlorin Soret region, as reduction of the porphyrin skeleton by addition of the strongly electron withdrawing dicyanomethide group results in two prominent absorption features between 400–500 nm, each split into primary and secondary peaks. To our knowledge, assignment of these transitions has not been made and their assignment without a detailed spectroscopic investigation is tenuous at best. We do note however, that their energy and oscillator strength are comparable to the B transitions and the weaker so-called  $\eta_1$  and  $\eta_2$  transitions of chlorophylls.<sup>144</sup> Notwithstanding, only the lowest energy transitions in this region are displaced from beneath the intense Zn porphyrin Soret band. Thus, chlorin bands at 472 nm and 480 nm (and the associated 464 nm shoulder) appear to the low energy side of the Zn-porphyrin based Soret transitions at 400 and 392 nm in Zn—H<sub>2</sub>(=C(CN)<sub>2</sub>) and Zn—Cu(=C(CN)<sub>2</sub>), respectively. The higher energy chlorin transitions of Figure 26 are totally obscured by the envelope of the Zn-porphyrin Soret band. The remaining absorption features in the optical spectra of the Zn—H<sub>2</sub>(=C(CN)<sub>2</sub>) and Zn—Cu(=C(CN)<sub>2</sub>) dimers are characteristic of Zn-porphyrin and dicyanomethide chlorin Q bands between 500–700 nm. The Zn-porphyrin based Q(1,0) and Q(0,0) bands at 536 and 574 nm are essentially isoenergetic in both porphyrin-chlorin complexes and only slightly shifted (<3 nm) relative to monomer. The chlorin based Q<sub>x</sub> and Q<sub>y</sub> transitions are observed at the same energies in both Zn—H<sub>2</sub>(=C(CN)<sub>2</sub>) and Zn—Cu(=C(CN)<sub>2</sub>) spectra. However, the 640



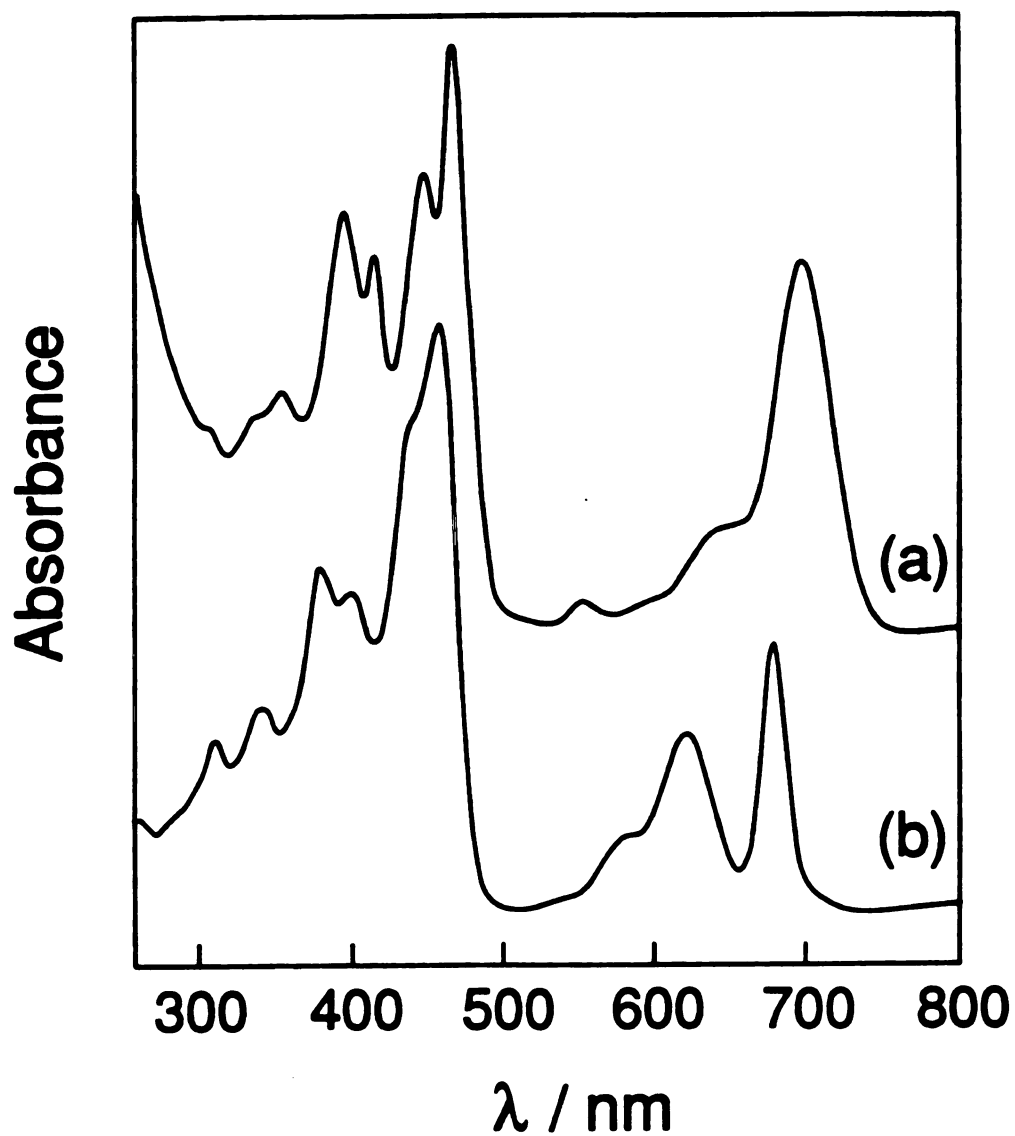


**Figure 26.** Electronic absorption spectra of (a)  $\text{Cu}(=\text{C}(\text{CN})_2)$  and (b)  $\text{H}_2(=\text{C}(\text{CN})_2)$  in  $\text{CH}_2\text{Cl}_2$ .



and 693 nm bands of  $\text{Zn—H}_2(=\text{C}(\text{CN})_2)$  are red-shifted by  $\sim 15$  nm from the  $\text{H}_2(=\text{C}(\text{CN})_2)$  chlorin monomer whereas the 640 nm and 696 nm bands of  $\text{Zn—Cu}(=\text{C}(\text{CN})_2)$  are only weakly shifted from their positions in the  $\text{Cu}(=\text{C}(\text{CN})_2)$  chlorin monomer absorption profile. The shoulder on the low energy side of the  $\text{Q}_y$  band for  $\text{Zn—Cu}(=\text{C}(\text{CN})_2)$  is specific to the heterodimer and is clearly related to the  $\text{Cu(II)}$  chlorin subunit as it is not observed for the free base heterodimer. Addition of anions such as chloride and acetate does not perturb the intensity or shape of the feature.

One advantage of these systems over those discussed in Chapter III is that more preferential excitation of the metalloporphyrin donor subunit can be achieved due to the shift in the Q transitions of the acceptor chlorin by addition of the dicyanomethide group. This substitution redshifts the  $\text{Q}_y$  transitions of the chlorin beyond 680 nm, permitting the  $\sim 580$  nm excitation pulse to be predominantly resonant with the  $\text{Q}(0,0)$  absorption band of the Zn-porphyrin moiety. Estimates of the extinction coefficients at the pump wavelength for  $\text{Zn—H}_2(=\text{C}(\text{CN})_2)$  and  $\text{Zn—Cu}(=\text{C}(\text{CN})_2)$  suggest that better than 83 % of all photons absorbed by the dimer are localized to Zn-porphyrin monomer. Selectivity in sample excitation better defines the spectroscopic intermediates prepared upon excitation and enhances the accuracy of excited state kinetics measurements.

As with the cofacial systems in Chapter III, many of the absorption and emission characteristics of the heterodimers are derived from spectroscopic transitions native to the respective monomeric units. For both compounds, the metalloporphyrin exhibits modest luminescence at 646 nm, while a distinct emission band is observed at 690 nm for the free base dicyanomethide chlorin (Figure 27). A weak emission band at 690 nm is also observed in the emission spectrum of  $\text{Zn—Cu}(=\text{C}(\text{CN})_2)$ , which is

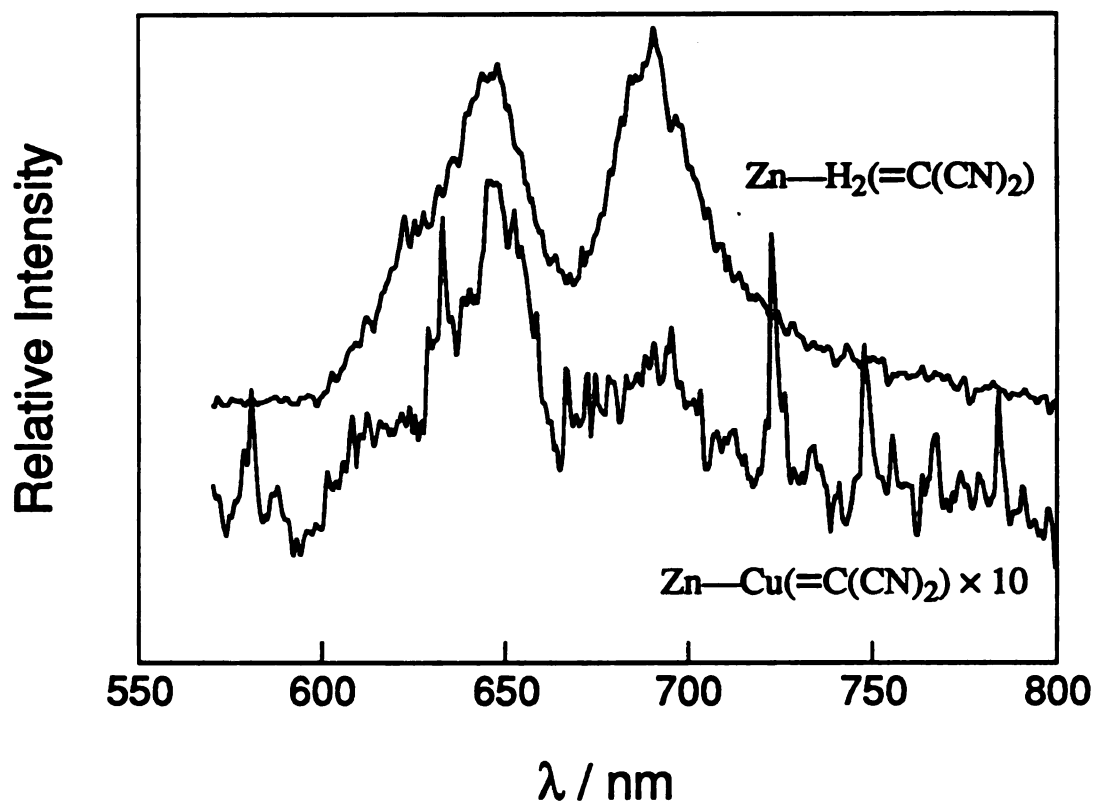


**Figure 27.** Luminescence spectra of  $\text{Zn-H}_2(=\text{C}(\text{CN})_2)$  and  $\text{Zn-Cu}(=\text{C}(\text{CN})_2)$  in degassed  $\text{CH}_2\text{Cl}_2$ . Samples were prepared in 1 cm quartz cuvettes with absorbances of 0.1 at  $\lambda_{\text{exc}} = 585 \text{ nm}$ . The emission spectrum of  $\text{Zn-H}_2(=\text{C}(\text{CN})_2)$  has been offset for clarity.



predominantly due to trace amounts of the  $\text{H}_2(=\text{C}(\text{CN})_2)$  subunit.

In general, luminescence from these compounds is weak, as evidenced by the low emission quantum yields shown in Table V. Since emission quantum yields of Zn-octaalkylporphyrins and free base and Cu-chlorins are  $\sim 0.04$ ,<sup>145</sup> and  $\sim 0.12$ ,<sup>146</sup> respectively, the yields given in Table V are lowered by two orders of magnitude from those expected on the basis of the monomer quantum yields. Introduction of the dicyanomethide group enhances the driving force for production of ion pair intermediates, thus promoting a nonradiative decay pathway out of the luminescent excited state of the porphyrin-chlorin dimer. Electron transfer quenching also contributes to the poor quantum yield observed for the Zn— $\text{Cu}(=\text{C}(\text{CN})_2)$  complex, as  $\Delta E$  of the  $\text{Zn}^+—\text{Cu}(=\text{C}(\text{CN})_2)^-$  charge-separated state is similar to that of the free base analog. The additional nonradiative decay pathway introduced by Cu insertion into the chlorin further quenches the Zn— $\text{Cu}(=\text{C}(\text{CN})_2)$  luminescence through coupling to low-lying d-d states localized on the  $\text{Cu}^{+2}$  center.

Luminescence decay rate constants for Zn— $\text{H}_2(=\text{C}(\text{CN})_2)$  and Zn— $\text{Cu}(=\text{C}(\text{CN})_2)$  measured at 640 nm following 575 and 580 nm excitation respectively, are summarized in Table VI. The luminescence of Zn— $\text{H}_2(=\text{C}(\text{CN})_2)$  decays biexponentially in all solvents (shown in Figure 28 for BuOAc) with lifetimes virtually identical to those observed for the  $^1(\pi\pi^*)$  luminescence of the Zn-porphyrin and free base dicyanomethide chlorin monomers.<sup>147</sup> Similar results are obtained for the Zn— $\text{Cu}(=\text{C}(\text{CN})_2)$  complex following 580 nm sample excitation. Luminescence from Zn— $\text{Cu}(=\text{C}(\text{CN})_2)$  decays according to monoexponential kinetics with solvent-independent rate constants of  $\sim 5 \times 10^8 \text{ s}^{-1}$ . Interestingly, although intensity quenching of the Zn-porphyrin and free base

**Table V.** Optical Properties of Zn—H<sub>2</sub>(=C(CN)<sub>2</sub>) and Zn—Cu(=C(CN)<sub>2</sub>) Porphyrin-Chlorin Heterodimers in CH<sub>2</sub>Cl<sub>2</sub>

| Heterodimer                              | $\lambda_{\text{em,max}}$ / nm | $\phi_{\text{e}}$ / 10 <sup>-3</sup> <sup>a</sup> | $\tau$ /ns <sup>b</sup> |
|--|--------------------------------|---|-------------------------|
| Zn—H <sub>2</sub> (=C(CN) <sub>2</sub> ) | 646, 690                       | 2.3   | 1.5 (50), 6.2 (50)      |
| Zn—Cu(=C(CN) <sub>2</sub> )              | 646                            | 0.16  | 1.5                     |

<sup>a</sup>Luminescence quantum yields referenced to Mo<sub>2</sub>Cl<sub>4</sub>(PMe<sub>3</sub>)<sub>4</sub> in 2-methylpentane ( $\lambda_{\text{exc}}$  = 585 nm). <sup>b</sup>Decay profiles fit to biexponential kinetics indicated by two lifetimes. Numbers in parenthesis represent percentage contribution of lifetime to the decay curve.





**Table VI. Luminescence Lifetimes of Zn—H<sub>2</sub>(=C(CN)<sub>2</sub>) and Zn—Cu(=C(CN)<sub>2</sub>) in Selected Solvents**

| Solvent <sup>a</sup> | Zn—H <sub>2</sub> (=C(CN) <sub>2</sub> ) | Zn—Cu(=C(CN) <sub>2</sub> ) |
|----------------------|--|-----------------------------|
|                      | $\tau/\text{ns}^{\text{b,c}}$            | $\tau/\text{ns}^{\text{d}}$ |
| DCM                  | 1.5 (49), 6.2 (51)                       | 1.5                         |
| Ac                   |  | 2.0                         |
| DMF                  |  | 2.0                         |
| PN                   |  | 2.0                         |
| BN                   |  | 2.0                         |
| VN                   |  | 1.9                         |
| MeOAc                |  | 1.7                         |
| EtOAc                |  | 1.8                         |
| PrOAc                |  | 1.9                         |
| BuOAc                | 1.6 (18), 6.5 (82)                       | 1.7                         |
| MeOH                 | 1.9 (56), 6.3 (44)                       |                             |
| EtOH                 | 1.8 (22), 6.1 (78)                       |                             |
| PrOH                 | 1.5 (24), 5.8 (76)                       |                             |

<sup>a</sup>Solvents are abbreviated as follows: dichloromethane (DCM), acetone (Ac), N,N-dimethylformamide (DMF), propionitrile (PN), butyronitrile (BN), valeronitrile (VN), methyl, ethyl, *n*-propyl and *n*-butyl acetates, (MeOAc, EtOAc, PrOAc and BuOAc, respectively), methanol (MeOH), ethanol (EtOH) and 1-propanol (PrOH). <sup>b</sup>Luminescence lifetimes measured at  $\lambda_{\text{exc}} = 575$  nm. <sup>c</sup>Decay profiles fit to biexponential kinetics indicated by two lifetimes. Numbers in parenthesis represent fractional contribution of lifetime to decay curve. <sup>d</sup>Luminescence lifetimes measured at  $\lambda_{\text{exc}} = 580$  nm. A weak 6 ns component to the luminescence was also observed and has been attributed to trace H<sub>2</sub>(=C(CN)<sub>2</sub>) impurities.

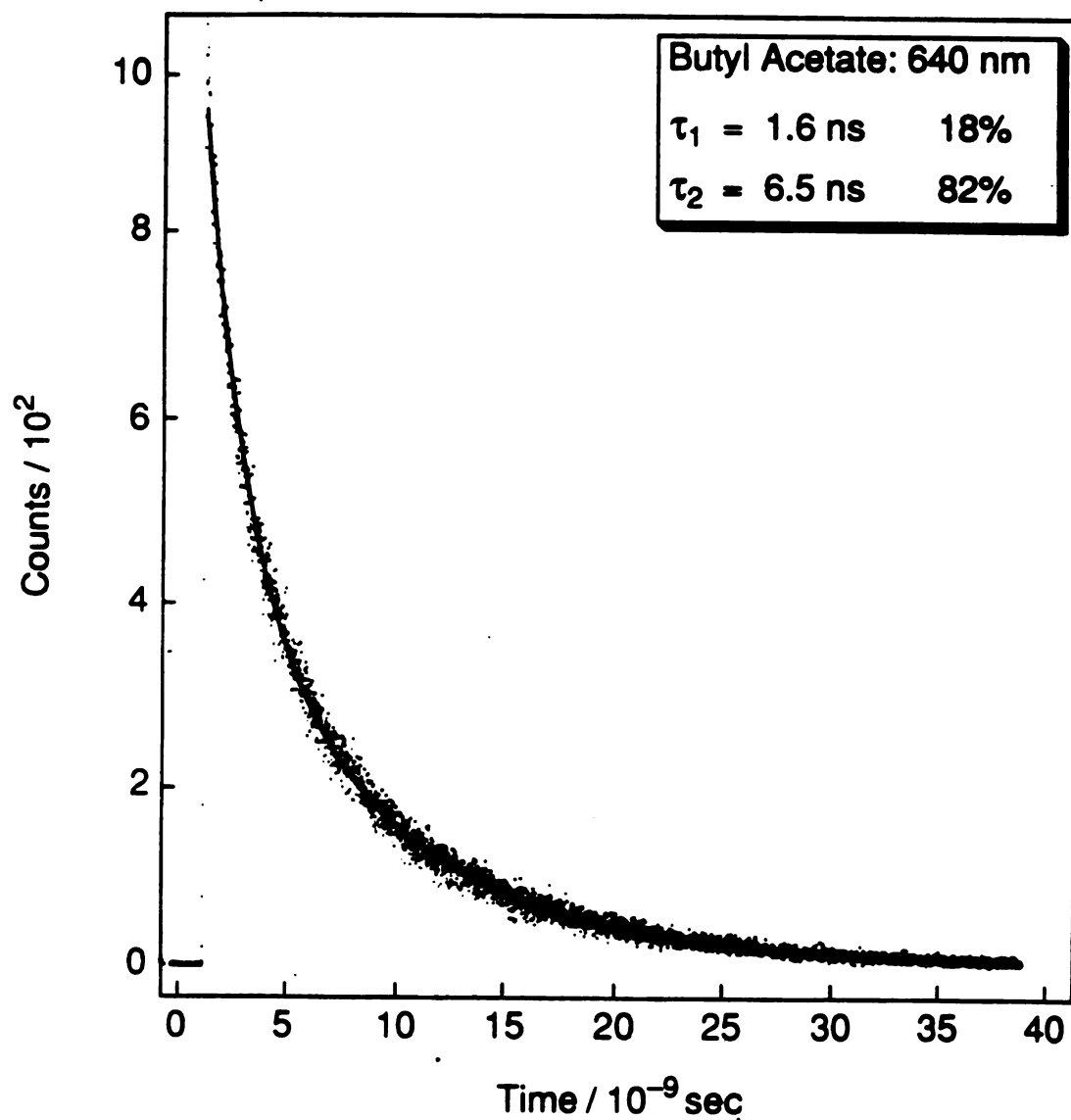


**Figure 28.** Luminescence decay of the of  $\text{Zn—H}_2(\text{=C(CN)}_2)$  in *n*-butyl acetate following 575 nm sample excitation with a 6 ps pulse. The inset shows the lifetime components and relative percentages of the decay.

dicyanomethide chlorin monomers luminescence is observed for both the  $\text{Zn—Cu(=C(CN)}_2\text{)}$  and  $\text{Zn—H}_2\text{(=C(CN)}_2\text{)}$  dimer, the decay rate constants of the individual monomeric subunits are conserved. This suggests a luminescent Zn-porphyrin and  $\text{H}_2\text{(=C(CN)}_2\text{)}$  based  $^1\pi\pi^*$  excited state which is uncoupled from the simultaneously populated charge-separated state. The luminescent states contain low population, as emission from the  $\text{Zn—Cu(=C(CN)}_2\text{)}$  dimer, where only the Zn-porphyrin is emissive, is extremely weak. The lifetimes of the emissive excited states of both  $\text{Zn—H}_2\text{(=C(CN)}_2\text{)}$  and  $\text{Zn—Cu(=C(CN)}_2\text{)}$  are essentially solvent independent and show no correlation with the rate constants for photoinduced charge recombination, as measured by picosecond transient absorption.

### 3. *Transient Absorption Spectroscopy*

The transient absorption spectrum of  $\text{Zn—H}_2\text{(=C(CN)}_2\text{)}$  in *n*-butyl acetate following 575 nm excitation into the  $^1\pi\pi^*$  manifold of the porphyrin-chlorin dimer is shown in Figure 29. The transient absorption spectrum between 450-550 nm is predominantly characterized by a strong band at 505 nm and weaker transient absorption at 450 nm, which are identified with the free base chlorin anion and zinc porphyrin cation, respectively. The transient spectrum to the red of the excitation is characterized by a bleach of the intense chlorin  $\text{Q}_y$  band at 690 nm, and the appearance of prominent absorption bands at 670 and 750 nm. These latter features are not simply due to excited states of the Zn-porphyrin or free base dicyanomethide chlorin, as is evident from the transient absorption spectra of these subunits shown in Figure 30. Rather, the absorption

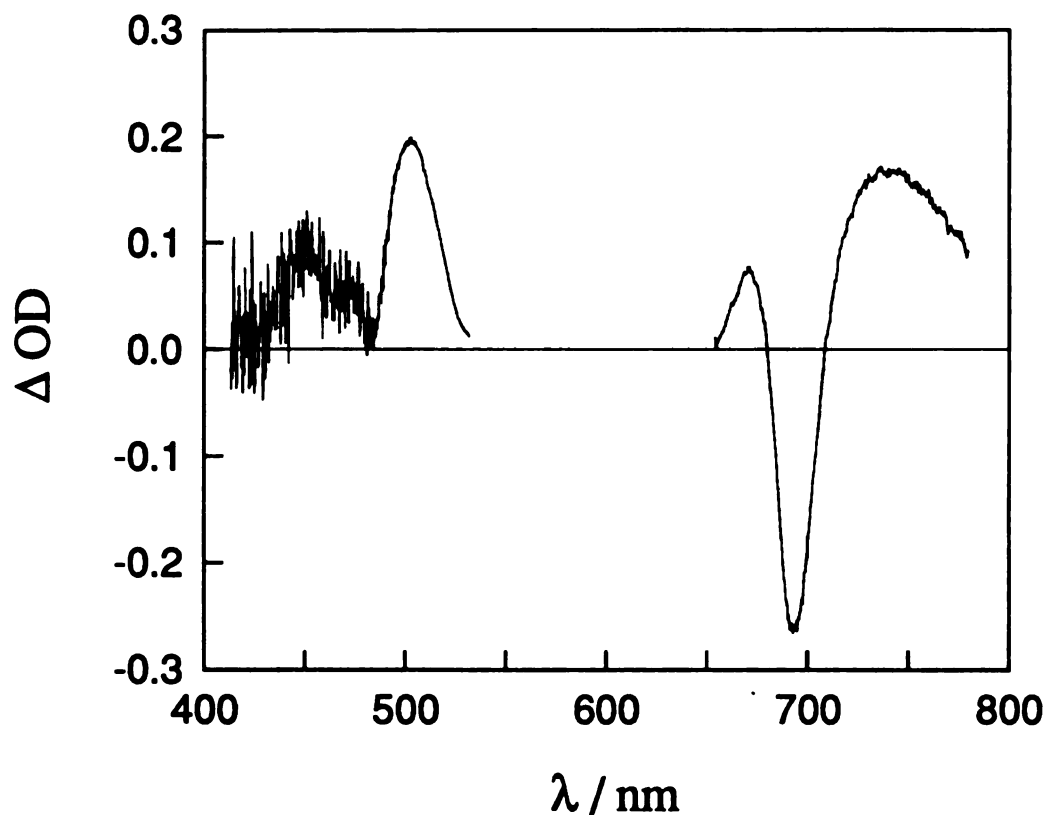


**Figure 29.** Transient absorption spectrum of  $\text{Zn}^+ - \text{H}_2(\text{C}=(\text{CN})_2)^-$  in BuOAc immediately after sample excitation at 575 nm with a 6 ps pulse. Absorption features at 450 and 670 are related to the Zn-porphyrin cation, while those at 505 and 745 are characteristic of the  $\text{H}_2(\text{C}=(\text{CN})_2)$  anion. A strong bleaching of the ground state  $\text{Q}_y$  band is also observed at 690 nm. Samples were prepared in 2 mm quartz cuvettes at concentrations of  $5 \times 10^{-4}$  M.

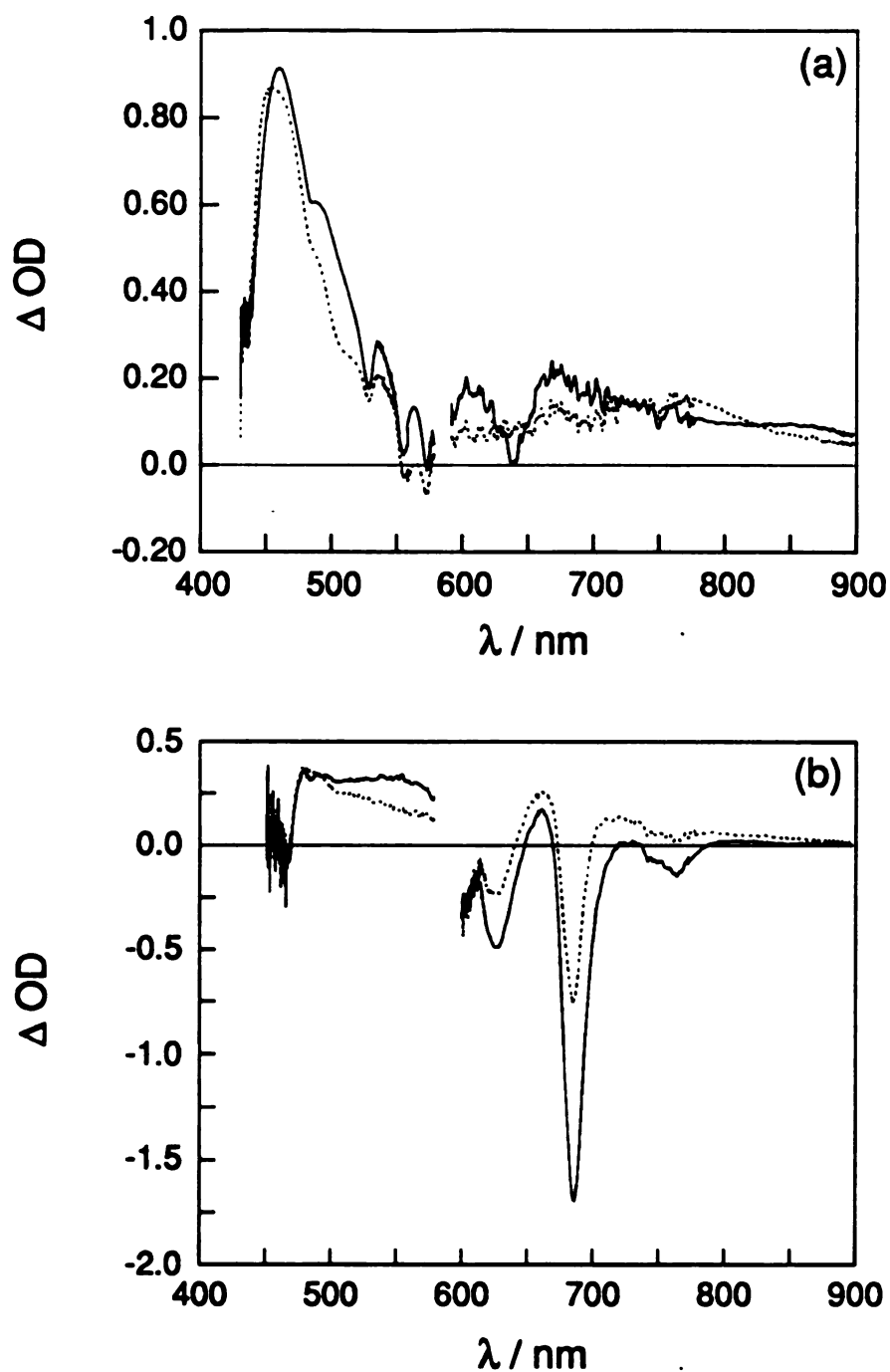


**Figure 30.** Transient absorption spectra of the (a) Zn-porphyrin and (b) free base dicyanomethide chlorin subunits at 15 ps (solid) and 5 ns (dashed) in *n*-propyl acetate following 6 ps excitation at 575 nm. Samples were prepared at concentrations of  $1 \times 10^{-3}$  M in 2 mm quartz cuvettes.

profile between 650-800 nm is that of the  $\text{Zn}^+ - \text{H}_2(=\text{C}(\text{CN})_2)^-$  state. The strong absorbance of Zn-porphyrin cation radical, typically observed between 625-700 nm,<sup>148</sup> is dominated by the intense  $Q_y$  bleach. The absorption band at 750 nm, which we attribute to the radical anion of the dicyanomethide chlorin, is slightly blue-shifted from the 745-825 nm absorption range characteristic of chlorin anion radicals.<sup>149</sup> The presence of a strong ground state bleaching and ion pair state absorption in the same spectral region enables the disappearance of the photogenerated charge-separated state and ground state repopulation to be monitored simultaneously. A distinct difference between the spectrum of  $\text{Zn} - \text{H}_2(=\text{C}(\text{CN})_2)$  and those of the  $\text{Mg} - \text{H}_2$  or  $\text{Zn} - \text{H}_2(=\text{O})$  systems is that the CS state decays with little residual absorption observed at long times, as shown by the time evolution of the transient absorption profile of the porphyrin-chlorin dimer between 650-800 nm in *n*-propyl acetate (Figure 31). Accordingly, as shown in the inset in Figure 31, the kinetics at 750 nm are described by a simple first-order decay at 750 nm. Comparable unimolecular kinetics are also observed for the decay of the transient absorption band at 505 nm in *n*-butyl acetate as shown in Figure 32. Addition of the dicyanomethide group to the chlorin ring makes reaction from the  $^1(\pi\pi^*)$  localized excited state of either subunit of the heterodimer to the ion pair considerably more favored ( $\Delta G^\circ(\text{CS}) \geq -0.4$  eV) than the  $-0.1$  V driving force of the  $\text{Mg} - \text{H}_2$  or  $\text{Zn} - \text{H}_2(=\text{O})$  systems. Apparently, the increased driving force makes ion-pair formation from the singlet more competitive with population of a long-lived emissive state. Thus, luminescence is quenched as evidenced by the attenuated emission quantum yield of  $\text{Zn} - \text{H}_2(=\text{C}(\text{CN})_2)$ , and the transient absorption spectrum reveals no discernible transient at long times. This is even more effectively

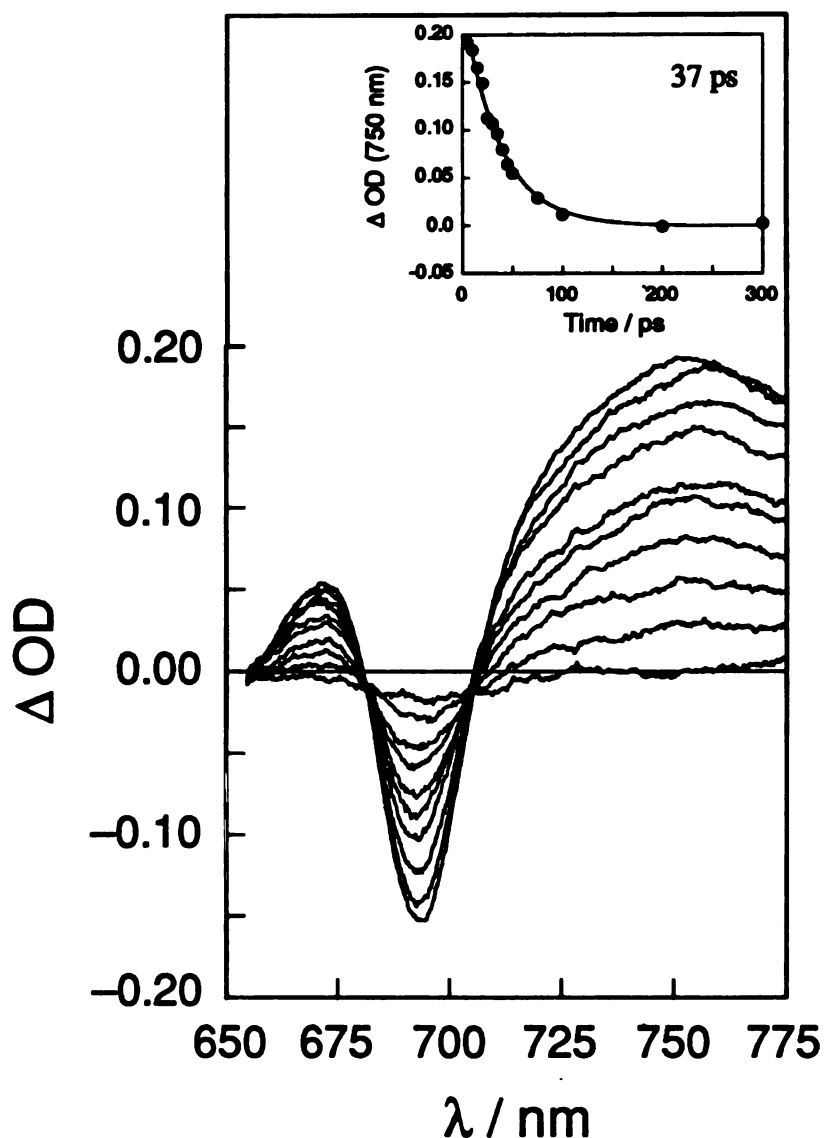


**Figure 31.** Picosecond transient absorption spectra of  $\text{Zn}^+ \text{—} \text{H}_2(\text{=C}(\text{CN})_2)^-$  in *n*-propyl acetate obtained at pump/probe delay times of 5, 10, 15, 20, 25, 30, 40, 50, 75 and 200 ps. The inset shows the monoexponential decay of the transient absorption of the free base chlorin anion at 750 nm.

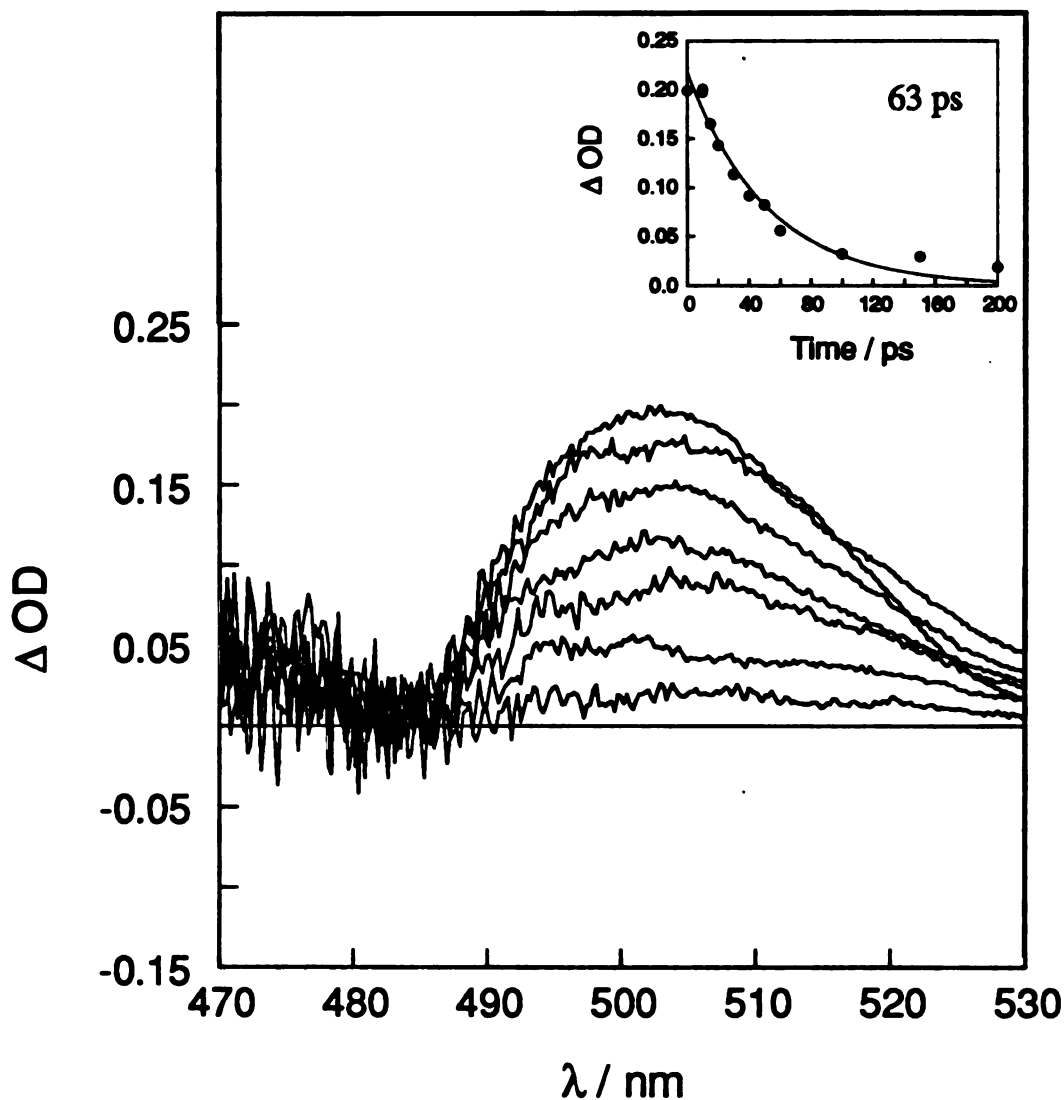


**Figure 32.** Picosecond transient absorption spectra of the  $\text{Zn}^+ \text{—} \text{H}_2(\text{C} \equiv \text{CN})_2^-$  charge separated state *n*-butyl acetate at 0, 20, 30, 40, 60, 100 and 1000 ns after the 6 ps 575 nm excitation pulse. The transient absorption at 502 nm decays according to unimolecular kinetics with a rate constant  $1.6 \times 10^{10} \text{ s}^{-1}$ , as shown by the inset.



illustrated by the transient absorption spectrum of  $\text{Zn—H}_2(=\text{C}(\text{CN})_2)$  in acetone as shown in Figure 33.

Many spectral features of the  $\text{Zn—H}_2(=\text{C}(\text{CN})_2)$  system are retained in the picosecond transient absorption spectrum of  $\text{Zn—Cu}(=\text{C}(\text{CN})_2)$ , which is shown in Figure 34, in *n*-propyl acetate. Excitation of  $\text{Zn—Cu}(=\text{C}(\text{CN})_2)$  at 580 nm populates the predominantly Zn porphyrin based  $^1\pi\pi^*$  manifold producing the  $\text{Zn}^+—\text{Cu}(=\text{C}(\text{CN})_2)^-$  charge-separated state, which is characterized by the sum of the absorptions of the Zn-porphyrin cation and Cu-chlorin anion at 650 and 725-800 nm, respectively, and the strong bleaching contribution from the Cu-chlorin  $Q_y$  ground state absorption at 695 nm. The absorption profile of the charge-separated state in the 650-800 nm region at zero pump/probe delay time bears strong resemblance to that observed for  $\text{Zn}^+—\text{H}_2(=\text{C}(\text{CN})_2)^-$ , as described previously. This derives in part from the strong similarity between the ground state absorption spectra of these particular dimers. The transient absorption spectrum in the 450–600 nm region shows a weak bleaching at 475 nm and a strong excited state absorption profile between 500 and 575 nm. Interestingly, the Zn-porphyrin cation radical transient absorption typically observed at 450 nm<sup>122</sup> is dominated by the strong bleach of the Cu-chlorin bands at 475 nm. Consequently, a weak bleaching feature, with a maximum at 475 nm, is observed in the blue spectral region usually characterized by the Zn-porphyrin cation. Associated with the initial decay of the absorption profile is a redshift of the peak maximum between 500–530 nm (Figure 35), which signifies the depopulation of the charge-separated state. The rate constants for the decay of this feature were determined from the maximum of the absorption profile as a function of time and not simply from the decay of the absorption at a given

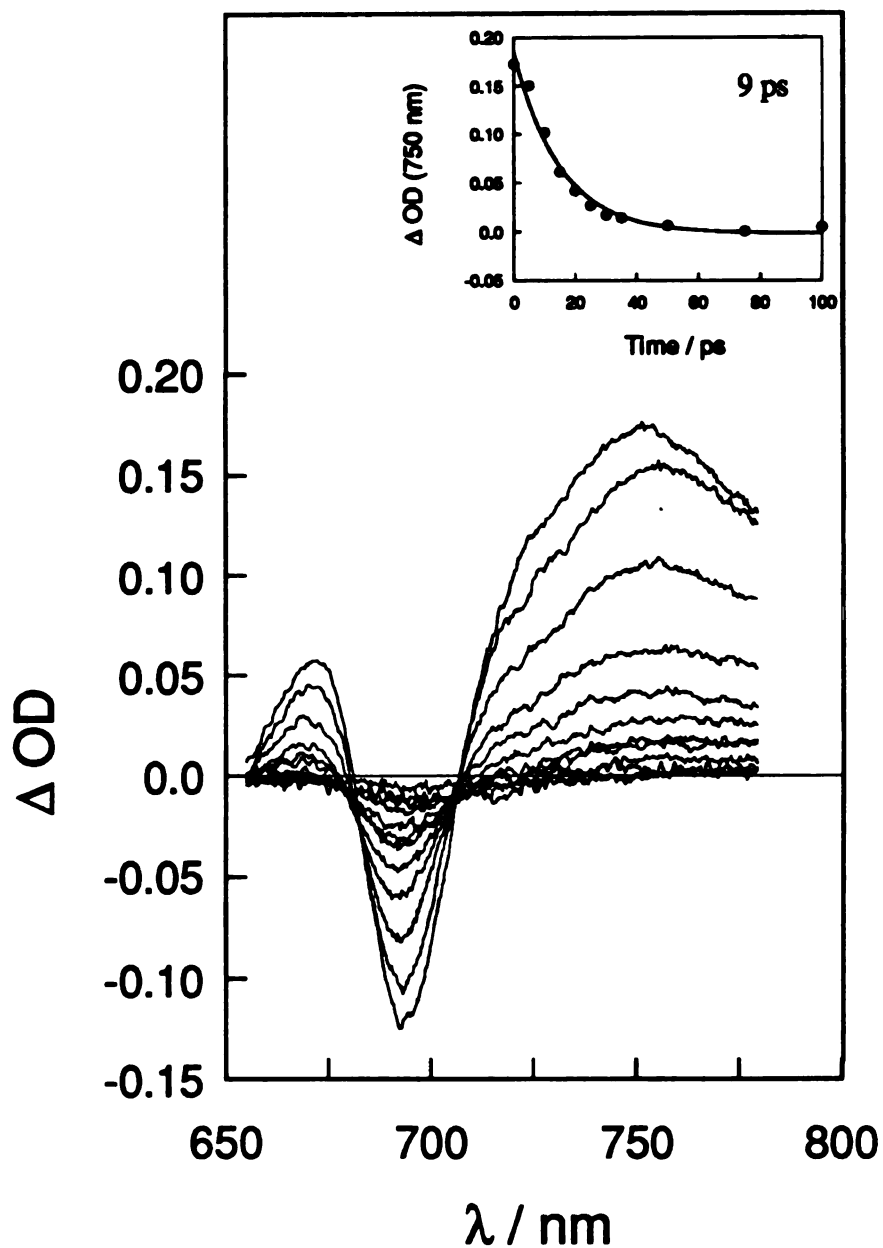


**Figure 33.** Picosecond transient absorption spectra of  $\text{Zn}^+ - \text{H}_2(\text{=C}(\text{CN})_2)^-$  in acetone obtained at pump/probe delay times of 0, 5, 10, 15, 20, 25, 30, 35, 50, 75 and 100 ps. The inset shows the monoexponential decay of the transient absorption of the free base chlorin anion at 750 nm.

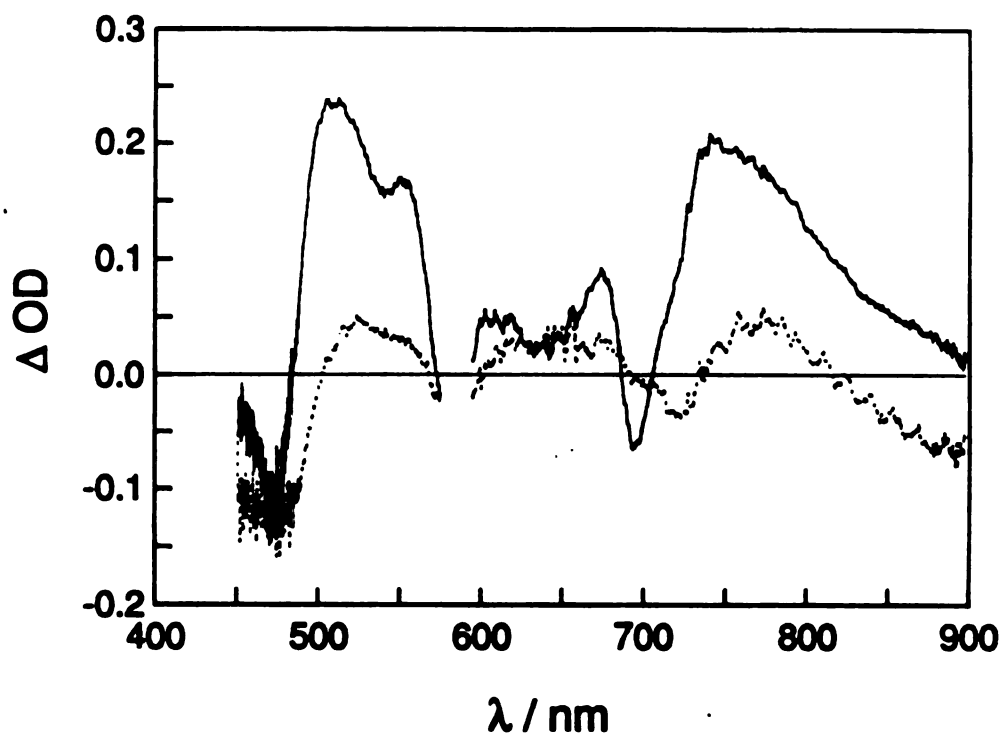


**Figure 34.** Transient absorption spectrum of  $\text{Zn—Cu(=C(CN)}_2\text{)}$  in *n*-propyl acetate following 6 ps excitation at 580 nm. The sample was prepared at a concentration of  $5 \times 10^{-4}$  M in a 2 mm quartz cuvette. Spectra are displayed at 15 ps (solid) and 5 ns (dashed).

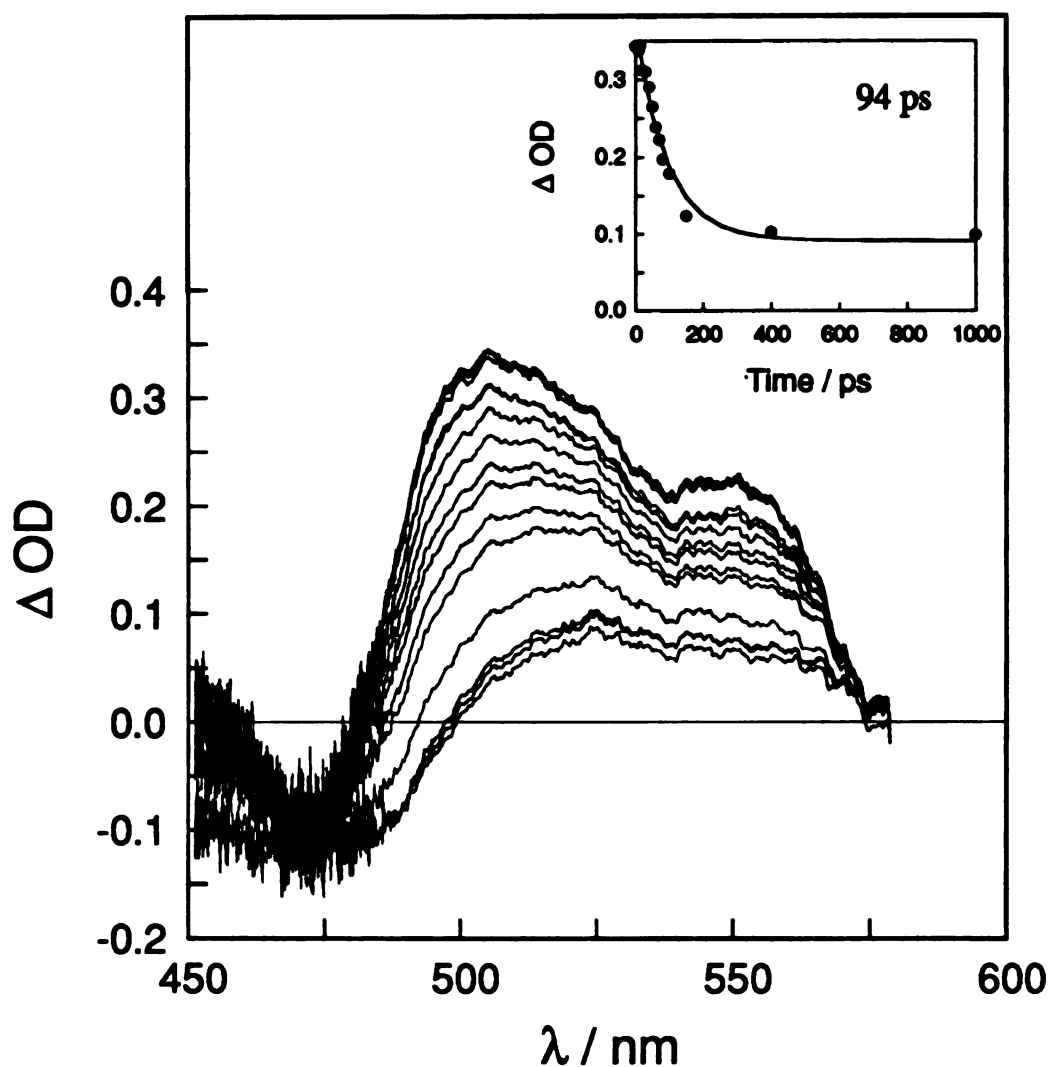


**Figure 35.** Time evolution of the transient absorption of Zn—Cu(=C(CN)<sub>2</sub>) in degassed *n*-propyl acetate at 0, 5, 10, 15, 20, 30, 40, 50, 60, 70, 80, 100, 150, 400, 1000 and 5000 ps following 580 nm excitation. Samples were prepared in 2 mm quartz cuvettes at concentrations of  $5 \times 10^{-5}$  M. The inset shows the biexponential fit to the decay of the charge separated state, and the characteristic lifetime.

wavelength. The residual transient absorption profile present following the decay of the charge-separated state lives for tens of nanoseconds in all solvents and decays with a rate constant of  $1.67 \times 10^7 \text{ s}^{-1}$  in *n*-propyl acetate at 530 nm.

The absorption profile in the 600-800 nm region also shows the presence of a transient at long times. As shown in Figure 36, a dip in the transient profile is observed at 730 nm immediately after excitation. The feature is largely concealed by the strong absorption of the Cu-chlorin radical anion at 770 nm at early times but becomes clearly apparent as the charge-separated state is depopulated. The energy of the bleach in the transient spectrum is coincident with the shoulder on the low energy side of the  $Q_y$  band in the ground state absorption spectrum. The transition responsible for this 730-nm absorption feature in the ground state and bleach in the excited state is unique to the dimeric species, neither appearing in the ground state nor the transient difference spectra of Zn-porphyrin or Cu-chlorin monomers as shown in Figure 37. However, the similarity between the long-lived transient absorption spectrum of Zn—Cu(=C(CN)<sub>2</sub>) and the Cu-chlorin monomer between 500–600 nm suggests that population of the Cu-chlorin excited state manifold within the dimer persists for >10 ns. This postulate is supported by the comparable transient absorption decay rate constants of the long-lived Zn—Cu(=C(CN)<sub>2</sub>) transient species at 530 nm ( $1.67 \times 10^7 \text{ s}^{-1}$ ) and 730 nm ( $3.03 \times 10^7 \text{ s}^{-1}$ ) (Figure 38) to the values of  $1.41 \times 10^7 \text{ s}^{-1}$  at 530 nm and  $1.16 \times 10^7 \text{ s}^{-1}$  at 730 nm (Figure 39) obtained for the Cu-chlorin monomer in *n*-propyl acetate by nanosecond transient absorption measurements. Unlike the Mg—H<sub>2</sub> or Zn—H<sub>2</sub>(=O) heterodimers, this long-lived transient is not related to an emissive excited state. The emission quantum yield of

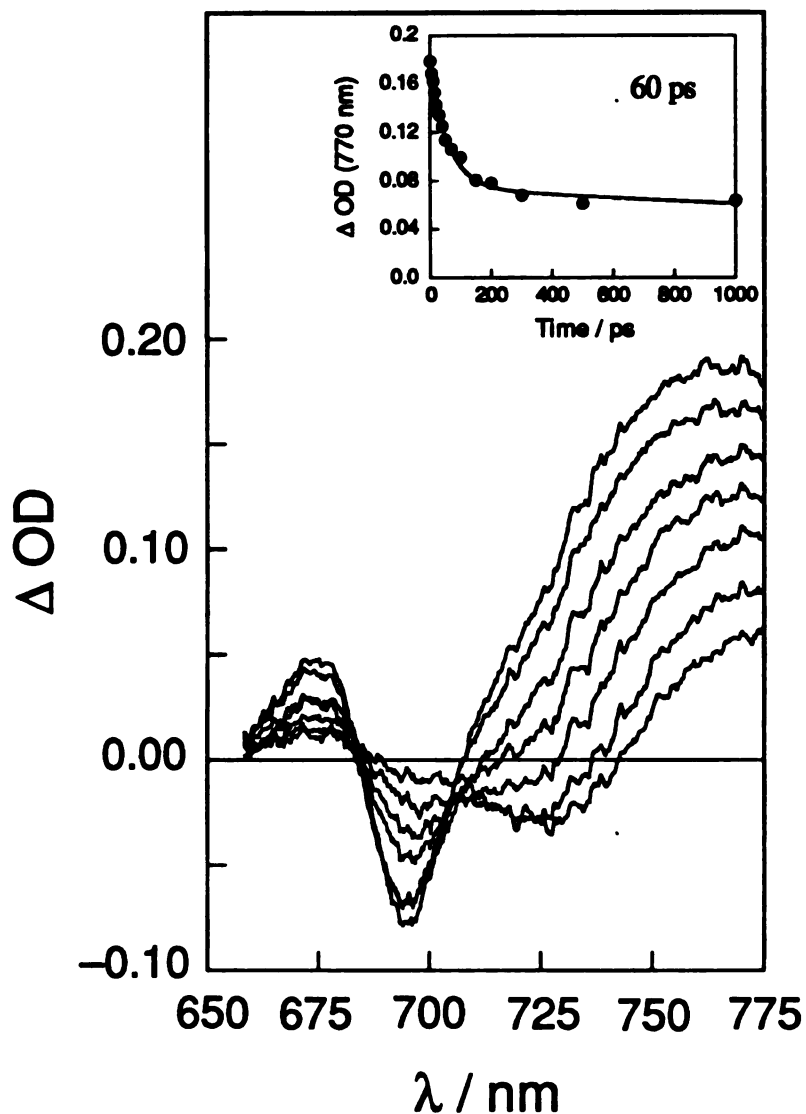


**Figure 36.** Time dependent transient absorption spectra of  $\text{Zn}^+—\text{Cu}(=\text{C}(\text{CN})_2)^-$  in *n*-propyl acetate at pump/probe delay times of 0, 10, 20, 40, 70, 150 and 1000 ps. The inset shows the biexponential decay of the transient absorption of the Cu chlorin anion at 770 nm.

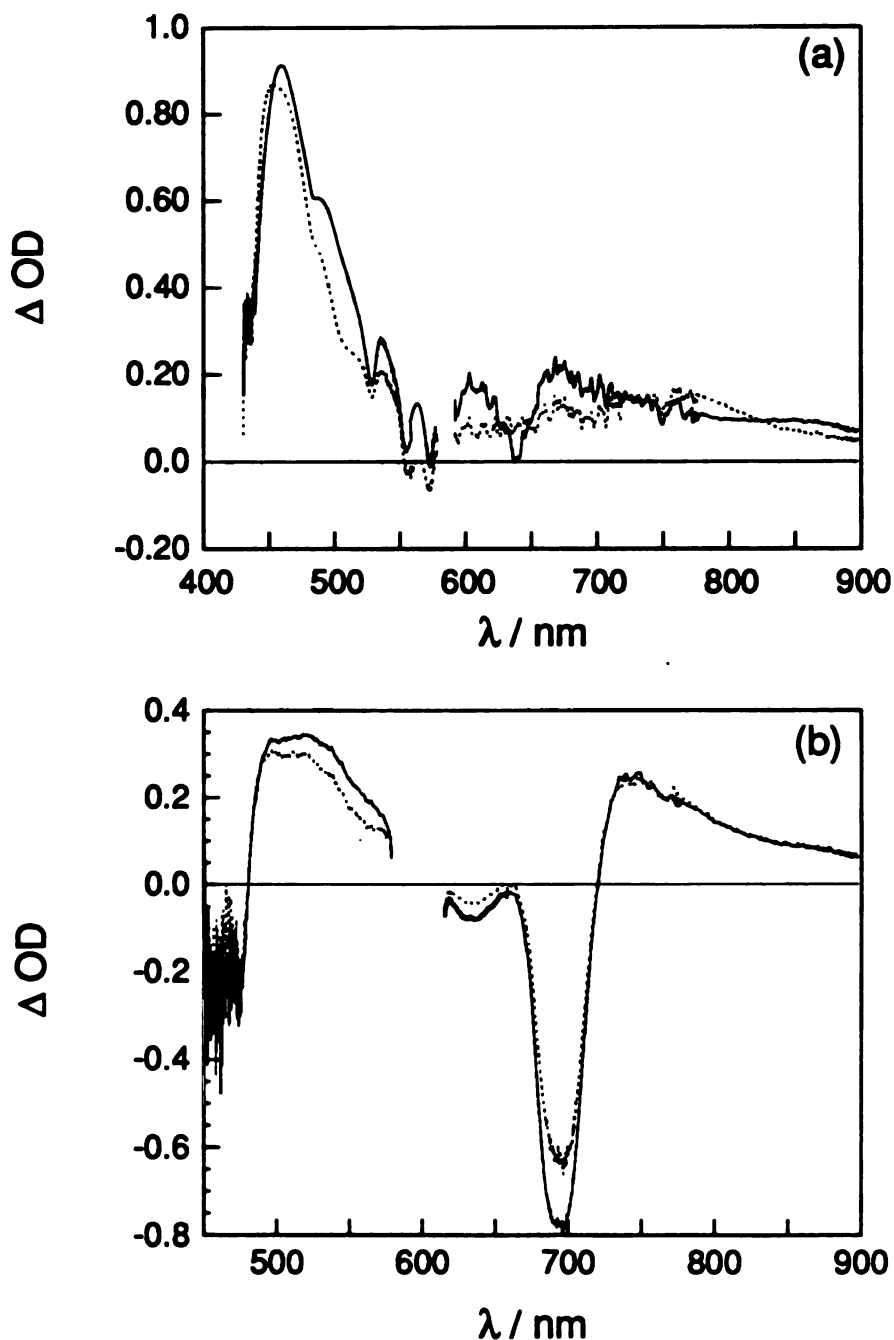


**Figure 37.** Transient absorption spectra of the (a) Zn-porphyrin and (b) Cu dicyanomethide chlorin subunit at 15 ps (solid) and 5 ns (dashed) in *n*-propyl acetate following 6 ps excitation at 575 nm. (Spectra of the Zn-porphyrin are repeated for convenience.) Samples were prepared at  $\sim 1$  mM concentrations in 2 mm quartz cells.

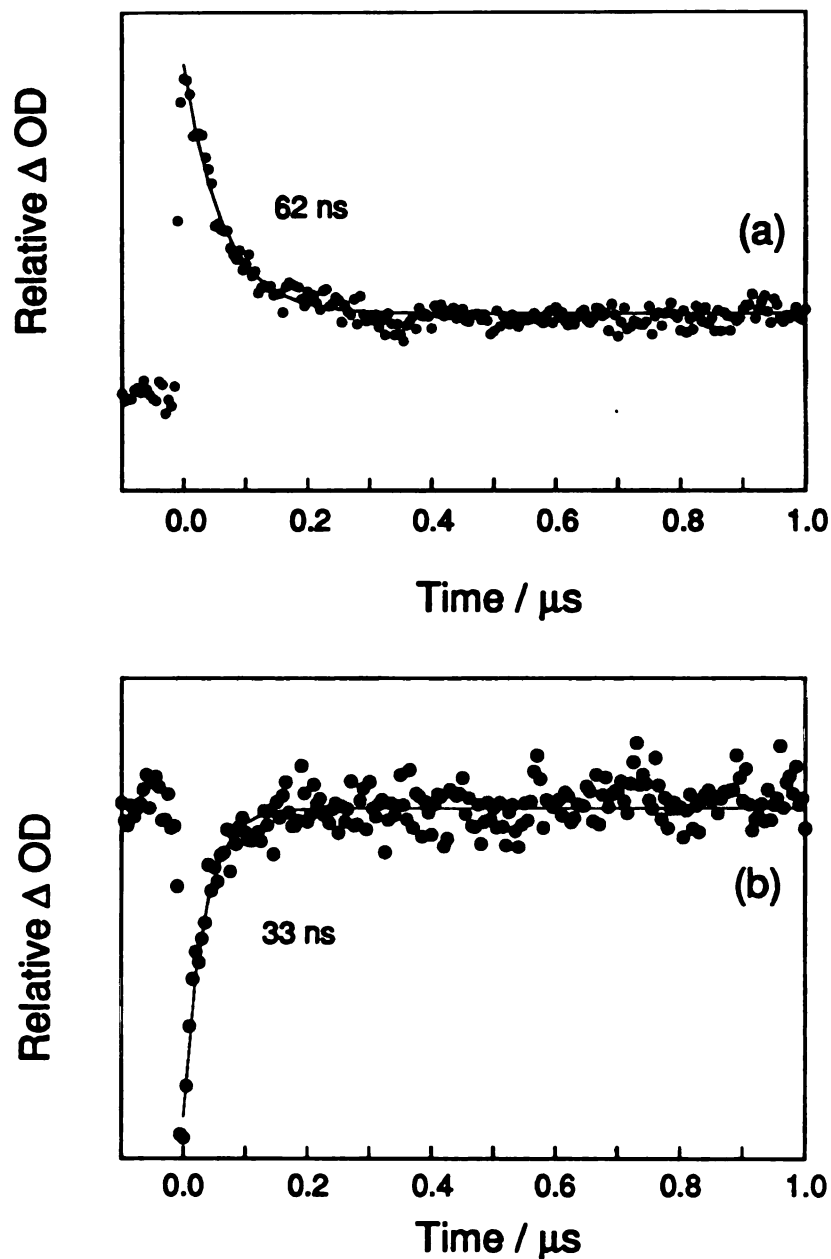


**Figure 38.** Decay of the long-lived Zn—Cu(=C(CN)<sub>2</sub>) transient absorption spectrum in *n*-propyl acetate at (a) 530 nm and (b) 730 nm. Samples ( $5 \times 10^{-4}$  M) were excited with a 580-nm, 10 ns pulse. The residual absorption in (a) is assigned to population of the  $^3(\pi\pi^*)$  state of the Zn-porphyrin because it is efficiently quenched by addition of O<sub>2</sub> to the sample.



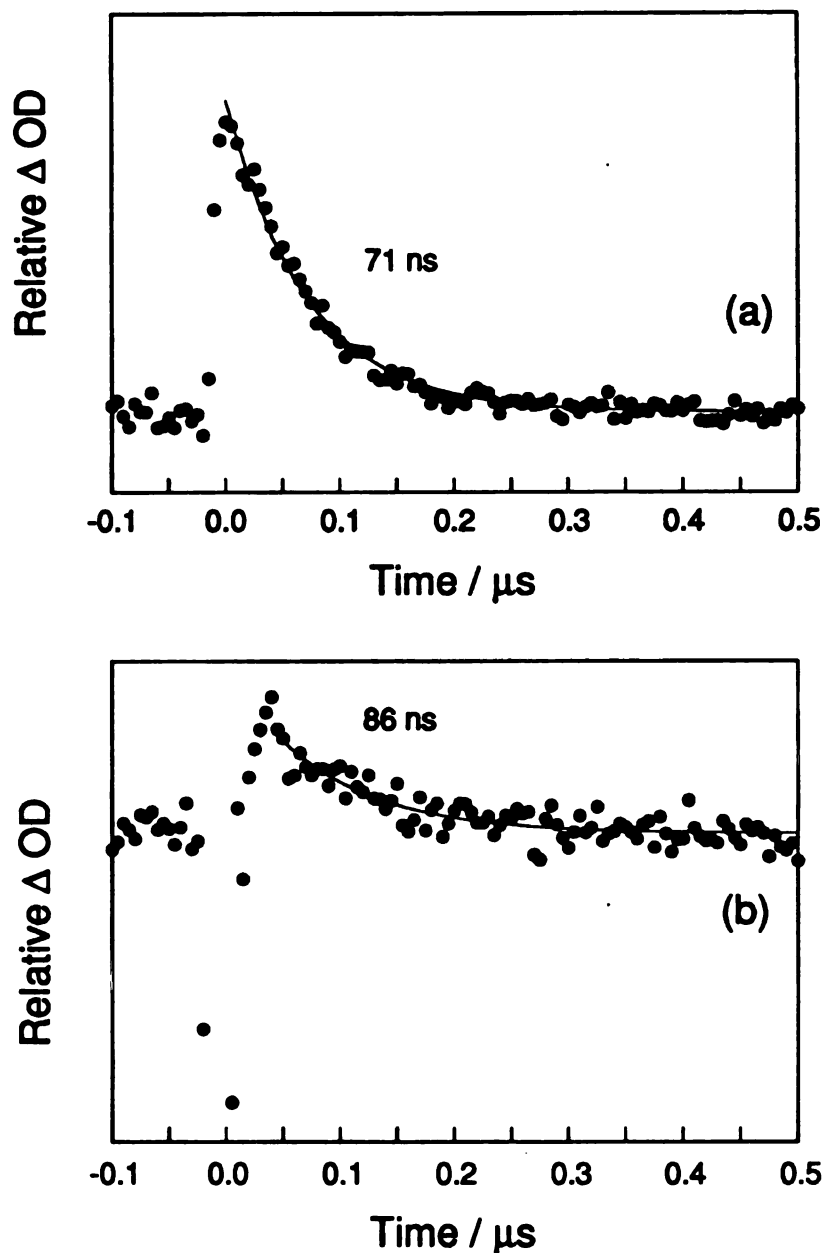


**Figure 39.** Decay of the long-lived Cu(=C(CN)<sub>2</sub>) transient absorption spectrum in *n*-propyl acetate at (a) 530 nm and (b) 730 nm following sample excitation at 580 nm with a 10 ns pulse. Transient absorption were obtained at sample concentrations of  $5 \times 10^{-4}$  M in a 2 mm cell. The lifetimes derived from these monoexponential fits are labeled appropriately. The negative signal at 0 μs in (b) is the result of stimulated emission from a trace amount of the free base complex.

$\text{Zn—Cu(=C(CN)}_2\text{)}$  is very small owing to the well established ability of the  $d^9$  Cu(II) macrocycle to nonradiatively dissipate excited state energy,<sup>139-141</sup> in addition to the appreciable driving force for charge separation. Inasmuch as the transient is specific to the Cu(II) chlorin, it is tempting to attribute the long-lived transient to the well-known tripdouplet or tripquartet states localized on the Cu-chlorin ring.<sup>150</sup> However the oscillator strengths of these transitions are weak, and they are seldom observed in ground state absorption spectra. The transient bleaching signal corresponding to the ground state absorption at 730 nm persists long after the decay of the ion pair. Our observation of a long-lived transient at 730 nm in *n*-propyl acetate has precedence in the transient spectroscopy of other Cu-porphyrin<sup>126,139-141</sup> and Cu-chlorin<sup>151</sup> complexes, yet the nature of the excited state responsible for these long-lived species remains ill-defined. These kinetic and spectroscopic trends are maintained in all solvents, as evidenced by the decay of the transient absorption spectra of  $\text{Zn—Cu(=C(CN)}_2\text{)}$  in acetone shown in Figures 40 and 41.

The decay of the absorptions of the Cu-chlorin anion at 510/550 nm and 770 nm, and the  $Q_y$  bleach at 695 nm, exhibit biexponential kinetics owing to the presence of the long-lived transient. We find that these absorptions of the charge-separated ion-pair all decay on similar time-scales. The CR rate constants, which range from  $4.55 \times 10^{10} \text{ s}^{-1}$  in *n*-propionitrile to  $1.02 \times 10^{10} \text{ s}^{-1}$  in *n*-butyl acetate, are comparable to those observed for the decay of the  $\text{Zn}^+ \text{—H}_2(\text{=C(CN)}_2)^-$  in the same solvent series. This behavior is not surprising, given that the driving forces for the CR step involving the  $\text{Zn}^+ \text{—H}_2(\text{=C(CN)}_2)^-$  and  $\text{Zn}^+ \text{—Cu(=C(CN)}_2)^-$  charge-separated states are nearly equivalent.

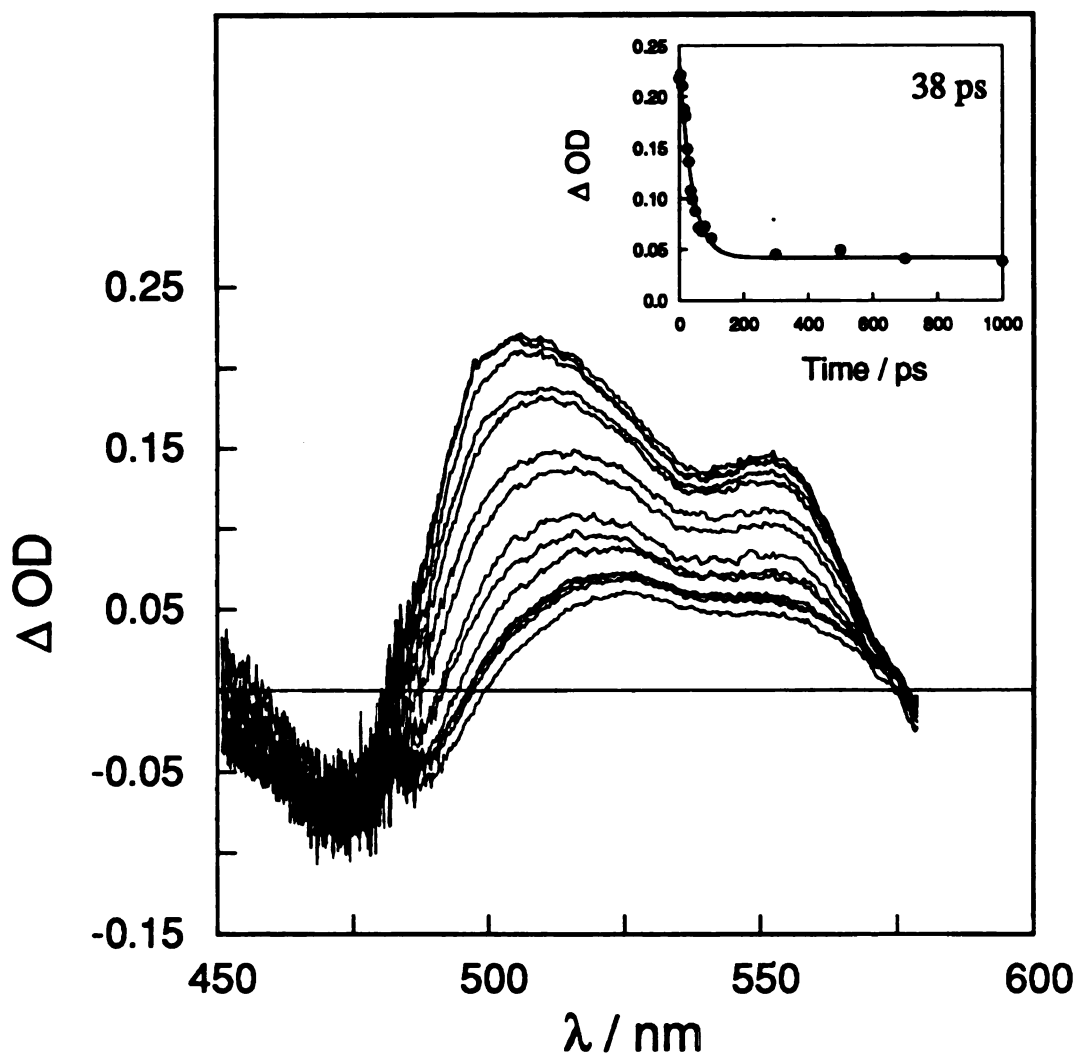


**Figure 40.** Picosecond transient absorption spectra of the  $\text{Zn}^+ - \text{Cu}(\text{C}\equiv\text{CN})_2^-$  charge separated state in acetone at 0, 5, 10, 15, 20, 25, 30, 35, 40, 50, 60, 70, 80 and 100 ps after the 6 ps 580 nm excitation pulse. The transient absorption at the peak maximum between 510-530 nm decays biexponentially as shown by the inset. The lifetime of the charge transfer state is 38 ps.

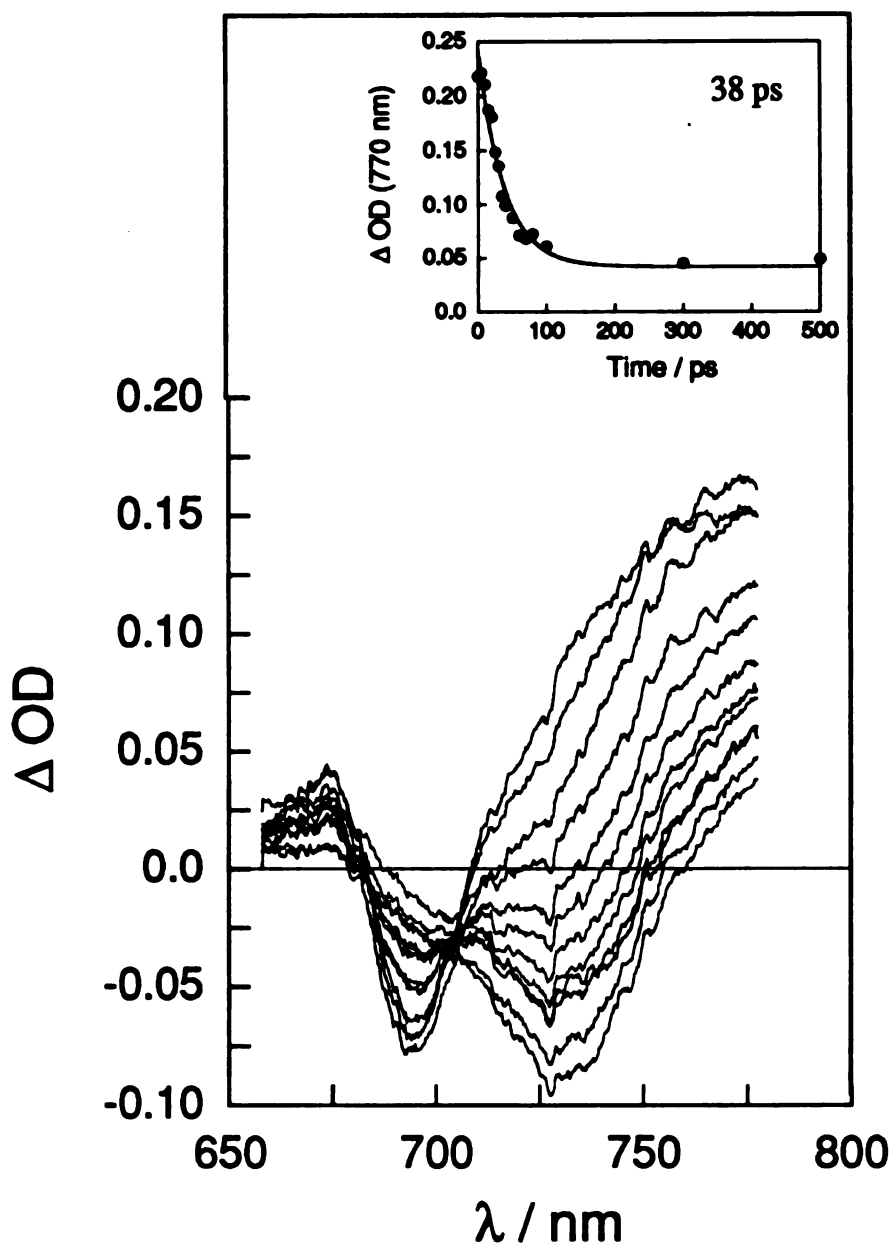


**Figure 41.** The time-dependence of the picosecond transient absorption spectrum of the  $\text{Zn}^+ - \text{Cu}(=\text{C}(\text{CN})_2)^-$  charge separated state in acetone. Spectra are shown at pump/probe delay times of 0, 10, 15, 20, 25, 30, 35, 40, 50, 60, 70, 80 and 100 ps. The biexponential decay of the transient absorption of the Cu-chlorin anion at 770 nm is shown as an inset.

#### 4. Solvent Dynamics

The CR rate constants for Zn—Cu(=C(CN)<sub>2</sub>) and Zn—H<sub>2</sub>(=C(CN)<sub>2</sub>) exhibit a pronounced solvent dependence, but the disparate behavior of these rate constants across different solvents observed in for the Mg—H<sub>2</sub> diporphyrin system is minimized. Figures 42 and 43 plot the observed rate constant for charge recombination vs the inverse of the solvent relaxation time  $\tau_s$ , for Zn—Cu(=C(CN)<sub>2</sub>) and Zn—H<sub>2</sub>(=C(CN)<sub>2</sub>), respectively. The CR rate constants for Zn—Cu(=C(CN)<sub>2</sub>) depend linearly on  $1/\tau_s$  for the non-nitrogen donor solvents; within the nitrogen donor solvent series, a different linear dependence is observed. In all solvents, population of a nonemissive transient is coincident with charge separation, but the slow decay rate constant of this state allows dynamics information to be extracted without interference. For Zn—H<sub>2</sub>(=C(CN)<sub>2</sub>), the linear relationship between  $k_{\text{obs}}(\text{CR})$  and  $1/\tau_s$  is independent of the solvent series, coincident with the absence of a long-lived transient absorption. This result is quite remarkable in view of the large differences in solvent properties (dielectric constant, polarity, etc.) across nitriles, acetates, alcohols, ketones, and halocarbons.

#### C. Discussion

Disparate dynamics behavior for different solvent series should disappear as the CR reaction approaches an activationless limit. It was with this motivation that we undertook studies on the Zn—Cu(=C(CN)<sub>2</sub>). Introduction of the dicyanomethide group on the porphyrin ring decreases

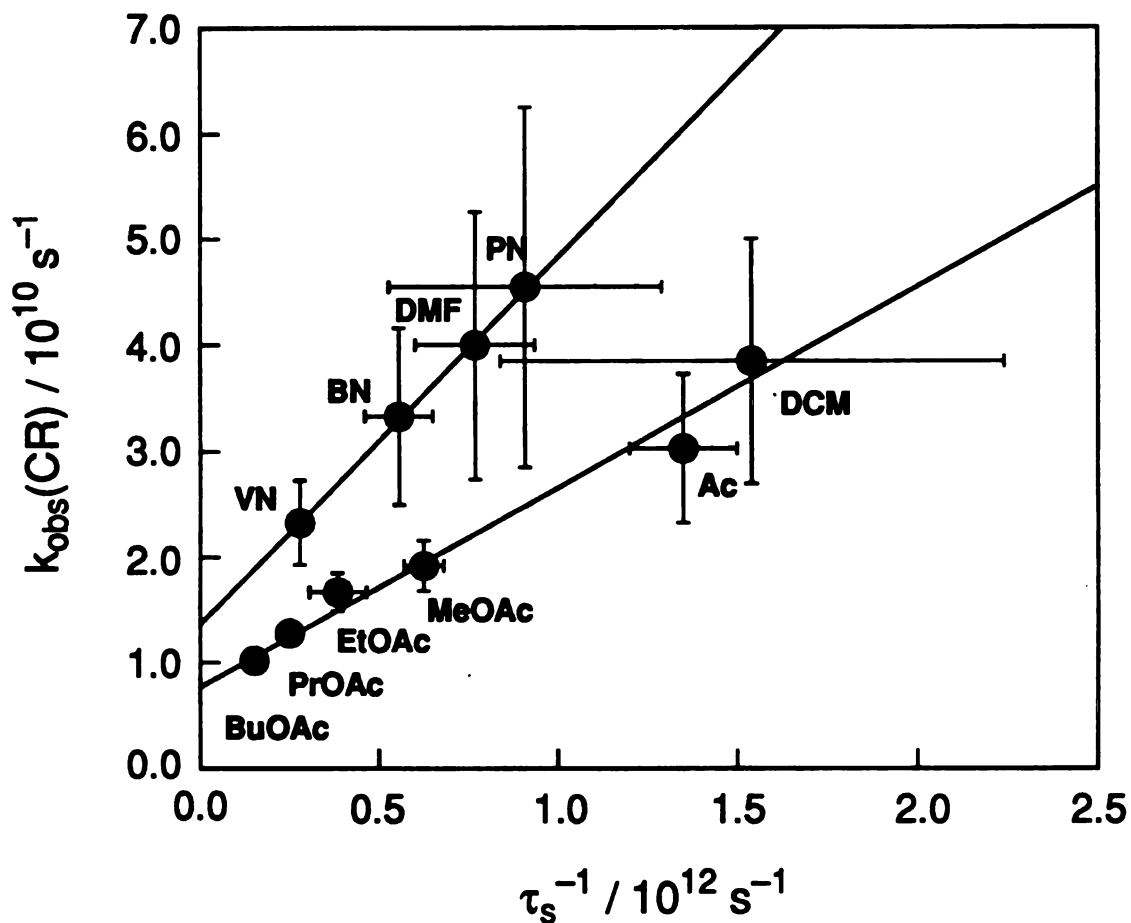


**Figure 42.** Dependence of the CR rate constants for the  $\text{Zn}^+ - \text{Cu}(\text{=C}(\text{CN})_2)^-$  charge separated state on the inverse of the solvent relaxation time ( $\tau_s$ ). Solvents compared include dichloromethane (DCM) acetone (Ac), N,N-dimethyl formamide (DMF), propionitrile (PN), *n*-butyronitrile (BN), *n*-valeronitrile (VN) and methyl, ethyl, *n*-propyl, and *n*-butyl acetates (MeOAc, EtOAc, PrOAc, BuOAc, respectively).  $\tau_s$  values taken from ref. 76.

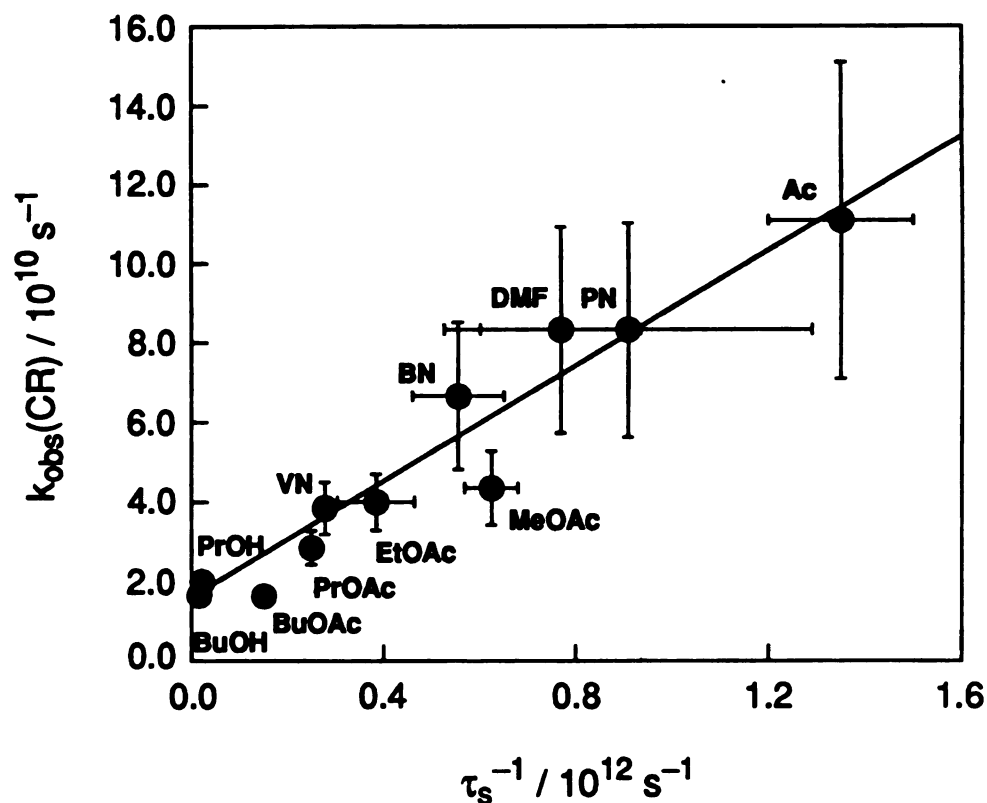


**Figure 43.** Plot of the observed CR rate constants of  $\text{Zn}^+ - \text{H}_2(=\text{C}(\text{CN})_2)^-$  in acetone (Ac), N,N-dimethyl formamide (DMF), propionitrile (PN), *n*-butyronitrile (BN), *n*-valeronitrile (VN) and methyl, ethyl, *n*-propyl, and *n*-butyl acetates (MeOAc, EtOAc, PrOAc, BuOAc, respectively) as well as 1-propanol (PrOH) and 1-butanol (BuOH) vs. the reciprocal of the microscopic relaxation times (taken from ref. 76).

the magnitude of the free energy for CR by  $\geq 0.3$  V with respect to  $\text{Mg}—\text{H}_2$ , thereby lowering the diffusional activation barrier in the inverted region. In the context of eqs 1.1 and 1.2, by reducing the driving force of the CR reaction, we have made the reaction less inverted and the contributions of  $\Delta G^*$  to the observed rate constant will be minimized. Thus contributions of static solvent effects to the dynamically-controlled CR reaction are attenuated as the activationless regime is approached and the same linear dependence of the CR electron transfer rate on dynamics is expected, regardless of the solvent series. This is observed in part for the solvent dependence of the CR kinetics for  $\text{Zn}^+—\text{Cu}(=\text{C}(\text{CN})_2)^-$ . Figure 42 reveals that the CR rate constants depend linearly on  $1/\tau_s$  for the non-nitrogen donor solvents. In the presence of nitrogen donor ligands, copper porphyrins form five-coordinate complexes in both ground<sup>139</sup> and excited states.<sup>140</sup> A different linear dependence for the nitrogen donor solvents suggests that an increased activation energy is incurred from solvent coordination to Cu(II) ion during the CR event. Within this framework, it stands to reason that removal of the Cu(II) from the chlorin macrocycle would eliminate this added contribution to the activation energy for CR. In this case, we would expect the CR kinetics for  $\text{Zn}—\text{H}_2(=\text{C}(\text{CN})_2)$  to approach the simple relation  $k_{\text{obs}}(\text{CR}) \cong 1/\tau_s$  regardless of the solvent in which the CR reaction is performed.<sup>135</sup> This is observed in Figure 43.

Correlation of  $k_{\text{obs}}(\text{CR})$  with  $1/\tau_s$  for low barrier ET reactions, as described by Bixon and Jortner, demonstrates that the CR process in  $\text{Zn}—\text{Cu}(=\text{C}(\text{CN})_2)$  and  $\text{Zn}—\text{H}_2(=\text{C}(\text{CN})_2)$  are not truly activationless. In this case, no dependence of the CR rate constant on solvent dynamics would be observed.<sup>71</sup> By applying estimates of the outer-sphere reorganization energy for fixed-distance, porphyrin-porphyrin D—A



complexes ( $\lambda_0 \cong 0.8-1.5$  eV),<sup>133</sup> the CR reaction for  $\text{Zn—Cu(=C(CN)}_2)$  and  $\text{Zn—H}_2(\text{=C(CN)}_2)$  is determined to lie near the activationless limit, but remains in the inverted region. This is further substantiated by the magnitudes of the CR rate constants being slightly greater than the solvent relaxation time, indicating that this process is not exclusively limited by  $1/\tau_s$ . The strict correlation of  $k_{\text{obs}}(\text{CR})$  with  $1/\tau_s$  for  $\text{Zn—H}_2(\text{=C(CN)}_2)$  in all solvents, demonstrates that low barrier reactions in the inverted region can be an opportune window for viewing solvent dynamics effects on ET reactions.

## CHAPTER V

### CONCLUDING REMARKS

With the exception of the correlation between  $k_{\text{obs}}(\text{CR})$  and  $1/\tau_s$  (Figure 44), it is difficult to assess whether the cofacial heterodimers accurately represent the strong-coupling limit of the consecutive reaction formalism described by eqs 1.5-1.7. As this question has not been addressed experimentally, determination of the electronic coupling and the nonadiabatic ET rate (eq 1.6) have been made computationally. From the driving force for the CR reaction of  $\text{Mg}-\text{H}_2$  and  $\text{Zn}-\text{H}_2(=\text{C}(\text{CN})_2)$ , and reasonable estimates of the electronic coupling ( $|V| = 200 \text{ cm}^{-1}$ ) as well as the reorganization energy ( $\lambda = 1.08 \text{ eV}$ ), the experimentally determined CR rate constants (Table VII) can be accurately reproduced for solvents of a given  $\tau_s$ . However, the value of the electronic coupling is not unique as a range of energies ( $150\text{-}250 \text{ cm}^{-1}$ ) will satisfy eq 1.5 for a given  $\lambda$ ,  $\Delta G^\circ$  and  $\tau_s$ . Although the breadth of  $|V|$  is large, the values remain in the strong-coupling limit. This claim is substantiated by the ratios of  $k_{\text{ET}}$  to  $k_{\text{D}}$  from eq 1.6 and 1.7 for the solvents given in Figure 44. For  $\text{Zn}-\text{H}_2(=\text{C}(\text{CN})_2)$   $k_{\text{ET}}/k_{\text{D}}$  spans the range 8-75, while the scope of values for  $\text{Mg}-\text{H}_2$  is only slightly smaller ( $k_{\text{ET}}/k_{\text{D}} \cong 5\text{-}45$ ), as expected for strongly coupled systems.

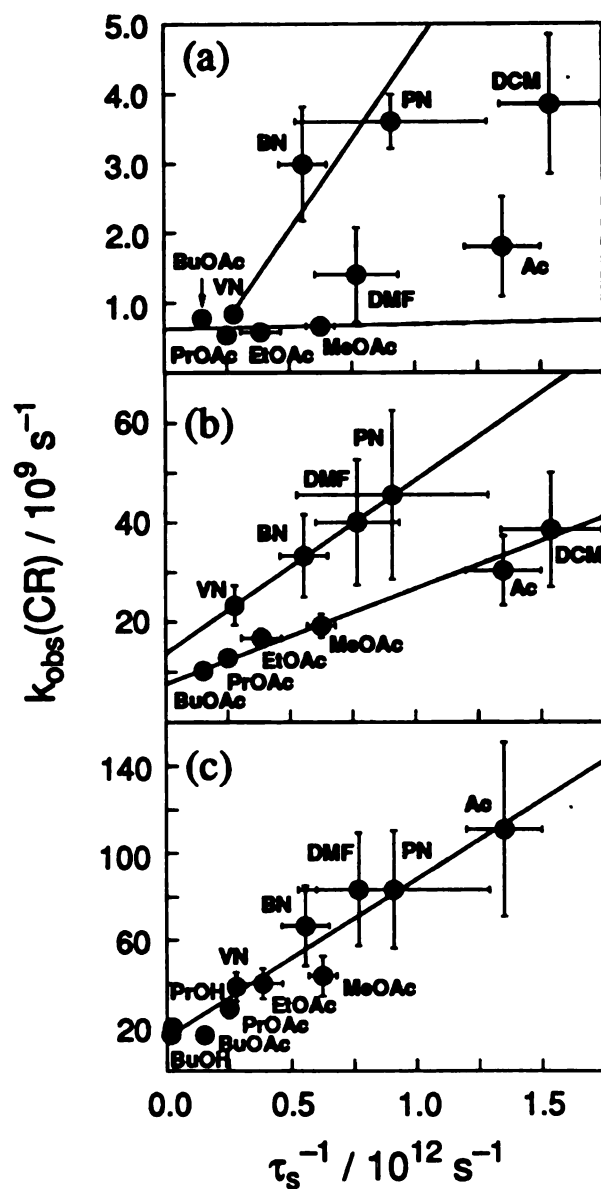
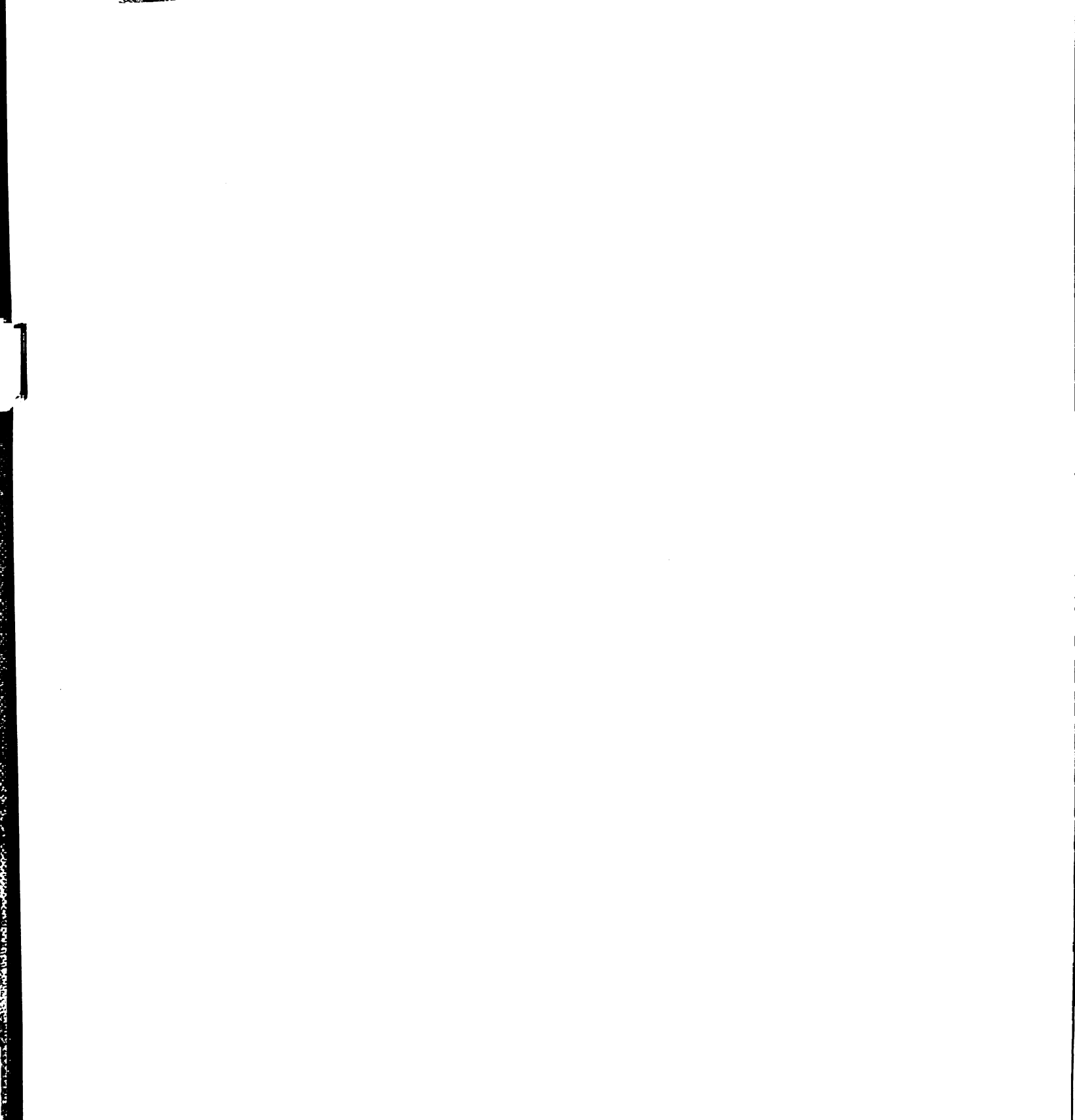


**Figure 44.** Cumulative plot of the observed CR rate constants of (a)  $\text{Mg}^+ - \text{H}_2^-$ , (b)  $\text{Zn}^+ - \text{Cu}(=\text{C}(\text{CN})_2)^-$ , and (c)  $\text{Zn}^+ - \text{H}_2(=\text{C}(\text{CN})_2)^-$  vs. the reciprocal of the microscopic relaxation times of dichloromethane (DCM), acetone (Ac), *N,N*-dimethyl formamide (DMF), propionitrile (PN), *n*-butyronitrile (BN), *n*-valeronitrile (VN) and methyl, ethyl, *n*-propyl, and *n*-butyl acetates (MeOAc, EtOAc, PrOAc, BuOAc, respectively) as well as 1-propanol (PrOH) and 1-butanol (BuOH).

**Table VII.** Comparison of Solvent Dependence of the Charge Recombination Rate Constants of Mg—H<sub>2</sub>, Zn—Cu(=C(CN)<sub>2</sub>) and Zn—H<sub>2</sub>(=C(CN)<sub>2</sub>)

| Solvent <sup>a</sup> | Mg—H <sub>2</sub> | $k_{\text{obs}}(\text{CR}) / 10^9$ |  |
|----------------------|-------------------|------------------------------------|--|
|                      |                   | Zn—Cu(=C(CN) <sub>2</sub> )        | Zn—H <sub>2</sub> (=C(CN) <sub>2</sub> ) |
| DCM                  | 3.85              | 38.5                               | 50.0 <sup>b</sup>                        |
| Ac                   | 1.80              | 30.3                               | 111.0                                    |
| DMF                  | 1.40              | 40.0                               | 83.3                                     |
| PN                   | 3.86              | 45.5                               | 83.3                                     |
| BN                   | 2.99              | 33.3                               | 66.6                                     |
| VN                   | 0.84              | 23.3                               | 38.5                                     |
| MeOAc                | 0.66              | 19.2                               | 43.5                                     |
| EtOAc                | 0.58              | 16.7                               | 40.0                                     |
| PrOAc                | 0.84              | 12.8                               | 28.6                                     |
| BuOAc                | 0.66              | 10.2                               | 16.4                                     |
| PrOH                 |                   |                                    | 20.0                                     |
| BuOH                 |                   |                                    | 16.6                                     |

<sup>a</sup>Solvents are abbreviated as in Figure 44. <sup>b</sup>Value not included in Figure 44 due to low confidence in the measurement.



This indicates that  $k_{\text{obs}}(\text{CR})$  is strictly rate limited by  $k_{\text{D}}$ , as described by the consecutive reaction model of eq 1.5-1.7, and that changes in the CR rate constant between the Mg—H<sub>2</sub> diporphyrin and the dicyanomethide porphyrin-chlorin systems are accounted for by the change in the driving force for the reaction. Although these calculations are consistent with the data in Figure 44, some caution must be exercised in relying on the values  $\lambda$ ,  $\Delta G^\circ$  and  $|V|$ . Specifically, variations in  $\lambda$  or  $\Delta G^\circ$  of 0.1 eV can change the calculated values of  $k_{\text{obs}}(\text{CR})$  by an order of magnitude and therefore, many combinations of  $\lambda$ ,  $\Delta G^\circ$  and  $|V|$  exist that will provide adequate evaluation of eq 1.5-1.7. Nevertheless, the values given above are the most reasonable estimates of these parameters available and as such, support the use of the strong-coupling limit of the consecutive reaction scheme to investigate the role of solvent dynamics in ET.

Quantification of the above parameters would be worthy of future study as static contributions to the correlations shown in Figure 44 could be compensated for. Changes in the driving force of the CR reaction can be approximated by performing a strict solvent dependence of the redox potentials for the cofacial heterodimers. As  $\Delta G^\circ$  is not the only contributor to the barrier height, determination of the solvent dependence of the reorganization energy from a temperature dependence of the CR rate constant would also provide a better estimate of the magnitude of static solvent effects for media of different polarity. By investigating the CR rate constants of a series of the cofacial heterodimers linked by varying length side chains, accurate values for the electronic coupling could also be obtained, providing deeper insight into the applicability of the strong-coupling limit of the consecutive reaction formalism to ET in these systems. Furthermore, determination of the solvent dependence of the

forward ET rates would demonstrate the effects of solvent dynamics in the normal region ET and could have profound implications in lieu of Bixon and Jortner's recent results concerning the invariance of the ET rate on solvent dynamics in the activationless case.<sup>71</sup>

In conclusion, the CR reactions of the porphyrin-porphyrin and porphyrin-chlorin heterodimers described herein emphasize the ability to use activated ET in the inverted region to uncover the influence of solvent dynamics. The fact that CR rate constants in these dimers occurs in the inverted region allows us to reliably isolate solvent dynamics from static solvent effects.<sup>152</sup> Moreover, an intramolecular approach circumvents the solvent's role to govern precursor formation between reactants in bimolecular reactions.<sup>153</sup> An important result exemplified by these studies is that solvation dynamics may dominate the reactivity of electron transfer, even when the overall rate for the electron transfer reaction is slow because the rate constant  $k_D$  is an activated process. To this end, the overall ET reaction is gated by solvent dynamics. When this activation barrier is large, static contributions of the solvent to the electron transfer are also important, and dynamics contributions may be unambiguously observed only when these two effects are isolated. This may be accomplished by studying the inverted region ET in a homologous solvent series. Alternatively, reducing the activation barrier can provide a more transparent view of the solvent controlled adiabatic limit than do studies of more highly activated ET processes, as surface diffusion more clearly governs the overall ET rate constant. As the activation barrier for CR is diminished, the dependence of the electron transfer rate on static solvent parameters is minimized and the characteristic  $1/\tau_s$  dependence expected





for low barrier ET reactions involving strongly-coupled D—A complexes is observed.

Finally, our observations emphasize the important role that solvent can play in governing the rates of electron transfer in biological and chemical charge separating networks. In a static sense, the importance of solvent in mediating CS and CR kinetics by affecting the activation energy of electron transfer is well documented. Yet as shown here, the dynamics of solvation may dominate the reactivity of charge-separated states, even when the overall rate for the electron transfer reaction is slow.

## **LIST OF REFERENCES**

**LIST OF REFERENCES**

1. Lavoisier, A. L. (1789) *Traite Elementaire de Chimie*, 2nd Ed.; translated by R. Kerr: Edinburgh, 1793.
2. Gesner, C. *The Practise of the New and Old Phisicke*, Short; London, 1599, p. 23.
3. Priestley, J. *Phil. Trans. Roy. Soc. (London)* **1772**, 62, 147.
4. (a) Stryer, L. *Biochemistry* 3rd Ed.; W. H. Freeman and Co: New York, 1988. (b) Darnell, J.; Lodish, H.; Baltimore, D. *Molecular Cell Biology* 2nd Ed.; W. H. Freeman and Co: New York, 1990.
5. Deisenhofer, J.; Epp, O.; Miki, K.; Huber, R.; Michel, H. *J. Mol. Biol.* **1984**, 180, 385.
6. (a) Chang, C.-H.; Tiede, D. M.; Tang, J.; Norris, J. R.; Schiffer, M. *FEBS Lett.* **1986**, 205, 82. (b) Allen, J. P.; Feher, G.; Yeates, T. O.; Komiyama, H.; Rees, D. C. *Proc. Natl. Acad. Sci. U. S. A.* **1987**, 84, 6162.
7. Holten, D.; Kirmaier, C. *Photosynth. Res.* **1987**, 13, 225.
8. Hoff, A. *Photochem. Photobiol.* **1986**, 43, 727.
9. Martin, J.-L.; Breton, J.; Hoff, A.; Migus, A.; Antonetti, A. *Proc. Natl. Acad. Sci. U. S. A.* **1986**, 83, 957.

10. (a) Breton, J.; Martin, J.-L.; Migus, A.; Antonetti, A. *Proc. Natl. Acad. Sci. U. S. A.* **1986**, *83*, 5121. (b) Wasielewski, M. R.; Tiede, D. M. *FEBS Lett.* **1986**, *204*, 368.
11. (a) Holzapfel, W.; Finkele, U.; Kaiser, W.; Oesterheld, D.; Scheer, H.; Stilz, H. U.; Zinth, W. *Chem. Phys. Lett.* **1989**, *160*, 1. (b) Dressler, K.; Umlauf, E.; Schmidt, S.; Hamm, P.; Zinth, W.; Buchanan, S.; Michel, H. *Chem. Phys. Lett.* **1991**, *183*, 270.
12. Parson, W. W. *Ann. Rev. Biophys. Bioeng.* **1982**, *11*, 57.
13. Norris, J. R.; Uphaus, R. A.; Crespi, H. L.; Katz, J. J. *Proc. Natl. Acad. Sci. U. S. A.* **1971**, *68*, 625.
14. Wasielewski, M. R.; Fenton, J. M.; Govindjee. *Photosynth. Res.* **1987**, *12*, 181.
15. Petersen, J.; Stehlik, D.; Gast, P.; Thurnauer, M. *Photosynth. Res.* **1987**, *14*, 15.
16. Fenton, J. M.; Pellin, M. J.; Govindjee; Kaufman, K. J. *FEBS Lett.* **1979**, *100*, 1.
17. Wasielewski, M. R.; Johnson, D. G.; Seibert, M.; Govindjee. *Proc. Natl. Acad. Sci. U. S. A.* **1989**, *86*, 524.
18. Schatz, G. H.; Brock, H.; Holzwarth, A. R. *Proc. Natl. Acad. Sci. U. S. A.* **1987**, *84*, 8414.
19. Hansson, O.; Duranton, J.; Mathis, P. *Biochim. Biophys. Acta* **1988**, *932*, 91.
20. (a) Bowes, J. M.; Crofts, A. R. *Biochim. Biophys. Acta* **1980**, *590*, 373. (b) Robinson, H. H.; Crofts, A. R. *FEBS Lett.* **1983**, *153*, 221. (c) Crofts, A. R.; Wraight, C. A. *Biochim. Biophys. Acta* **1983**, *726*, 149.
21. Debus, R. J. *Biochim. Biophys. Acta* in press.

22. In *Protein Structure, Molecular and Electronic Reactivity*; Ausin, R.; Buhks, E.; Chance, B.; De Vault, D.; Dutton, P. L.; Frauenfelder, H.; Gol'danskii, V. I., Eds.; Springer-Verlag: New York, 1987.
23. Okamura, M. Y.; Feher, G. *Proc. Natl. Acad. Sci. U. S. A.* **1986**, *83*, 8152.
24. (a) Hopfield, J. J. *Proc. Natl. Acad. Sci. U. S. A.* **1974**, *71*, 3640. (b) Jortner, J. *J. Chem. Phys.* **1976**, *64*, 4860. (c) Sarai, A. *Biochim. Biophys. Acta* **1980**, *589*, 71. (d) Kakitani, T.; Kakitani, H. *Biochim. Biophys. Acta* **1981**, *635*, 498.
25. (a) Bowler, B. E.; Raphael, A. L.; Gray, H. B. *Progr. Inorg. Chem. U. S. A.* **1990**, *38*, 259. (b) Boxer, S. G. *Annu. Rev. Biophys. Chem.* **1990**, *19*, 267. (c) Huber, R. *Eur. J. Biochem. Int.* **1990**, *187*, 283.
26. (a) Peterson-Kennedy, S. E.; McGourty, J. L.; Ho, P. S.; Sutoris, C. J.; Liang, N.; Zemel, H.; Blough, N. V.; Zemel, H.; Margoliash, E.; Hoffman, B. M. *Coord. Chem. Rev.* **1985**, *65*, 125. (b) Gingrich, D. J.; Nocek, J. M.; Natan, M. J.; Hoffman, B. M. *J. Am. Chem. Soc.* **1987**, *109*, 7533. (c) Natan, M. J.; Hoffman, B. M. *J. Am. Chem. Soc.* **1989**, *111*, 6468.
27. Winkler, J. R.; Gray, H. B. *Chem. Rev.* **1992**, *92*, 369.
28. (a) Winkler, J. R.; Nocera, D. G.; Yocom, K. M.; Bordignon, E.; Gray, H. B. *Coord. Chem. Rev.* **1982**, *104*, 5798. (b) Nocera, D. G.; Winkler, J. R.; Yocom, K. M.; Bordignon, E.; Gray, H. B. *J. Am. Chem. Soc.* **1984**, *106*, 5145.
29. Meade, T. J.; Gray, H. B.; Winkler, J. R. *J. Am. Chem. Soc.* **1989**, *111*, 4353.

30. Churg, A. K.; Weiss, R. M.; Warshel, A.; Takano, T. *J. Phys. Chem.* **1983**, *87*, 1683.
31. (a) Beratan, D. N.; Betts, J. N.; Onuchic, J. N. *J. Phys. Chem.* **1992**, *96*, 2852. (b) Betts, J. N.; Beratan, D. N.; Onuchic, J. N. *J. Am. Chem. Soc.* **1992**, *114*, 4043. (c) Onuchic, J. N.; Beratan, D. N.; Winkler, J. R.; Gray, H. B. *Annu. Rev. Biophys. Biomol. Struct.* **1992**, *21*, 349.
32. Wuttke, D. S.; Bjerrum, M. J.; Winkler, J. R.; Gray, H. B. *Science* **1992**, *256*, 1007.
33. McLendon, G.; Hake, R. *Chem. Rev.* **1992**, *92*, 481.
34. Conklin, K. T.; McLendon, G. *J. Am. Chem. Soc.* **1988**, *110*, 3345.
35. Hazzard, J.; McLendon, G. L.; Cusanovich, M.; Tollin, G. *Biochem. Biophys. Res. Commun.* **1988**, *151*, 249.
36. McCammon, J. A.; Harvey, S. C. *Dynamics of Proteins and Nucleic Acids*; Cambridge University Press: Cambridge, 1987.
37. (a) Northrup, S. H.; Pear, M. R.; Morgan, J. D.; McCammon, J. A.; Karplus, M. *J. Mol. Biol.* **1981**, *153*, 1087. (b) Mao, B.; Pear, M. R.; McCammon, J. A.; Northrup, S. H. *Biopolymers* **1982**, *21*, 1979. (c) Morgan, J. D.; McCammon, J. A.; Northrup, S. H. *Biopolymers* **1983**, *22*, 1579. (d) Morgan, J. D.; McCammon, J. A.; Northrup, S. H. *Biopolymers* **1983**, *22*, 1579. (e) McCammon, J. *Reports on Progress in Physics* **1984**, *47*, 1.
38. Elber, R.; Karplus, M. A. *J. Am. Chem. Soc.* **1990**, *112*, 9161.
39. (a) Levy, R. M.; Sheridan, R. P.; Keepers, J. W.; Dubey, G. S.; Swaminathan, S.; Karplus, M. A. *Biophysical Journal* **1985**, *48*, 509. (b) Levy, R. M.; Keepers, J. W. *Comments on Molecular and Cellular Biophysics* **1985**, *48*, 509.

40. Scheer, J.; Beese, D.; Steiner, R.; Angerhofer, A. In *The Photosynthetic Bacterial Reaction Center*; Vermeglio, A., Ed.; Plenum: London, 1988, p. 101.
41. *Perspectives in Photosynthesis; The Jerusalem Symposia on Quantum Chemistry and Biochemistry 22*, Jortner, J.; Pullman, B., Eds.; Kluwer Academic Publishers: Dordrecht, 1990.
42. (a) Ringe, D.; Petsko, G. A.; Kerr, D. E.; Ortiz de Montellano, P. R. *Biochemistry* **1984**, *23*, 2. (b) Ringe, D.; Petsko, G. A. *Progress in Biophysics and Molecular Biology* **1985**, *47*, 197.
43. Levy, R. M.; Karplus, M.; McCammon, J. A. *J. Am. Chem. Soc.* **1981**, *103*, 994.
44. (a) Richarz, R.; Nagayama, K.; Wüthrich, K. *Biochemistry* **1980**, *19*, 5189. (b) Lipari, G.; Szabo, A. *J. Am. Chem. Soc.* **1982**, *104*, 4559.
45. Lipari, G.; Szabo, A.; Levy, R. M. *Nature* **1982**, *300*, 197.
46. (a) Wagner, G.; Wüthrich, K. *J. Mol. Biol.* **1982**, *160*, 343. (b) Griffey, R. H.; Redfield, A. G.; Loomis, R. E.; Dahlquist, F. W. *Biochemistry* **1985**, *24*, 817.
47. (a) Nadler, W.; Schulten, K. *Proc. Natl. Acad. Sci., U. S. A.* **1984**, *81*, 5719. (b) Parak, F.; Knapp, E. W. *Proc. Natl. Acad. Sci., U. S. A.* **1984**, *81*, 7088.
48. Hartmann, H.; Parak, F.; Steigemann, W.; Petsko, G. A.; Ringe Ponzi, D.; Frauenfelder, H. *Proc. Natl. Acad. Sci., U. S. A.* **1982**, *79*, 4967.
49. (a) Kasprzak, A.; Weber, G. *Biochemistry* **1982**, *21*, 5924. (b) Lakowicz, J. R.; Maliwal, B. P. *J. Biol. Chem.* **1983**, *258*, 4794.

50. (a) Hynes, J. T.; In *The Theory of Chemical Reactions*; Baer, M., Ed.; CRC Press: Boca Raton, FL, 1985; Vol.4, p 171.
51. McManis, G. E.; Gochev, A.; Weaver, M. J. *J. Chem. Phys.* **1991**, *152*, 107.
52. Marcus, R. A. *J. Chem. Phys.* **1956**, *24*, 966; 979.
53. Marcus, R. A. *Ann. Rev. Phys. Chem.* **1964**, *15*, 155.
54. (a) Levich, V. G.; Dogonadze, R. R. *Dokl. Acad. Nauk SSSR* **1959**, *124*, 123. (b) Levich, V. G. *Electrochem. Eng.* **1965**, *4*, 249.
55. (a) Landau, L. *Phys. Z. Sowj. U.* **1932**, *1*, 88. (b) Zener, C. *Proc. R. Soc. Lond. A* **1932**, *137*, 696.
56. Zusman, L. D. *Chem. Phys.* **1980**, *49*, 295.
57. Alexandrov, I. V. *Chem. Phys.* **1980**, *51*, 449.
58. (a) Tembe, B. L.; Friedman, H. L.; Newton, M. *Chem. Phys.* **1982**, *76*, 1490. (b) Newton M. D.; Friedman, H. L.; *J. Chem. Phys.* **1988**, *88*, 4460.
59. (a) Sumi, H.; Marcus, R. A. *J. Chem. Phys.* **1986**, *84*, 4894. (b) Nadler, W.; Marcus, R. A. *J. Chem. Phys.* **1987**, *86*, 3906.
60. Calef, D. F.; Wolynes, P. G. *J. Phys. Chem.* **1983**, *87*, 3387.
61. Garg, A.; Onuchic, J. N.; Ambegaokar, V. *J. Chem. Phys.* **1985**, *83*, 4491. (b) Onuchic, J. N. *J. Chem. Phys.* **1987**, *86*, 3925.
62. Sparpaglione, M.; Mukamel, S. *J. Phys. Chem.* **1987**, *91*, 3938. (b) Sparpaglione, M.; Mukamel, S. *J. Chem. Phys.* **1988**, *88*, 3263; 4300.
63. (a) Hynes, J. T. *J. Phys. Chem.* **1986**, *90*, 3701. (b) van der Zwan, G.; Hynes, J. T. *Chem. Phys.* **1991**, *152*, 169.
64. Belousov, A.A.; Kuznetsov, A.M.; Ulstrup, J. *Chem. Phys.* **1989**, *129*, 311.



65. (a) Rips, I.; Jortner, J. *J. Chem. Phys.* **1987**, *87*, 2090. (b) Rips, I.; Jortner, J. *J. Chem. Phys.* **1987**, *87*, 6513. (c) Rips, I.; Jortner, J. *Chem. Phys. Lett.* **1987**, *133*, 411. (d) Rips, I.; Jortner, J. *J. Chem. Phys.* **1988**, *88*, 818.
66. (a) Morillo, M.; Cukier, R. I. *J. Chem. Phys.* **1988**, *88*, 6736. (b) Yang, D. Y.; Cukier, R. I. *J. Chem. Phys.* **1989**, *91*, 281.
67. Cukier, R. I. *J. Chem. Phys.* **1988**, *88*, 5584.
68. Marcus, R. A.; Sutin, N. *Biochem. Biophys. Acta.* **1985**, *811*, 265.
69. Ulstrup, J.; In *Charge Transfer Processes in Condensed Media, Lecture Notes in Chemistry*; Springer: Berlin, 1979.
70. Nocera, D. G.; Cukier, R. I. *J. Chem. Phys.* **1992**, *87*, 7375.
71. Bixon, M.; Jortner J. *Chem. Phys.* **1993**, in press.
72. Marcus, R. A. *J. Chem. Phys.* **1963**, *38*, 1858. (b) Marcus, R. A. *J. Chem. Phys.* **1965**, *43*, 1261.
73. Böttcher, C. J. F.; Bordewijk, P.; *Theory of Electronic Polarization*; Elsevier: Amsterdam, 1978 vol. 2.
74. (a) Bakshiev, N. G. *Opt. Spectrosc.* **1964**, *16*, 446. (b) Mazurenko, Y. T.; Bakshiev, N. G. *Opt. Spectrosc.* **1970**, *28*, 490.
75. (a) Friedman, H. L. *J. Chem. Soc., Faraday Trans. 2*, **1983**, *79*, 1465. (b) Bagchi, B.; Oxtoby, D. W.; Fleming, G. R. *Chem. Phys.* **1984**, *86*, 257. (c) van der Zwan, G.; Hynes, J. T. *J. Phys. Chem.* **1985**, *89*, 4181.
76. (a) Barbara, P. F.; Jarzeba; W. *Adv. Photochem.* **1990**, *15*, 1. (b) Barbara, P. F.; Walker, G. C.; Smith, T. P. *Science* **1992**, *256*, 975.
77. (a) Maroncelli, M.; MacInnis, J.; Fleming, G. R. *Science* **1989**, *243*, 1674. (b) Maroncelli, M. *J. Mol. Liqs.*, in press.

78. (a) Simon, J. D. *Acc. Chem. Res.* **1988**, *21*, 128. (b) Simon, J. D. *Pure. Appl. Chem.* **1990**, *62*, 2243.
79. (a) Kosower, E. M.; Huppert, D. *Ann. Rev. Phys. Chem.* **1986**, *37*, 127. (b) Ittah, V.; Kosower, E. M. *Chem. Phys. Lett.* **1988**, *144*, 15. (c) Ittah, V.; Kosower, E. M. *Chem. Phys. Lett.* **1988**, *150*, 349.
80. (a) Castner, E. W., Jr.; Fleming, G. R.; Bagchi, B. *Chem. Phys. Lett.* **1988**, *143*, 270. (b) Castner, E. W.; Bagchi, B.; Fleming, G. R. *Chem. Phys. Lett.* **1988**, *148*, 269. (c) Castner, E. W., Jr.; Fleming, G. R.; Bagchi, B.; Maroncelli, M. *J. Chem. Phys.* **1988**, *89*, 3519.
81. (a) Rips, I.; Klafter, J.; Jornter, J. *J. Chem. Phys.* **1988**, *88*, 3246. (b) Rips, I.; Klafter, J.; Jornter, J. *J. Chem. Phys.* **1988**, *89*, 4288.
82. (a) Wolynes, P. G. *J. Chem. Phys.* **1987**, *86*, 5133. (b) Friedrich, V.; Kivelson, D. *J. Chem. Phys.* **1988**, *86*, 6425. (c) Nichols, A. L., III; Calef, D. F. *J. Chem. Phys.* **1988**, *89*, 3783.
83. Onsager, L. *Can. J. Chem.* **1977**, *55*, 1819.
84. Papzyan, A.; Maroncelli, M. *J. Chem. Phys.* **1993**, in press.
85. Bagchi, B.; Fleming, G. R. *J. Phys. Chem.* **1990**, *94*, 9.
86. Weaver, M. J. *Chem. Rev.* **1992**, *92*, 463.
87. Wasielewski, M. R. *Chem. Rev.* **1992**, *92*, 435.
88. (a) Gust, D.; Moore, T. A.; Moore, A. L.; Lee, S. J.; Bittersmann, E.; Luttrull, D. K.; Rehms, A. A.; DeGraziano, J. M.; Ma, X. C.; Gao, F.; Belford, R. E.; Trier, T. T. *Science* **1990**, *248*, 199. (b) Gust, D.; Moore, T. A. *Adv. Photochem.* **1991**, *16*, 1.
89. (a) Osuka, A.; Yamada, H.; Maruyama, K. *Chem. Lett.* **1990**, 1905. (b) Osuka, A.; Yamada, H.; Maruyama, K.; Mataga, N.; Asahi, T.; Yamazaki, I.; Nishimura, Y. *Chem. Phys. Lett.* **1991**, *181*, 419.

90. (a) Smit, K. J.; Warman, J.; De Haas, M. P.; Paddon-Row, M. N.; Oliver, A. M. *Chem. Phys. Lett.* **1988**, *152*, 177. (b) Oliver, A. M.; Craig, D. C.; Paddon-Row, M. N.; Kroon, J.; Verhoeven, J. W. *Chem. Phys. Lett.* **1988**, *150*, 366. (c) Warman, J. A.; Smit, K. J.; de Haas, M. P.; Jonker, S. A.; Paddon-Row, M. N.; Oliver, A. M.; Kroon, J.; Oevering, H.; Verhoeven, J. W. *J. Phys. Chem.* **1991**, *95*, 1979.
91. (a) Closs, G. L.; Calcaterra, L. T.; Green, N. J.; Penfield, K. W.; Miller, J. R. *J. Phys. Chem.* **1986**, *90*, 3673. (b) Closs, G. L.; Miller, J. R. *Science* **1988**, *240*, 440.
92. Calcaterra, L. T.; Closs, G. L.; Miller, J. R. *J. Am. Chem. Soc.* **1983**, *105*, 670.
93. (a) Helms, A.; Heiler, D.; McLendon, G. *J. Am. Chem. Soc.* **1991**, *113*, 4325. (b) Helms, A.; Heiler, D.; McLendon, G. *J. Am. Chem. Soc.* **1992**, *114*, 6227.
94. Cave, R.; Marcus, R.; Siders, P. *J. Phys. Chem.* **1986**, *90*, 1436.
95. Osuka, A.; Maruyama, K. *Chem. Lett.* **1987**, 825.
96. (a) Wasielewski, M. R.; Johnson, D. G.; Svec, W. A.; Kersey, K. M.; Minsek, D. W. *J. Am. Chem. Soc.* **1988**, *110*, 7219. (b) Wasielewski, M. R.; Gaines, G. L. III; O'Neil, M. P.; Niemczyk, M. P.; Svec, W. A. *J. Am. Chem. Soc.* **1990**, *112*, 4559. (c) Gaines, G. L. III; O'Neil, M. P.; Svec, W. A.; Niemczyk, M. P.; Wasielewski, M. R. *J. Am. Chem. Soc.* **1991**, *113*, 719.
97. (a) Cowan, J. A.; Sanders, J. K. M.; Beddard, G. S.; Harrison, R. J. *J. Chem. Soc., Chem. Comm.* **1987**, 55. (b) Harrison, R. J.; Pearce, B.; Beddard, G. S.; Cowan, J. A.; Sanders, J. K. M. *Chem. Phys.* **1987**, *116*, 429.

98. (a) Asahi, T; Ohkohchi, M.; Matsusaka, R.; Mataga, N.; Zhang, R. P.; Osuka, A.; Maruyama, K. *J. Am. Chem. Soc.* **1993**, *115*, 5665.
99. (a) Osuka, A.; Natgata, T; Maryuma, K. *Chem. Lett.* **1991**, 481 (b) Osuka, A.; Maruyama, K.; Mataga, N.; Asahi, T; Yamazaki, I.; Tamai, N.; Nishimura, Y. *Chem. Phys. Lett.* **1991**, *181*, 413. (c) Osuka, A.; Nakajima, S.; Maruyama, K.; Mataga, N.; Asahi, T; *Chem. Lett.* **1991**, 1003.
100. Chang, C. K., private communication.
101. Turró, C. T.; Chang, C.-K.; Leroi, G. E.; Cukier, R. I.; Nocera, D. G. *J. Am. Chem. Soc.* **1992**, *114*, 4013.
102. (a) Harriman, A.; Kubo, Y.; Sessler, J. *J. Am. Chem. Soc.* **1992**, *114*, 388. (b) Harriman, A.; Kubo, Y.; Sessler, J. *J. Am. Chem. Soc.* **1993**, in press.
103. Chang, C. K. *Heterocycl. Chem.* **1977**, *14*, 1285.
104. Eaton, S. S.; Eaton, G. R.; Chang, C. K. *J. Am. Chem. Soc.* **1985**, *107*, 3177.
105. (a) Chang, C.K.; Sotiriou, C. *J. Heterocycl. Chem.* **1985**, *22*, 1739. (b) Chang, C.K.; Sotiriou, C.; Wu, W. *J. Chem. Soc., Chem. Comm.* **1986**, 1213.
106. Chang, C. K.; Wu, W. U.S. Patent #5,064,952, November 12, 1991.
107. Gagne, R. R.; Kival, C. A.; Lisensky, G. C. *Inorg. Chem.* **1980**, *19*, 2854.
108. Mussell, R. D.; Nocera, D. G. *J. Am. Chem. Soc.* **1988**, *110*, 2764.
109. Hopkins, M. D.; Gray, H. B. *J. Am. Chem. Soc.* **1984**, *106*, 2468.
110. Demas, J. N.; Crosby, G. A. *J. Phys. Chem.* **1971**, *75*, 991.
111. *Ultrafast Light Pulses*; Shapiro, S. L., Ed; Springer-Verlag: Berlin; **1977**.

112. Atkins, P. W. *Physical Chemistry* 4th Ed.; Freeman: New York, 1990.
113. Declémy, A.; Rullière, C. *Rev. Sci. Instrum.* **1986**, *57*, 2773.
114. (a) Jackson, J. A.; Turro, C. T.; Newsham, M. D.; Nocera, D. G. *J. Phys. Chem.* **1990**, *94*, 4500. (b) Turro, C. T. Ph.D. Dissertation, Michigan State University, 1992.
115. Bowman, L. E.; Berglund, K. A.; Nocera, D. G. *Rev. Sci. Instrum.* **1993**, *64*, 338.
116. Weaver, M. J.; McManis, G. E. *Acc. Chem. Res.* **1990**, *23*, 294.
117. Mussell, R. D.; Nocera, D. G. *J. Phys. Chem.* **1991**, *95*, 6919.
118. Nielson, R. M.; McManis, G. E.; Golovin, M. N.; Weaver, M. J. *J. Phys. Chem.* **1988**, *92*, 2441.
119. (a) Fujita, I.; Fajer, J.; Chang, C. K.; Wang, C. B.; Bergkamp, M. A.; Netzel, T. L. *J. Phys. Chem.* **1982**, *86*, 3754. (b) Netzel, T. L.; Bergkamp, M. A.; Chang, C. K. *J. Am. Chem. Soc.* **1982**, *104*, 1952. (c) Fujita, I.; Netzel, T. L.; Chang, C. K.; Wang, C. B.; *Proc. Natl. Acad. Sci., U. S. A.* **1982**, *79*, 413.
120. (a) Petke, J. D.; Maggiora, G. M. *Chem. Phys. Lett.* **1983**, *97*, 231. (b) Petke, J. D.; Maggiora, G. M. *J. Chem. Phys.* **1986**, *84*, 1640.
121. Hugerat, M.; Galili, T.; Chang, C. K.; Fajer, J.; Levanon, H. *J. Phys. Chem.* **1993**, *in press*.
122. Mest, Y. L.; L'Her, M.; Hendricks, N. H.; Kim, K.; Collman, J. P. *Inorg. Chem.* **1992**, *31*, 835.
123. Kadish, K. M. In *Progress in Inorganic Chemistry*; Lippard, S. J., Ed.; Wiley: New York, 1986; Vol. 34.
124. This value is referenced to  $\Delta E$  measured for the Mg—H<sub>2</sub> dimer in dichloromethane solution as reported in reference 119a.

125. Chang, C. K. In *Inorganic Compounds with Unusual Properties – II*; King, R. B., Ed.; Advances in Chemistry Series 173; American Chemical Society: Washington, DC, 1979; p 162.
126. Rodriguez, J.; Kirmaier, C.; Holten, D. *J. Am. Chem. Soc.* **1989**, *111*, 6500.
127. The luminescence lifetimes of the Zn-porphyrin and free base keto-chlorin monomeric subunits were determined by time-correlated single photon counting with 575 nm excitation. Lifetimes of 1.8 ns and 7.2 ns, respectively, in *n*-propyl acetate were extracted from monoexponential fits to the luminescence decay at 640 nm.
128. (a) Zaleski, J. M.; Chang, C. K.; Leroi, G. E.; Cukier, R. I.; Nocera, D. G. *J. Am. Chem. Soc.* **1992**, *114*, 3564. (b) Zaleski, J. M.; Chang, C. K.; Leroi, G. E.; Cukier, R. I.; Nocera, D. G. *Chem. Phys.* **1993**, in press. (c) Zaleski, J. M.; Chang, C. K.; Nocera, D. G. *J. Phys. Chem.* **1993**, submitted for publication.
129. Fuhrhop, J.-H.; Kadish, K. M.; Davis, D. G. *J. Am. Chem. Soc.* **1973**, *95*, 5140.
130. (a) Wasielewski, M. R.; Johnson, D. G.; Niemczyk, M. P.; Gaines, G. L. III; O'Neil, M. P.; Svec, W. A. *J. Am. Chem. Soc.* **1990**, *112*, 6482. (b) Johnson, D. G.; Niemczyk, M. P.; Minsek, D. W.; Wiederrecht, G. P.; Svec, W. A.; Gaines, G. L. III; Wasielewski, M. *R J. Am. Chem. Soc.* **1993**, *115*, 5692.
131. (a) Mialocq, J. C.; Giannotti, C.; Maillard, P.; Momenteau, M. *Chem. Phys. Lett.* **1984** *112*, 87. (b) Ohno, O.; Ogasawara, Y.; Asano, M.; Kajii, Y.; Kaizu, Y.; Obi, K.; Kobayashi, H. *J. Phys. Chem.* **1987** *91*, 4269. (c) Sessler, J. L.; Capuano, V. L.; Harriman, A. *J. Am. Chem. Soc.* **1993**, *115*, 4618.

132. An excited state for the chlorin of 1.85 eV is estimated from the overlap of the absorption and emission spectra in the 0,0 spectral region.
133. (a) Gaines, G. L. III; O'Neil, M. P.; Svec, W. A.; Niemczyk, M. P.; Wasielewski, M. R. *J. Am. Chem. Soc.* **1991**, *113*, 719. (b) Harriman, A.; Heitz, V.; Sauvage, J.-P. *J. Phys. Chem.* **1993**, *97*, 5940.
134. (a) Åkesson, E.; Walker, G. C.; Barbara, P. F. *J. Chem. Phys.* **1991**, *95*, 4188. (b) Åkesson, E.; Johnson, A. E.; Levinger, N. E.; Walker, G. C.; Barbara, P. F. *J. Chem. Phys.* **1992**, *96*, 7859.
135. Jortner, J.; Bixon, M. *J. Chem. Phys.* **1988**, *88*, 167.
136. This model is commonly illustrated by Barbara as an excited state D—A surface being intersected at several points by a series of ground state  $D^+—A^-$  surfaces representing high frequency vibrational modes of the ground state.
137. Pöllinger, F.; Heitele, H.; Michel-Beyerle, M. E.; Anders, C.; Futscher, M.; Staab, H. A. *Chem. Phys. Lett.* **1992**, *198*, 645.
138. Kobayashi, T.; Takagi, Y.; Kandori, H.; Kemnitz, K.; Yoshihara, K. *Chem. Phys. Lett.* **1991**, *180*, 416.
139. Kim, D.; Holten, D.; Gouterman, M. *J. Am. Chem. Soc.* **1984**, *106*, 2793.
140. (a) Hudson, B. P.; Sou, J.; Berger, D. J.; McMillin, D. R. *J. Am. Chem. Soc.* **1992**, *114*, 8997. (b) McMillin, D. R.; Hudson, B. P.; Liu, F.; Sou, J.; Berger, D. J.; Meadows, K. A. in *Photosensitive Metal-Organic Systems*; Kutal, C., Serpone, N., Eds.; Advances in Chemistry Series 238; American Chemical Society: Washington, DC, 1993; p 211.

141. (a) Brookfield, R. L.; Ellul, H.; Harriman, A. *J. Chem. Soc., Faraday Trans. 2* **1985**, *81*, 1837.
142. Anton, J. A.; Loach, P. A.; Govindjee *Photochem. Photobiol.* **1978**, *28*, 235.
143. Davis, D. G. In *The Porphyrins*; Dolphin, D., Ed.; Academic Press: New York, 1978; Vol. V.
144. Weiss, C. In *The Porphyrins*; Dolphin, D., Ed.; Academic Press: New York, 1978; Vol. III, p. 211.
145. Seybold, P. G.; Gouterman, M. *J. Mol. Spec.* **1969**, *31*, 1.
146. Weber, G.; Teale, F. W. J. *Trans. Faraday Soc.* **1957**, *53*, 646.
147. The luminescence lifetimes of the Zn-porphyrin and free base dicyanomethide chlorin monomers were determined by time-correlated single photon counting with 575 nm excitation. Lifetimes of 1.8 ns (*n*-propyl acetate) and 6.3 ns (dichloromethane), respectively, were obtained from monoexponential fits to the luminescence decay at 640 nm.
148. Fajer, J.; Borg, D. C.; Forman, A.; Dolphin, D.; Felton, R. H. *J. Am. Chem. Soc.* **1970**, *92*, 3451.
149. Fujita, I.; Davis, M. S.; Fajer, J. *J. Am. Chem. Soc.* **1978**, *100*, 6280.
150. (a) Magde, D.; Windsor, M. W.; Holten, D.; Gouterman, M. *Chem. Phys. Lett.* **1974**, *29*, 183. (b) Kobayashi, T.; Huppert, D.; Straub, K. D.; Retzepis, P. M. *Photochem. Photobiol.* **1979** *70*, 1720.
151. Matthews, J. I.; Braslavsky, S. E.; Camilleri, P. *Photochem. Photobiol.* **1980** *32*, 733.



152. (a) Gaines, G. L. III; O'Neil, M. P.; Svec, W. A.; Niemczyk, M. P.; Wasielewski, M. R. *J. Am. Chem. Soc.* **1991**, *113*, 719. (b) Tapolsky, G.; Duesing, R.; Meyer, T. J. *J. Phys. Chem.* **1991**, *95*, 1105. (c) Liu, J.; Schmidt, J. A.; Bolton, J. R. *J. Phys. Chem.* **1991**, *95*, 6924. (d) Katritzky, A. R.; Zhu, D. W.; Schanze, K. S. *J. Phys. Chem.* **1991**, *95*, 5737. (e) Wasielewski, M. R.; Johnson, D. G.; Niemczyk, M. P.; Gaines, G. L. III; O'Neil, M. P.; Svec, W. A. *J. Am. Chem. Soc.* **1990**, *112*, 6482. (f) Isied, S. S.; Vassilian, A.; Wishart, J. F.; Creutz, C.; Schwarz, H. A.; Sutin, N. *J. Am. Chem. Soc.* **1988**, *110*, 635.
153. Nielson, R. M.; McManis, G. E.; Golovin, M. N.; Weaver, M. J. *J. Phys. Chem.* **1988**, *92*, 2441.

MICHIGAN STATE UNIV. LIBRARIES



31293010517849